DEPARTAMENTO DE ASTROFÍSICA

Universidad de La Laguna

# *Unveiling the Nature of the Most Luminous Galaxies at the Cosmic Noon*

Memoria que presenta
Rui Marques Chaves
para optar al grado de
Doctor por la Universidad de La Laguna.


INSTITUTO Đ ASTROFISICA Đ CANARIAS
julio de 2018

Examination date: September, 2018
Thesis supervisor: Dr. Ismael Pérez Fournon

**Resumen**

Esta tesis se centra en el estudio de las propiedades físicas de galaxias con desplazamientos al rojo entre 2.3 y 3.3, un período de tiempo donde las galaxias forman activamente estrellas y evolucionan rápidamente. El trabajo estudia diferentes poblaciones de galaxias, desde galaxias jóvenes emisoras en la línea de Ly$\alpha$ (LAEs) y con salto de Lyman (LBGs), hasta otras más evolucionadas detectadas en el rango submilimétrico con el *Observatorio Espacial Herschel* (SMGs). Debido al bajo brillo aparente de estas galaxias, se emplea el efecto de lente gravitatoria en estudios de alta señal a ruido (S/N) para explorar en profundidad sus propiedades en una perspectiva pancromática, con un énfasis particular en la emisión del ultravioleta (UV) en el sistema en reposo.

Primero, se presenta el proyecto BELLS GALLERY, un cartografiado dedicado a identificar sistemas de lentes gravitatorias con galaxias emisoras de Ly$\alpha$ a $2 < z < 3$ como fuentes de fondo. Dentro de este proyecto, el trabajo de la tesis presenta el descubrimiento de dos nuevas LAEs, de las más brillantes e intrínsecamente más luminosas conocidas hasta la fecha. Además, se lleva a cabo un estudio fotométrico y espectroscópico con el Gran Telescopio Canarias y el Telescopio William Herschel de seis de estas LAEs amplificadas por lente. Se derivan las propiedades principales de estas galaxias, como las luminosidades en la línea Ly$\alpha$ y el UV, las tasas de formación de estrellas y la atenuación del polvo. También se emplean varios diagnósticos en el UV en sus espectros para estudiar la cinemática del medio interestelar y la distribución espacial observada del continuo UV y la emisión Ly$\alpha$.

En segundo lugar, se presenta una análisis detallado de HLock01 a $z = 2.96$, una de las SMGs amplificadas por lente más brillantes conocidas. Se muestra que HLock01 es un sistema en fusión compuesto por una galaxia SMG masiva y una LBG satélite, separadas por 3.3 kpc en proyección. Además, el espectro UV de la LBG evidencia movimientos de gas a gran escala, incluyendo gas que sale a alta velocidad de la LBG, caída de gas sobre la SMG, y un reservorio de gas a 110 kpc en proyección. Estos resultados constituyen una de las primeras confirmaciones observacionales de que la acreción de gas, junto con las fusiones continuadas de galaxias, son los principales mecanismos responsables de las tasas de formación de estrellas extremadamente grandes que se observan en muchas SMGs.

Por último, se presenta el descubrimiento y primer análisis de una gran región de emisión de Ly$\alpha$ a $z = 3.325$, no relacionada con HLock01, pero cercana en proyección. La nebulosa presenta emisión en la línea de Ly$\alpha$ con un tamaño de 110 kpc y una luminosidad $L_{\mathrm{Ly}\alpha} = (6.00 \pm 0.08) \times 10^{44}$ erg s$^{-1}$, siendo una de las nebulosas de Ly$\alpha$ más luminosas conocidas hasta la fecha. También presenta emisión extendida en líneas metálicas, tales como C IV, He II, y C III] con tamaños de $\sim 90$, 50 y 35 kpc, respectivamente. El origen de esta nebulosa está probablemente asociado con una galaxia activa de tipo 2 y su emisión en radio contenida en los $\sim 8$ kpc centrales.

**Summary**

This thesis focus on understanding the physical properties of galaxies at redshifts $2.3 < z < 3.3$, a time period called *Cosmic Noon* when galaxies were actively forming stars and evolving rapidly. The work involves the study of different galaxy populations, from young Ly$\alpha$ emitters (LAEs) and Lyman break galaxies (LBGs), to more evolved, and very actively star forming submillimeter galaxies (SMGs) detected with the *Herschel Space Observatory*. Because of the faintness of these high redshift galaxies, this work employ the power of the gravitational lens effect in high signal-to-noise (S/N) studies to probe deeply into their physical properties in a multi-wavelength approach, with particular emphasis to the rest-frame ultra-violet (UV) emission.

First, the BELLS GALLERY project is presented, a dedicated survey aimed to search for strong gravitationally lensed systems with $2 < z < 3$ LAEs as background sources. Within this project, the thesis work reports the discovery of two very bright lensed LAEs, that are within the brightest and intrinsically most luminous LAEs known so far at any redshift. In addition, results from a deep optical imaging and spectroscopic survey with the Gran Telescopio Canarias and the William Herschel Telescope targeting six of this new type of strong galaxy-scale lensed LAEs are described and discussed. The main properties of these lensed LAEs are derived, such as their Ly$\alpha$ and UV luminosities, star formation rates, and dust attenuation. Several rest-frame UV diagnostics are also employed on their high S/N spectra to study the kinematics of the interstellar medium and the observed spatial distribution of the UV continuum and Ly$\alpha$ emission.

Second, a detailed imaging and spectroscopic analysis of one of the brightest gravitationally lensed SMG, HLock01 at $z = 2.96$, is presented. It is shown that HLock01 is a merger system composed of a massive *Herschel*-selected SMG and an optically bright, satellite LBG, separated by only 3.3 kpc in projection. The high S/N rest-frame UV spectrum of the LBG also shows evidence of large scale gas motions, including gas outflows from the LBG, inflowing gas falling onto the *Herschel* SMG, and an extended reservoir of neutral gas at an impact parameter of 110 kpc. These results are one of the first observational confirmation that gas accretion, along with on-going mergers, are the main mechanisms responsible for the extremely large star formation rates seen in many SMGs.

Lastly, the serendipitous discovery of a large, extended Ly$\alpha$ nebula at $z = 3.325$ is presented. The nebula shows Ly$\alpha$ emission extended over 110 kpc with a total luminosity $L_{\mathrm{Ly}\alpha} = (6.00 \pm 0.08) \times 10^{44}$ erg s$^{-1}$, being one of the most luminous Ly$\alpha$ nebula known so far. It also shows extended emission of C IV, He II, and C III] over $\sim$ 90, 50, and 35 kpc, respectively. The origin of this nebula is likely associated with a massive type 2 active galaxy and the two faint radio lobes or jets contained within its central $\sim$ 8 kpc.

# Contents

# 1

# Introduction

The history of the Universe is a complex chain of events starting with the Big Bang 13.8 billion years ago, and ending with the structures that we observe. 380 000 years after the Big Bang (at a redshift $z \simeq 1100$), the temperature of the pre-existing hot plasma had cooled sufficiently (to $T \sim 3000\ K$), so that free electrons became bound to protons to form the first hydrogen and helium atoms, in a process called "recombination." Because the neutral Hydrogen is transparent to light, these photons could propagate freely with little scattering, and were able to travel long distances. Due to the expansion of the Universe, this primordial radiation, known as the Cosmic Microwave Background (CMB), can be observed today at long wavelengths ($1-2$ mm), equivalent to that emitted by a black body at a temperature of $T = 2.73\ K$ (Penzias & Wilson 1965).

The $\Lambda$ cold dark matter ($\Lambda$CDM) cosmology model is now widely accepted as the one that best explains our Universe. This model, known also as the standard model of Big Bang cosmology, contains a gravitationally repulsive effect (the cosmological constant $\Lambda$), associated with the so-called dark energy, inducing an observed accelerating expansion of the Universe (Riess et al. 1998; Perlmutter et al. 1999). Observations indicate that galaxies are distributed in a filament-dominated web-like structure (e.g., Jõeveer et al. 1978; Geller & Huchra 1989), commonly known as the "cosmic web." The large scale structure consists of early over-dense regions, the "nodes," which gravitationally pull more material from the surroundings.

The baryonic material that evolves within these structures is attracted and trapped by the strong potential wells of dark matter halos (Silk 1977). The gas can then collapse and contract to form the first stars and galaxies, the still elusive Population III (Pop III). Pop III stars mark the end of the cosmic dark ages, leading to a fundamental

transformation of the early Universe through the production of the first hydrogen-ionizing photons and the initial enrichment with chemical elements heavier than the hydrogen and helium. It is believed that the first generation of stars and galaxies had formed around 250 million years after the Big Bang (Hashimoto et al. 2018), beginning the so-called epoch of "reionization" (EoR), when young stars[1] within these early galaxies ionize hydrogen atoms in the neutral intergalactic medium (IGM). Th epoch of reionization ends when the IGM is fully ionized, about 1 Gyr after the Big Bang ($z \sim 6$).

## 1.1 Cosmic Star Formation History

Understanding how galaxies form and evolve throughout cosmic time is one of the most fundamental questions in observational cosmology today. Over the past decades, observational measurements of star formation rates (SFRs) of galaxies, from the EoR at $z \sim 8$ to the present time, show a consistent picture of the cosmic star formation history (see Lilly et al. 1996; Madau et al. 1996; Madau & Dickinson 2014, and references therein). Measurements of the total, comoving volume-normalized SFR, a quantity referred to as SFR density (SFRD), show that typical galaxies build up their mass with time from $z = 8$ to $z = 3$ in a rising phase, scaling as $\propto (1+z)^{-2.8}$, until the SFRD peaks at around $z \simeq 2$. After $z = 1$, when the Universe was $\sim 6$ Gyr old, the SFRD declines toward present times, roughly as $\propto (1+z)^{2.7}$ (see Figure 1.1; Madau & Dickinson 2014).

This Thesis focus on the specific epoch of the Universe when the star formation rate density reaches its peak, the cosmic "noon" around $z = 2-3$. Half of the present-day cosmic stellar mass density was already in place by $z \sim 2$ (Dickinson et al. 2003). Probing the formation mechanisms at this epoch is crucial to constrain the rapid phase of mass assembly in early galaxies and their overall evolution, having direct influence on the stellar populations and overall properties of galaxies seen in present times.

## 1.2 Different types of galaxies at high redshift

Over the past decades, several multi-wavelength surveys have been used to find galaxies at high redshift. Since these surveys select galaxies via different parts of their electromagnetic spectrum, from the X-ray to the sub-millimeter and radio, they probe a diverse population of galaxies. In the following subsections I will summarize the most common galaxies found in the high-$z$ Universe, with particular emphasis to the type of galaxies studied in this Thesis.

[1] Although see Madau & Haardt (2015) for other alternative sources contributing to the reionization.

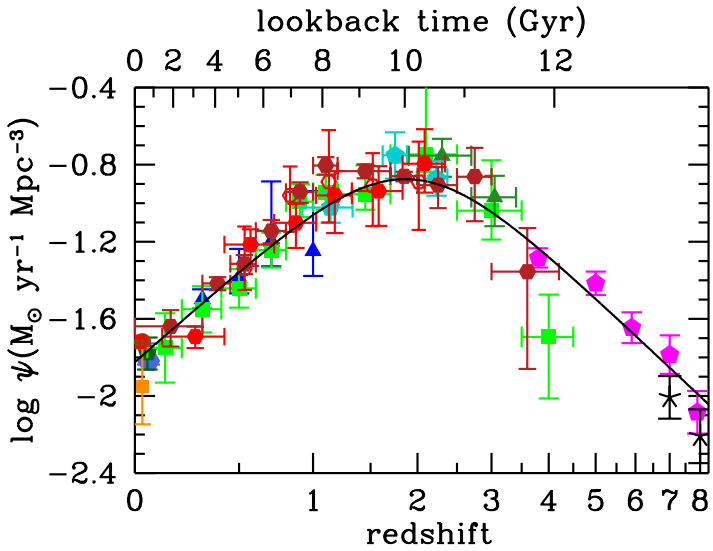


Figure 1.1: The cosmic evolution of the star formation rate density, obtained from a compilation of multiple surveys (selected from the rest-frame ultraviolet or the infrared). The best-fitting model is plotted as a black line and shows a strong peak at $z \sim 2$ (figure adapted from Madau & Dickinson 2014).

### 1.2.1 Lyman break galaxies

Lyman break galaxies (LBGs) are star-forming galaxies selected through multi-band imaging across the rest-frame 912 Å Lyman-continuum discontinuity. This technique exploits the effects of both the neutral hydrogen opacity within a galaxy and IGM absorption along the line of sight.

At high redshift, the 912 Å Lyman limit is redshifted into the optical, being accessible to ground-based broad-band observations. The Lyman break technique was originally explored 25 five years ago by Steidel & Hamilton (1993) and Steidel et al. (1995) using three optical bands $U_{\rm n}GR$ to select LBGs at $z \sim 3$ (see Figure 1.2). The selection of LBGs at $z \sim 3$ of those studies was:

$$(U_{\rm n} - G) \geq 1.0 + (G - R); \quad (G - R) \leq 1.2, \tag{1.1}$$

where the $U_{\rm n}$, $G$, and $R$ optical bands (in the AB system Oke & Gunn 1983) probe respectively the rest-frame 870, 1120, and 1550Å at $z \sim 3$, i.e., on either side of the

redshifted break. These $z \sim 3$ galaxies are also called $U_n$-band dropouts, since they are fainter in the $U_{\rm n}$ band than in the $R$ band. An additional requirement of $R < 25.5$ is usually imposed to select relatively *bright* galaxies for spectroscopic follow-up (e.g., Giavalisco et al. 1994; Steidel et al. 1996; Shapley et al. 2003).

Since the selection is based on the rest-frame UV, these techniques select galaxies with ongoing star formation and are not sensitive to passive galaxies. For the same reason, the selection criteria may exclude galaxies with significant dust reddening.

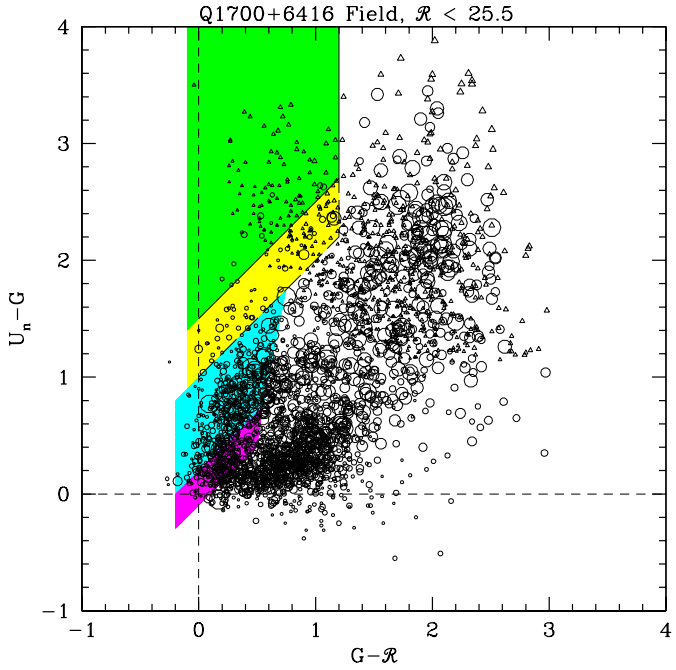


Figure 1.2: This figure is taken from Steidel et al. (2004) and shows the two-colour ($U_{\rm n} - G$ versus $G - R$) diagram demonstrating the Lyman break technique. Yellow and green shaded regions are the $z \sim 3$ LBG color select windows (the green shaded region selects "robust" $z \sim 3$ candidates, avoiding less contamination from low-$z$ objects than the original selection criteria from Equation 1.1), whereas the cyan and magenta regions select galaxies at $z \simeq 2 - 2.5$ and $z \simeq 1.5 - 2.0$, respectively.

The Lyman break or dropout technique is one of the most efficient methods to select high-$z$ galaxies.[2] Moreover, thanks to the improvement in the efficiency of near-IR

[2]Note that these techniques have also been applied to select lower-$z$ ($\sim 0.5 - 1.5$) LBGs using mainly

detectors, and in particular to the advent of the high sensitivity provided by the *Hubble Space Telescope* (*HST*) WFC3 near-infrared (near-IR) instrument, these techniques have also been successfully employed to select thousands of galaxies (candidates) up to $z \simeq 12$ (e.g., Bouwens et al. 2013; Ellis et al. 2013; Oesch et al. 2013; Bouwens et al. 2014; Laporte et al. 2014; Bouwens et al. 2015; Laporte et al. 2015, 2016), although only very few have been spectroscopically confirmed to be at $z \sim 7-9$ through the detection of Ly$\alpha$ emission (see: Oesch et al. 2015; Zitrin et al. 2015; Roberts-Borsani et al. 2016; Laporte et al. 2017; Hashimoto et al. 2018).

Large and deep multi-wavelength surveys using rest-frame UV colors have provided an almost complete census of these star-forming galaxies by measuring their luminosity functions (LFs) to constrain the overall abundance of these galaxies and the integrated luminosity density (e.g., Steidel et al. 1999; Bouwens et al. 2007; Reddy et al. 2008; Reddy & Steidel 2009; Bouwens et al. 2015). Due to the faintness of LBGs in all the spectral range, even in their rest-frame UV where they are selected ($m_{\rm UV} \simeq 24.5$ AB at $z \sim 3$, e.g., Reddy et al. 2008), they have been studied mainly by collecting large amounts of imaging and spectroscopic datasets (e.g., Shapley et al. 2003; Magdis et al. 2010a,b,c; Steidel et al. 2010; Jones et al. 2012; Talia et al. 2012; Du et al. 2018). These UV-selected galaxies are roughly characterized by star formation rates of $10-100\ M_\odot\ {\rm yr}^{-1}$, moderate amounts of dust extinction ($E(B-V) \sim 0.1-0.2$), and stellar masses $M_* \sim 10^{10}\ M_\odot$ (see e.g., Shapley et al. 2003; Erb et al. 2006). They also show relatively compact morphologies, with typical sizes (half-light radius) of 2 kpc at $z \simeq 2$ to 1 kpc at $z \simeq 4$ (see: van der Wel et al. 2014; Curtis-Lake et al. 2016; Ribeiro et al. 2016).

### 1.2.2 Lyman-alpha emitters

Lyman-$\alpha$ emitting galaxies, or simply Lyman-$\alpha$ emitters (LAEs), are young, dwarf, star-forming galaxies that emit Ly$\alpha$ radiation from the photoionization of neutral hydrogen by young hot stars.

LAEs have been detected mainly with narrow-band imaging of their strong Ly$\alpha$ emission line (with large rest-frame equivalent widths, $EW_0 > 20$ Å), with additional galaxies detected in spectroscopy (for example by using the $1' \times 1'$ wide Multi Unit Spectroscopic Explorer, MUSE; see: Wisotzki et al. 2016; Leclercq et al. 2017).

Over the past decades, deep narrow-band surveys over small areas have routinely detected LAEs over a wide range of redshifts. Originally, LAEs were detected by Cowie & Hu (1998) and Hu et al. (1998) at $z \simeq 3.4$ in the *Hubble* Deep Field and the Hawaii Deep Field SSA 22. More recently, other surveys, such as the Large Area Lyman Alpha Survey (LALA: Rhoads et al. 2000; Malhotra & Rhoads 2004) and, in

UV space observatories such as the *Galaxy Evolution Explorer* (*GALEX*) or *Swift* (e.g., Burgarella et al. 2006; Ly et al. 2009; Basu-Zych et al. 2011; Oteo et al. 2013).

particular, the Subaru deep field surveys (e.g., Ajiki et al. 2003; Ouchi et al. 2003; Kashikawa et al. 2004; Ouchi et al. 2005; Taniguchi et al. 2005; Iye et al. 2006; Murayama et al. 2007; Ouchi et al. 2010; Matthee et al. 2015; Ouchi et al. 2018; Songaila et al. 2018), have used specific narrow-band filters centered in regions of low contamination of OH nigh sky emission to extend the detection of LAEs to much higher redshifts (e.g., at $z = 5.7$, 6.6 or 7.0, see Figure 1.3). They have also allowed the discovery of galaxies at the epoch of reionization ($z > 6$) with extreme luminosities in the Ly$\alpha$ line (up to $4 \times L^*_{\mathrm{Ly}\alpha}$, where $L^*_{\mathrm{Ly}\alpha} = 2 \times 10^{43}$ erg s$^{-1}$ is the typical Ly$\alpha$ luminosity at $z \simeq 6.6$, Santos et al. 2016), such as the Himiko galaxy (Ouchi et al. 2009), the Cosmic Redshift 7 galaxy (CR7: Sobral et al. 2015), and few others (e.g., Kashikawa et al. 2011; Sobral et al. 2015; Hu et al. 2016; Matthee et al. 2017; Shibuya et al. 2018).

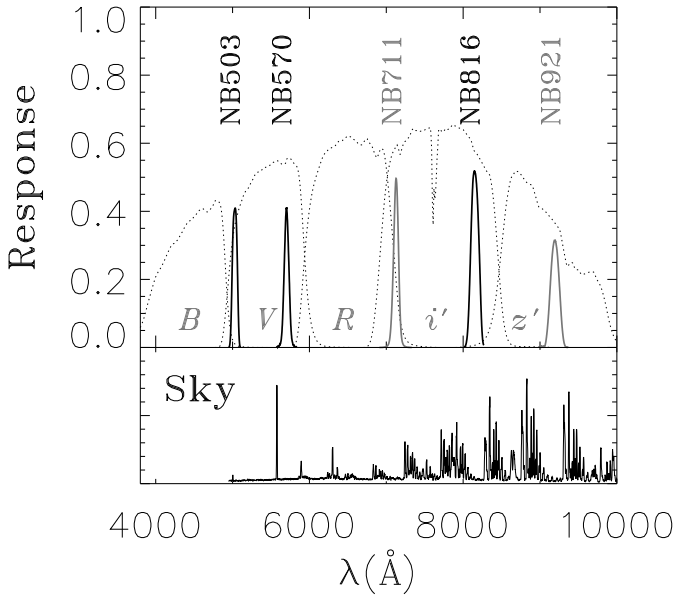


Figure 1.3: This figure is taken from Ouchi et al. (2008) and shows five narrow-band filters specifically designed to select Ly$\alpha$ emission at several redshifts, between $z = 3.1$ and $z = 6.6$. Note that the passbands of the narrow-band filters do not include a strong sky emission.

Moreover, these surveys have provided statistical properties of LAEs up to $z \sim 7$, including the evolution of Ly$\alpha$ LFs (e.g., Malhotra & Rhoads 2004; Ouchi et al. 2008, 2010; Zheng et al. 2016, 2017; Ota et al. 2017). Multi-wavelength follow-up

imaging and spectroscopy have revealed that typical ($L^*$) LAEs, with Ly$\alpha$ luminosities ranging between $L_{\mathrm{Ly}\alpha} \sim 10^{42-43}$ erg s$^{-1}$ at $z \sim 2-3$, respectively, have relatively low stellar masses ($M_* \simeq 10^8 - 10^9\ M_\odot$; e.g., Gawiser et al. 2007; Ono et al. 2010; Hagen et al. 2014), show modest star-formation rates (SFR $\sim 10\ M_\odot$ yr$^{-1}$, e.g., Nakajima et al. 2012; Sobral et al. 2018b), and present, on average, low gas-phase metallicity ($\sim 0.1 Z_\odot$, e.g., Finkelstein et al. 2011b; Kojima et al. 2017).

Typical LAEs show also compact morphologies (effective radius $r_{\mathrm{eff}} \simeq 1$ kpc) with little to no evolution with redshift (e.g., Bond et al. 2009; Taniguchi et al. 2009; Bond et al. 2012; Paulino-Afonso et al. 2018). Since LAEs have low stellar mass and present strong Ly$\alpha$ emission, which is indicative of a young starburst, they have been used as probes of the very first galaxies in the Universe.

Although LAEs may share several of its physical properties with those of LBGs (in particular with LBGs showing strong Ly$\alpha$ emission, e.g., Shapley et al. 2003; Verhamme et al. 2008), given the nature of the search strategy, narrow-band selected LAEs are typically much fainter in the continuum than the UV broad-band selected LBGs. LAEs present, in general, lower metallicity and younger stellar population than LBGs. Furthermore, LAEs appear to have bluer UV continua than non-emitters, with little or no dust content. LAEs present also much higher [O III]/[O II] line ratios, indicative of the high ionization state of the interstellar medium (ISM) originated by intense ionizing radiation from young massive stars (e.g., Nakajima & Ouchi 2014; Nakajima et al. 2016).

Another important observable feature of LAEs is the spatially extended Ly$\alpha$ emission, which can exceed several 10 kpc (e.g., Steidel et al. 2011; Momose et al. 2014; Wisotzki et al. 2016; Sobral et al. 2017). Because of the resonant nature of the Ly$\alpha$ line, Ly$\alpha$ photons are scattered by H I gas, both in the ISM and in the circumgalactic medium (CGM), allowing them to be directly observed at high redshift. Furthermore, the combination of the emergent Ly$\alpha$ flux (line profile) and radiation transfer models provide important information about the ISM and the CGM (e.g., Verhamme et al. 2008; Schaerer & Verhamme 2008; Hashimoto et al. 2015; Momose et al. 2016).

### 1.2.3 Sub-millimeter galaxies

Dusty, star-forming galaxies at high redshift selected at sub-millimeter wavelengths (commonly referred to as submm galaxies, SMGs) represent a population of the most massive and luminous galaxies in the early Universe (see Blain et al. 2002; Casey et al. 2014, for reviews).

Since their discovery two decades ago (Smail et al. 1997; Barger et al. 1998; Hughes et al. 1998; Ivison et al. 1998, see Figure 1.4), their study has revolutionized our understanding of the cosmic history of star formation and galaxy evolution (e.g., Lagache et al. 2005). The first estimates of their star formation rates were of

the order of several 100 $M_{\odot}$ yr$^{-1}$, implying that SMGs significantly contribute to star formation history at high redshift. One decade later, the launch of the *Herschel Space Observatory* (Pilbratt et al. 2010) has provided, for the first time, a systematic study of these galaxies at far-infrared and sub-millimeter wavelengths ($\sim 55-500$ $\mu$m), enhancing dramatically the ability to use this information in the context of multiwavelength studies of galaxy evolution.

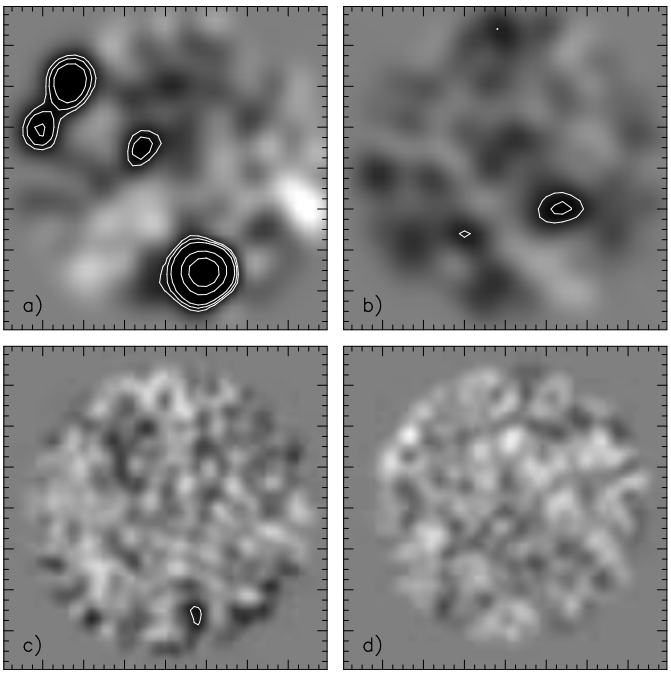


Figure 1.4: This figure is taken from Smail et al. (1997) and shows the first detection reported of high-$z$ SMGs using the Sub-mm Common-User Bolometer Array (SCUBA). Panels a) and c) show respectively the 850 and 450 $\mu$m maps of the massive cluster A370 at $z = 0.37$, whereas panels b) and d) refer to the cluster Cl2244-02 at $z = 0.33$.

The 250, 350, and 500 $\mu$m bands of the SPIRE instrument (Griffin et al. 2010) onboard the *Herschel Space Observatory* have been extensively used to select high-$z$ SMGs (e.g., Bussmann et al. 2013; Asboth et al. 2016; Nayyeri et al. 2016). The peak of the rest-frame spectral energy distribution of the dust emission in galaxies lies at

approximately 100 $\mu$m[3], and is redshifted through the 250, 350 and 500 $\mu$m bands. In addition, observations of SMGs at high redshift benefit from the negative $K$-correction (see Figure 1.5), which becomes very effective at wavelengths probed by the SPIRE instrument and longer wavelengths, leading to an almost constant observed flux for galaxies of the same total infrared luminosity between $1 < z < 5$ (see Casey et al. 2014). Many efforts have been made to discover the most distant SMGs by selecting sources with "red" colors in the SPIRE bands, with $S_{500\mu m} > S_{350\mu m} > S_{250\mu m}$ (e.g., Dowell et al. 2014; Ivison et al. 2016). These techniques have led to the discovery of SMGs into the epoch of reonization at $z > 6$ (Riechers et al. 2013; Strandet et al. 2017; Marrone et al. 2018; Zavala et al. 2018), challenging theoretical models of galaxy formation and evolution that predict much less far-IR luminous galaxies at high redshift.

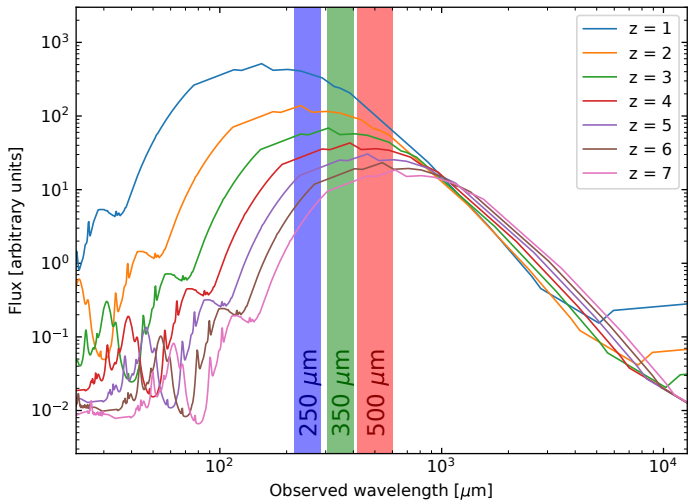


Figure 1.5: Negative $K$-correction: the far-IR continuum emission of the ultra luminous infrared galaxy Arp220 is plotted at various $z$. The negative $K$-correction compensates the luminosity distance term at high redshifts.

Although relatively rare, with typical space densities of $10^{-5} - 10^{-6}$ Mpc$^{-3}$ peaking around $z \sim 2 - 3$, SMGs were confirmed to be among the bolometrically most luminous galaxies, showing infrared luminosities of $L_{\rm IR} > 10^{12-13}\ L_{\odot}$. They host

[3]Note, however, that the shape and the peak of the SED far-infrared dust emission also depends on the dust temperature, $T_{\rm d}$, the emissivity index, $\beta$, and the rest-frame wavelength, $\lambda_0$, where the optical depth reaches unity.

the most intense bursts of star formation known, in excess of 1000 $M_\odot$ yr$^{-1}$ in some extreme cases, that emerge from compact regions of only few kpc in diameter (e.g., Riechers et al. 2014; Hodge et al. 2016; Oteo et al. 2016). Because of their rarity, it is believed that SMGs represent fairly short lasting episodes of star formation (the so-called starburst phase, with duration $\sim 100-200$ Myr; e.g., Greve et al. 2005), yet with star formation rates enhanced by more than an order of magnitude over typical galaxies of the same mass (e.g., Daddi et al. 2007). However, due to the high dust content, originated by their intense star formation, the stellar light in SMGs seen at short wavelengths (mainly in the rest-frame UV and optical) is severely obscured. Due to variation in opacity of the dust (i.e. non-uniform screen of dust) and the non uniform galaxies' temperature, the infrared spectral energy distribution is modeled as a modified blackbody of the form:

$$S(\nu,T) \propto \frac{(1-e^{-\tau(\nu)})\nu^3}{e^{h\nu/\kappa_B T}-1}, \tag{1.2}$$

where $S(\nu,T)$ is the flux density at a given frequency $\nu$ and temperature $T$, $\kappa_B$ is the Boltzmann constant, $h$ is the Planck constant, and $\tau(\nu)$ is the optical depth, commonly represented as:

$$\tau(\nu) = (\nu/\nu_0)^\beta, \tag{1.3}$$

where $\beta$ is the spectral emissivity index and $\nu_0$ is the frequency where optical depth equals unity (Draine 2006).

Despite the huge progress made over the past decades in understanding the properties of SMGs (e.g., Greve et al. 2005; Magnelli et al. 2012; Riechers et al. 2013; Dowell et al. 2014; Ivison et al. 2016; Michałowski et al. 2017; Oteo et al. 2018), the main mechanism that drives the intense star formation responsible for the high far-IR luminosities is still a matter of debate (e.g., Swinbank et al. 2008; González et al. 2011; Michałowski et al. 2012; Hayward et al. 2013; Narayanan et al. 2015). On one hand, almost all ultraluminous galaxies in the local Universe are interacting galaxies and mergers (e.g., Farrah et al. 2001, 2002; Bridge et al. 2007; Haan et al. 2011). At high redshift, a considerable number of SMGs are also found to be galaxy mergers (e.g., Capak et al. 2008; Ivison et al. 2008, 2013; Tacconi et al. 2008; Fu et al. 2013; Messias et al. 2014; Rawle et al. 2014; Oteo et al. 2016; Marrone et al. 2018; Riechers et al. 2017), although isolated, clumpy, gas-rich disk galaxies can also reach extremely large SFRs (e.g., Tacconi et al. 2010; Bournaud et al. 2014). On the other hand, some authors suggest, based on simulations, that high star-formation rates (SFRs $\gtrapprox 1000$ M$_\odot$ yr$^{-1}$) in some SMGs are difficult to explain by a merger scenario alone (e.g., Kereš et al. 2005; Dekel et al. 2009; Narayanan et al. 2015). These studies propose that the predominant mechanism of the sub-millimeter luminous phase is

smooth accretion of cold gas or infall of gas previously ejected via stellar feedback at earlier times, not through major mergers. These models predict massive gaseous inflows and clumps of gas infalling into the central regions. Recent observations support these models by the detection of molecular gas on large scales (several tens of kpc) in proto-cluster galaxies (e.g., Emonts et al. 2016, 2018).

### 1.2.4 Active galactic nuclei

Active galactic nuclei (AGN) are among the most powerful sources in the Universe. They produce very high luminosities over all the electromagnetic spectrum. It is widely accepted that such higher than normal luminosity is not produced by stars, but results from the accretion of matter onto a supermassive black hole (SMBH) at the center of the host galaxy (Rees 1984).

The study of AGNs started with the identification of nearby galaxies having bright nuclei with unusually broad emission lines (Seyfert galaxies Seyfert 1943) and the first high redshift quasi stellar objects (QSOs: Greenstein & Matthews 1963; Matthews & Sandage 1963). AGNs can be classified based on the properties of their optical and ultraviolet spectra. AGNs showing broad emission lines are classified as Type 1, whereas the ones showing narrow emission lines are classified as Type 2. Within the two classifications, AGNs can also be sub-classified based on their radio emission (radio-loud or radio-quiet), rapid variability and strong continuum emission (Blazars: OVV and BL Lac objects), or the presence of broad absorption lines (BAL QSOs).

Antonucci (1993) presented an unified AGN model (see also: Rowan-Robinson 1977; Lawrence & Elvis 1982; Antonucci & Miller 1985; Urry & Padovani 1995), in which the central SMBH activity is common to all AGNs, and the observed differences results in different viewing angles of the SMBH and its accretion disk. Apart from the viewing angle of the SMBH, other properties of an AGN may change the observed characteristics, such as the rate of gas accretion onto the SMBH (and its mass), the degree of obscuration by dust in the nucleus, and the presence or absence of jets.

## 1.3 Rest-frame UV spectroscopic features

The (rest-frame) UV spectrum of a typical star-forming galaxy is dominated by the continuum emission from massive, hot, and luminous stars. The dust content inherent to the galaxy (or in the line of sight) may also change the overall slope of the spectrum, making it "redder" when high dust extinction is present. Superposed to the stellar continuum there are several absorption and emission features associated to the photospheres and winds of massive stars, neutral and ionized gas associated with large-scale outflows, and ionized gas in H II regions where star formation is taking place. A comprehensive compilation of the four types of absorption/emission lines can be found in

Leitherer et al. (2011) from *HST* observations of several local starburst galaxies (see also, e.g., Conti et al. 1996; González Delgado et al. 1998; Heckman et al. 1998).

The characterization of these spectral features requires, however, significant signal-to-noise ratio (S/N) in the continuum, which is severely limited by the faintness of typical star-forming galaxies at high redshift, even for $8-10$m-class telescopes. To overcome this limitation, the study of UV spectral features in high-redshift galaxies has been achieved by building large samples of hundreds to thousands of individual spectra to construct high S/N composite spectra (e.g., Shapley et al. 2003; Steidel et al. 2010; Talia et al. 2012; Du et al. 2018; Rigby et al. 2018b; Nakajima et al. 2018a, see Figure 1.6). Alternatively, high S/N studies have been performed in individual high redshift galaxies (e.g., Pettini et al. 2000, 2002; Quider et al. 2009; Dessauges-Zavadsky et al. 2010; Quider et al. 2009; James et al. 2014; Marques-Chaves et al. 2017; James et al. 2018; Marques-Chaves et al. 2018), by taking advantage on the flux magnification produced by strong gravitational lensing, such as the ones studied in this Thesis.

### 1.3.1 Photospheric Absorption

Stellar absorption lines are generated in the photospheres of stars, i.e. the deepest region of a star that is transparent to photons (e.g., Prinja 1990). There are a handful of well-developed photospheric absorption features, such as C III $\lambda$1176, O IV $\lambda$1342, Si III $\lambda$1417, or S V $\lambda$1501, although many of them are comprised of groups of neighboring lines. These absorption features are typically very weak ($< 1$ Å) and appear only detectable in significantly high signal-to-noise (S/N $> 15$) continuum spectra. On the other hand, these features are of interest because they can be used to define the rest-velocity of the galaxy (systemic redshift). Moreover, they can be also used to trace the metallicity of the young stellar population. By using theoretical stellar models, Leitherer et al. (2001), Rix et al. (2004), and Sommariva et al. (2012) showed that the strength (equivalent width) of several weak photospheric features are correlated with the metallicity. These studies focus on modeling the strongest photospheric absorption blends near 1370, 1425, 1460, 1501 and 1978 Å, whose metallicity dependence is well correlated with the measured equivalent widths in these regions. These methods have been applied to determine the stellar metallicity of star-forming galaxies at redshift $z \approx 2-3.5$ (e.g., Halliday et al. 2008; Quider et al. 2009, 2010; Patrício et al. 2016, see also chapter 4).

### 1.3.2 Wind P-Cygni Profile

In addition to the photospheric absorption lines, the most massive and hottest stars ($M_* > 10\ M_\odot$ and $T_{\rm eff} > 25000\ K$) also produce strong outflows of material from

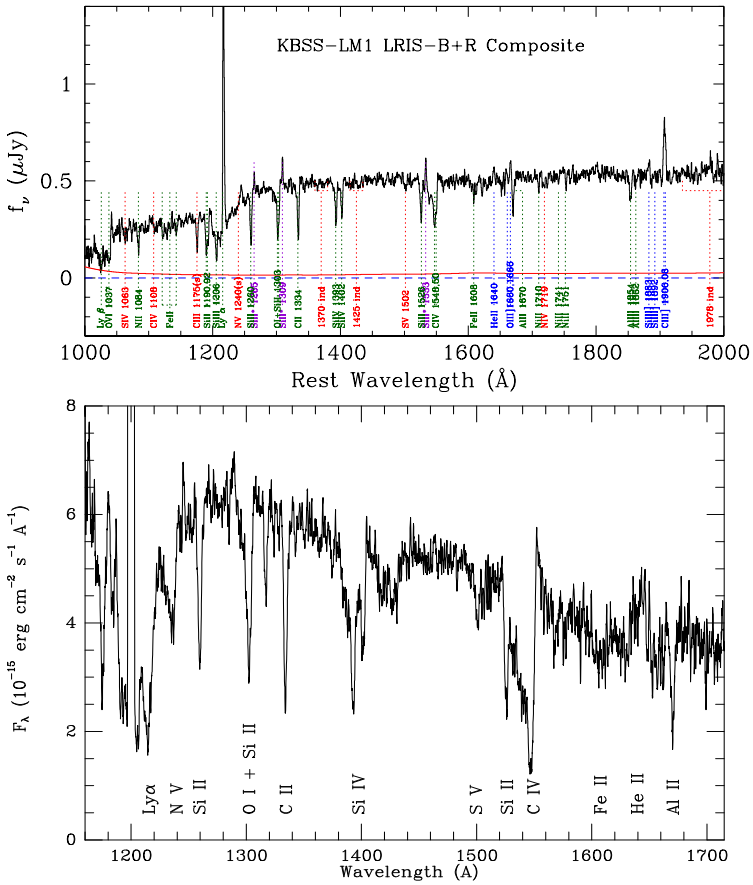


Figure 1.6: Top panel: Stacked composite rest-frame UV spectrum of 30 galaxies with $z \simeq 2.4$ (figure taken from Steidel et al. 2016). Emission and absorption features are identified with different colors: stellar photospheric absorption (red), interstellar absorption (both low- and high-ionization state, dark green), nebular emission (blue), and excited fine-structure emission (dark violet). Bottom panel: UV spectrum of the nearby starburst galaxy NGC 1741 observed with the Faint Object Camera instrument on board *HST* (figure taken from Conti et al. 1996).

powerful stellar winds and expanding shells of gas, resulting in a spectroscopic feature called as P-Cygni profile (see Kudritzki & Puls 2000, for a review). This spectral profile (see an example in Figure 1.7) is characterized by a strong emission with a corresponding blueshifted absorption line produced by material moving away from the star (reaching velocities up to $\sim 1000$ km s$^{-1}$).

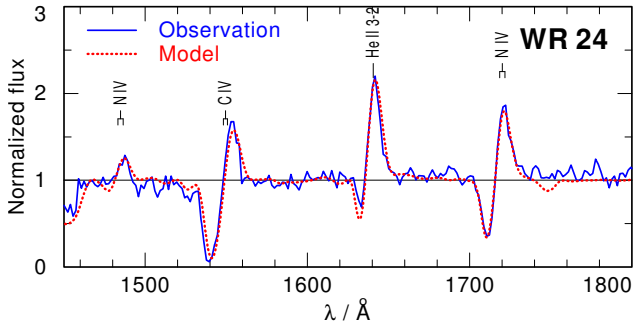


Figure 1.7: Spectrum of a Galactic Wolf-Rayet (WR) star (WR24) showing P-Cygni profiles in the UV lines C IV $\lambda$1548,1550, He II $\lambda$1640, and N IV $\lambda$1719 (figure taken from Hamann et al. (2011)).

The most prominent resonance lines showing P-Cygni profiles are the N V $\lambda$1240, Si IV $\lambda$1393,1400, and C IV $\lambda$1548,1550. The absorption component of the P-Cygni profile is usually very broad ($\sim 2000$ km s$^{-1}$ or even more, see: Pettini et al. 2000, 2002, and chapter 4) and can also be very strong, in particular for C IV, with equivalent widths up to $\approx 15$ Å.

P-Cygni profiles have been extensively studied by combining stellar evolution models and libraries of empirical and synthetic spectra generated by codes such as STARBURST99[4] (Leitherer et al. 1999, 2010, 2014) or BPASS (Binary Population and Spectral Synthesis code: Eldridge & Stanway 2009, 2016; Eldridge et al. 2017).[5] The line strength and shape of the P-Cygni profile vary with the stellar population properties. Both emission and absorption components are stronger for a young stellar population ($\sim 2-6$ Myr) and stabilizes over $\sim 20$ Myr. The strength of the emission component increases with the number of massive stars (i.e., with a flat slope of the IMF or high upper mass cutoff), and decreases at low stellar metallicities. On the other hand, as the winds are driven by metal lines, the strength of the absorption component depends on the density of the stellar wind and therefore on the mass loss rate. Since mass loss rates are lower at lower metallicities, the absorption components are

[4] http://www.stsci.edu/science/starburst99/docs/default.htm
[5] http://bpass.auckland.ac.nz/

weaker at lower metallicities.

However, apart from the dependence on the stellar metallicity, age, and the slope of the IMF, P-Cygni profiles can be affected by other external factors that are not related with stellar origin. High-ionization interstellar absorption in Si IV and C IV are usually present in the spectra of star-forming galaxies and must be carefully taken in consideration. Moreover, relatively strong nebular emission in C IV may also be detected in star-forming galaxies with very low metallicity (e.g., Amorín et al. 2017), although its spectral profile is typically much narrower (FWHM $\sim$ 100 km s$^{-1}$) than the emission component of the stellar P-Cygni profile, thus distinguishable with sufficient spectral resolution observations.

### 1.3.3 Interstellar Medium

Interstellar (ISM) lines are generally the strongest absorption features seen in the UV spectra of typical high redshift star-forming galaxies (e.g., Pettini et al. 2000, 2002; Shapley et al. 2003, but see also González Delgado et al. (1998); Heckman et al. (1998) for low-$z$ starburst galaxies). They are produced by the resonance transition of several ionic species (e.g., H, C, O, Al, Si, Fe, among others) in a variety of ionization stages, from neutral (e.g., H I, O I), to highly ionized species (e.g., C IV, Si IV), which predominantly trace gas at higher temperatures ($T \gtrsim 10^4$ $K$).

Since ISM absorption lines are seen against the continuum provided by the integrated light of O and B stars in a galaxy, they offer a unique probe of the kinematics of the gas. In nearly all star-forming galaxies, their spectra show interstellar absorption lines blueshifted with respect to the systemic redshift of the galaxy, i.e. the gas on the near side of the galaxy is moving towards the observer. Such kinematics were reported in several studies of high redshift star-forming galaxies,[6] both in large statistical samples (e.g., Shapley et al. 2003; Steidel et al. 2010) or individual strong gravitational lensed systems (e.g., Pettini et al. 2002; Quider et al. 2009; Dessauges-Zavadsky et al. 2010; Quider et al. 2010). The model invoked to explain such kinematics is of a nearly spherical, large-scale outflows caused by the mechanical energy input from supernova explosions and strong stellar winds (e.g., Shapley et al. 2003). However, for a few star-forming galaxies (e.g., Sato et al. 2009; Coil et al. 2011; Rubin et al. 2012; Martin et al. 2012, but see chapter 4), ISM absorption lines have been found redshifted with respect to the systemic redshift, interpreted as gas being accreted into the galaxy (see Figure 1.8).

The strength of the ISM absorption lines depends on the ion column densities, $N$, and the covering fraction of the outflowing/inflowing gas. Thus, ISM absorption lines can be also used to derive the metallicity of the gas (e.g., Spitzer 1978; Savage &

[6] Blueshifted ISM absorption lines are frequently observed in lower-$z$ star-forming galaxies as well (e.g., Martin 2005; Rupke et al. 2005a,b; Chisholm et al. 2017; Finley et al. 2017).

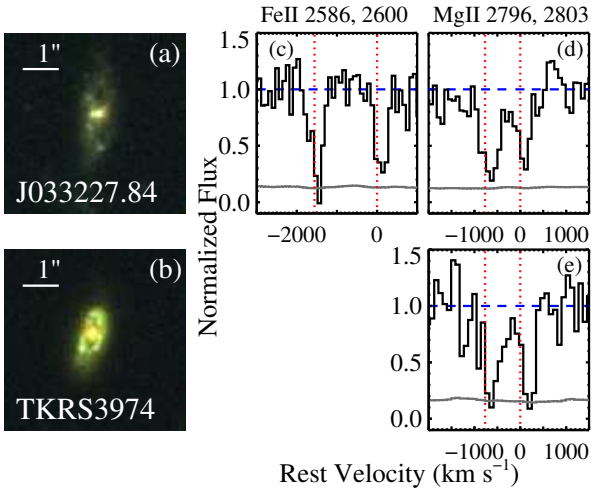


Figure 1.8: Two galaxies at $z \simeq 0.5$ showing evidence of inflows (with inflowing velocities $\sim 50-160$ km s$^{-1}$), by the detection of redshifted low-ionization ISM absorption lines (Fe II $\lambda$2586,2600 and Mg II $\lambda$2796,2803). Velocities are measured relative to the systemic velocities (red dashed lines). This figure is taken from Rubin et al. (2012).

Sembach 1991; Pettini et al. 2002), when used together with the H I column density (e.g., derived by the characterization of a damped Ly$\alpha$ absorption). For resolved[7] ISM absorption lines with unsaturated profiles, the apparent optical depth method (Savage & Sembach 1991) can be used to derive values of column density for ions of interest, by relating the apparent column density of an ion in each velocity bin, $N_a(v)$ in units of cm$^{-2}$ (km s$^{-1}$)$^{-1}$, to the optical depth in that bin, $\tau_a(v)$ using the following expression:

$$N_a(v) = \frac{\tau_a(v)}{f\lambda}\frac{m_e c}{\pi e^2} = \frac{\tau_a(v)}{f\lambda(\text{Å})}3.768 \times 10^4, \tag{1.4}$$

where $\lambda$ is the wavelength in Å, $c$ the speed of light, $f$ the transition oscillator strength, and $m_e$ the electron rest mass. The apparent optical depth can be measured directly from the observed line intensity at velocity $v$, $I_{\rm obs}(v)$, by:

$$\tau_a(v) = -\ln[I_{\rm obs}/I_0(v)], \tag{1.5}$$

[7]Relatively high spectral resolution, $\leq 50$ km s$^{-1}$, is needed to resolve the profiles of the ISM absorption lines.

where, $I_0(v)$ is the intensity in the continuum. Alternatively, one can assume that the gas is optically thin, i.e. in the linear part of the curve of growth, to infer lower limits to the column density and abundances. This is done by taking the optically thin approximation:

$$\log(N) < 19.053 + \log\left[\frac{EW_0}{\lambda^2 f}\right], \tag{1.6}$$

where $EW_0$ is the rest-frame equivalent width of the ISM line.

The strength of ISM lines depends strongly on the evolutionary state of the galaxy. The average absorption equivalent width of ISM lines (in particular the low-ionization ones) decreases with decreasing metallicity and dust attenuation. Moreover, the average strength of low-ionization ISM lines, decreases dramatically as the Ly$\alpha$ lines varies from strong absorption to strong emission (see Figure 1.9: Shapley et al. 2003). For this reason, ISM lines appear stronger in UV-selected LBGs than in LAEs, which, on average, present a younger stellar population with lower metallicity and dust content.

### 1.3.4 Nebular emission

The most massive and youngest stars produce photoionising radiation that ionize the surrounding interstellar atomic gas, in which star formation has recently taken place. This leads to the production of nebular emission lines.

Since H II regions are gravitational bound to the galaxy by gravity, nebular emission lines are commonly used to determine the systemic redshift of a galaxy, in particular in the cases where photospheric absorption lines are not detected in low S/N spectra.Moreover, the characterization of the emission line profile allows to determine the velocity dispersion of the ionized gas (typically less than 100 km s$^{-1}$; e.g., Hainline et al. 2009; Dessauges-Zavadsky et al. 2010; Richard et al. 2011).

The most prominent nebular emission lines in the rest-frame UV are O III] $\lambda$1661,1666, Si III] $\lambda$1882,1892, and C III] $\lambda$1906,1908, with the later being usually the strongest of the three. Other nebular emission lines may be present, such as N V $\lambda$1240, C IV $\lambda$1548,1550, or He II $\lambda$1640, but they require a hard-ionizing spectrum, and if present they may be associated with AGN activity (e.g., Feltre et al. 2016; Nakajima et al. 2018b). UV nebular lines are relatively weaker ($EW_{\rm CIII]} < 5$ Å; e.g., Maseda et al. 2017; Nakajima et al. 2018b) than those found in the rest-frame optical ([O III] $\lambda$4960,5008, H$\beta$ $\lambda$4862, H$\alpha$ $\lambda$6564), although they can be very strong ($EW_{\rm CIII]} \simeq 25$ Å) in low-metallicity star-forming galaxies (e.g., Erb et al. 2010; Rigby et al. 2015; Maseda et al. 2017).

Nebular emission can also provide valuable information on the nature of the ionizing radiation and the physical conditions in the ISM in a galaxy. They can be used to

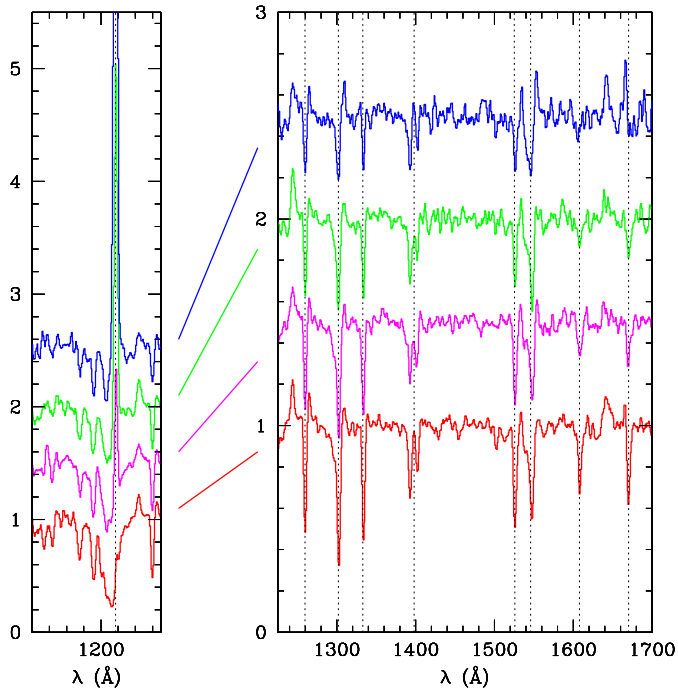


Figure 1.9: This figure is taken from Shapley et al. (2003) and shows the four quartiles of LBGs grouped according to Ly$\alpha$ strength. The average strength (equivalent width) of low-ionization ISM lines, decreases dramatically as the Ly$\alpha$ lines varies from strong absorption (red) to strong emission (blue).

identify the source(s) of photoionization (star formation and/or AGN; e.g., Feltre et al. 2016; Nakajima et al. 2018a,b), or to derive carbon and oxygen gas-phase abundances (see: Pérez-Montero & Amorín 2017).[8]

### 1.3.5 Ly$\alpha$ line

The Ly$\alpha$ line is intrinsically the most luminous spectral emission line in astrophysical nebulae, and has long been predicted as a good tracer of star forming galaxies at large cosmological distances (Partridge & Peebles 1967). Indeed, the Ly$\alpha$ line has proved

[8] https://www.iaa.csic.es/~epm/HII-CHI-mistry-UV.html

the way to find the highest redshift galaxies, currently as distant as $z = 9$ (Zitrin et al. 2015; Hashimoto et al. 2018).

Ly$\alpha$ photons are emitted from hydrogen atoms by the decay from the first excited state, ($2p$-state, i.e., $n = 2$, $l = 1$, where $n$ is the principle quantum number or the excitation state, and $l$ is the quantum state) to the ground state $1s$ ($n = 1$, $l = 0$). The energy levels of the hydrogen atom are quantized as:

$$E_n = -\frac{m_e e^4}{\hbar^2 n^2}, \tag{1.7}$$

where $m_e$ is the mass of the electron, $e$ is the charge of the electron, and $\hbar$ is the reduced Planck constant ($\hbar = h/2\pi$ where $h$ is the Planck constant). To excite an hydrogen atom from an initial state $n = 2$ to the ground state $n = 1$, the energy to be supplied is:

$$E_{n=1} - E_{n=2} = \Delta E = h\nu = \frac{hc}{\lambda}, \tag{1.8}$$

where $\nu$ is the frequency of the radiation, $\lambda$ is wavelength, and $c$ is the speed of the light. The energy difference between $2p$ and $1s$ levels dictates a photon energy of 10.2 eV or $\lambda = 1215.67$ Å. A hydrogen atom can emit Ly$\alpha$ in two different ways (see: Dijkstra 2017, for details):

- **Recombination.** The recombination of free electrons with protons results in a hydrogen atom in an excited state ($n$, $l$). As shown in Figure 1.10, atoms in any state with $n > 1$ radiatively cascade back down to the ground state $1s$ and produce Ly$\alpha$ photons via intermediate states ($n'$, $l'$).[9]

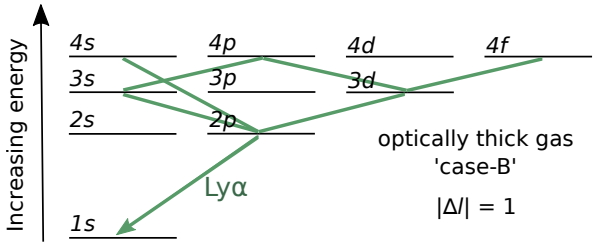


Figure 1.10: Allowed transitions ($|\Delta l| = 1$) where atoms in any state with $n > 1$ radiatively cascade back down to the ground state $1s$ originating a Ly$\alpha$ photon. In case-B recombination, higher order of Lyman series are re-absorbed (e.g., Ly$\beta$, Ly$\gamma$, ... , which correspond to $3p \rightarrow 1s$, $4p \rightarrow 1s$, ...).

[9] Because of quantum mechanical selection rules, only transitions where $|\Delta l| = 1$ are permitted.

The probability that a radiative cascade from the state ($n$, $l$) results in a Ly$\alpha$ photon is:

$$P(n,l \rightarrow Ly\alpha) = \sum_{n'l'} P(n,l \rightarrow n'l')P(n'l' \rightarrow Ly\alpha), \tag{1.9}$$

where $n > n'$ and $|l - l'| = 1$. Recombination of a free proton and electron generally results in a hydrogen atom in an excited state ($n$, $l$). Radiative cascades from an excited state ($n$, $l$) to the ground state $1s$ ($n = 1$, $l = 0$) can then produce a Ly$\alpha$ photon. The probability that recombination event results in a Ly$\alpha$ photon is given by summing all the quantum states and weighting the probability that a combined electron-proton pair ended up in state ($n$, $l$):

$$P(Ly\alpha) = \sum_{n_{\min}}^{\infty} \sum_{l=0}^{n-1} \frac{\alpha_{nl}(T)}{\alpha_{\rm tot}(T)} P(n,l \rightarrow Ly\alpha), \tag{1.10}$$

where $\alpha_{\rm tot}$ is the total recombination coefficient, and $\alpha_{nl}(T)$ is the temperature-dependent state specific recombination coefficient, so that:

$$\alpha_{\rm tot} = \sum_{n_{\min}}^{\infty} \sum_{l=0}^{n-1} \alpha_{nl}(T). \tag{1.11}$$

Assuming that recombination takes place in a medium that is opaque to all Lyman series photons (i.e. Ly$\alpha$, Ly$\beta$, Ly$\gamma$), the so-called 'case-B' approximation (Baker & Menzel 1938), so that direct recombination to the ground state produces an ionizing photon that is immediately absorbed by a nearby neutral H atom, we can set $n_{\min} = 2$ and the temperature dependence comes entirely through $\alpha_{nl}(T)$. For gas temperatures in the range $100K < T < 10^5 K$, the probability $P$(Ly$\alpha$) for case-B recombination is given by Cantalupo et al. (2008):

$$P_{\rm case-B}(Ly\alpha) = 0.686 - 0.106 \log T_4 - 0.009 (T_4)^{-0.44}, \tag{1.12}$$

where $T_4 \equiv T/10^4\ K$. For gas at $T = 10^4$, $P(Ly\alpha) = 0.68$.

- **Collisions.** This occurs when an electron and a hydrogen atom interact, leaving the atom in an excited state. This can produce a Ly$\alpha$ photon with the kinetic energy of the free electron. This process is also referred to as Ly$\alpha$ production via cooling radiation. The efficiency of this process depends on the relative velocity of both the free electron and the hydrogen atom, and the number density of both species. The total Ly$\alpha$ production rate through collisional excitation is:

$$R = n_e n_{\rm H} q_{1s2p} \quad [{\rm cm}^{-3}{\rm s}^{-1}], \tag{1.13}$$

where $n_e$ and $n_{\rm H}$ are the number density of the electron and hydrogen atoms, and $q_{1s2p}$ is the rate coefficient which quantifies the velocity dependence of this process. Assuming a Maxwellian distribution for the velocity distribution of electrons, this coefficient becames a function of the temperature $T$, so that:

$$q_{lu} = \frac{h^2}{(2\pi m_e)^{3/2}(\kappa_B T)^{1/2}} \frac{\langle \Omega_{lu} \rangle}{g_l} \exp\left(-\frac{\Delta E_{lu}}{\kappa_B T}\right), \tag{1.14}$$

where $l$ and $u$ refer to the lower and upper energy states, respectively, $\kappa_B$ is the Boltzmann constant, $g_l$ is the statistical weight of lower level of a radiative transition, and $\langle \Omega_{lu} \rangle$ is the velocity averaged collision strength.

In the context of galaxies, Ly$\alpha$ photons are mostly produced by the UV radiation from young massive stars, leading to the hydrogen recombination following ionization of the surrounding neutral hydrogen (see: Hayes 2015, for a review). Ly$\alpha$ radiation can also be produced in the outer regions of a galaxy by gravitational cooling. If intergalactic medium (IGM) or circumgalactic (CGM) gas is being accreted onto the strong potential wells of the galaxies, the gas may radiate away their gravitational potential energy in the Ly$\alpha$ line (e.g., Fardal et al. 2001; Dijkstra & Loeb 2009). In addition, powerful galactic-scale winds from starbursts and supernovae may produce ionizing photons by strong shocks (e.g., Taniguchi & Shioya 2000).

As a resonant transition, Ly$\alpha$ photons undergo a radiative transfer process and are only observed from the location where their last scattering took place (Osterbrock 1962), if not completely absorbed before. The path taken by the Ly$\alpha$ photon until it escapes from the galaxy is thus regulated by the distribution of neutral gas. Moreover, since H I gas has its own kinematics (outflows/inflows), the emitted Ly$\alpha$ line depends not only of the H I spatial distribution, but also on its kinematics.

Since outflows are present in many (if not all) star-forming galaxies, Lya photons are likely to escape the galaxy (in the direction of the observer) when they are back-scattered from the receding side of the outflowing neutral gas. These Ly$\alpha$ photons may acquire the necessary frequency shift (from the outflowing gas) that allows them to pass through the gas in the galaxy unimpeded. For this reason, Ly$\alpha$ emission is frequently seen with an asymmetric profile, comprising a blueshifted absorption component (outflowing foreground neutral gas) and a redshifted emission, i.e., Ly$\alpha$ photons back-scattered from the receding outflows (see Figure 1.11). For a few cases, when the covering fraction of the gas is lower, Ly$\alpha$ can escape throughout holes in the neutral gas, resulting in a spectral profile with both blueshifted and redshifted emission.

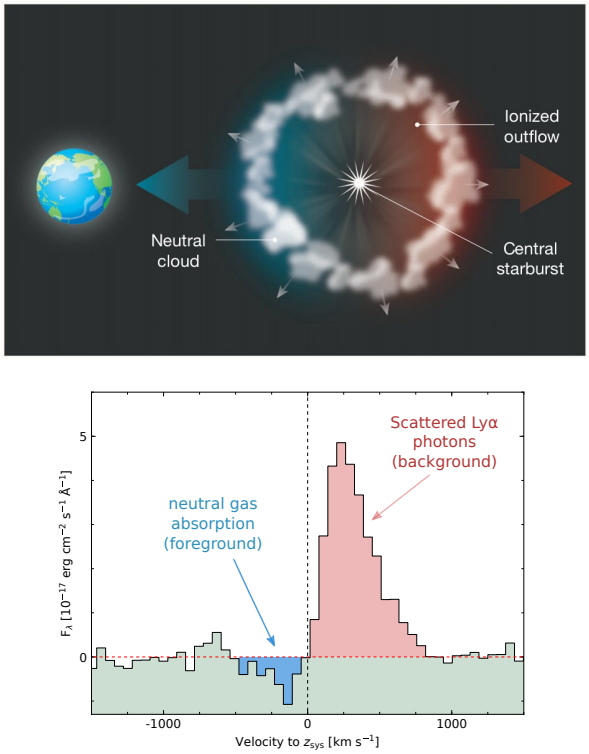


Figure 1.11: Top panel: schematic model of a spherical galactic outflow with a high covering fraction (figure taken from Erb 2015). Bottom panel: the resulting asymmetric Ly$\alpha$ profile (from an object analyzed in chapter 3), with a blueshifted absorption component due to the absorption of the outflowing foreground neutral gas, and a redshifted emission from the scattered Ly$\alpha$ photons from the receding outflows.

## 1.4 Strong Gravitational Lensing

Even the most outstanding high redshift galaxies are faint[10] and have small angular sizes ($\lessapprox 1''$), thus difficult to resolve spatially and obtain high S/N spectra even for current $8-10$m class telescopes. Fortunately, the strong gravitational lensing effect (see Treu 2010, for a review) acts as a natural telescope by boosting the observed

[10] With exceptions for luminous quasi stellar objects, QSOs.

flux of a high-$z$ galaxy, allowing its characterization with S/N and spatial resolutions approaching those accessible for local galaxies (see Figure 1.12). Such phenomenon occurs under rare circumstances, when a distant object (source) is sufficiently aligned with a foreground massive object(s) (lens or deflector), creating multiple images or arcs of the distant light source. Strong lensing occurs when the *lens equation* (derived in the following paragraphs) has multiple solutions, which correspond to multiple images, as opposed to weak gravitational lensing, in which the *lens equation* has only one solution.[11]

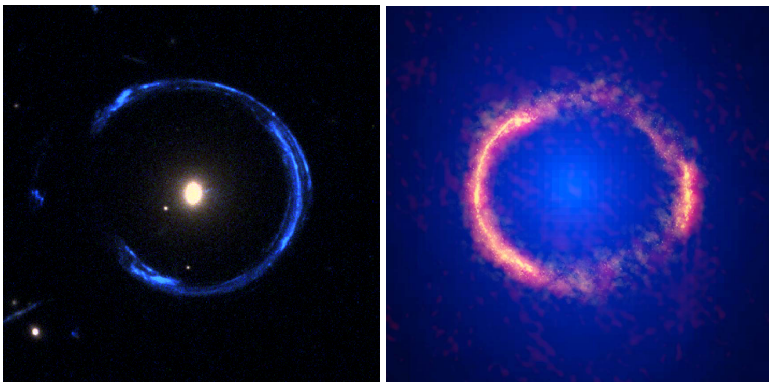

Figure 1.12: Two examples of strong gravitational lensed galaxies at high-$z$. Left: *HST* color composite image of the Cosmic Horseshoe LBG galaxy at $z = 2.38$ (image taken from James et al. 2018). Right: ALMA (red) and *HST* (blue) composite image of SDP.81, a sub-millimeter galaxy at $z = 3.04$ (Credit: ALMA (NRAO/ESO/NAOJ); B. Saxton NRAO/AUI/NSF; NASA/ESA Hubble, T. Hunter (NRAO)).

Although strong gravitational lensing was predicted almost one century ago (Zwicky 1937a,b), only in 1979 the first strong gravitational lensed extragalactic object was reported, a QSO at $z = 1.406$ showing two lensed images (Walsh et al. 1979). Over the past decades, the number of confirmed strong gravitationally lensed objects has exponentially increased (to few hundreds)[12] by employing sophisticated selection techniques in large photometric and spectroscopic datasets, from the optical (e.g., Bolton et al. 2006; Oguri et al. 2006; More et al. 2012; Sonnenfeld et al. 2018, see also chapter 2) to sub-mm and radio (e.g., Negrello et al. 2010; Bussmann et al. 2013; Vieira et al. 2013; Wardlow et al. 2013; Negrello et al. 2017). These findings have led to detailed studies of strong gravitational lensed LBGs, LAEs, QSOs, and

[11] See Refregier (2003) and references therein for week gravitational lensing.
[12] based on the Master Lens Database (`http://admin.masterlens.org/index.php?`).

SMGs at very high-$z$ (e.g., Smit et al. 2017; Zavala et al. 2018), but also of an individual supernova (Kelly et al. 2015) and star (Kelly et al. 2018) at $z \simeq 1.5$.

In the following paragraphs I will describe briefly some basic principles of gravitational lensing.

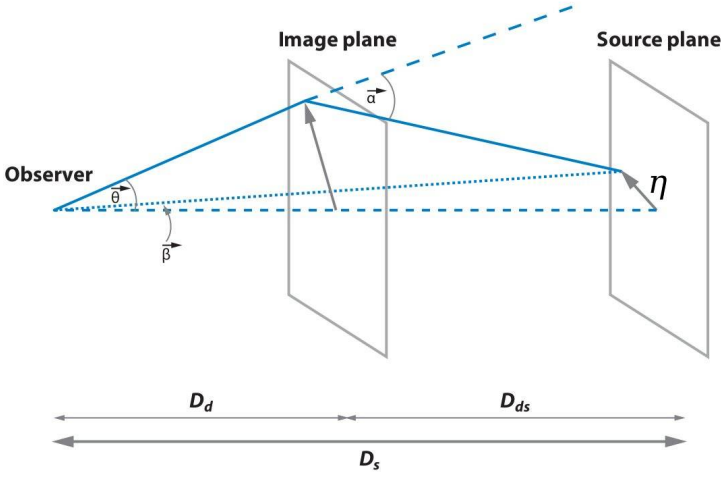


Figure 1.13: Illustration of the geometric angles and angular diameter distances involved in the lens equation (figure adapted from Treu 2010).

Figure 1.13 shows a schematic illustration of a gravitational lens system. The foreground massive object (deflector) is at redshift $z_{\rm d}$, which corresponds to an angular diameter distance $D_{\rm d}$, defined as:

$$D_{\rm d} = \frac{S_k(r)}{1+z_{\rm d}}, \tag{1.15}$$

where $r$ is the comoving distance and $S_k(r)$ is the coordinate of the FLRW metric defined as:

$$S_k(r) = \begin{cases} \sin(\sqrt{-\Omega_k}H_0 r)/(H_0\sqrt{|\Omega_k|}) & \Omega_k < 0 \\ r & \Omega_k = 0 \\ \sinh(\sqrt{\Omega_k}H_0 r)/(H_0\sqrt{|\Omega_k|}) & \Omega_k > 0, \end{cases} \tag{1.16}$$

where $\Omega_k$ is the curvature density and $H_0$ is the value of the Hubble parameter today. In a similar way, the background object (source) is at $z_{\rm s}$, corresponding

to a distance $D_s$. The angular diameter distance between the lens and the source is $D_{ds}$.[13] We define planes perpendicular to the observation axis that include the deflector and the source, the image and source plane, respectively. A certain position of the source in the source plane is given by $\eta = \beta D_s$. The deflection angle is given by $\alpha$ and is a function of the angle of the source seen in the image plane, $\theta$.

**Lens Equation**

For small intervening angles $\alpha$, $\beta$, and $\theta$, we can write the relation between angular diameter distances as:

$$\theta D_s = \beta D_s + \alpha(\theta) D_{ds}. \tag{1.17}$$

By defining the angular diameter distance between the deflector and source as:

$$\hat{\alpha}(\theta) = \frac{D_{ds}}{D_s}\alpha(\theta), \tag{1.18}$$

one can rewrite Equation 1.17 in the so-called *lens equation*:

$$\theta = \beta + \hat{\alpha}(\theta). \tag{1.19}$$

In strong gravitational lensing, $\theta$ has multiple solutions, indicating the angular positions of each lensed image of the background source. If we define $\phi$ as the two-dimensional Newtonian lensing potential, we can write the deflection angles in the form:

$$\alpha = \frac{D_s}{D_{ds}}\nabla\phi, \quad \text{which gives} \quad \theta = \beta + \nabla\phi, \tag{1.20}$$

meaning that the number of lensed images and their positions depend on the profile of mass distribution of the deflector and the relative positions between the deflector and the source. Moreover, for a given foreground mass distribution at a fixed $z_d$, the deflector will produce higher deflections for sources at higher $z_s$.

**Magnification Factor**

For a point-source approximation, the magnification factor produced by the deflector is given by the Jacobian matrix, $A$, between the source plane and image plane two-dimensional coordinates, which in turns is given by:

[13] Note that $D_{ds} \neq D_d - D_s$. Assuming $\Omega_k \sim 0$ (Planck Collaboration et al. 2016), $D_{ds} \sim \frac{1}{1+z_s}(S_k^s - S_k^d)$.

$$A = \frac{\partial \beta_i}{\partial \theta_j} = \delta_{ij} - \frac{\partial \alpha_i}{\partial \theta_j} = \delta_{ij} - \frac{\partial^2 \phi}{\partial \theta_i \partial \theta_j}. \tag{1.21}$$

We now define the convergence of the image, $\kappa$, as:

$$\kappa(\theta) \equiv \frac{\Sigma(D_d \theta)}{\Sigma_{crit}}, \tag{1.22}$$

where, $\Sigma_{crit}$ is the critical surface mass density:

$$\Sigma_{crit} = \frac{c^2}{4\pi G} \frac{D_s}{D_d D_{ds}} \tag{1.23}$$

that defines the occurrence of strong lensing features (e.g., multiple images or arcs).

Finally, by adding the term to account for the source distortion (shear components $\gamma_1$ and $\gamma_2$):

$$\gamma \equiv \gamma_1 + i\gamma_2 = |\gamma| e^{2i\phi}, \tag{1.24}$$

the Jacobian matrix (Equation 1.21) can be written as a function of the convergence and the shear:

$$A = \begin{pmatrix} 1 - \kappa - \gamma_1 & -\gamma_2 \\ -\gamma_2 & 1 - \kappa + \gamma_1 \end{pmatrix}. \tag{1.25}$$

The magnification of the source, $\mu$, is then given by the inverse of the determinant of the Jacobian matrix:

$$\mu = \frac{1}{\det A} = \frac{1}{(1-\kappa)^2 - |\gamma|^2} \tag{1.26}$$

The spatial locations that satisfy $1 - \kappa = \pm\gamma$ (i.e. $\det A = 0$) have infinite magnifications. These positions are called *critical* curves in the image plane. The *caustics* are the corresponding curves obtained by mapping the *critical* curves into the source plane via the lens equation (Equation 1.19).

However, for cases with extended sources, the magnification factor also depends on the distribution of the surface brightness of the background source. In such cases, the surface brightness of the source will enter in the calculation of the local magnification factor in each line-of-sight.

**Typical Configurations of Strong Lens Systems**

The configuration of the observed multiple images depends on the location of the source relative to the caustic in the source plane. The caustic of a typical lens is shown

in red in Figure 1.14, and commonly comprises four folds (the smooth portions of the caustic) and four cusps (regions where the folds intersect). Examples of the most common configurations of strong gravitationally lensed galaxies are shown in Figure 1.14.

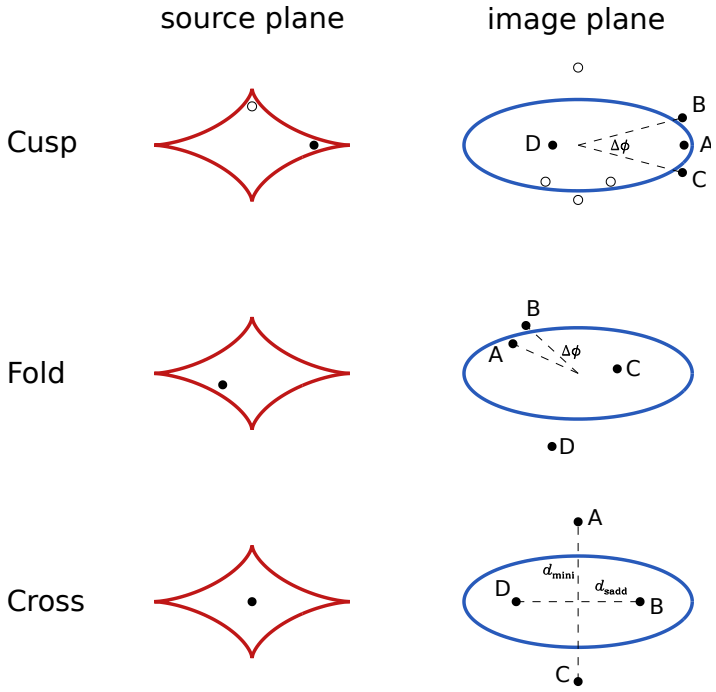


Figure 1.14: Illustration of three common configurations of quad lenses: *cusp* (top), *fold* (middle), and cross (bottom). On the left, it is shown the caustic (red) and the source position in the source plane. On the right, it is shown the critical curve (blue) and the lensing image positions in the image plane (figure adapted from Chu et al. 2016).

For a source located close to a cusp (upper panel in Figure 1.14), three close images (A, B, and C) will be produced near the critical line in the image plane (blue), whereas if the source is located close to a fold (middle panel in Figure 1.14), only two images (A and B) appear near the critical line. If the source is placed in the center (bottom panel in Figure 1.14) of the caustic, the lensed images will form a cross configuration.

**Einstein Radius**

The Einstein radius, $\theta_e$ , indicates the angular separations between the multiple lensed images, and defines the projected area in the image plane enclosing a surface density equal to the critical surface density. The mass within $\theta_e$ can then be written as:

$$M(r_e) = \pi \Sigma_{crit} \theta_e^2. \tag{1.27}$$

As shown in Equation 1.23, the critical surface density is a function of the angular distances between source, lens, and observer, and therefore, $\theta_e$ depends not only on the lensing mass, but also on the redshifts of the source and image planes.

The Einstein radius can be reduced to a simple expression by considering the lensing mass concentrated on a single point. In this assumption, the deflection angle is:

$$\alpha(r) = \frac{4GM}{c^2 r}, \tag{1.28}$$

with for small angles, $r \sim D_d \theta$. If the background source is strictly aligned with the lens, i.e. $\eta = \beta D_s = 0$, Equation 1.17 can be re-written as:

$$\theta D_s = \frac{4GM}{c^2 \theta D_d} \times D_{ds}, \tag{1.29}$$

in which $\theta$ is equal to $\theta_e$ in this configuration. Therefore, the gravitational image formed by the mass $M$ (assumed concentrated on a single point) is a Einstein ring centered on the lens and with radius:

$$\theta_e = \sqrt{\frac{4GM}{c^2} \frac{D_{ds}}{D_d D_s}}. \tag{1.30}$$

## 1.5 Thesis Outline

In this Thesis, I will present the results of the rest-frame UV analysis of high redshift galaxies ($2 < z < 3$), and on a multi wavelength study of a *Herschel*-selected, lensed galaxy merger.

In Chapter 2 I will introduce the Baryon Oscillation Spectroscopic Survey Emission-Line Lens Survey for the GALaxy-Ly$\alpha$ EmitteR sYstems (BELLS GALLERY) survey, which discovered 187 strong gravitational lens candidate systems with high-redshift LAEs as the background sources. I will also report the discovery of

one of the most brightest galaxy-scale lensed LAE known so far. Next, in Chapter 3, I will present an imaging and spectroscopic survey from the BELLS GALLERY sample, conducted with the Gran Telescopio Canarias and William Herschel Telescope. The main physical properties of these LAEs are derived and put in context with other unlensed LAEs. Chapter 4 presents a very high S/N spectroscopic study of a bright sub-millimeter galaxy. We found that this system is a merger composed of a SMG and a LBG, with large scale gas motions, including evidence of outflowing and inflowing gas. Chapter 5 presents the discovery and the first physical and morphological analysis of a high-$z$ luminous Ly$\alpha$ nebulae, physically unrelated, but very close in projection to the lensed *Herschel* source discussed in Chapter 4. This object is one of the most luminous Ly$\alpha$ nebulae known so far, and shows extended C IV and He II emission over $\sim$ 100 kpc. The final conclusions of this Thesis are provided in Chapter 6. I further discuss my plans for future direction of research in the last section.

# 2

# The BELLS GALLERY Survey: Discovery of BG1429+1202

In this Chapter I introduce the Baryon Oscillation Spectroscopic Survey Emission-Line Lens Survey for the GALaxy-Ly$\alpha$ EmitteR sYstems (BELLS GALLERY) survey, which led to the discovery of 187 galaxy-scale strong gravitational lens candidate systems with high-redshift Ly$\alpha$ emitting galaxies as the background sources. I also report the discovery of BG1429+1202, a very bright, highly magnified, and yet intrinsically very luminous Ly$\alpha$ emitting galaxy, based on Director Discretionary Time imaging and spectroscopic observations using the Gran Telescopio Canarias and the William Herschel Telescope.

This Chapter is part of the publication:

R. Marques-Chaves, I. Pérez-Fournon, Y. Shu, P. I. Martínez-Navajas, A. S. Bolton, C. S. Kochanek, M. Oguri, Z. Zheng, S. Mao, A. D. Montero-Dorta, M. A. Cornachione, and J. R. Brownstein, 2017, ApJL, 834, L18 *"Discovery of a Very Bright and Intrinsically Very Luminous, Strongly Lensed Ly$\alpha$ Emitting Galaxy at $z = 2.82$ in the BOSS Emission-Line Lens Survey"*

## 2.1 Introduction

Lyman-$\alpha$ emitters (LAEs) are young star-forming galaxies that show a prominent Ly$\alpha$ emission. They are typically faint at high-redshift ($m_R \simeq 25.4$ AB at $z \sim 3$; Ouchi et al. 2008), but hold important clues to the formation and evolution of galaxies at the time

when the universe was still young (e.g., Bouwens et al. 2007, 2011, 2015; Finkelstein et al. 2009; Laporte et al. 2017). LAEs are usually selected by narrow-band imaging of their strong Ly$\alpha$ emission line (typically defined with rest-frame equivalent widths $EW_0 > 20$ Å) from the photoionization of neutral hydrogen by young hot stars (e.g., Ajiki et al. 2003; Ouchi et al. 2005, 2008). They show very compact morphologies ($\simeq 1$ kpc; e.g., Bond et al. 2009; Taniguchi et al. 2009; Bond et al. 2012), with low stellar masses ($\sim 10^6 - 10^9\ M_\odot$), and in general have a small dust content (Ono et al. 2010).

However, the study of the physical properties of these high-redshift galaxies has been limited by their faintness, even for 8/10 m class telescopes. Such characterization has been only achievable using stacking techniques over large samples of hundreds to thousands of individual spectra or images (e.g., Shapley et al. 2003; Ono et al. 2010; Steidel et al. 2011, 2016; Wardlow et al. 2014; Momose et al. 2016). Although these techniques have been very successful, they require a large amount of observing time and only probe the average physical properties of these galaxies.

Another way to study high-redshift galaxies in detail is to use the fortuitous alignments with foreground massive structures, which provide natural magnification and associated amplification produced by strong gravitational lensing. Hundreds of strong lensed star-forming galaxies have been discovered by employing various observational techniques. These include the use of spectroscopic selection techniques in large datasets (e.g., Bolton et al. 2004, 2006, 2008a,b; Brownstein et al. 2012; Shu et al. 2015, 2016b,c, 2017), automatic lens finding algorithms in large area imaging (e.g., Cabanac et al. 2007; More et al. 2012; Sonnenfeld et al. 2018), using Principal Component Analysis or neural network gravitational arc finders (e.g., Paraficz et al. 2016; Bom et al. 2017; Jacobs et al. 2017), with the contribution from citizen scientists (e.g., More et al. 2016), or by serendipitous discoveries (e.g., Yee et al. 1996; Allam et al. 2007; Belokurov et al. 2007; Smail et al. 2007). However, only a handful of optically very bright ($m_R \sim 20$), strongly magnified high-redshift galaxies have been discovered so far (Allam et al. 2007; Belokurov et al. 2007; Smail et al. 2007; Lin et al. 2009; Dahle et al. 2016), allowing detailed spectroscopic studies of their individual properties, such as their stellar populations, chemical composition, and kinematics of the interstellar medium (e.g., Pettini et al. 2000, 2002; Quider et al. 2009, 2010; Dessauges-Zavadsky et al. 2010; Rigby et al. 2018b; James et al. 2018).

In this chapter, I introduce the BELLS GALLERY survey, which discovered, for the first time, a large sample of galaxy-scale strong gravitationally lensed LAE candidate systems (Shu et al. 2016b). From the total sample of 187 lensed LAE candidates, 21 were imaged with the *Hubble Space Telescope* (*HST*) and the results presented in Shu et al. (2016c) and Cornachione et al. (2018). I also report the discovery of a very bright ($R \sim 20$, AB), quadruply gravitationally lensed LAE, based on GTC and WHT

Director Discretionary Time imaging and spectroscopic observations. I provide the first physical and morphological analysis of the lensing galaxy and the lensed LAE. Throughout this Chapter, a cosmology with $\Omega_{\rm m} = 0.274$, $\Omega_\Lambda = 0.726$, and $H_0 = 70$ km s$^{-1}$ Mpc$^{-1}$ is adopted. All quoted magnitudes are in the AB system.

## 2.2 The BELLS GALLERY Survey

### 2.2.1 Lens Candidate Identification

The selection of high-$z$ lensed LAEs candidates from the BELLS GALLERY Survey is based on spectroscopic techniques, similar to the ones already employed in previous surveys, such as the Sloan Lens ACS Survey (SLACS: Bolton et al. 2006), the Baryon Oscillation Spectroscopic Survey (BOSS) Emission-Line Lens Survey (BELLS: Brownstein et al. 2012), and the SLACS for the Masses Survey (S4TM: Shu et al. 2015). However, in the case of the BELLS GALLERY survey, the selection method was substantially modified to specifically select lensed high-redshift LAEs. The methodology is fully described in Shu et al. (2016b). Here, I briefly summarize the methodology of the selection.

The principle of the selection technique is the detection of a secondary and asymmetric emission line (Ly$\alpha$ $\lambda$1215 emission redshifted to the optical: high-$z$ background source) in the spectra of lower-redshift massive galaxies (lens galaxy: lower-$z$ foreground source). Figure 2.1 shows an example of this procedure.

The BELLS GALLERY project uses a parent sample of $\sim 1.5 \times 10^6$ optical spectra obtained with the 2.5m Sloan telescope from the Data Release 12 (DR12) of the BOSS (Dawson et al. 2013) of the Sloan Digital Sky Survey III (SDSS-III: Eisenstein et al. 2011). The BOSS optical spectra have a wavelength coverage from 3500 to $10,000$ Å and a spectral resolution R $\approx 2000$ (or $\delta v \approx 150$ km s$^{-1}$).

From the almost $1.4 \times 10^6$ optical spectra with confident redshifts (and classification as galaxies), the individual best-fit galaxy template (which is provided by the SDSS automated analysis pipeline) is subtracted to each optical spectrum, in order to obtain the galaxy-subtracted residual spectrum. A Gaussian kernel of 150 km s$^{-1}$ dispersion is then applied to detect emission lines with a significance $\geq 6\sigma$. However, this search is confined only to the wavelength window between 3600 to 4800 Å (i.e., Ly$\alpha$ emission at $2 \lesssim z \lesssim 3$) to avoid the detection of both low-redshift interlopers (H$\alpha$ $\lambda$6564, [O III] $\lambda$4960,5007, and H$\beta$ $\lambda$4862 at lower redshift) and spurious detections from strong airglow features (e.g., [O I] $\lambda$5577) associated with bad sky subtraction. Low-redshift [O II] $\lambda$3727,3729 interlopers are rejected by checking the corresponding H$\alpha$, [O III], and H$\beta$ emission. Finally, a pixel-integrated skewed normal profile is fitted to the remaining emission lines in order to quantify the line flux, line width, and most importantly, its skewness, as the Ly$\alpha$ line usually presents an asymmetric

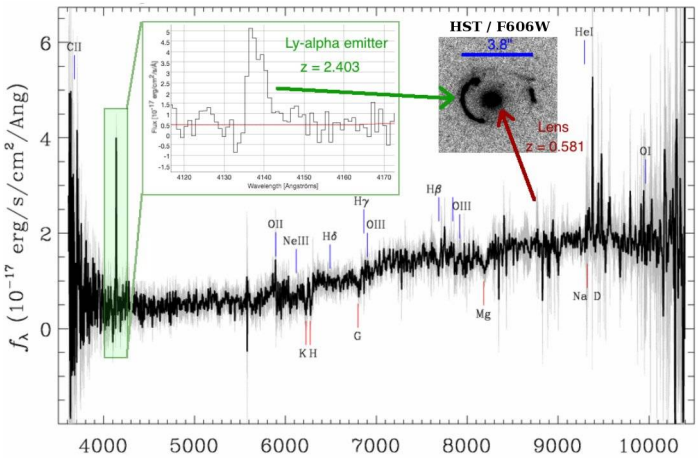


Figure 2.1: Example of the selection procedure showing one of the sources in the BELLS GALLERY sample. A massive galaxy at redshift $z = 0.58$ is lensing a background LAE galaxy at $z = 2.40$. The zoom-in view of the Ly$\alpha$ emission (green) shows the asymmetric profile characteristic of LAEs at high-$z$.

profile at high-$z$ (e.g., Dijkstra et al. 2007), due to absorption by neutral hydrogen. This procedure yielded a final sample of 187 candidates systems.

### 2.2.2 Hubble Space Telescope Observations

From the final sample of 187 gravitational lensed LAE candidates, 21 highest-quality systems were selected to be observed with the $V$-band F606W filter of the Wide Field Camera 3 (WFC3) instrument onboard the *Hubble Space Telescope* (*HST*) under the Cycle 23 program ID 14189 (PI: A. Bolton).

The main goal of this project was to confirm the lensing nature of these LAEs and carry out a lensing modeling of each system. Furthermore, studies of dark substructures in these galaxy-scale systems can be achieved by combining the strong lensing magnification with the unmatched spatial resolution and sensitivity provided by the *HST* in order to deliver new constraints on the nature of dark matter. Once the lensing nature of the background LAEs is confirmed, further analysis of the physical properties of these galaxies can be achieved with much detail thanks to the boost in the apparent flux produced by gravitational lensing.

The 21 highest-quality lensed LAEs candidates were selected to have a detection

Table 2.1: 21 lensed LAE candidates with *HST* observations.

| Target | $z_{\rm lens}$ | $z_{\rm LAE}$ | R.A. (J2000.0) | Dec. (J2000.0) |
|---|---|---|---|---|
| BG002927.38+254401.7 | 0.5869 | 2.4504 | 00:29:27.38 | +25:44:01.78 |
| BG005409.97+294450.8 | 0.4488 | 2.7176 | 00:54:09.97 | +29:44:50.88 |
| BG011300.57+025046.2 | 0.6230 | 2.6088 | 01:13:00.57 | +02:50:46.20 |
| BG020121.39+322829.6 | 0.3957 | 2.8209 | 02:01:21.39 | +32:28:29.66 |
| BG023740.63−064112.9 | 0.4859 | 2.2491 | 02:37:40.63 | −06:41:12.99 |
| BG074249.68+334148.9 | 0.4936 | 2.3633 | 07:42:49.68 | +33:41:48.98 |
| BG075523.52+344539.5 | 0.7224 | 2.6347 | 07:55:23.52 | +34:45:39.59 |
| BG085621.59+201040.5 | 0.5074 | 2.2335 | 08:56:21.59 | +20:10:40.55 |
| BG091807.86+451856.7 | 0.5238 | 2.3440 | 09:18:07.86 | +45:18:56.76 |
| BG091859.21+510452.5 | 0.5811 | 2.4030 | 09:18:59.21 | +51:04:52.59 |
| BG111027.11+280838.4 | 0.6073 | 2.3999 | 11:10:27.10 | +28:08:38.46 |
| BG111040.42+364924.4 | 0.7330 | 2.5024 | 11:10:40.42 | +36:49:24.39 |
| BG111634.55+091503.0 | 0.5501 | 2.4536 | 11:16:34.55 | +09:15:03.04 |
| BG114154.71+221628.8 | 0.5858 | 2.7624 | 11:41:54.71 | +22:16:28.89 |
| BG120159.02+474323.2 | 0.5628 | 2.1258 | 12:01:59.02 | +47:43:23.19 |
| BG122656.45+545739.0 | 0.4980 | 2.7322 | 12:26:56.45 | +54:57:39.04 |
| BG151641.22+495440.7 | 0.5479 | 2.8723 | 15:16:41.22 | +49:54:40.77 |
| BG152926.41+401548.8 | 0.5308 | 2.7920 | 15:29:26.41 | +40:15:48.84 |
| BG222825.76+120503.9 | 0.5305 | 2.8324 | 22:28:25.76 | +12:05:03.95 |
| BG224505.93+004018.3 | 0.7021 | 2.5413 | 22:45:05.93 | +00:40:18.35 |
| BG234248.68−012032.5 | 0.5270 | 2.2649 | 23:42:48.68 | −01:20:32.53 |

significance of the Ly$\alpha$ emission line $\geq 15\sigma$, observed emission line flux $\geq 2\times10^{-16}$ erg cm$^{-2}$ s$^{-1}$, and positive skewness relative to the best-fit symmetric Gaussian profile. Table 2.1 summarizes the main properties of the 21 lensed LAE candidates selected for *HST* observations.

Out of the 21 highest-quality candidates observed with the *HST*, 17 systems are confirmed to be definite gravitational lenses with unambiguous evidence of Einstein rings, arcs, or quadruple or double images of the high-$z$ background LAEs (see four examples in Figure 2.2 and Shu et al. 2016c, for more details). This represents a 80% success rate of finding strong gravitational lenses (17 lenses from 21 candidates), much higher than in other previous surveys using similar spectroscopic selection tech-

niques (SLACS, BELLS, and S4TM surveys, all with ≈ 50% success rate).

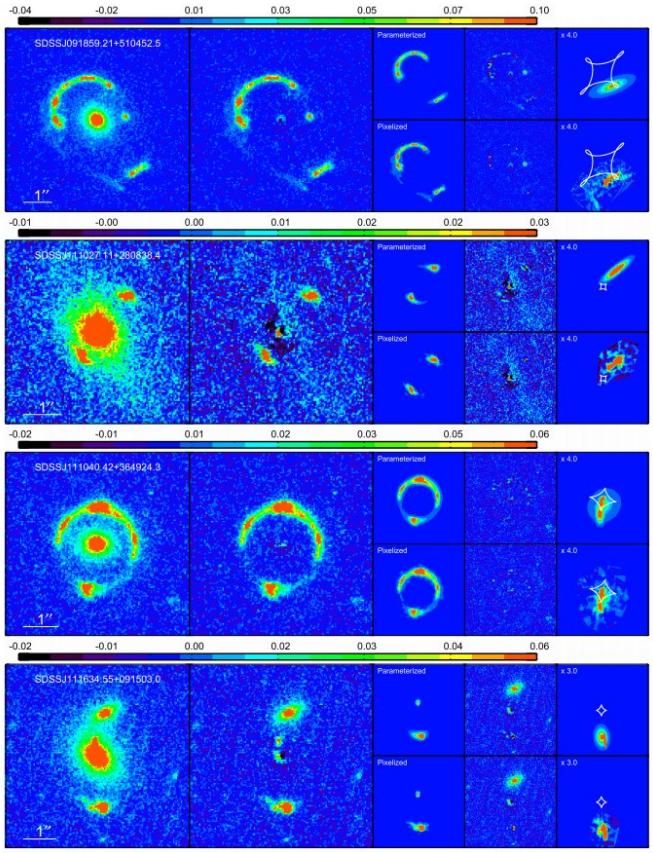


Figure 2.2: This figure is taken from Shu et al. (2016c) and shows *HST* F606W-band images of four gravitational lensed LAEs with unambiguous evidence of arcs and multiple images (left panels). Their lens models are shown in the right panels (parameterized source model on the top and the pixelized source model on the bottom). The caustics of the lens model are marked with white lines in the source plane. The images are oriented such that north is up and east is to the left. The color bars indicate the intensity levels in units of electrons per second per pixel$^2$. The source plane images are zoomed with respect to the observers' plane by the factor indicated in the figure.

### 2.2.3 UV continuum structure of LAEs down to 100-parsec scales

In the analysis of the *HST* images, Shu et al. (2016c) found lensing magnifications of the background high-$z$ LAEs ranging from $4-26$ (with an average of 13), after modeling the systems with a smooth lens model consisting of singular isothermal ellipsoid (SIE) models for the mass distribution of the lens, and, in some cases, an additional external shear to model the higher-order effect from the environment. The background high-$z$ LAEs are resolved into individual star-forming knots, with sizes from less than 100 pc to several kpc and typical separations of 500 pc to 2 kpc in the source plane.

Later on, Cornachione et al. (2018) presented a more detailed morphological analysis of the 17 confirmed BELLS GALLERY lensed LAEs. By using lens-model reconstructions of the LAE rest-frame UV morphology in the source plane, they found $1-9$ clumps per LAE (see Figure 2.3). This gives a clumpiness fraction of $\approx 88\%$, significantly higher than that found in previous studies of unlensed LAEs (e.g., Elmegreen & Elmegreen 2005; Guo et al. 2015). Such large clumpiness fraction in the BELLS GALLERY LAEs is the result of the enhanced spatial resolution provided by the gravitational lensing effect in the BELLS GALLERY survey, as well as the improved flux detection limit.

These clumps have characteristic sizes of 350 pc (half-light radius), far beyond the typical physical resolution of $\simeq 80$ pc provided by the combination of the gravitational lensing and the *HST* resolution in the BELLS GALLERY. The high-$z$ star-forming knots found in the BELLS GALLERY LAEs are significantly larger than most H II regions in local star-forming galaxies which have typical characteristic half-light radii of 200 pc (e.g., Gallagher & Hunter 1983; Kennicutt et al. 2003).

## 2.3 Discovery and Confirmation of the most luminous LAE known

### 2.3.1 Discovery and follow-up

By visual inspection of SDSS and DECaLS[1] color images of the remaining 166 lensed LAEs candidates not observed with the *HST*, we found one candidate showing blue emission features roughly $3.3''$ from the z $= 0.5531$ massive early-type galaxy, SDSS J142954.80+120235.6 (hereafter ETG). Its BOSS spectrum (Plate-MJD-Fiber: 5463-56003-121) shows a secondary emission line at 4652 Å (likely Ly$\alpha$ at z $= 2.8253$). The positions of the blue emission features with respect to the ETG are consistent with a *fold* lensing configuration: a bright lensed image pair, A and B (with a separation of $\simeq 1.5''$), and two fainter images, C and D (see Figure 2.4). The lensed image pair, A and B, is identified in the SDSS photometric catalog as a single source,

[1]Dark Energy Camera Legacy Survey: `http://legacysurvey.org/decamls/`

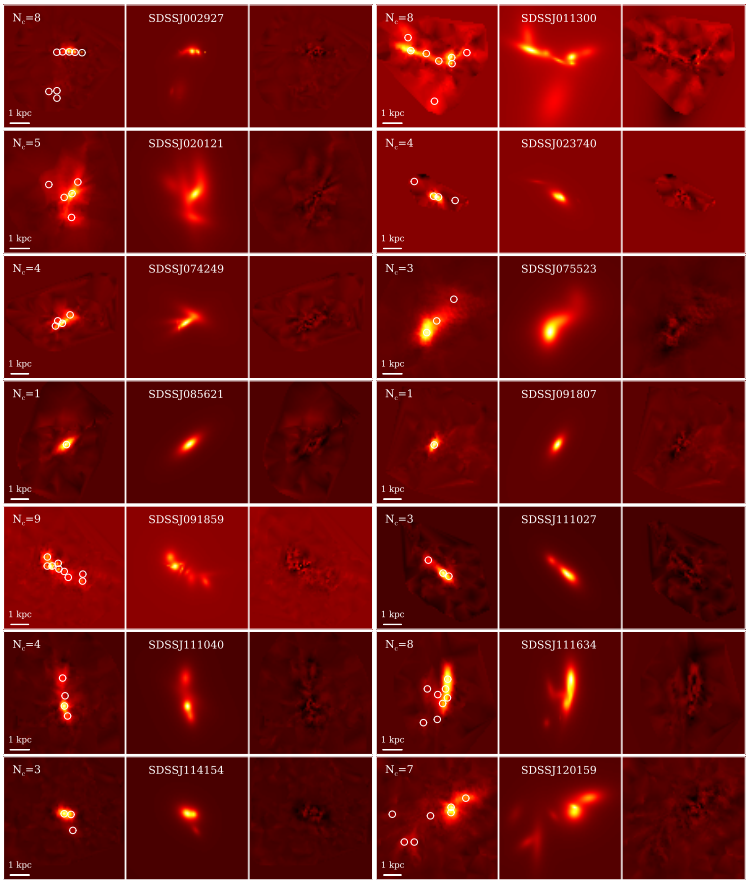


Figure 2.3: Lens-model reconstruction of the rest-frame UV morphology in the source plane of several BELLS GALLERY LAEs (data: left, model: middle, and residuals: right panels). Several LAEs show multiple clumpls (white circles) in the source plane with characteristic sizes of 350 pc (figure is taken from Cornachione et al. 2018).

SDSS J142954.88+120238.3 (hereafter BG1429+1202 for the lensed LAE, where BG stands for BELLS GALLERY), showing blue colors in DECaLS and SDSS photometry (Table 2.2). The lensed images A and B are also detected in the UKIRT Infrared

Deep Sky Survey (UKIDSS: Lawrence et al. 2007) Large Area Survey (LAS), only in Y-band with $21.06 \pm 0.19$ mag and $21.12 \pm 0.20$ mag (in the AB system), respectively.

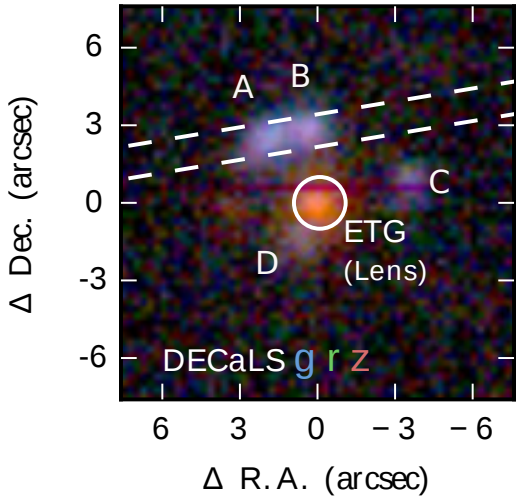


Figure 2.4: DECaLS *grz* color image of BG1429+1202 showing the orientation of the WHT/ACAM and GTC/OSIRIS long slits (white dashed lines). The four lensed images of the background LAE are labeled A, B, C, and D. The position of the spectroscopic $1''$-radius BOSS fibre is marked with a white circle. The image is centered on the lensing galaxy and oriented such that North is up and East is to the left.

We carried out Director Discretionary Time (DDT) optical imaging and long-slit spectroscopic observations in visitor mode on 2016 June 29 using the Auxiliary-port Camera (ACAM: Benn et al. 2008) at the William Herschel Telescope (WHT) to confirm the lensing nature of this LAE. The ACAM long-slit was oriented at a sky position angle $(\mathrm{PA}) = 103^{\circ}.35$, and positioned so as to encompass the two brightest lensed images, A and B, as shown in Figure 2.4. Despite the poor seeing conditions that night ($\sim 4''$ FWHM), we could confirm the lensing nature of this system with the detection in the long-slit spectrum of strong rest-frame UV continuum (with Si IV and C IV in absorption) and Ly$\alpha$ emission at a redshift $\mathrm{z} = 2.823 \pm 0.008$, in agreement with the redshift of the Ly$\alpha$ line detected in the BOSS fiber spectrum, likely from the lensed image D (see Figure 2.4).

Additional observations of BG1429+1202 were carried out on 2016 July 29, this time in very good seeing conditions ($\simeq 0.75''$ FWHM, measured in the 330 s *g*-band acquisition image), using the Optical System for Imaging and low-Intermediate-

Table 2.2: Properties of the system

| ID | R.A.[(1)] (J2000.0) | Dec.[(1)] (J2000.0) | $g^{(2)}$ | $r^{(3)}$ | $z^{(4)}$ |
|---|---|---|---|---|---|
| ETG | 14:29:54.806 | +12:02:35.53 | 22.88 | 20.51 | 19.00 |
| | | | ±0.12 | ±0.07 | ±0.10 |
| A[(5)] | 14:29:54.936 | +12:02:38.23 | 21.48 | 21.23 | 21.32 |
| | | | ±0.08 | ±0.03 | ±0.04 |
| B[(5)] | 14:29:54.831 | +12:02:38.48 | 21.64 | 21.34 | 21.31 |
| | | | ±0.08 | ±0.03 | ±0.04 |
| C | 14:29:54.570 | +12:02:36.69 | 22.27 | 22.22 | 22.02 |
| | | | ±0.09 | ±0.08 | ±0.09 |
| D | 14:29:54.848 | +12:02:34.24 | 22.57 | 22.30 | 21.85 |
| | | | ±0.11 | ±0.10 | ±0.11 |
| Total LAE | | | 20.40 | 20.16 | 20.07 |

NOTE. — (1) positions with 0.11″ astrometric r.m.s. using GAIA DR1 (Gaia Collaboration et al. 2016);
(2) photometry and $1\sigma$ errors from the GTC/OSIRIS $g$-band image;
(3) and (4) photometry and $1\sigma$ errors from the DECaLS DR2 Tractor catalog, except for the lens which were taken from the SDSS DR12 photometric catalog due to image artifacts in DECaLS co-adds;
(5) the lensed images A and B were deblended using GALFIT (Peng et al. 2002, 2010). The magnitudes listed have not been corrected for the Galactic dust extinction, which is 0.104, 0.072, and 0.040 mag for $g$, $r$, and $z$, respectively, in the direction of BG1429+1202. (Schlafly & Finkbeiner 2011).

Resolution Integrated Spectroscopy camera (OSIRIS[2]) on the Gran Telescopio Canarias (GTC). We used the R1000B grism, which provides a spectral coverage of 3630 - 7500 Å (950 - 1960 Å, rest-frame at the redshift of the lensed LAE) and a dispersion of 2.12 Å px$^{-1}$. The OSIRIS 1.2″ wide long-slit was oriented in the same PA used in the WHT/ACAM spectroscopic observations (Figure 2.4). Given this configuration, the corresponding spectral resolution is $\simeq 8$ Å (or $\simeq 500$ km s$^{-1}$ FWHM). The total integration time was 44 minutes, split into $4 \times 660$ s. The data were reduced with IRAF and PYTHON tasks (see chapter 3 for more details on the imaging and spectroscopic reductions).

[2] http://www.gtc.iac.es/instruments/osiris/

### 2.3.2 Source Properties

The rest-frame UV spectrum of the brightest lensed images A and B, is shown in Figure 2.5. Despite the relatively short exposure time, the high S/N GTC/OSIRIS spectrum ($\sim 25$ in the continuum) shows a strong Ly$\alpha$ emission, and a series of strong absorption lines, similar to those seen in the composite spectrum of hundreds of $z \sim 3$ Lyman break galaxies (LBGs) (Shapley et al. 2003). The strongest absorption features are associated to the interstellar medium and stellar winds in a variety of ionization states, from neutral (O I) to highly ionized species (Si IV or C IV). High ionization features with a strong P-Cygni profile are seen both in C IV $\lambda$1548,1550 and Al III $\lambda$1854,1862 doublets, which is indicative of stellar winds from very young massive stars. We identify also additional absorption features unrelated to BG1429+1202 (nine absorption features associated to an intervening metal-line system at $z_{abs} = 2.179 \pm 0.001$, and one broad absorption line at 5183 Å with an observed equivalent width $EW_{obs} = 6.95 \pm 0.2$ Å that remains unidentified). Analysis of the spectra for the individual lensed images A and B shows no differences in the profiles of Ly$\alpha$ and the absorption features neither evidence for velocity offsets between them, as expected if they are both images of the same, non variable, background source.

The same happens to their rest-frame UV continuum slope, $\beta_{UV}$, which is essentially flat in $F_\nu$. Adopting a simple power-law approximation for the UV spectral continuum shape $F_\lambda \propto \lambda^{\beta_{UV}}$, the UV slope can be estimated using the following equation:

$$\beta_{UV} = -\frac{m_1 - m_2}{2.5\log_{10}(\lambda_{m_1}/\lambda_{m_2})} - 2, \tag{2.1}$$

and using the observed $r$ ($m_1$, $\lambda_1 = 6231$ Å) and $z$ ($m_2$, $\lambda_2 = 9134$ Å) bands (which correspond to $\sim 1600$ - 2400 Å in the rest frame), we measure $\beta = -2.1 \pm 0.1$ (however, see chapter 3 for a new measurement of the slope based on new imaging data). Following Calzetti et al. (2000), $\beta_{UV}$ is related with the UV dust attenuation $A_{UV}$ in the form:

$$A_{UV} = 2.31(\beta_{obs} - \beta_0), \tag{2.2}$$

where $\beta_0$ is the intrinsic UV spectral slope of the stellar population. The value of $\beta_0$ is assumed to be $-2.1$ when $\beta > -1.4$, and $-2.35$ otherwise. This implies an effective UV extinction $A_{1600} \sim 0.6$ or $E(B-V) \sim 0.13$, reflecting a modest dust content in BG1429+1202.

In the absence of strong nebular emission lines (C III] $\lambda$1906,1908 doublet is detected, but with low significance), we use faint stellar photospheric lines, formed in the photospheres of massive O and B stars, to derive the systemic redshift of

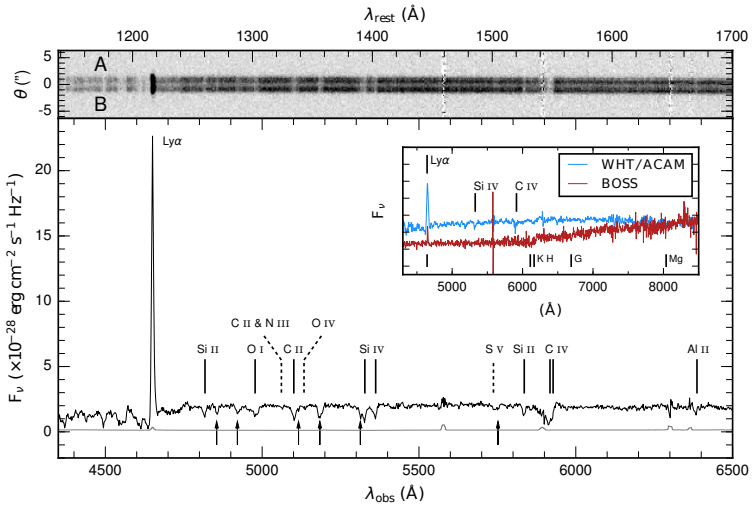


Figure 2.5: GTC/OSIRIS spectrum of BG1429+1202 (black solid line) and its $1\sigma$ error (grey solid line). Ticks mark the positions of the strong interstellar absorption features (solid lines) and photospheric lines (dashed lines) of BG1429+1202, as well as other absorption features related to intervening systems at lower redshifts (black solid arrows). The 2D spectrum is also shown on the top. In the inset panel we show the BOSS and WHT spectra with the positions of the Ly$\alpha$ emission as well as the absorption features related to the ETG at z = 0.5531 from the BOSS fiber spectrum.

BG1429+1202. Using the cleanest photospheric lines in the GTC spectrum, O IV $\lambda$1343, and a close blend of C II and N III at $\lambda$1324 Å, we measure the systemic redshift $z_{\rm sys} = 2.8224 \pm 0.0013$.

The Ly$\alpha$ emission line has an observed (A + B) flux of $F_{\rm Ly\alpha} = (2.1 \pm 0.3) \times 10^{-15}$ erg s$^{-1}$ cm$^{-2}$, $\approx 10$ times higher than the Ly$\alpha$ flux measured within the 1″-radius BOSS fibre ($F^{\rm BOSS}_{\rm Ly\alpha} = 0.256 \times 10^{-15}$ erg s$^{-1}$ cm$^{-2}$). The measured rest-frame equivalent width of Ly$\alpha$ is $EW_0({\rm Ly\alpha}) = 39 \pm 15$ Å. The errors reflect the uncertainty in the determination of the stellar continuum redward of Ly$\alpha$. Although the line appears unresolved in our low resolution spectrum (FWHM $\simeq$ 500 km s$^{-1}$), it is resolved in the BOSS spectrum. Fitting a Gaussian to the BOSS Ly$\alpha$ line, we measured a FWHM of $382 \pm 50$ km s$^{-1}$, after accounting for the instrumental broadening. The nebular C III] $\lambda$1906,1908 doublet is also detected in emission but with low significance ($4\sigma$) and not resolved in our GTC/OSIRIS spectrum. This galaxy can be classified as a LAE, given the rest-frame equivalent width and the velocity width of the Ly$\alpha$ line

(e.g., Ouchi et al. 2008). From our spectrum and available photometric data we do not find any evidence of an active galactic nucleus (AGN).

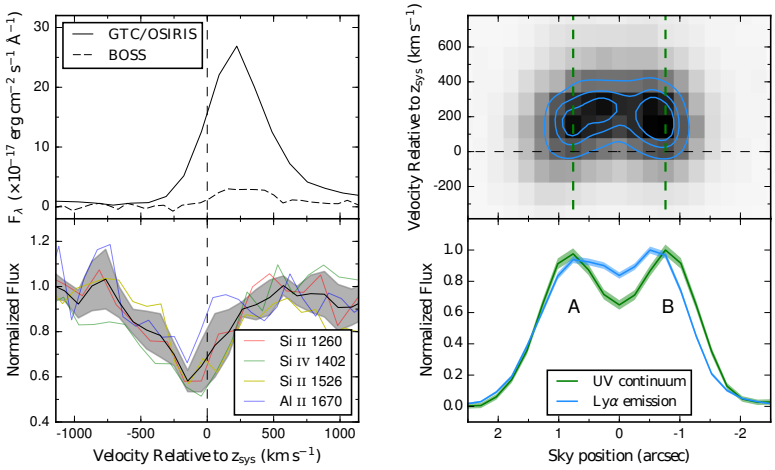


Figure 2.6: Left: Spectral profiles of the Ly$\alpha$ emission (upper panel) and interstellar absorption features (lower panel) on rest velocity. The Ly$\alpha$ emission appears to be redshifted, $v_{Ly\alpha} \sim +200$ km s$^{-1}$, while the interstellar absorption lines are blueshifted by $v_{abs} \sim -150$ km s$^{-1}$ (mean profile in black with the standard deviation in grey shadow). Right: 2D Ly$\alpha$ emission in the position-velocity plane (upper panel) where a spatial gradient of velocity is seen in both A and B images. In the lower panel we show the normalized spatial profiles of the rest-frame UV continuum (green line) and the Ly$\alpha$ emission (blue line). The shaded regions show the 1$\sigma$ errors of the spatial profiles. The Ly$\alpha$ emission appears more extended (large spatial FWHM) between A and B than the rest-frame UV continuum.

The relatively high S/N of the GTC/OSIRIS spectrum allows us to find differences in the kinematics of the Ly$\alpha$ emission and interstellar features, despite the low spectral resolution provided by the GTC R1000B grism (chapter 3 presents new GTC spectroscopic observations of BG1429+1202 with higher spectral resolution). Figure 2.6 (left panel) shows velocity plots of the Ly$\alpha$ emission line and several normalized interstellar absorption lines, relative to $z_{sys}$. The Ly$\alpha$ emission profile has its peak redshifted (with respect to the systemic redshift using photospheric lines) with a velocity $v_{Ly\alpha} \sim +200$ km s$^{-1}$, while the interstellar absorption lines appear blueshifted by $\sim -150$ km s$^{-1}$. This is consistent with galaxy-scale outflows of material from the galaxy in the form of a wind, similar to those seen in other star-forming galaxies at $z \sim 3$ (Shapley et al. 2003; Steidel et al. 2010).

We also notice that a spatial gradient of the Ly$\alpha$ velocity is present in the 2D

spectrum (Figure 2.6, right upper panel). This velocity structure is seen both in A and B but appears mirrored, as expected for those images in this system as A and B images straddle the fold critical curve (see Figure 2.7). We checked carefully the 2D spectrum to see if this pattern is present in other lines, but we found none with this signature. The 1D spatial distribution of Ly$\alpha$ is also compared with that of the rest-frame UV continuum (Figure 2.6, right lower panel). The Ly$\alpha$ emission appears more extended in the inner region between A and B than the UV continuum.

### 2.3.3 Lens Model

To interpret the properties of the lensed system in more detail, we used the 330 s GTC/OSIRIS $g$-band image obtained in $\simeq 0.75''$ FWHM seeing for accurate lens modeling. As shown in Figure 2.7, the lens system comprises four images forming a so-called *fold* configuration, when the source lies very close to a *fold* caustic.

The lens modeling is performed using a non-linear optimizer (similar to previous works: Bolton et al. 2008b; Brownstein et al. 2012; Shu et al. 2015, 2016a,c), consisting on minimizing a $\chi^2$ function (where the observational data is compared to the model) using the Levenberg-Marquardt algorithm with the `LMFIT` package (Newville et al. 2014). The foreground-light is modeled using an elliptical Sérsic profile and its subtraction is performed jointly with the lens modeling. The lens model includes a mass distribution of the foreground lens, parameterized as a singular isothermal ellipsoid (SIE), and an additional external shear is included to model the higher-order effect from the environment. The surface brightness distribution of the background source is reconstructed parametrically using an elliptical Sérsic model. The foreground-light model is combined with the predicted lensed images and convolved with the point-spread function (PSF), which was modeled with a star in the GTC/OSIRIS $g$-band field-of-view.

The best fit lens model ($\chi^2/\mathrm{dof} = 3494/3709$) determines for the lens an Einstein radius $b_{\rm SIE} = 2.95'' \pm 0.10''$, minor-to-major axis ratio $q = 0.34$ and a position angle P.A. $= 165.5$ deg. The strength and position angle of the external shear is $\gamma = 0.059 \pm 0.008$ and $\phi_\gamma = 89.9$ deg, respectively. The characteristic lensing galaxy velocity dispersion, defined as:

$$\sigma_{\rm SIE} = c\sqrt{\frac{b_{\rm SIE}}{4\pi}\frac{D_{\rm L}}{D_{\rm LS}}}, \tag{2.3}$$

is 390$\pm$6 km s$^{-1}$, where $D_{\rm LS}$ and $D_{\rm S}$ are the angular diameter distances from the lens and the observer to the source, respectively. We also find a minor-to-major axis ratio of the SIE component (0.34), smaller than that of the light distribution from the $g$-band model result (0.85). The large lensing velocity dispersion suggests that

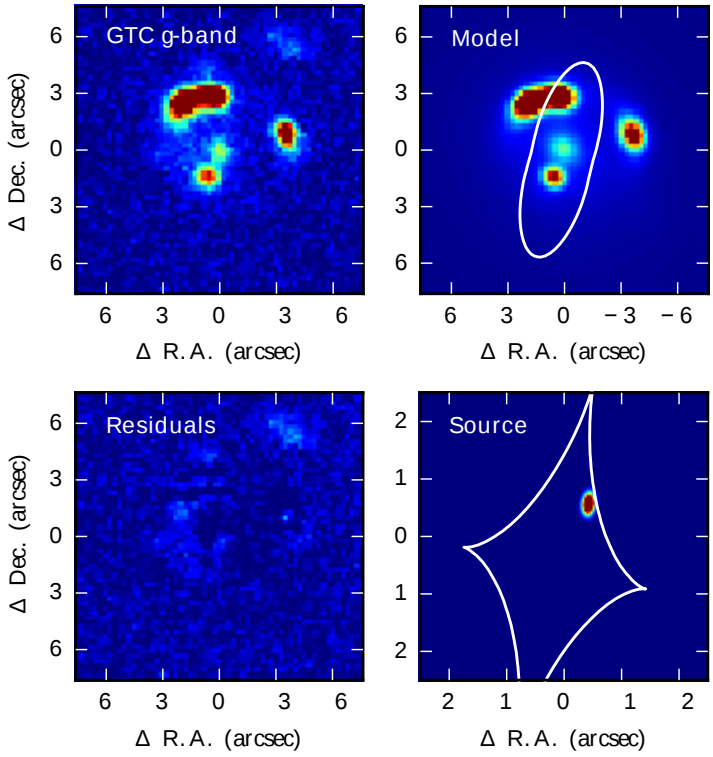


Figure 2.7: Lens model of BG1429+1202. Upper left: GTC/OSIRIS $g$-band image; Upper right: modeled lensed and foreground images with the critical line (white contour); Bottom left: final residuals from the best-fit model; Bottom right: the position of the LAE in the source plane relative to the caustic. All the images are centered on the lensing galaxy and oriented such that north is up and east is to the left.

cluster or line-of-sight structures also contribute a substantial fraction of convergence. There is no clear evidence of a crowded environment around the ETG, either by visual inspection of color images or in the SDSS photometric redshifts, but $\sim 1'$ to the North there is a galaxy, SDSS J142953.71+120333.9, with a BOSS spectroscopic redshift $z = 0.5527 \pm 0.0002$, very close to the lensing ETG, indicating that a cluster or group of galaxies at $z \simeq 0.55$ may be present, as suggested by the external shear field.

For the source, the lens model gives local magnifications of 3.2, 3.1, 1.8 and 0.7 for

images A, B, C and D, respectively, which means that the total magnification is $8.8 \pm 0.4$. The source has an effective radius $R_{\rm eff} = 0.159'' \pm 0.007''$, which corresponds to $R_{\rm eff} = 1.28 \pm 0.06$ kpc for the adopted cosmology. The source has a minor-to-major axis ratio $q = 0.56$ and Sérsic index n $= 3.9$. It is centered at $\Delta$R.A. $= -0.43''$ and $\Delta$Dec. $= 0.56''$ relative to the center of the lensing galaxy.

### 2.3.4 Intrinsic Properties

Having determined the magnification of BG1429+1202 we can estimate its intrinsic properties. From the total DECaLS DR2 *r*-band magnitude, we determine a rest-frame 1600 Å luminosity $L_{1600} = (6.12 \pm 0.48) \times 10^{30}$ erg s$^{-1}$ Hz$^{-1}$. Using the Kennicutt (1998) conversion, this rest-frame UV luminosity translates into an intrinsic star formation rate (SFR) of $\simeq 90\ M_{\odot}{\rm yr}^{-1}$, when corrected for magnification, reddening and the lower proportion of low-mass stars in the Chabrier (2003) stellar IMF relative to the standard Salpeter (1955) adopted by Kennicutt (a factor of $1/1.8$).

Turning to Ly$\alpha$, assuming the space distribution of Ly$\alpha$ in the source plane and its lensing magnification are similar to those of the rest-frame UV continuum, and applying the correction for the magnification and the slit losses (the GTC/OSIRIS slit captured a fraction $\simeq 0.60$ of the total light of BG1429+1202), we derive an intrinsic Ly$\alpha$ luminosity $L_{{\rm Ly}\alpha} = (2.80 \pm 0.39) \times 10^{43}$ erg s$^{-1}$.

Assuming case-B recombination and the Kennicutt (1998) conversion, this luminosity translates in a SFR(Ly$\alpha$) $\simeq 25\ M_{\odot}{\rm yr}^{-1}$. Comparing the estimates of SFR from the rest-frame UV and Ly$\alpha$, we measure $f_{\rm esc}^{{\rm Ly}\alpha} \sim 0.3$, consistent with that estimated from LAEs at z $\sim 3$ (e.g., Verhamme et al. 2008; Zheng et al. 2016). However, we should note that the measured $f_{\rm esc}^{{\rm Ly}\alpha}$ results from the assumption that the spatial distribution of Ly$\alpha$ (and its magnification) follows the rest-frame UV continuum. Ly$\alpha$ halos are hard to be resolved in individual LAEs, and have been studied mainly by using stacking techniques (Steidel et al. 2011; Momose et al. 2016; Sobral et al. 2017), or in nearby high-redshift analogs (e.g. Yang et al. 2017). However, for a few cases, strong gravitational lensing allows spatially resolved studies of high-redshift galaxies (e.g., Patrício et al. 2016).

In order to establish how typical are the intrinsic properties of this galaxy, we compare it with other UV-selected z $\sim 3$ LBGs and LAEs. BG1429+1202 is intrinsically more luminous in the rest-frame UV by factors of 7 and 19, relatively to $L^*$ from the luminosity functions of Reddy & Steidel (2009) for z $\sim 3$ LBGs and z $\sim 3.1$ LAEs selected by narrow-band imaging by Ouchi et al. (2008), respectively. It is also intrinsically very luminous in the Ly$\alpha$ line, when compared with $L^*_{{\rm Ly}\alpha}$ from the luminosity functions of LAEs at z $\sim 3.1$ (factor of $\sim 5$; Ouchi et al. 2008) and LAEs at z $= 2.8$ in CDFS (factor of $\sim 5-9$; Zheng et al. 2016).

A comparison is also presented in Table 2.3 with other well known, exceptionally

Table 2.3: Intrinsic properties of BG1429+1202 and other bright galaxy-galaxy lenses

| Object | z | $m_{\rm UV}$ | $\mu$ | $L_{\rm UV}$ | $L_{{\rm Ly}\alpha}$ |
|---|---|---|---|---|---|
| | (1) | (2) | (3) | (4) | (5) |
| **BG1429+1202** | **2.822** | **20.16** | **8.8** | **6.99** | **28.0** |
| MS 1512-cB58[a,b] | 2.726 | 20.64 | 30 | 1.16 | – |
| Cosmic Eye[c] | 3.073 | 20.30 | 28 | 2.08 | – |
| 8 o'clock[d] | 2.735 | 19.22 | 12.3 | 10.55 | – |
| Cosmic Horseshoe[e,f] | 2.381 | 19.70 | 24 | 2.74 | 3.3 |
| LBGs[g] | $\sim 3$ | 24.61 | – | 1.06 | – |
| LAEs[h] | $\sim 3.1$ | 25.84 | – | 0.36 | 5.8 |

NOTE. — 1) redshift;
2) rest-frame UV apparent magnitudes ($\simeq 1500-1700$ Å) using *r*- or *i*-bands, depending on the redshift;
3) total magnification factor;
4) and 5) intrinsic rest-frame UV and Ly$\alpha$ luminosities in units of $10^{29}$ erg s$^{-1}$ Hz$^{-1}$ and $10^{42}$ erg s$^{-1}$, respectively, corrected for the lensing magnification;
References — [a)] Ellingson et al. (1996); [b)] Seitz et al. (1998); [c)] Smail et al. (2007); [d)] Allam et al. (2007); [e)] Belokurov et al. (2007); [f)] Quider et al. (2009); [g)] Reddy & Steidel (2009); [h)] Ouchi et al. (2008).

bright in the optical, galaxy-galaxy z $\sim 3$ lenses: the Cosmic Eye (Smail et al. 2007), MS 1512-cB58 (Yee et al. 1996), the 8 o'clock (Allam et al. 2007), and at lower redshift the Cosmic Horseshoe (Belokurov et al. 2007). BG1429+1202 has similar brightness, but is intrinsically very luminous in the rest-frame UV continuum and Ly$\alpha$. It is also the only one which can be classified as Ly$\alpha$ emitter (the Ly$\alpha$ emission of the Cosmic Horseshoe galaxy shares many of the properties of the Ly$\alpha$ emitters, but its $EW_0({\rm Ly}\alpha)$ is below the threshold generally adopted to define it as Ly$\alpha$ emitter; Quider et al. 2009). This puts BG1429+1202 in the small group of very bright z $\sim 3$ galaxies that, due to the high magnification and its high intrinsic luminosity, provides the unique opportunity to obtain high S/N spectroscopy to study in detail its physical properties. Additional studies of this lensed LAE using higher spectral resolution OSIRIS spectroscopy as well as narrow band imaging are presented in Chapter 3.

## 2.4 Conclusion

In this Chapter I introduced the BELLS GALLERY Survey (Shu et al. 2016b,c), which identified 187 high-probability lensed LAE candidates systems at $2 \lesssim z_{\rm LAE} \lesssim 3$

through the detection of a secondary and asymmetric emission line (Ly$\alpha$ emission) in the spectra of massive galaxies at redshift of approximately 0.5. Among these, 21 of the highest quality candidates were observed with *HST*/WFC3 confirming their lensing nature (Shu et al. 2016c), and providing a detailed characterization of their rest-frame UV continuum surface brightness profiles and substructure down to scales of 100 pc (Cornachione et al. 2018).

I also reported the discovery of a bright quadruply lensed LAE at z = 2.8224. BG1429+1202 is one of the brightest and most luminous galaxy-scale lensed LAEs known so far. The very bright apparent magnitude results partially from gravitational lensing by a z = 0.5531 luminous red galaxy, which provides a magnification of $8.8 \pm 0.4$. After accounting for the lensing magnification, BG1429+1202 is also intrinsically very luminous in the rest-frame UV and Ly$\alpha$ emission by about 19 and 5 times the typical $L^*_{\rm UV}$ and $L^*_{\rm Ly\alpha}$ of LAEs at $z \sim 3$, respectively, showing low dust content and indications of massive recent star formation. Compared with the few other bright strongly lensed galaxies known, BG1429+1202 is the most luminous one in the Ly$\alpha$ line. This makes this source another good laboratory for further detailed studies of the physics of star formation and Ly$\alpha$ emission in galaxies in the epoch of the Universe when the star formation rate density reached its peak. The new method presented in Shu et al. (2016b) opens a new window to the study of high redshift galaxies by the combination of massive spectroscopic surveys, large-area multi-band imaging, gravitational lensing and follow-up with 10m telescopes like GTC.

# 3

# Imaging and Spectroscopic Study of the BELLS GALLERY LAEs

In this Chapter, I present the results of the recent follow-up observations of six strong gravitationally lensed LAEs discovered within the BELLS GALLERY survey. This survey is conducted using Gran Telescopio Canarias (GTC) and William Herschel Telescope (WHT) imaging and spectroscopic data to study several rest-frame UV physical properties of these LAEs.

## 3.1 Introduction

In addition to the morphological characterization of the *HST* BELLS GALLERY sample presented in Shu et al. (2016c) and in Cornachione et al. (2018), we have carried out imaging and spectroscopic observations with the GTC and the WHT, both in the Observatorio del Roque de los Muchachos. This Chapter presents an imaging and spectroscopic study of several rest-frame UV properties of BELLS GALLERY LAEs. The natural burst in the flux produced by strong gravitational lensing offers the unique opportunity to carry out higher S/N studies than otherwise achievable, providing a close-up look of LAE's properties during the epoch when cosmic star formation activity was at its peak.

### 3.1.1 Sample Selection

Shu et al. (2016c) presented *HST* observations of 21 BELLS GALLERY LAEs. From these, 17 systems were confirmed to be gravitationally lensed, showing multiple im-

ages or Einstein rings of the high-$z$ background LAEs.

We restricted the GTC spectroscopic follow-up to LAEs showing large *HST* $V$-band flux densities, since even with the magnification provided by gravitational lensing, some of these LAEs appear to be relatively faint for high S/N spectroscopic studies. In addition, since these observations are seeing-limited, we selected those LAEs showing larger background image separations, avoiding the contamination of foreground lens galaxies in their spectra. The best candidates for GTC spectroscopy are the LAEs SDSS J020121.39+322829.6, SDSS J074249.68+334148.9, SDSS J075523.52+344539.5, and SDSS J091859.21+510452.5 (hereafter BG0201+3228, BG0742+3341, BG0755+3445, and BG0918+5104, where "BG" stands for BELLS GALLERY). Figure 3.1 shows the *HST* images of these 4 lensed LAEs (with false color for visual purpose).

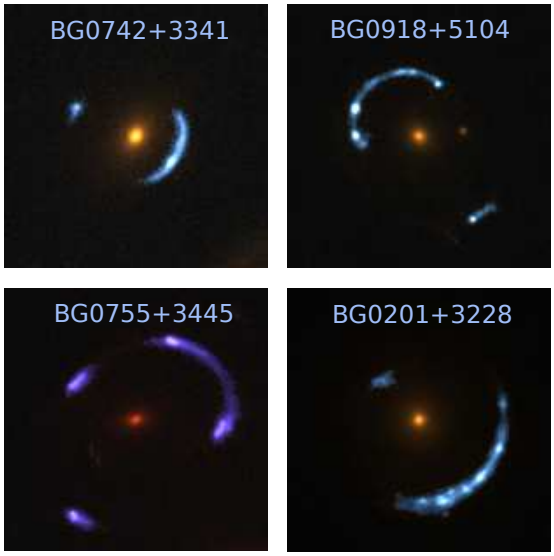


Figure 3.1: *HST* images of four lensed LAEs analyzed in this chapter. Multiple images and arcs of the background high-$z$ LAEs (bluish color) are seen and represent an unambiguous evidence of the lensing nature in these systems. All the images are centered on the lensing ETGs (reddish color) and oriented such that north is up and east is to the left.

We also re-observed BG1429+1202 (already discussed in chapter 2), this time with higher spectral resolution and deeper imaging. In addition, by visual inspection of the color images (SDSS SkyServer and DECaLS SkyViewer) of the parent sample com-

posed of 166 BELLS GALLERY lensed LAE candidates, we found another promising candidate, hereafter BG1501+3042, showing bluish features $\approx 3.7''$ SE from the ETG SDSS J150114.60+304230.8 ($z_{\rm lens} = 0.638$). Its BOSS spectrum (Plate-MJD-Fiber: 3875-55364-935) shows a secondary emission line at $\simeq 4438$ Å, likely Ly$\alpha$ emission at $z \simeq 2.65$. Figure 3.2 shows the SDSS color images of BG1429+1202 and BG1501+3042 where clear bluish features are visible around the ETGs. In Table 3.1 we summarize the properties of these six lensed systems.

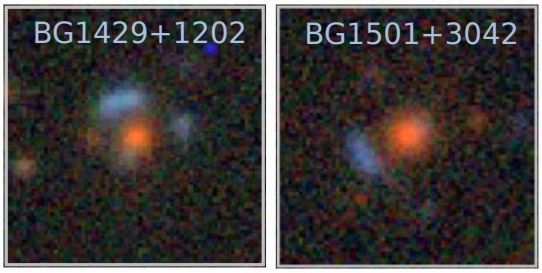


Figure 3.2: 20"×20" DECaLS color images of the lens systems SDSS J142954.80+120235.6 (left panel, hereafter BG1429+1202) and SDSS J150114.60+304230.8 (right panel, hereafter BG1501+3042). Multiple bluish features are seen around the massive early-type galaxies (reddish color), suggesting a lensing nature of these systems. The images are centered on the lensing ETGs and oriented such that north is up and east is to the left.

Table 3.1: Properties of the lensed LAEs.

| LAE | R.A.$^{(1)}$ | Dec.$^{(1)}$ | $z_{\rm lens}^{(2)}$ | $z_{\rm LAE}^{(3)}$ |
|---|---|---|---|---|
| | (J2000.0) | (J2000.0) | | |
| BG0201+3228 | 02:01:21.39 | +32:28:29.7 | 0.396 | 2.821 |
| BG0742+3341 | 07:42:49.68 | +33:41:49.0 | 0.494 | 2.363 |
| BG0755+3445 | 07:55:23.52 | +34:45:39.6 | 0.722 | 2.635 |
| BG0918+5104 | 09:18:59.21 | +51:04:52.6 | 0.581 | 2.403 |
| BG1429+1202 | 14:29:54.80 | +12:02:35.6 | 0.553 | 2.825 |
| BG1501+3042 | 15:01:14.61 | +30:42:30.8 | 0.638 | 2.649 |

**Notes. —** (1) positions of the lens galaxy; (2) redshift of the lens; (3) redshift of the LAE measured using the Ly$\alpha$ line.

## 3.2 Follow-up Observations

### 3.2.1 GTC Spectroscopic Observations

The spectroscopic survey was conducted with the GTC OSIRIS instrument. Details of these observations are listed in Table 3.2. The observations were obtained in service mode over ten different nights, between 2017 January 26 and 2018 February 16, as part of several GTC programs (GTC47-16B, GTC67-17A, and GTCMULTIPLE2F-17B; PI: Marques-Chaves).

Table 3.2: OSIRIS spectroscopic observations.

| LAE | PA (°) | Grism | Time (sec) | Seeing (arcsec) |
|---|---|---|---|---|
| BG0201+3228 | −47 | R2000B; R2500R | 2100; 2800 | 0.8 |
| BG0742+3341 | 63 | R2000B | 3600 | 0.8 |
| BG0755+3445 | −30; 75 | R2000B; R2500R | 7200; 3600 | 0.8 |
| BG0918+5104 | 10.8 | R2000B; R2500R | 7200; 3600 | 0.7 |
| BG1429+1202 | −76.7 | R2500V; R2500R | 3600; 3600 | 0.8 |
| BG1501+3042 | 29.8 | R1000B | 3000 | 1.1 |

The data were reduced using IRAF. For each individual 2D dimensional spectrum, the bias were subtracted using calibration data provided by the GTC staff for each observing block. The characterization of the lamp shape's flats is done using the IRAF task `apnormalize` from the NOAO `twodspec` package. Two-dimensional spectra are then corrected from flat-fielding (i.e. normalized) using the `ccdproc` task from the `ccdred` package. Wavelength calibrations are done for every observing night using arc lamps provided by the GTC staff. To do so, we add wavelength solutions to each spectrum using `identify` and `reidentify` tasks from the `onedspec` package. We calculated the 2D wavelength solution using the `fitcoords` task from the `longslit` package, and then applied those corrections to our scientific data using the `transform` task. The background subtraction is performed for each individual 2D spectrum using the `background` task. We use a two order Chebyshev function to fit two or more sky regions on both sides of the object spectrum. The 1D spectra were then extracted using the `apall` task from the `apextract` package, and were corrected for the instrumental response using observations of standard stars provided for each observation. The individual 1D spectra are then median combined and pixels exceeding a specific threshold (e.g., cosmic rays) are rejected. This is done using the

`scombine` task.

### 3.2.2 Imaging Observations

In addition, we carried out imaging observations with the GTC and WHT of five of these lensed LAEs:

• *BG0201+3228* was observed on 2015 September 16 in the *g*- and *i*-bands using the Auxiliary-port Camera (ACAM: Benn et al. 2008) at the WHT. ACAM has a circular field of view of 8′ diameter with a plate scale of 0.254″ pixel$^{-1}$. The total integration time was 500 and 300 seconds for *g*- and *i*-bands respectively, under sub-arsec seeing conditions ($\approx 0.85''$ full width at half maximum, FWHM).

• *BG0755+3445* was observed on 2015 April 24 in the *r*-band using ACAM. The total integration time was 300 seconds under $\approx 0.55''$ FWHM seeing. We later observed this object on 2017 February 17 in the *g*-, *i*-, and *z*-bands using the OSIRIS instrument on the GTC as part of the GTC program GTC47-16B (PI: R. Marques-Chaves). OSIRIS has a field of view of $7.8' \times 8.5'$ with a plate scale of 0.254″ pixel$^{-1}$. The total exposure time was 900 s for each band, split into 9 individual exposures of 100 s. The seeing of the final images was $\sim 0.9''$, $0.7''$, and $0.8''$ FWHM for the *g*-, *i*-, and *z*-bands, respectively.

• *BG0918+5104* was observed on 2017 February 17 in the *g*- and *z*-bands using OSIRIS on GTC (same program as BG0755+3445). The total exposure time was 900 s for each band, split into 9 individual exposures of 100 s. The seeing of the final images was $\sim 0.9''$ and $0.8''$ FWHM for the *g*- and *z*-bands, respectively. Additionally, we have used archival *R* and *I* wide-field images from MEGACAM on the Canada-France-Hawaii Telescope (CFHT), processed and stacked using the MegaPipe image staking pipeline (Gwyn 2008), and downloaded from the Canadian Astronomy Data Centre (CADC[1]). Total exposure times are 3200 and 2560 s in *R* and *I* bands, with an average seeing of $0.85''$ and $0.55''$ FWHM, respectively.

• *BG1429+1202* was first observed on 2016 July 29 in the *g*-band using OSIRIS on the GTC as part of the GTC DDT program GTC09-16ADDT (already presented in chapter 2). Later on, we observed this system again on 2017 April 24 in the *r*-, *i*-, and *z*-band on the GTC as part of the program GTC67-17A (PI: Rui Marques Chaves). The total exposure time was 540 s for each band, split into 9 individual exposures of 60 s. The seeing of the final images was $\sim 0.8''$, $0.7''$, and $0.8''$ FWHM for the *r*-, *i*-,

[1] `http://www.cadc-ccda.hia-iha.nrc-cnrc.gc.ca/en/cfht/`

and $z$-bands, respectively.

• *BG1501+3042* was observed on 2017 May 22 in the $g$-, $r$-, and $i$-bands using OSIRIS on GTC (same GTC program as BG1429+1202). The total exposure time was 420 s for each band, split into 7 individual exposures of 60 s. The seeing of the final $g$-, $r$-, and $i$-band images are respectively $\sim 0.9''$, $0.77''$, and $0.85''$ FWHM.

For all imaging observations, each frame was reduced individually following standard reduction procedures in IRAF. These include subtraction of the bias and further correction of the flat-field using, when possible, skyflats from low crowded fields. The registration and combination were done using SCAMP (Bertin 2006) and SWARP (Bertin 2010), and the astrometry was improved using Gaia stars from the first data release DR1 (Gaia Collaboration et al. 2016), yielding a typical r.m.s of $\simeq 0.07''$. Finally, the images were flux-calibrated against SDSS (Data Release 9 catalog, Ahn et al. 2012) using stars in the field of view (i.e. `CLASS STAR` $\simeq 1$ in the SExtractor output; Bertin & Arnouts 1996).

## 3.3 Imaging analysis

### 3.3.1 Photometry

The morphology of the LAEs in this sample consists of complex arc-like features and/or multiple lensed images seen in the observer plane (see Figure 3.3).

Given the typical $\sim 0.8''$ FWHM seeing of the GTC and WHT images, there is light contamination from the foreground lens galaxies. In order to perform a clean photometry of the lensed images of these LAEs, we use the two-dimensional fitting program GALFIT (Peng et al. 2002, 2010) to model the light distribution of the foreground lens (and in some cases additionally nearby objects). We use Sérsic profiles centered at the centroids of each ETG light emission allowing only two pixels freedom ($\sim 0.5''$). For the four lensed LAEs with *HST* imaging, we use the models of the foreground lens (i.e. effective radius, minor-to-major axis ratio, and major-axis position angle) presented in Shu et al. (2016c) as priors in our modeling. Nearby stars were used as PSF models.

We further use SExtractor (Bertin & Arnouts 1996) to measure the magnitudes in each band. To do so, we use aperture photometry using effective apertures with diameters of 2.5 times the FWHM of the PSF. Aperture photometry was performed for compact lensed morphologies, such as the lensed images of BG0755+3445, BG1429+1202 and the faint lensed counter-images of BG0201+3228 or BG1501+3042. For more complex morphologies, such as bright extended arcs seen in BG0201+3228, BG0918+5104 and BG1501+3042, we derived total magnitudes us-

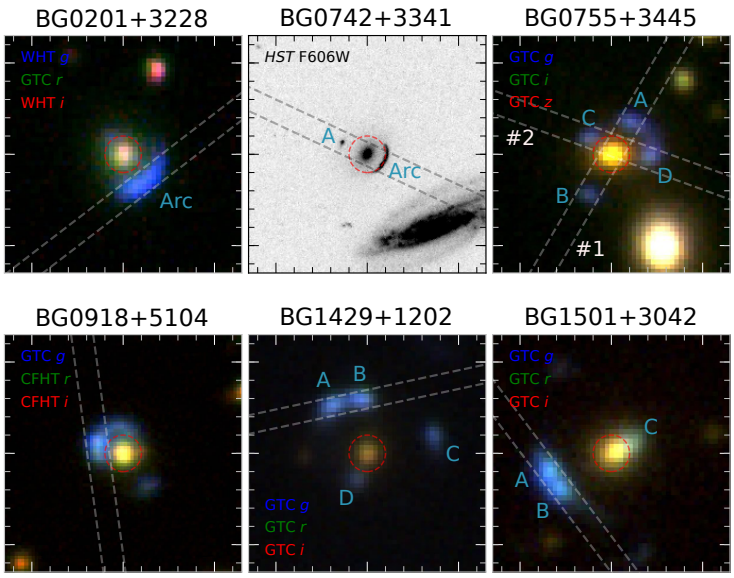


Figure 3.3: 13"×13" color images of the 6 lensed LAEs analysed in this work using GTC, WHT, and CFHT imaging as indicated. The orientations of the GTC/OSIRIS long slit are marked with grey dashed lines, as well as the position of the spectroscopic 1″-radius BOSS fiber (red dashed circles). The images are centered on the lensing ETGs and oriented such that north is up and east is to the left.

ing the corresponding SExtractor's `MAG_AUTO` output. Table 3.3 summarizes the photometric measurements for each lensed LAE.

### 3.3.2 Lens Model

In addition to the lens models presented in Shu et al. (2016c) for the four lensed LAEs imaged with the *HST*, BG0201+3228, BG0742+3341, BG0755+3445, and BG0918+5104, and in chapter 2 for BG1429+1202, we also performed a new lens modeling for BG1501+3042.

We use the 420 s GTC *r*-band image ($\simeq 0.9''$ FWHM) for accurate lens modeling of BG1501+3042. We assume the same methodology already discussed in chapter 2 and in previous works (Bolton et al. 2008a; Brownstein et al. 2012; Shu et al. 2015, 2016a,c), consisting in a nonlinear optimizer, which minimizes a $\chi^2$ function using

Table 3.3: Integrated magnitudes of the lensed LAEs.

| LAE | $g$ | $r$ | $i$ | F606W |
|---|---|---|---|---|
| | (AB) | (AB) | (AB) | (AB) |
| BG0201+3228 | $20.94 \pm 0.09$ | $20.62 \pm 0.08$ | $20.47 \pm 0.20$ [a] | $20.56 \pm 0.05$ |
| BG0742+3341 | – | – | – | $22.18 \pm 0.05$ |
| BG0755+3445 | $21.68 \pm 0.10$ | $21.16 \pm 0.08$ | $21.04 \pm 0.06$ | $21.11 \pm 0.05$ |
| BG0918+5104 | $21.69 \pm 0.09$ | $21.01 \pm 0.09$ | $20.91 \pm 0.09$ | $20.87 \pm 0.05$ |
| BG1429+1202 | $20.40 \pm 0.08$ | $20.14 \pm 0.05$ | $20.08 \pm 0.05$ | – |
| BG1501+3042 | $21.32 \pm 0.10$ | $21.00 \pm 0.05$ | $20.98 \pm 0.07$ | – |

**Notes.**
[a] The ACAM/WHT *i* band data of BG0201+3228 are affected by a high background.

the Levenberg-Marquardt algorithm with the `LMFIT` package (Newville et al. 2014) (see Shu et al. 2016c, for details).

Briefly, the lens model assumes a mass distribution of the foreground lens parameterized as a singular isothermal ellipsoid (SIE). The surface brightness distribution of both lens and background source is reconstructed parametrically using an elliptical Sérsic model. The foreground-light model is combined with the predicted lensed images and convolved with the point-spread function that was modeled with stars in the field of view of the GTC/OSIRIS image.

Figure 3.4 shows the *r*-band image of BG1501+3042. The lensed system is composed of two bright and close lensed images,"A" and "B", and another one, "C", partially blended with the lens galaxy "G" (in section 3.4 we show that "A", "B", and "C" are lensed images of the same background LAE). Such configuration with three lensed images is uncommon in galaxy-scale lensed systems, which typically present two or four lensed images (see, however, other lensed configurations produced by groups or clusters of galaxies: e.g., Oguri et al. 2008; Dahle et al. 2013, and chapter 4).

Our best-fit lens model, assuming a simple SIE for the mass distribution of the lens (bottom left panel in Figure 3.4), is able to recover reasonably well the light emission of the lensed images, but fails to reproduce the two different lensed images "A" and "B". This may suggest that an additional deflecting structure may be present and is perturbing the lensed image $3.7''$ SE from the lens, splitting it in two pieces, "A" and "B". To take into account this, we add to our model an additional sub-halo modeled with a NFW profile, and, for simplicity, assume that it is at the redshift of the lens (i.e. $z_{\rm lens} = 0.638$). Our best-fit lens model (shown in the bottom right panel in Figure 3.4), now involving an extra NFW sub-halo, is able to reproduce the three lensed images of BG1501+3042. We find that this NFW sub-halo, with a mass of $\simeq 2.6 \times 10^9 M_{\odot} h^{-1}$,

is located $\approx 26$ kpc SE from the lens, very close to the lensed image "B" (marked with a red circle in Figure 3.4). No extra light emission is visible at this position on the available images.

The lens model (top right panel of Figure 3.4) gives local magnifications of 2.2, 2.2, and 1.4 for the lensed images A, B, and C, respectively, compared with the modeled flux of the source, which means that the total magnification is $\simeq 5.8$. The source has an effective radius $R_{\rm eff} = 0.21'' \pm 0.02''$, which corresponds to $R_{\rm eff} = 1.7 \pm 0.1$ kpc at $z \simeq 2.65$ for the adopted cosmology.

Table 3.4 summarizes the main source properties and lensing magnification factors derived for the six LAEs studied in this Thesis. Note, however, that the lensed LAEs modeled with *HST* data presented in Shu et al. (2016c) and Cornachione et al. (2018) show multiple components in the source plane due to the improved high spatial resolution provided by *HST* imaging.

Table 3.4: Source LAE properties and lensing magnification.

| LAE | ΔR.A. (arcsec) | ΔDecl. (arcsec) | $R_{\rm eff}$ (pc) | $\mu$ | Reference |
|---|---|---|---|---|---|
| BG0201+3228 | $+0.25$ | $-0.25$ | $1066 \pm 89$ | 15 [a] | Shu et al. (2016c) |
| | $+0.24$ | $-0.10$ | $1756 \pm 223$ | | |
| | $+0.21$ | $-0.30$ | $821 \pm 5$ | | |
| BG0742+3341 | $-0.22$ | $+0.15$ | $115 \pm 6$ | 16 [a] | Shu et al. (2016c) |
| | $-0.17$ | $+0.15$ | $162 \pm 4444$ | | |
| | $-0.23$ | $+0.13$ | $980 \pm 64$ | | |
| BG0755+3445 | $+0.07$ | $-0.36$ | $1058 \pm 10$ | 14 [a] | Shu et al. (2016c) |
| | $-0.01$ | $-0.28$ | $264 \pm 2$ | | |
| | $+0.65$ | $+0.48$ | $1170 \pm 50$ | | |
| BG0918+5104 | $+0.08$ | $-0.27$ | $86 \pm 35$ | 18 [a] | Shu et al. (2016c) |
| | $+0.27$ | $-0.15$ | $90 \pm 5$ | | |
| | $+0.17$ | $-0.22$ | $1232 \pm 36$ | | |
| BG1429+1202 | $-0.43$ | 0.56 | $1280 \pm 60$ | 8.8 | Chapter 2 |
| BG1501+3042 | $+1.01$ | $-0.64$ | $1700 \pm 100$ | 5.8 | This Chapter |

**Notes.**
[a] The lensing magnification factor refers to the combination of all sub-components derived in the Shu et al. (2016c) models.

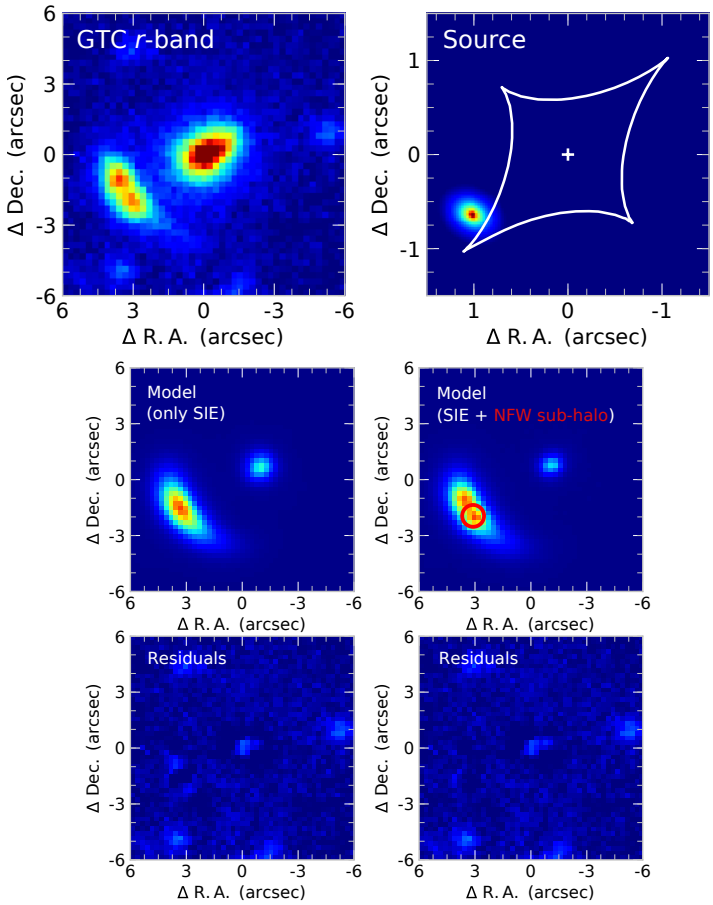


Figure 3.4: Lens model of BG1501+3042. Upper left: GTC/OSIRIS *r*-band image; Upper right: the position of the LAE in the source plane showing the caustic line; In the bottom panels we show the two best-fit models assuming a simple singular isothermal ellipsoid (left) and with an additional NFW sub-halo (right). The latter is able to reproduce the three lensed images of BG1501+3042. All the images are centered on the lensing galaxy and oriented such that north is up and east is to the left.

### 3.3.3 UV Luminosity

Knowing the total magnification of these galaxies, we can now determine their intrinsic luminosities in the rest-frame UV ($M_{\rm UV}$), which is typically defined at $\approx 1500-1700$ Å. The UV luminosity (in units of erg s$^{-1}$ Hz$^{-1}$) can be determined using the formula:

$$L_{\rm UV} = \frac{4\pi \times D_{\rm L}^2 \times 9.5214 \times 10^{+36}}{(1+z)} \times \frac{1}{\mu} \times 10^{-0.4(m+48.6)}, \quad (3.1)$$

where $m$ is the apparent AB magnitude in the closest observed band to rest-frame 1700 Å, $D_L$ is the luminosity distance in pc at a given redshift $z$, and $\mu$ is the total magnification factor. In a similar way, apparent magnitudes can be converted into intrinsic absolute UV magnitudes, $M_{\rm UV}$, in units of AB magnitudes, using the following formula:

$$M_{\rm UV} = m - 5\log_{10}(D_{\rm L}({\rm pc})) + 5 + 2.5\log_{10}(1+z) + 2.5\log_{10}(\mu), \quad (3.2)$$

Table 3.5: Corrections for the Galactic dust extinction following Schlafly & Finkbeiner (2011).

| LAE | $g$ | $r$ | $i$ | F606W |
|---|---|---|---|---|
| | (AB) | (AB) | (AB) | (AB) |
| BG0201+3228 | 0.229 | 0.158 | 0.117 | 0.137 |
| BG0742+3341 | – | – | – | 0.093 |
| BG0755+3445 | 0.174 | 0.120 | 0.089 | 0.104 |
| BG0918+5104 | 0.051 | 0.035 | 0.026 | 0.030 |
| BG1429+1202 | 0.104 | 0.072 | 0.054 | 0.063 |
| BG1501+3042 | 0.061 | 0.042 | 0.031 | 0.036 |

We use the *HST* F606W band ($\lambda_{\rm eff} = 5778$ Å) to trace the rest-frame 1700 Å of BG0742+3341 ($z = 2.363$) and BG0918+5104 ($z = 2.400$), whereas for the highest-redshift LAEs we use the ground-based $r$-band apparent magnitudes ($\lambda_{\rm eff} = 6231$ Å). However, the magnitudes listed in Table 3.3 have not been corrected for the Galactic dust extinction. To do so, we use the values from Schlafly & Finkbeiner (2011) to correct them (Table 3.5).

The intrinsic absolute magnitudes of the LAEs in this sample are found to be in the range of $-20 > M_{\rm UV} > -23$. Considering the UV luminosity of typical $z \sim 2.3$ star-forming galaxies as $M^*_{\rm UV} = -20.70$ (Reddy & Steidel 2009), the galaxies in this sample span a wide range of luminosities, from $0.5L^*_{\rm UV}$ to $10L^*_{\rm UV}$.

Table 3.6: Physical properties of the lensed LAEs.

| LAE | $M_{\rm UV}^{(1)}$ (AB) | $r-i^{(2)}$ (AB) | $\beta_{\rm UV}^{(3)}$ | $A_{\rm UV}^{(4)}$ (AB) | $\rm SFR_{UV}^{(5)}$ ($M_\odot \rm yr^{-1}$) |
|---|---|---|---|---|---|
| BG0201+3228 | $-22.00\pm0.08$ | 0.11 | $-1.50\pm0.98$ | 1.45 | 81 |
| BG0742+3341 | $-19.98\pm0.05$ | – | – | – | 3 |
| BG0755+3445 | $-21.37\pm0.08$ | 0.09 | $-1.59\pm0.45$ | 1.26 | 38 |
| BG0918+5104 | $-20.99\pm0.05$ | 0.09 | $-1.58\pm0.58$ | 1.28 | 27 |
| BG1429+1202 | $-22.98\pm0.05$ | 0.04 | $-1.81\pm0.32$ | 0.83 | 113 |
| BG1501+3042 | $-22.43\pm0.05$ | 0.01 | $-1.96\pm0.39$ | 0.53 | 53 |

**Notes.** — (1) UV absolute magnitudes of the LAEs; (2) rest-frame UV colors ($1600-2200$ Å); (3) stellar UV continuum slope (equation 3.3); (4) UV dust extinction (equation 3.4); (5) UV star formation rate (equation 3.5).

### 3.3.4 Beta Slope and Dust Attenuation

The stellar UV continuum slope $\beta_{\rm UV}$ is a useful indicator of the dust content in star-forming galaxies, in the sense that larger quantities of dust produce redder UV SEDs. Assuming a simple power law $f_\lambda \propto \lambda^{\beta_{\rm UV}}$, the slope can be estimated as:

$$\beta_{\rm UV} = -\frac{m_1 - m_2}{2.5\log_{10}(\lambda_{m_1}/\lambda_{m_2})} - 2. \tag{3.3}$$

In all cases we use the $r$ ($m_1$, $\lambda_1 = 6231$ Å) and $i$ ($m_2$, $\lambda_2 = 7625$ Å) bands, which at $z = 2.4-2.8$ correspond to a wavelength coverage of about $1600-2200$ Å.

Following Meurer et al. (1999), $\beta_{\rm UV}$ is correlated with the UV dust extinction $A_{\rm UV}$ in the form:

$$A_{\rm UV} = 1.99(\beta_{\rm UV} - \beta_0), \tag{3.4}$$

where $\beta_0 = -2.23$ and represents the intrinsic UV spectral slope in the absence of dust absorption.

Finally, using the Kennicutt's conversion (Kennicutt 1998), the rest-frame UV luminosity (already corrected for the lensing magnification) can be translated into an intrinsic UV star formation rate ($\rm SFR_{UV}$ in units of $M_\odot$ $\rm yr^{-1}$):

$$\rm SFR_{UV} = 1.48\times10^{-28}\times L_{UV}\times 10^{(0.4A_{UV})}. \tag{3.5}$$

Note that, however, this expression assumes the standard Salpeter (1955) stellar initial mass function (IMF). In order to correct for the lower proportion of low-mass

stars (e.g., Chabrier 2003, IMF), we divide the SFR by 1.8. The measurements of $\beta$, UV dust attenuation, and $\mathrm{SFR_{UV}}$ are listed in Table 3.6.

## 3.4 Rest-frame UV spectroscopic analysis

### 3.4.1 Individual Source Spectral Properties

In this Section we analyze each individual rest-frame UV spectrum of these lensed LAE systems. All spectra, shown in Figure 3.5, have relatively high S/N per pixel in the continuum, despite the short exposure time, ranging from $\sim 7$ for the faintest LAE (BG0742+3341) to $\sim 20$ for the brightest ones.

These spectra show a prominent Ly$\alpha$ emission spatially consistent with the lensed images of the background LAEs. The achieved S/N is also sufficient to detect a wealth of other absorption/emission features associated with interstellar medium gas (ISM), ionized nebular gas, and stars (see appendix A for the measurements of these features).

- *BG0201+3228*: This object is the brightest BELLS GALLERY lensed LAE observed with the *HST*, with $m_{\mathrm{F606W}} = 20.56 \pm 0.05$. The OSIRIS/GTC long slit was oriented in order to include the bright arc $\approx 2''$ SW from the $z \simeq 0.40$ lens galaxy to maximize the flux captured in the slit. Its spectrum shows several faint stellar photospheric absorption lines including C III $\lambda$1247, Si III $\lambda$1294,1298, C III $\lambda$1426, and S V $\lambda$1501, which are useful to determine the systemic redshift of the galaxy, since they are formed in the photospheres of the stars. We use the mean of them to define the systemic redshift of BG0201+3228 as $z = 2.8174 \pm 0.0007$. Nebular O III] $\lambda$1666 and C III] $\lambda$1906,1908 emission lines are barely detected, although they fall in regions of relatively strong night sky lines, making it difficult their measurements. Low-ionization ISM absorption lines are detected (e.g., Si II $\lambda$1260,1304, C II $\lambda$1334, Al II $\lambda$1670) and all of them appear slightly blueshifted by $-110 \pm 70$ km s$^{-1}$ relative to the systemic redshift of the galaxy. High-ionization ISM absorption lines, such as Si IV $\lambda$1393,1402 , C IV $\lambda$1548,1550, and Al III $\lambda$1854,1862, are also detected and share the same velocity offset as the low-ionization ISM lines. The Ly$\alpha$ emission line has a rest-frame equivalent width $EW_0(\mathrm{Ly}\alpha) = 21 \pm 6$ Å, where the error reflects the uncertainty in the determination of the stellar continuum on both sides of the Ly$\alpha$ line. The Ly$\alpha$ line is spectrally resolved with a FWHM $= 395 \pm 50$ km s$^{-1}$, by fitting a Gaussian and correcting it for the instrumental broadening ($\mathrm{FWHM_{instr.}} \simeq 215$ km s$^{-1}$). The Ly$\alpha$ observed flux is found to be $F_{\mathrm{Ly}\alpha} = (6.6 \pm 0.3) \times 10^{-16}$ erg s$^{-1}$.

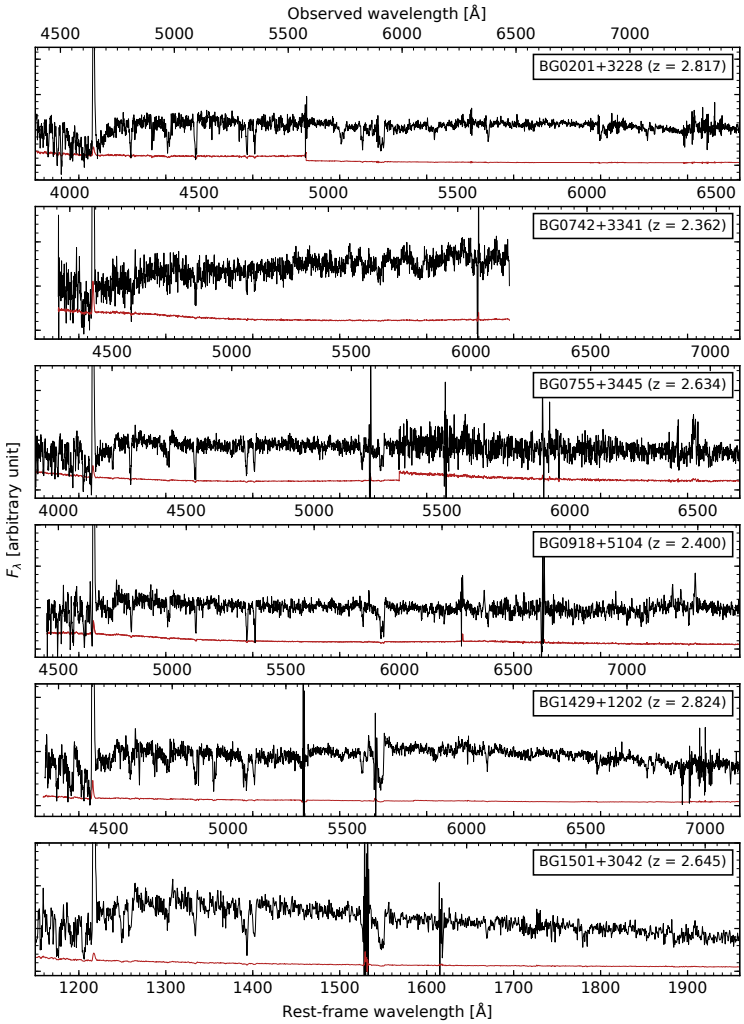


Figure 3.5: Portions of the rest-frame UV spectra of the 6 LAEs observed with OSIRIS. From top to bottom we show respectively the spectra of BG0201+3228, BG0742+3341, BG0755+3445, BG0918+5104, BG1429+1202, and BG1501+3042. Their redshifts are given in the right top corner. The 1$\sigma$ uncertainties are plotted in red. For more details, see appendix A.

- *BG0742+3341*: This object shows similar lensing morphology as the lensed LAE BG0201+3228 discussed above, but with a smaller Einstein radius. It shows an extended arc $1''$ SW from the $z \simeq 0.49$ lens galaxy and a relatively compact counter-image on the other side of the lens. However, BG0742+3341 is relatively faint compared to the other five lensed LAEs analyzed in this work. In addition, the bright lens galaxy is relatively close ($\approx 1''$) to the lens arc, and as a result, the OSIRIS spectrum of BG0742+3341 is noisy and shows a redder UV slope, likely due to foreground light contamination from the lens galaxy. The limited wavelength range of the spectrum of BG0742+3341 (it was not observed with the R2500R grism), from 1180 to 1700 Å in the rest-frame, does not cover the nebular C III] $\lambda$1906,1908 emission. Nevertheless, despite the relatively modest S/N ($\sim 7$) we detect three fine-structure emission lines, Si II* $\lambda$1197, Si II* $\lambda$1264, and Si II* $\lambda$1533, at a redshift $z = 2.3625 \pm 0.0009$. Although the origin behind these fine-structure emission lines is still not well understood (see Shapley et al. 2003; Jones et al. 2012), it has been showed that these lines are at the galaxy rest velocity when observed with significant high spectral resolution (e.g., France et al. 2010; Steidel et al. 2016).[2] The close blend of the stellar phostospheric line C II and N III $\lambda$1324 is also barely detected at $z = 2.3626 \pm 0.0009$, consistent with the redshift derived from the fine-structure emission lines. We thus assume the redshift of the fine-structure emission lines as the systemic redshift of BG0742+3341. The spectrum also shows ISM low-ionization absorption lines, including Si II $\lambda$1260, O I $\lambda$1302, Si II $\lambda$1304, C II $\lambda$1334, and Si II $\lambda$1526, as well as high-ionization absorption lines such as Si IV $\lambda$1393,1402. These lines appear to be at the systemic redshift of the galaxy, with $\Delta v = -20 \pm 50$ km s$^{-1}$. The galaxy shows a prominent emission in the Ly$\alpha$ line, with a rest-frame equivalent width of $EW_0 = 38 \pm 7$ Å. It presents a narrow profile with FWHM $= 251 \pm 30$ km s$^{-1}$. The measured total observed flux is $F_{\mathrm{Ly}\alpha} = (7.1 \pm 0.1) \times 10^{-16}$ erg s$^{-1}$.

- *BG0755+3445*: This LAE is composed of four bright lensed images in the image plane (A to D in Figure 3.3), forming an Einstein-cross-like configuration. Observations were obtained in two different slits, oriented in order to include the four lensed images. We do not find any differences in the profiles of the emission and absorption features and no evidence for velocity offsets between the individual spectra of each lensed image, as expected, since they are images of the same background source. The combined spectrum shows a prominent and resolved C III $\lambda$1906,1908 nebular emission at $z_{\mathrm{neb}} = 2.6345 \pm 0.0005$,

[2] Avoiding the contamination from the neighboring red component of resonance absorption features (Si II $\lambda$1193, Si II $\lambda$1260, and Si II $\lambda$1526).

as well as faint stellar photospheric absorption lines, C III $\lambda$1247 and Si III $\lambda$1298, at $z_{\rm stars} = 2.6340 \pm 0.0007$. We use both nebular emission and stellar absorption lines to measure the systemic redshift $z_{\rm sys} = 2.6342 \pm 0.0008$. Fine-structure emission lines Si II* $\lambda$1197 and Si II* $\lambda$1264 are also detected at $z_{\rm FS} = 2.6348 \pm 0.0007$, very close to the systemic velocity of the galaxy. Both low- and high-ionization ISM lines appear to share the same global kinematics, with the minimum intensity blueshifted by $\simeq -170 \pm 60$ km s$^{-1}$ relative to the H II regions and stars. On the other hand, the peak of the Ly$\alpha$ emission line is redshifted by $\sim +150$ km s$^{-1}$. We measured a total Ly$\alpha$ flux of $F_{\rm Ly\alpha} = (5.2 \pm 0.2) \times 10^{-16}$ erg s$^{-1}$, a rest-frame equivalent width of Ly$\alpha$ $EW_0 = 25 \pm 6$ Å, and a FWHM $= 440 \pm 50$ km s$^{-1}$.

- *BG0918+5104*: The GTC long slit was oriented to include the two bright knots of the lensed LAE $\approx 1.5''$ East from the lens galaxy (see Figure 3.3). From the lens modeling presented in Shu et al. (2016c), these two knots are the same lensed images of a compact and almost unresolved clump ($86 \pm 35$ pc) seen in the source plane. The spectrum of BG0918+5104 only shows one photospheric stellar absorption line, Si III $\lambda$1294, barely detected at $z_{\rm stars} = 2.3993 \pm 0.0009$. However, several nebular emission lines are detected with high significance ($\sigma \gtrapprox 5$), including the O III] $\lambda$1661,1666, and Si III] $\lambda$1882,1892 doublets, for which we derive the systemic redshift of $z_{\rm sys} = 2.4000 \pm 0.0003$ (see Figure 3.6). The nebular C III] $\lambda$1908 emission is also detected with high significance, but not the corresponding C III] $\lambda$1906 line, which is highly affected by the absorption of the Mg II $\lambda$2796,2803 doublet from an intervening absorption system at $z = 1.312 \pm 0.001$ (see Section 3.4.3 for more details). He II $\lambda$1640 emission appears to be also present, but unfortunately falls in the spectral region of the strong airglow feature at $\sim 5578$ Å. In addition, the fine-structure emission line Si II* $\lambda$1533 is also detected at $z_{\rm FS} = 2.4004 \pm 0.0006$, consistent with the systemic redshift from H II regions.

  The kinematics of interstellar lines, both in low- and high-ionization state, appear to be consistent with the systemic velocity of the galaxy, only slightly blueshifted by $-30 \pm 40$ km s$^{-1}$. The Ly$\alpha$ emission line has a relatively low rest-frame equivalent width $EW_0({\rm Ly\alpha}) = 16 \pm 3$ Å, and its spectral profile is quite narrow (FWHM $= 284 \pm 30$ km s$^{-1}$). We measured a total Ly$\alpha$ flux of $F_{\rm Ly\alpha} = (2.5 \pm 0.1) \times 10^{-16}$ erg s$^{-1}$, similar than the one measured within the BOSS fiber ($F_{\rm Ly\alpha}^{\rm BOSS} \simeq 2.3 \times 10^{-16}$ erg s$^{-1}$).

- *BG1429+1202*: This lensed LAE is the brightest galaxy in this sample and was

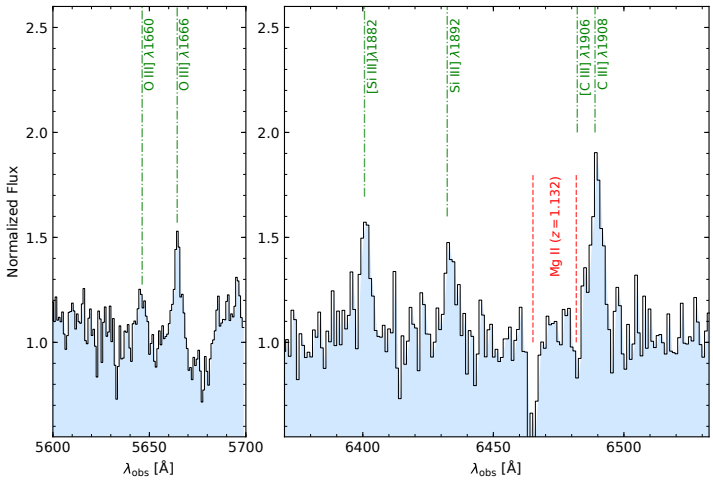


Figure 3.6: Nebular emission lines in BG0918+5104 for which the systemic redshift of $z = 2.4002 \pm 0.0006$ was measured. Note that the C III] $\lambda$1906 emission line is highly affected by the absorption of the Mg II $\lambda$2796,2803 doublet from an intervening absorption system at $z = 1.312 \pm 0.001$.

already discussed in chapter 2. It comprises four images in the observer plane, forming a *fold* configuration: a bright lensed image pair, A and B (with a separation of $\approx 1.5''$), and two fainter images, C and D. The GTC long slit was positioned so as to encompass the two brightest lensed images A and B. The new spectroscopic observations, with higher spectral resolution than the data discussed in chapter 2, allow us to identify several photospheric absorption features, C III $\lambda$1247, Si III $\lambda$1294,1298, the close blend of C II and N III $\lambda$1324, S V $\lambda$1501, and N IV $\lambda$1718. Using these stellar absorption lines, we derive the systemic redshift of BG1429+1202 as $z_{\rm sys} = 2.8244 \pm 0.0004$, with much better precision than the one measured in chapter 2 using lower-resolution spectroscopic observations. Nebular emission in the lines of O III] $\lambda$1666 and in C III] $\lambda$1906,1908 is also detected, but with low significance. Fine-structure emission lines Si II* $\lambda$1264, Si II* $\lambda$1309, and Si II* $\lambda$1533 are clearly detected and their peak lie at $z_{\rm FS} = 2.8243 \pm 0.0008$, consistent with the systemic velocity of the galaxy. Low-ionization interstellar absorption lines are blueshifted by $-180 \pm 50$ km s$^{-1}$. The same velocity offset is also present in high-ionization ISM features such as in C IV $\lambda$1548,1550 and Al III $\lambda$1854,1862 doublets, although in these cases their profiles show additional stellar P-Cygni features in-

dicative of stellar winds from very young massive stars. The Lya emission line has an observed flux of $F_{\mathrm{Ly}\alpha} = (11.8 \pm 0.2) \times 10^{-16}$ erg s$^{-1}$. The measured rest-frame equivalent width of Ly$\alpha$ is $EW_0 = 37 \pm 4$ Å, where the errors reflect the uncertainty in the determination of the stellar continuum redward of Ly$\alpha$. We measured a FWHM $= 310 \pm 50$ km s$^{-1}$, after accounting for the instrumental broadening.

- *BG1501+3042*: This system is composed of three lensed images in the observer plane, two of them very bright, A and B, located $\approx 3.7''$ SE from the lens galaxy (see Figure 3.3 and 3.4). Another lensed image, C, is almost blended with the foreground lens galaxy ($\simeq 0.5''$ separation) and is likely the source of the Ly$\alpha$ emission detected in the BOSS fiber. The GTC long slit was oriented to include the two lensed images A and B. Despite the relatively modest S/N continuum and the low spectral resolution provided by the R1000B grism ($\sim 400$ km s$^{-1}$), the spectrum of BG1501+3042 shows both stellar absorption lines (Si III $\lambda$1294, C II and Si III $\lambda$1296, and Si III $\lambda$1298), and nebular emission lines in O III $\lambda$1666 and in C III $\lambda$1906,1908 at $z_{\mathrm{sys}} = 2.645 \pm 0.001$. Fine-structure emission lines of Si II* $\lambda$1264 and Si II* $\lambda$1309 are also detected at $z = 2.643 \pm 0.001$. A careful analysis of the kinematics of this LAE goes beyond this work given the low spectral resolution of the data. However, there are clear differences in the kinematics of the Ly$\alpha$ emission and interstellar features. The Ly$\alpha$ emission has its peak redshifted with a velocity $v_{\mathrm{Ly}\alpha} \simeq +330$ km s$^{-1}$, while the interstellar absorption lines appear blueshifted by $\sim -190$ km s$^{-1}$. The Ly$\alpha$ emission line has a low rest-frame equivalent width $EW_0(\mathrm{Ly}\alpha) = 13 \pm 2$ Å, and its profile is almost unresolved in our spectrum with FWHM $\simeq 300$ km s$^{-1}$. The observed Ly$\alpha$ flux is $F_{\mathrm{Ly}\alpha} = (2.6 \pm 0.2) \times 10^{-16}$ erg s$^{-1}$.

In all cases, the Ly$\alpha$ emission has its peak redshifted relative to the systemic redshift, which was determined using nebular emission lines, stellar photospheric absorption lines, and, in some cases (BG0742+3341) fine-structure emission lines (see Figure 3.7). On the other hand, the interstellar absorption lines appear blueshifted in almost all LAEs, which is consistent with galaxy-scale outflows of material from the galaxy in the form of a wind, similar to those seen in other star-forming galaxies at $z \sim 3$ (e.g., Shapley et al. 2003; Steidel et al. 2010). The exceptions are the LAEs BG0742+3341 and BG0918+5104, where the ISM absorption lines have the minimum intensity very close to the systemic velocity of these galaxies, although they show a slightly asymmetric profile with a pronounced blueshifted absorption tail. Figure 3.8 shows velocity plots of the Ly$\alpha$ emission line and several normalized interstellar absorption lines, relative to the systemic redshift of each lensed LAE.

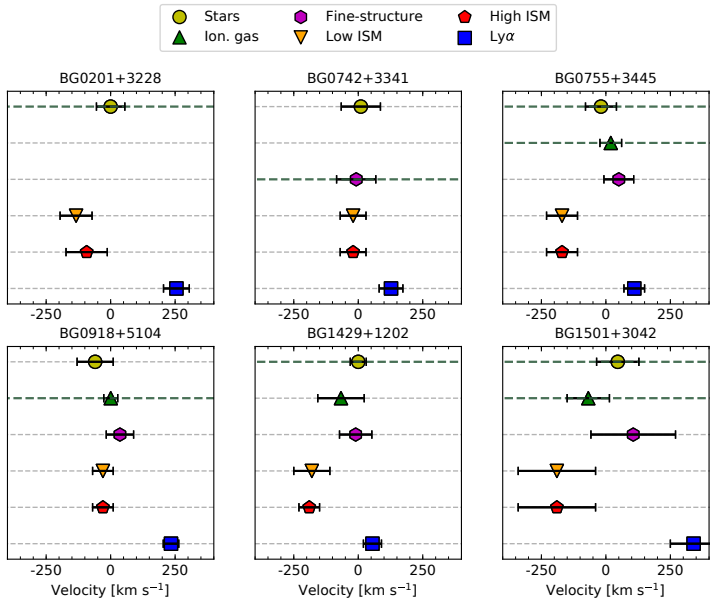


Figure 3.7: Kinematics of different spectral features observed in the BELLS GALLERY lensed LAEs: photospheric absorption lines from OB stars (yellow), ionized gas from H II regions (green), fine-structure emission (purple), low- and high-ionization lines from the ISM (orange and red, respectively), and the Ly$\alpha$ emission (blue). The systemic velocities were determined using stellar photospheric absorption lines, nebular emission, and fine-structure emission lines (indicated with a green horizontal line).

### 3.4.2 Spatial Distribution of the Ly$\alpha$ emission

In this Section the 1D spatial distribution of Ly$\alpha$ is compared with that of the rest-frame UV continuum. To do so, spatial profiles of Ly$\alpha$ and UV continua were extracted along the slit direction by summing the spectra in specific wavelength ranges along the dispersion direction: $\approx 1210 - 1224$ Å rest-frame for the Ly$\alpha$ line, and several tens Angstroms redward and blueward of Ly$\alpha$ for the UV continuum. Both Ly$\alpha$ and UV continuum profiles are then normalized to their maximum. Figure 3.9 shows the normalized spatial profiles of the UV continuum and Ly$\alpha$ line.

The peaks of the Ly$\alpha$ emission in three lensed LAEs, BG0201+3228, BG1429+1202, and BG1501+3042, are found to be spatially offset with respect to the peaks of their UV continua. Furthermore, the Ly$\alpha$ emission in the lensed LAEs BG0201+3228 and BG1501+3042 presents a more extended profile than the UV con-

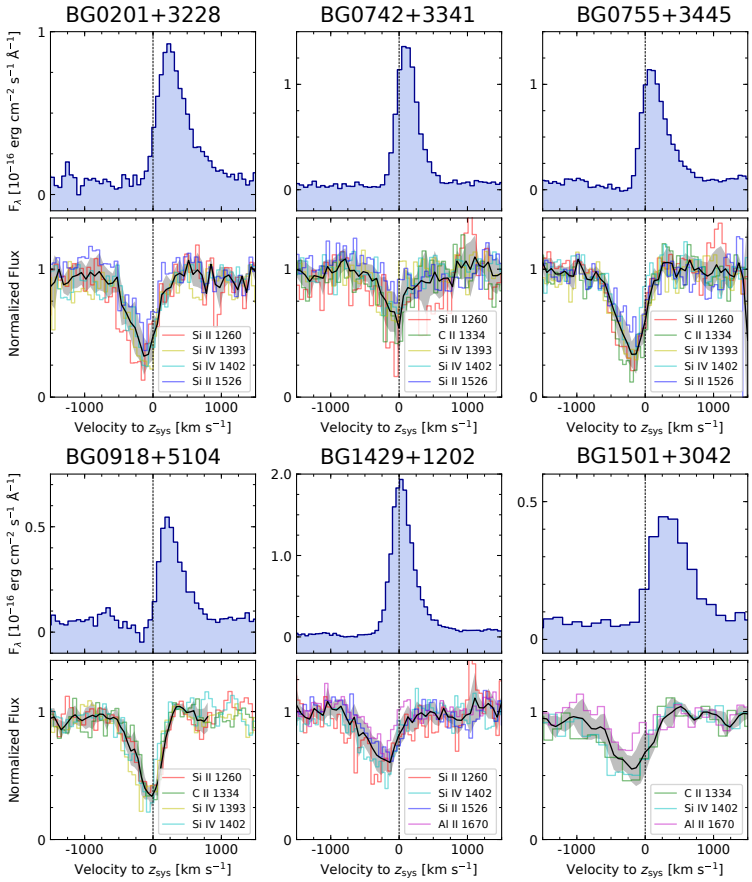


Figure 3.8: Ly$\alpha$ emission (upper panels) and interstellar absorption features (lower panels) on systemic velocity derived using either nebular emission lines, stellar photospheric features, or fine-structure lines. The Ly$\alpha$ line appears to be redshifted, while the interstellar absorption lines are blueshifted (mean profile in black with the standard deviation in gray shadow), which is consistent with galaxy-scale outflows of material from these galaxies in the form of a wind, similar to those seen in other star-forming galaxies at $z \sim 3$ (e.g., Shapley et al. 2003; Steidel et al. 2010). The interstellar absorption lines in the LAEs BG0742+3341 and BG0918+5104 show, however, a minimum intensity very close to the systemic velocity of these galaxies.

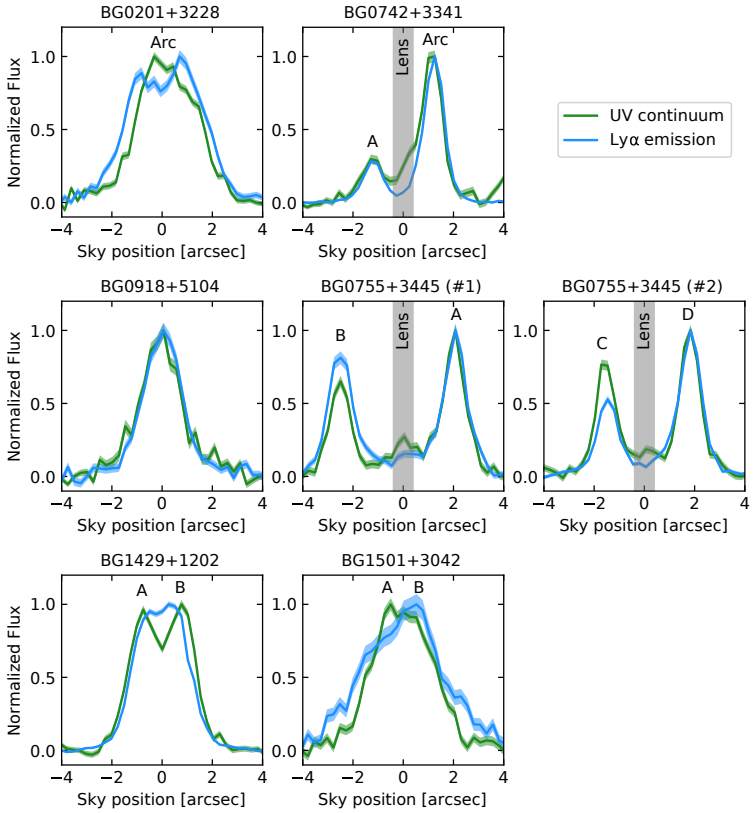


Figure 3.9: Normalized spatial profiles of the rest-frame UV continuum (green) and Ly$\alpha$ emission (blue). Shaded regions show the 1$\sigma$ errors of the spatial profiles.

tinuum, while for BG1429+1202 the Ly$\alpha$ emission appears brighter in the inner region between A and B than its UV continuum. It is also worth to note that the Ly$\alpha$ and UV continuum emission of the lensed images B and C in BG0755+3445 show different Ly$\alpha$ to UV continuum ratios compared with the lensed images A and D. Finally, the spatial distribution of Ly$\alpha$ in BG0742+3341 and BG0918+5104 appears to follow the UV continuum, although we stress that the orientation of the long slit in BG0742+3341 is not ideal to look for extended Ly$\alpha$ emission, since it was placed

perpendicular to the extended arc.

### 3.4.3 Lower-z Intervening Metal-Line Systems

In addition to the absorption lines associated with the interstellar medium gas and stars of each lensed LAE, we also detect other absorption lines from intervening metal-systems at lower redshifts. In total we find 5 intervening metal-systems at redshifts between 1.31 and 2.70. None of these systems is associated to the LAEs or their corresponding lens, but originates in intervening systems along the line of sight to the LAEs. Table 3.7 lists the identified intervening metal-absorption lines for each lensed LAE with their redshifts and rest-frame equivalent widths.

### 3.4.4 Absolute Flux Calibration and Ly$\alpha$ Luminosity

Our GTC spectra are subject to variable slit-losses, since the observations were carried out through narrow slits ($1.0''$ and $1.2''$ wide) covering only a fraction of the total flux of these LAEs. In order to put our spectra on an absolute flux scale, the extracted fluxes are compared to the photometry listed in Table 3.3. The PYTHON package PYSYSP 1.0.1[3] was used to compute synthetic photometry from the GTC extracted spectra. The comparison is done using the $g$ band ($\lambda_{\rm min} \simeq 4000$ Å, $\lambda_{\rm max} \simeq 5350$ Å) in order to avoid strong contamination of the stellar light redward the rest-frame 4000 Å break of the foreground lens, which is redshifted to the optical $i$-band in all cases.

Having the GTC spectra on an absolute flux scale, it is now possible to get an estimate of the intrinsic Ly$\alpha$ luminosity of these LAEs. This is done by using the following formula:

$$L_{\rm Ly\alpha} = 4\pi D_{\rm L}^2 F_{\rm Ly\alpha}^{\rm obs} \times \frac{1}{\mu} \times \frac{1}{f}, \tag{3.6}$$

where $L_{\rm Ly\alpha}$ is given in units of erg s$^{-1}$, $D_{\rm L}$ in cm, and $f$ is the correction factor to account for slit-losses (see Table 3.8). Assuming case-B recombination and the Kennicutt (1998) conversion, the Ly$\alpha$ luminosity can be translated into a star formation rate (SFR$_{\rm Ly\alpha}$):

$${\rm SFR}_{\rm Ly\alpha} = 9.1 \times 10^{-43} {\rm L}_{\rm Ly\alpha} \times 10^{(0.4 \times {\rm A}_{\rm UV})} \times \frac{1}{1.8}, \tag{3.7}$$

assuming the Chabrier (2003) IMF. Comparing the measurements of SFRs from the rest-frame UV (Section 3.3.4) and Ly$\alpha$, we found Ly$\alpha$ escape fractions, defined as

[3] https://pypi.python.org/pypi/pysysp

Table 3.7: Intervening Metal-Absorption Line Systems.

| $\lambda_{obs}$ (Å) | Line | $z_{abs}$ | $EW_0$ (Å) |
|---|---|---|---|
| BG0201+3228 − System 1: $z_{abs} = 2.705$ | | | |
| 5164.45 | Si IV 1393.75 | 2.7055 | 0.47 |
| 5197.65 | Si IV 1402.77 | 2.7050 | 0.45 |
| 5734.79[a] | C IV 1548.19 | 2.7042[a] | 0.38[a] |
| 5734.79[a] | C IV 1550.77 | 2.7040[a] | 0.57[a] |
| 6872.02[b] | Al III 1854.71 | 2.7052[b] | 0.89[b] |
| 6900.53 | Al III 1862.79 | 2.7044 | 0.94 |
| BG0918+5104 − System 1: $z_{abs} = 1.3121$ | | | |
| 5419.80 | Fe II 2344.21 | 1.3120 | 0.47 |
| 5490.11 | Fe II 2374.46 | 1.3121 | 0.09 |
| 5508.68 | Fe II 2382.76 | 1.3119 | 0.72 |
| 6011.78 | Fe II 2600.17 | 1.3121 | 0.65 |
| 6465.10 | Mg II 2796.35 | 1.3120 | 0.86 |
| 6482.65[c] | Mg II 2803.53 | 1.3123[c] | 0.29[c] |
| BG1429+1202 − System 1: $z_{abs} = 2.1804$ | | | |
| 4855.53 | Si II 1526.70 | 2.1804 | 0.75 |
| 4923.25 | C IV 1548.19 | 2.1800 | 0.75 |
| 4931.90 | C IV 1550.77 | 2.1803 | 0.38 |
| 5115.58 | Fe II 1608.45 | 2.1804 | 0.49 |
| 5313.99 | Al II 1670.78 | 2.1805 | 0.88 |
| 7455.35 | Fe II 2344.21 | 2.1803 | 0.70 |
| 7551.81 | Fe II 2374.46 | 2.1804 | 0.50 |
| 7578.35 | Fe II 2382.76 | 2.1805 | 1.04 |
| BG1429+1202 − System 2: $z_{abs} = 2.3472$ | | | |
| 5182.16 | C IV 1548.19 | 2.3472 | 1.37 |
| 5190.61 | C IV 1550.70 | 2.3473 | 0.92 |
| BG1502+3042 − System 1: $z_{abs} = 2.269$ | | | |
| 4556.67 | Si IV 1393.75 | 2.2694 | 1.67 |
| 4584.17[d] | Si IV 1402.77 | 2.2680[d] | 1.22[d] |
| 5064.80[e] | C IV 1548.19 | 2.2687[e] | 1.84[e] |
| 5064.80[e] | C IV 1550.70 | 2.2687[e] | 1.84[e] |

**Notes.**
[a] Blended with the stellar photospheric absorption S V $\lambda$1501 of BG0201+3228. [b] This intervening absorption line falls in the region of a telluric absorption line (B-band). [c] Blended with the nebular emission C III] $\lambda$1906 of BG0918+5104. [d] Blended with the absorption from Si II $\lambda$1260 of BG1502+3042. [e] The measured values refer to the C IV $\lambda$1548,1550 doublet given the low spectral resolution of the GTC R1000B grism.

Table 3.8: Absolute flux calibration and Ly$\alpha$ luminosity.

| LAE | $m_{\rm syn}$ | $f$ | $L_{\rm Ly\alpha}$ | $f_{\rm esc}^{\rm Ly\alpha}$ |
|---|---|---|---|---|
| | (AB) | | ($\times 10^{42}$ erg s$^{-1}$) | |
| BG0201+3228 | 21.14 | 0.83 | 3.52 | 0.08 |
| BG0742+3341 | – | – | 1.93 | 0.31 |
| BG0755+3445 | 21.81 | 0.89 | 2.36 | 0.10 |
| BG0918+5104 | 22.41 | 0.52 | 1.20 | 0.07 |
| BG1429+1202 | 20.96 | 0.59 | 28.05 | 0.21 |
| BG1501+3042 | 22.08 | 0.50 | 5.20 | 0.08 |

$f_{\rm esc}^{\rm Ly\alpha} = {\rm SFR}_{\rm Ly\alpha}/{\rm SFR}_{\rm UV}$, between 0.07 and 0.21.[4] All quantities are summarized in Table 3.8.

## 3.5 Discussion

### 3.5.1 Ly$\alpha$ and UV Luminosities

Figure 3.10 shows rest-frame UV and Ly$\alpha$ intrinsic luminosities of the six BELLS GALLERY LAEs studied in this chapter (already corrected for gravitational lensing). These galaxies present rest-frame UV luminosities in the range of $0.5 \times L^*_{\rm UV}$ to $10 \times L^*_{\rm UV}$, where $L^*_{\rm UV}$ is the UV luminosity of typical $z \sim 2.3$ star-forming galaxies ($L^*_{\rm UV} = 8.3 \times 10^{28}$ erg s$^{-1}$ Hz$^{-1}$: Reddy & Steidel 2009). In the Ly$\alpha$ line, five of the BELLS GALLERY LAEs present Ly$\alpha$ luminosities bellow $L^*_{\rm Ly\alpha}$ , which is defined as the Ly$\alpha$ luminosity of typical $z \sim 2.5$ LAEs ($L^*_{\rm Ly\alpha} = 5.8 \times 10^{42}$ erg s$^{-1}$: Sobral et al. 2018a). The exception is BG1429+1202, which is very luminous in the Ly$\alpha$ line, 5 times higher than $L^*_{\rm Ly\alpha}$.

We also add to Figure 3.10 the remaining 13 BELLS GALLERY LAEs imaged with *HST*. To do so, we used the *HST* F606W magnification-corrected rest-frame UV magnitudes calculated from the best-fit source model presented in Shu et al. (2016c). On their Ly$\alpha$ luminosities we use the Ly$\alpha$ flux measured from the 1″-radius BOSS fibers (see Shu et al. 2016b) and correct them for the lensing magnification (assuming again that the spatial distribution of Ly$\alpha$ emission in the source plane and the corresponding lensing magnification are similar to those of the rest-frame UV continuum). However, the plotted Ly$\alpha$ luminosities are only lower limits, since no corrections on

[4] Assuming that the spatial distribution of Ly$\alpha$ emission in the source plane and its lensing magnification are similar to that of the rest-frame UV continuum, which is not necessarily true, as discussed in Section 3.4.2.

the flux-losses from the BOSS fibers were applied. These galaxies present relatively fainter UV luminosities than those from the GTC survey, with UV absolute magnitudes ranging from $-17.6$ to $-21.0$ (AB magnitudes), or 0.05 to $1.2 \times L^*_{\rm UV}$.

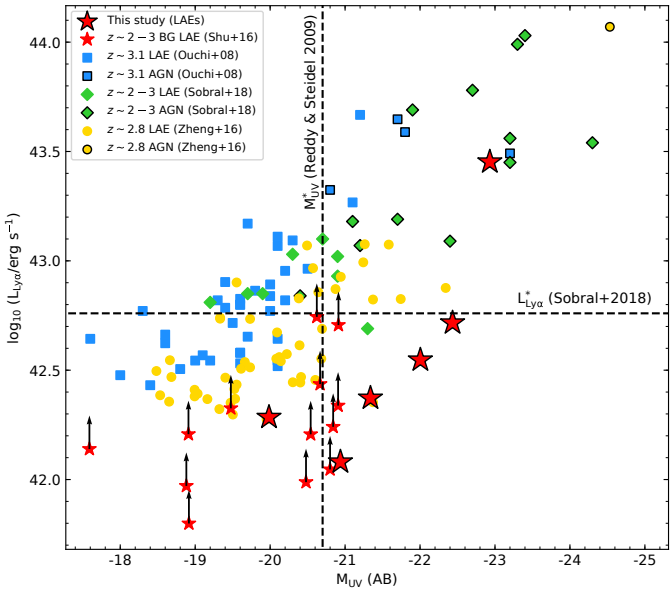


Figure 3.10: Relation between rest-frame UV and Ly$\alpha$ luminosities. The six BELLS GALLERY LAEs studied in this chapter are marked with red stars. Other $z \sim 2-3$ LAEs selected from dedicated narrow-band surveys with spectroscopic follow-up are shown with different colors, as indicated (Ouchi et al. 2008; Zheng et al. 2016; Sobral et al. 2018b).

Figure 3.10 also includes other $z \sim 2-3$ LAEs selected from dedicated narrow-band surveys with spectroscopic follow-up. These include 41 $z \simeq 3.1$ LAEs within the 1 deg$^2$ Subaru/*XMM*-Newton Deep Survey Field (Ouchi et al. 2008), 50 $z \simeq 2.8$ LAEs in the 2.23 deg$^2$ Extended *Chandra* Deep Field South (Zheng et al. 2016), and 21 additional LAEs at $z \simeq 2.2$ and $z \simeq 3.1$ selected from several wide-field (up to 4.53 deg$^2$) Ly$\alpha$ surveys (including UDS, COSMOS, GOODS-N, SA22, and Boötes fields, see: Sobral et al. 2018b). From these surveys, a significant fraction of LAEs have been found to be AGNs (see Ouchi et al. 2008; Zheng et al. 2016; Sobral et al. 2018b), by the detection of broad (FWHM $> 1000$ km s$^{-1}$) emission lines (e.g., Ly$\alpha$ $\lambda$1215, C IV $\lambda$1550, or C III $\lambda$1908), or slightly narrow high-ionization lines (such as N V $\lambda$1242,

C IV $\lambda$1550, and He II $\lambda$1640) with N V/Ly$\alpha$ ratios $> 0.1$, which are typically seen in AGNs (e.g., Hainline et al. 2011a).

Very recently, Sobral et al. (2018b) showed that the fraction of AGN-dominated sources increases strongly with high UV and Ly$\alpha$ luminosities, reaching to about 100% for LAEs with luminosities above $2 \times L^*_{\rm UV}$ or $L^*_{\rm Ly\alpha}$ (i.e., $M_{\rm UV} < -21.5$ or $L_{\rm Ly\alpha} > 10^{43.3}$ erg s$^{-1}$). They argued that the dust formed in very luminous, purely star-forming galaxies prevents such galaxies being observed in the UV and Ly$\alpha$ if they are more luminous than this limit, which is equivalent to a SFR $\simeq 20\ M_\odot$ yr$^{-1}$. Since in principle, AGNs do not create dust (or their high ionization radiation may destroy it), it was suggested that the very bright-end of the UV and Ly$\alpha$ luminosity function is fully populated by AGNs, rather than purely star-forming galaxies.

However, as shown in Figure 3.10, there are several LAEs with luminosities larger than $2 \times L^*$, including three out of the six BELLS GALLERY LAEs observed with the GTC. Their spectra (see Section 3.4.1) exhibit stellar photospheric absorption lines and stellar wind features (P-Cygni profiles), showing that the strong UV continuum is dominated by stellar emission, rather than an AGN component. Furthermore, the lens modeling shows that all of them present resolved structure, removing most of the evidence for an AGN component.

Dust formed in actively star-forming galaxies and the consequent obscuration of their stellar continua may provide a natural explanation for the lack of UV-luminous LAEs detected in these surveys. Such examples are the galaxies selected in the sub-millimeter, SMGs, which show extremely obscured luminosities in the rest-frame UV and optical ($A_{\rm UV} \sim 8$ and $A_V \sim 4$; e.g. see chapter 3), despite their intense ionizing flux from a young, massive stellar population that dominates the rest-frame UV, with intrinsic (i.e. dust corrected) absolute magnitudes of $M_{\rm UV} \sim -25$.

The luminous BELLS GALLERY LAEs BG0201+3228, BG1429+1202, and BG1501+3042 show large star formation rates, up to $\sim 110$ M$_\odot$ yr$^{-1}$ for the most luminous one (BG1429+1202), yet present steeper rest-frame UV slopes, in the range of $-1.5$ to $-2.0$, suggesting low dust attenuation (following the $A_V - \beta$ correlation of Meurer et al. 1999). However, the Meurer et al. (1999) correlation assumes an intrinsic UV spectral slope (i.e. UV slope in the absence of dust absorption) $\beta_0 = -2.23$ inferred from models with continuous star-formation histories with age $> 100$ Myr. Such considerations may probably be invalid for some luminous high-$z$ star-forming galaxies (see Figure 3.11), since they may have a younger stellar population and non-uniform star-formation histories (e.g., bursts of star formation). Since $\beta_0$ probes the rest-frame UV region, $1300 - 2200$ Å, it is strongly affected by the nature of young and hot stars that dominate the UV (mainly O and B stars). Such massive stars evolve quickly and are prominent in young star-forming galaxies. As a result, $\beta_0$ decreases for lower ages of the stellar population, in particular for instantaneous star-formation

histories (reaching slopes as steep as $\beta_0 = -3$; e.g., Wilkins et al. 2012; Stanway et al. 2016). The shape of the stellar UV continuum also depends on the metallicity of galaxies, since stars formed by gas of lower metallicity will be bluer (e.g., PopIII-like stars Schaerer & Pelló 2002; Schaerer 2003). Furthermore, the IMF may also play an important role in shaping the UV continuum, since a top-heavy IMF will provide many more massive stars, decreasing $\beta_0$ (e.g., Weidner et al. 2011).

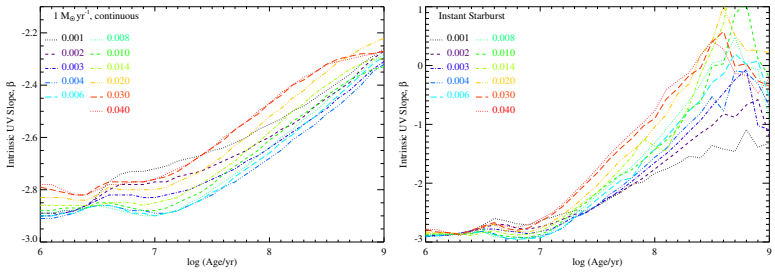


Figure 3.11: Intrinsic stellar UV slope as a function of age and metallicity for continuous (left) and instantaneous (right) star formation models (Figure adapted from Stanway et al. 2016).

It is interesting to note that for the few intrinsically[5] UV-luminous high-$z$ star-forming galaxies known with high S/N spectra, the 8 o'clock galaxy ($\approx 10 \times L^*_{\rm UV}$; Allam et al. 2007), FORJ0332-3557 ($\approx 2 \times L^*_{\rm UV}$; Cabanac et al. 2005), SGAS J105039.6+001730 ($\approx 3 \times L^*_{\rm UV}$; Bayliss et al. 2014), and HLock01-B ($\approx 10 \times L^*_{\rm UV}$; see chapter 4 or Marques-Chaves et al. 2018), a broad line emission was found in He II $\lambda$1640 (Cabanac et al. 2008; Dessauges-Zavadsky et al. 2010; Bayliss et al. 2014), which is believed to be associated with very massive stars, in particular Wolf-Rayet (WR) stars. These features are present only in the first 10 Myr after the burst (e.g., Schaerer & Vacca 1998; Brinchmann et al. 2008). Furthermore, analysis of their star-formation histories are better explained by young bursts of star-formation, rather than using continuous star formation scenarios.

It is possible that Ly$\alpha$- and UV-luminous star-forming galaxies, such as the three luminous BELLS GALLERY LAEs analyzed in this chapter, had experienced recent burts of star formation. Their steep UV slopes may suggest that they have only had time to form small amounts of dust, and/or their intrinsic slopes are lower than the ones assumed in standard $A_{\rm UV} - \beta$ correlations due to non-uniform star-formation histories. It is, therefore, necessary to probe the dust content of these galaxies in the far-IR and sub-millimeter (e.g., with ALMA, NOEMA, or SMA), to better constrain the early phase of dust growth in luminous starburst galaxies and determine their total SFRs

[5]Because these galaxies are magnified by gravitational lensing.

$(\mathrm{SFR_{UV}} + \mathrm{SFR_{IR}})$.

### 3.5.2 Ly$\alpha$ Spatial Distribution

The Ly$\alpha$ line is intrinsically the most luminous spectral feature in astrophysical nebulae, and has long been recognized as key to studying high-$z$ star-forming galaxies. Although the bulk of the Ly$\alpha$ photons are produced in central star-forming regions of galaxies[6], the scattering by neutral hydrogen makes a significant fraction of the photons escape far from the center.

Extended Ly$\alpha$ emission has been frequently observed on scales larger than 100 kpc around some high-$z$ QSOs (e.g., Cantalupo et al. 2014), radio galaxies (e.g., Nesvadba et al. 2006; Villar-Martín et al. 2007a; North et al. 2012), and in the so-called Ly$\alpha$ blobs (e.g., Steidel et al. 2000; Matsuda et al. 2004, 2011, see also chapter 5). However, in *normal* star-forming galaxies, such as in LAEs or LBGs, the morphological characterization of the Ly$\alpha$ emission has been performed mainly using stacking techniques because of sensitivity (and resolution) limitations (e.g., Rauch et al. 2008; Finkelstein et al. 2011a; Steidel et al. 2011; Matsuda et al. 2012; Momose et al. 2014, 2016; Sobral et al. 2017). These results show that the Ly$\alpha$ emission in star-forming galaxies is more spatially extended than the rest-frame UV stellar emission, with Ly$\alpha$ halos exceeding several 10 kpc or more (e.g., Steidel et al. 2011; Momose et al. 2014). These Ly$\alpha$ halos were recently detected in individual LAEs (e.g., Wisotzki et al. 2016; Leclercq et al. 2017) through very deep IFU MUSE observations (reaching a surface brightness sensitivity of $\simeq 5.5 \times 10^{-20}$ erg s$^{-1}$ cm$^{-2}$ Å$^{-1}$ arcsec$^{-2}$). A high fraction (80%) of objects showing Ly$\alpha$ emission more extended than the rest-frame UV continuum was found, with typical scale length of 4.5 kpc.

The strong gravitational lensing effect aids in the observation of the Ly$\alpha$ emission in star-forming galaxies through the magnification of the apparent flux and size, since the surface brightness is conserved. In Section 3.4.2 we analyzed the 1D spatial distribution of Ly$\alpha$ and found spatial offsets between the peaks of the Ly$\alpha$ emission and the UV continuum in three lensed LAEs, BG0201+3228, BG1429+1202, and BG1501+3042 (see Figure 3.9). The Ly$\alpha$ emission in BG0201+3228 and BG1501+3042 presents a more extended profile than the UV continuum, while for BG1429+1202 the Ly$\alpha$ emission appears brighter (relative to the UV continuum) in the inner region between the lensed images A and B, than its UV continuum. We also detected different ratios of Ly$\alpha$/UV intensities in the lensed images B and C in BG0755+3445.

[6]Note, however, that other processes may produce Ly$\alpha$ photons in the outer regions of a galaxy, such as cooling radiation from cold-mode accretion (e.g. Haiman et al. 2000; Fardal et al. 2001), shock-heated gas by galactic superwinds (e.g., Taniguchi & Shioya 2000), or by reprocessed emission from the cool circumgalactic medium (CGM).

Although these data alone are insufficient for further conclusions on the *intrinsic* morphology and extension of Ly$\alpha$, our results show that the Ly$\alpha$ emission in some of these LAEs presents different spatial morphology than their rest-frame UV continuum. Note that, however, this may also lead to differential magnification, and the intrinsic properties of Ly$\alpha$ (e.g, luminosity and escape fraction, see Section 4.5) may be different than the ones calculated using the UV continuum magnification. The BELLS GALLERY LAEs are thus ideal targets for further IFU spectroscopic observations or narrow-band imaging of their Ly$\alpha$ emission. In particular, the BELLS GALLERY LAEs BG0201+3228, BG0755+3445, BG1429+1202, and BG1501+3042 are priority targets, since the GTC long-slit spectra already show evidence of different spatial morphology of the Ly$\alpha$ emission relative to their rest-frame UV continua. Furthermore, these LAEs are the ones that show high Ly$\alpha$ observed fluxes (in part due to magnification, but see the case of BG1429+1202) and present large image separations, making high S/N studies of faint Ly$\alpha$ surface brightness accessible with moderate observing time.

Such an example is shown in Figure 3.12, that shows very recent, yet preliminary results from a 2.5m Nordic Optical Telescope (NOT) deep image of the Ly$\alpha$ emission of BG1429+1202 with the Stromgren b medium-band filter ($\lambda_{\rm cent} = 4670$, FWHM $= 180$ Å). Our lens model shows that the Ly$\alpha$ distribution is spatially offset by $\sim 0.25''$ (or $\sim 2$ kpc) with respect to the rest-frame UV continuum. Resolving different components with such small angular separations would be impossible without the lensing effect with seeing-limited observations.

## 3.6 Conclusion

In this chapter I have presented the results of a GTC and WHT imaging and spectroscopic follow-up of six BELLS GALLERY lensed LAEs. They were chosen to have large image separations and flux densities in optical bands in order to perform high S/N studies of their properties. These LAEs, with redshifts between 2.36 and 2.82, are lensed by massive early type galaxies at $z \simeq 0.39 - 0.72$, providing total magnifications of $\simeq 9 - 18$. From the analysis of these data we obtain the following results:

1. We spectroscopically confirmed the lensing nature of these systems through the detection of emission/absorption spectral features in several lensed images of each LAE. One of these, BG1501+3042, is a new confirmed lensed LAE and shows three lensed images in the observer plane, quite uncommon in galaxy-scale lensed systems (which typically show two or four lensed images). Additional follow-up observations are needed to investigate the presence of sub-halos of dark matter in this system.

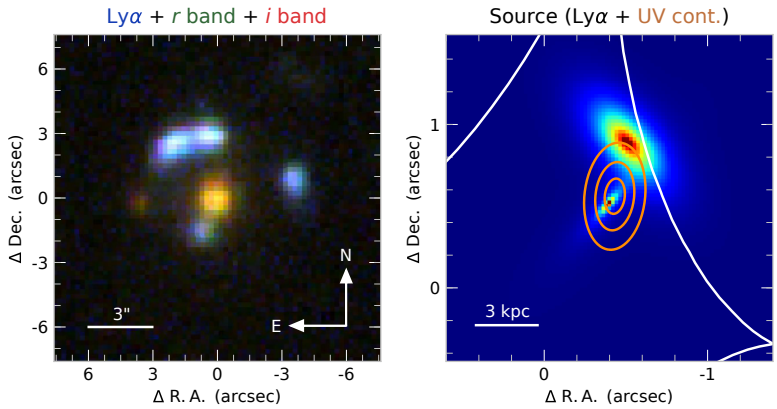


Figure 3.12: Recent NOT medium-band observations of the Ly$\alpha$ emission in BG1429+1202. Left: color image of BG1429+1202 using the NOT Ly$\alpha$ emission (blue) and the rest-frame UV continuum from the GTC *r*- and *i*-bands (green and red, respectively). Right: Source plane reconstruction of the Ly$\alpha$ emission. Orange contours represent the UV continuum source plane reconstruction from the GTC *g*-band (discussed in chapter 2).

2. We could measure the systemic redshifts of BG0201+3228, BG0742+3341, BG0755+3445, BG0918+5104, BG1429+12020, and BG1501+3042 as 2.817, 2.362, 2.634, 2.400, 2.824, and 2.645, respectively. We used either nebular emission from H II regions, stellar absorption from the photospheres of massive OB stars, and fine-structure emission lines. We showed that fine-structure emission lines can also be used to recover the systemic redshift of a galaxy when observed with significant spectral resolution (with uncertainties lower than 100 km s$^{-1}$).

3. On the ISM, we found that both low- and high-ionization lines of the ISM share the same global kinematics. For some of these LAEs (BG0201+3228, BG0755+3445, BG1429+1202, and BG1501+3042) the ISM absorption lines appear blueshifted up to 200 km s$^{-1}$ relative to their systemic redshift, which is indicative of large galaxy-scale outflows due to radiation pressure of the most massive and luminous stars and/or SNe feedback. These LAEs are the ones that present larger UV luminosities, and, therefore, larger star formation rates.

4. In all cases, the Ly$\alpha$ line shows an asymmetric spectral profile with its peak redshifted by $\simeq 70-250$ km s$^{-1}$, consistent with Ly$\alpha$ photons being scat-

tered by receding outflowing gas. Assuming case-B recombination, we find Ly$\alpha$ escape fractions of $0.07-0.31$ by comparing the estimates of star formation rates from the UV and Ly$\alpha$. However, such measurements require the assumption that the spatial distribution of Ly$\alpha$ follows the UV continuum. Our analysis of the 1D spatial distribution of Ly$\alpha$ shows that Ly$\alpha$ emission in BG0201+3228, BG0755+3445, BG1429+1202, and BG1501+3042 present different spatial morphologies than their rest-frame UV continua. Our results are insufficient for definitive conclusions on the intrinsic morphology and extension of Ly$\alpha$. IFU and/or narrow-band imaging observations of the Ly$\alpha$ emission are required to better constrain the morphology of Ly$\alpha$ and investigate possible differential magnification.

5. These LAEs span a wide range of star formation rates, $\mathrm{SFR_{UV}} \simeq 3-110\ M_{\odot}$ $\mathrm{yr}^{-1}$, and appear relatively blue ($\beta_{\mathrm{UV}} \simeq -1.6$ to $-1.9$) showing evidence of little dust attenuation. They present rest-frame UV and Ly$\alpha$ intrinsic luminosities in the range of $(0.5-10)\times L^{*}_{\mathrm{UV}}$ and $(0.5-5)\times L^{*}_{\mathrm{Ly}\alpha}$, respectively, where $L^{*}_{\mathrm{UV}}$ and $L^{*}_{\mathrm{Ly}\alpha}$ are the UV and Ly$\alpha$ luminosities of typical $z\sim 2.5$ LBGs and LAEs. Recently, it has been suggested that LAEs more luminous than $2\times L^{*}$ are AGN-dominated, since the dust formed in very UV-luminous, purely star-forming galaxies prevents such galaxies from being observed if they are more luminous than this limit. However, three BELLS GALLERY LAEs show luminosities larger than this limit, and their spectral and morphological properties exclude the presence of an AGN component. These LAEs may be particular cases of very young and luminous starburst galaxies that have only had time to form small amounts of dust.

# 4

# Rest-frame UV properties of the submillimeter galaxy HLock01

This Chapter presents the spectroscopic analysis of the submillimeter galaxy (SMG) HERMES J105751.1+573027 (hereafter HLock01) at $z = 2.9574 \pm 0.0001$, one of the brightest gravitationally lensed sources discovered in the *Herschel* Multi-tiered Extragalactic Survey. Based on deep spectroscopic observations with the Gran Telescopio Canarias of the optically bright lensed images of HLock01, it is shown that HLock01 is a merger system composed of the *Herschel*-selected SMG and an optically bright Lyman break-like galaxy (LBG), separated by only 3.3 kpc in projection. Detailed analysis of the high signal-to-noise (S/N) rest-frame UV spectrum of the LBG shows complex kinematics of the gas, exhibiting large-scale high-velocity gas motions with both outflow and inflow absorption components. This Chapter is part of the publication:

R. Marques-Chaves, I. Ismael Pérez-Fournon, R. Gavazzi, P. I. Martínez-Navajas, D. Riechers , D. Rigopoulous, A. Cabrera-Lavers, D. L. Clemenst, A. Cooray, D. Farrah, R. J. Ivison, C. Jiménez-Ángel, H. Nayyeri, S. Oliver, A. Omont, D. Scott, Y. Shu, and J. Wardlow, 2018, ApJ, 854, 151 *"The Strong Gravitationally Lensed Herschel Galaxy HLock01: optical spectroscopy reveals a close galaxy merger with evidence of inflowing gas"*.

## 4.1 Introduction

High-$z$ submillimeter galaxies (SMGs) represent a population of the most massive and luminous galaxies in the early Universe. They are characterized by dust-enshrouded vigorous star formation, assembling their mass very rapidly over short time scales, the so-called starburst phase (see Blain et al. 2002; Casey et al. 2014, for reviews).

Whatever the mechanisms responsible for such extremely large SFRs are, this active phase of SMGs is a clear indication of intense ionizing flux from a young, massive stellar population that dominates the rest-frame ultra-violet (UV). It is thus important to provide detailed characterization of the physical properties of the early episodes of star formation in these galaxies, via spectral diagnostics in the rest-frame UV. However, such studies are limited by the faintness of these galaxies at short wavelengths, with the massive stars giving rise to the UV continuum being embedded in large quantities of dust. Considerable effort has been successfully put to obtain accurate spectroscopic redshifts, probe for signs of active galactic nucleus (AGN) activity, and investigate properties of the ionized gas in SMGs, mainly by using rest-frame optical nebular emission lines (e.g, Chapman et al. 2004, 2005; Swinbank et al. 2004, 2005, 2006; Alaghband-Zadeh et al. 2012; Olivares et al. 2016; Casey et al. 2017; Danielson et al. 2017). However, the typical faintness of high-$z$ galaxies and the dust obscuration of SMGs make it almost impossible with current facilities to obtain high signal-to-noise (S/N) spectra, a requirement for properly studying the properties of the young stars, and to look for signatures of outflowing/inflowing gas.

## 4.2 The submm galaxy HLock01

One exception to this principle is the galaxy discussed in this paper, the strong gravitationally lensed SMG HERMES J105751.1+573027 (hereafter HLock01), that is unusually bright in both the optical ($R \simeq 19.7$ mag) and in the far-IR ($S_{250\,\mu\mathrm{m}} \simeq 400$ mJy). HLock01 was identified with *Herschel*/SPIRE in the *Herschel* Multi-tiered Extragalactic Survey (HerMES; Oliver et al. 2012), and investigated in a series of papers (Conley et al. 2011; Gavazzi et al. 2011; Riechers et al. 2011; Scott et al. 2011; Bussmann et al. 2013; Wardlow et al. 2013). Here I give a summary of the main results from those papers. The discovery and its lensing nature was first presented by Conley et al. (2011), based on 880 $\mu$m Submillimeter Array (SMA) interferometry and near-IR $K_\mathrm{p}$ adaptive optics (AO) observations using NIRC2 on the Keck II telescope, in which the *Herschel* source was resolved into four components with a large separation of around $9''$ (see Figure 4.1). Using the Plateau de Bure Interferometer (PdBI), the Combined Array for Research in Millimeter-wave Astronomy (CARMA), and the Green Bank Telescope (GBT), Riechers et al. (2011) and Scott et al. (2011) established the redshift of HLock01 from several CO molecular emission lines as $z_\mathrm{CO} = 2.9574 \pm 0.0001$. By

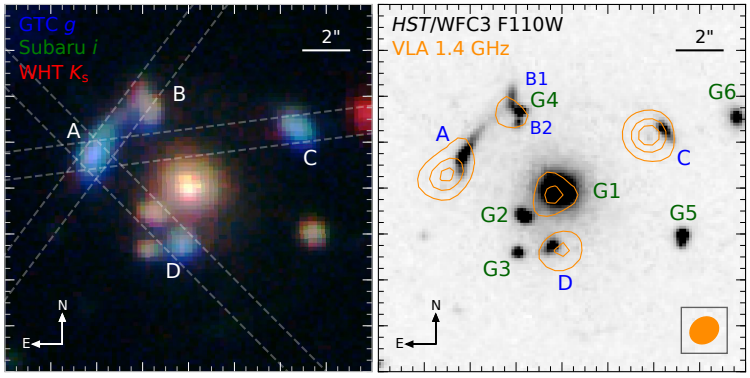


Figure 4.1: Left panel: $g$, $I$, and $K_s$ color image of HLock01 from GTC, Subaru, and WHT, respectively. Dashed lines show the positions of OSIRIS long-slit spectroscopic observations, all centered on the brightest lensed image A, and oriented so as to encompass the other bright lensed images B, C, and D. Right panel: near-IR high-resolution *HST*/WFC3 F110W image with labeled multiply lensed images at $z \simeq 2.95$ (blue) and foreground galaxies at $z \simeq 0.65$ (green). G4 is massive enough to split the lensed image B into two pieces on both sides (B1 and B2, see more details in Gavazzi et al. 2011). Orange contours show VLA data at 1.4 GHz and its beam is shown on the bottom right. A spatial offset of the bright lensed images is seen between the short (*HST* F110W, HLock01-B) and long wavelengths (VLA, HLock01-R). Each image is $16'' \times 16''$, centered on the brightest lensing galaxy, G1, and oriented such that north is up and east is to the left.

studying the kinematics of the gas reservoir, Riechers et al. (2011) found a resolved velocity structure in the CO ($J = 5 \rightarrow 4$) emission, similar to what is observed in gas-rich mergers, but the low spatial resolution did not allow a definitive conclusion. The lens modeling was performed by Gavazzi et al. (2011) using NIRC2 $K_p$ and IRAM CO ($J = 5 \rightarrow 4$) imaging, as well as deep optical $I$-band imaging with the Subaru Telescope. They showed that the rest-frame UV and optical emission is magnified by a factor of $\mu = 10.9 \pm 0.7$ by a small group of galaxies at $z_{\rm phot} \simeq 0.6$. However, an offset of 2.4 kpc in the source plane was found between the stars that emit at visible/near-IR wavelengths and the gas distribution traced by the molecular gas.

Later on, Bussmann et al. (2013), and Wardlow et al. (2013) presented new imaging data for this system, using *Hubble Space Telescope* (*HST*) WFC3 F110W, new 880 $\mu$m SMA observations with higher spatial resolution than the data presented in Conley et al. (2011), and Very Large Array (VLA) 1.4 GHz data (at $1.1''$ resolution). The new images show the same spatial offsets of the bright lensed images seen between the short and long wavelengths (see Figure 4.1), noticed by Conley et al. (2011) and Gavazzi et al. (2011). A new lens model was determined by Bussmann et al.

(2013) using the SMA 880 $\mu$m data, showing a large dust distribution, magnified by $9.2 \pm 0.4$ with an effective radius of 4 kpc in the source plane. Its centroid matches the position of the gas distribution traced by the molecular gas, which we attribute to the source of the luminous far-IR emission, but both are offset with respect to the stars that are seen in the visible/near-IR (UV/optical in the rest-frame). Finally, Rigopoulou et al. (2018) discuss the applicability of the [O III]88/[N II]122 line ratio as a metallicity indicator in high redshift submillimeter luminous galaxies and found that the gas metallicity of HLock01 is $0.6 < Z_{\rm gas}/Z_{\odot} < 1.0$.

Due to the high dust content of HLock01, one could expect that its rest-frame UV and optical light are heavily obscured by dust, as in most SMGs. However, HLock01 is unusually bright in its rest-frame UV, and its blue colors suggests low dust attenuation, similar to those of $z \sim 3$ Lyman break galaxies (LBGs; Steidel et al. 1996) with $(G-R) = 0.5$ and $(U-G) = 1.4$. In the following sections, I will present a detailed analysis of the optically bright lensed images of HLock01, based on deep spectroscopic observations with the 10.4 m Gran Telescopio Canarias (GTC). These observations, combined with multi-band imaging and a new analysis of the spectral energy distribution (SED), reveal that HLock01 is actually a close merger composed of the Herschel-selected submm galaxy and an optically bright LBG, separated by only 3.3 kpc in projection. Throughout this chapter, I adopt the name "HLock01-B" for the optically bright LBG-like galaxy, and "HLock01-R" for the *Herschel*-selected SMG (where "B" and "R" stand for blue and red galaxies, respectively). Thanks to the large collecting area of the GTC, to the lensing magnification of the source, and to the small obscuration towards HLock01-B, we can perform a detailed analysis of its physical properties.

A concordance cosmology with matter and dark energy density $\Omega_{\rm m} = 0.3$, $\Omega_{\Lambda} = 0.7$, and Hubble constant $H_0 = 70$ km s$^{-1}$ Mpc$^{-1}$ is assumed throughout this work. All magnitudes are given in the AB system.

## 4.3 Observations

### 4.3.1 GTC/OSIRIS spectroscopic and imaging observations

Rest-frame UV spectroscopic observations were obtained with the Optical System for Imaging and low-Intermediate-Resolution Integrated Spectroscopy instrument (OSIRIS[1]) on the 10.4 m GTC. The data used in this Chapter were obtained in service mode over seven different nights, between 2015 April 26 and 2015 June 21 in dark and gray Moon conditions as part of the GTC program GTCMULTIPLE2A-15A (PI: R. Marques-Chaves). We used the R2500V and R2500R grisms, with dispersions

[1] http://www.gtc.iac.es/instruments/osiris/

Table 4.1: OSIRIS spectroscopic observations of HLock01-B.

| Lensed images | PA (°) | Grism | Date | Time (sec) | Seeing (arcsec) | Moon |
|---|---|---|---|---|---|---|
| A/B | −39.5 | R2500V | 2015 May 09 | $5 \times 900$ | 0.7 | dark |
| | −39.5 | R2500R | 2015 May 09 | $5 \times 900$ | 0.8 | dark |
| A/C | −82.2 | R2500V | 2015 May 08 | $3 \times 900$ | 1.0 | gray |
| | −82.2 | R2500V | 2015 Jun 07 | $2 \times 900$ | 0.9 | gray |
| | −82.2 | R2500R | 2015 Apr 26 | $3 \times 900$ | 0.8 | gray |
| | −82.2 | R2500R | 2015 Jun 07 | $2 \times 900$ | 0.9 | gray |
| A/D | 44.0 | R2500V | 2015 May 09 | $3 \times 900$ | 0.8 | gray |
| | 44.0 | R2500V | 2015 Jun 11 | $2 \times 900$ | 0.8 | dark |
| | 44.0 | R2500R | 2015 Apr 26 | $3 \times 900$ | 0.7 | gray |
| | 44.0 | R2500R | 2015 Jun 11 | $2 \times 900$ | 0.8 | dark |

of 0.80 and 1.04 Å $\text{px}^{-1}$, respectively. These two grisms provide a full spectral coverage of $4500 - 7700$ Å, which corresponds to $1150 - 1950$ Å in the rest-frame at $z \simeq 2.95$. The OSIRIS $1.2''$ wide slit was centered on the brightest lensed image of HLock01-B (image A), and oriented so as to encompass the other lensed images B, C, and D, at sky positions angles (PA) of $-39°.4$, $-82°.9$, and $44°$, respectively (see Figure 4.1, left panel). Given this configuration, the corresponding instrumental resolution for the R2500V and R2500R grisms is $\simeq 180$ km $\text{s}^{-1}$. In total, 15 exposures of 900 s were acquired with each grism, equally split between different PAs. A summary of the rest-frame UV spectroscopic observations of HLock01-B used in this work is shown in Table 4.1.

The data were processed with standard IRAF[2] and PYTHON tasks. Each individual two-dimensional spectrum was bias-subtracted, and flat-field corrected. The wavelength calibration was done for every observing night using HgAr+Ne+Xe arc lamps. Finally, individual 2D spectra were background subtracted. The 1D spectra were then extracted and corrected for the instrumental response using observations of the standard stars Ross 640 and GD 153.

Additional spectra were obtained for the galaxies in the group responsible for the gravitational lensing of HLock01, with two additional long-slit spectra to encompass G1 − G4, and G3 − G5, respectively. For this, a lower spectral resolution grism,

[2] http://iraf.noao.edu/

R1000R, were used, providing a wider spectral range (5100 – 10000 Å), which with a 1.2″ wide slit gives a spectral resolution of $\simeq 400$ km s$^{-1}$. The other lensing galaxies G2, and G6 are covered by the long-slit spectra discussed before to study the lensed images of HLock01-B.

Additionally, broad-band imaging with the Sloan $g'$ filter was obtained with OSIRIS on 2017 January 24, as part of the GTC program GTCMULTIPLE3A-16B (PI: I. Pérez-Fournon). The total exposure time was 2160 s, spit into 12 individual exposures of 180 s each. Each frame was reduced individually following standard reduction procedures in IRAF. The registration and combination were done using SCAMP (Bertin 2006) and SWARP (Bertin 2010). The seeing of the final image is $\simeq 0.8''$" (full width at half maximum, FWHM).

### 4.3.2 WHT/LIRIS near-IR imaging

Near-IR broad-band imaging was obtained on 2011 March 22 in the $K_s$ filter (PI: I. Pérez-Fournon), using the Long-slit Intermediate Resolution Infrared Spectrograph instrument (LIRIS) mounted at the William Herschel Telescope (WHT). LIRIS has a field of view of $4.27' \times 4.27'$ with a plate scale of $0.25''$ pixel$^{-1}$. The total integration time was 60 minutes, spit into 180 individual exposures of 20 s, adopting a random dither pattern in 15 different positions. The data reduction was carried out using the IAC's IRAF LIRISDR[3] task. The seeing of the final image was $0.63''$ FWHM. The astrometric and flux calibrations were performed using 2MASS stars in the field.

### 4.3.3 Ancillary data

Additional data used in this work consist of a combination of shallow and deep images. Archival *U* and *R* wide-field images and catalogs from MEGACAM on the Canada-France-Hawaii Telescope (CFHT), processed and stacked using the MegaPipe image staking pipeline (Gwyn 2008), were downloaded from the Canadian Astronomy Data Centre (CADC[4]). Total exposure times are 4200 and 3300 s in *U* and *R* bands, with an average seeing of $0.83''$ and $0.73''$ FWHM, respectively. HLock01 was also imaged with WFC3 on *HST* under the snapshot program 12488 (PI: Negrello). The source was observed in the broad-band filter F110W with a total exposure time of 276.1 s. The *HST* imaging was initially presented in Bussmann et al. (2013) and Wardlow et al. (2013). *Spitzer*/IRAC images and catalogs in the 3.6 $\mu$m and 4.5 $\mu$m bands from the *Spitzer* Extragalactic Representative Volume Survey (SERVS; Mauduit et al. 2012) were obtained from the IRSA archive.[5] We also used the IRAC and MIPS imaging

[3] http://www.iac.es/galeria/jap/lirisdr/LIRIS_DATA_REDUCTION.html
[4] http://www.cadc-ccda.hia-iha.nrc-cnrc.gc.ca/en/cfht/
[5] http://irsa.ipac.caltech.edu/data/SPITZER/SERVS/

from the *Spitzer* Wide-Area InfraRed Extragalactic survey data (SWIRE; Lonsdale et al. 2003).

## 4.4 Rest-frame UV spectrum of HLock01-B

As in other star-forming galaxies, the rest-frame UV spectrum of HLock01-B, shown in Figure 4.2 is characterized by the integrated light from the hot young stellar population with superimposed resonant strong absorption lines produced by the interstellar medium (ISM) and stellar winds. These spectral features can provide detailed information on dynamical, physical, and chemical properties of the atomic and ionized gas in the galaxy, as well as insights on the properties of the young OB stars responsible for the bright continuum (e.g., Pettini et al. 2000, 2002; Shapley et al. 2003; Jones et al. 2012; Steidel et al. 2016; Rigby et al. 2018a,b). Large-scale outflows of interstellar gas, resulting from the kinetic energy deposited by the star formation activity, are a common feature in these galaxies (e.g., Shapley et al. 2003; Steidel et al. 2010).

Despite the differences in the S/N of the spectra of the different lensed images, there are no differences in the profiles of the absorption features and no evidence for velocity offsets between them, as expected. Spectra of the lensed images B and D show redder UV slopes ($\beta$), likely due to differential extinction from the proximity of their light path to the foreground galaxies. Thus, this work will focus on the spectrum of the lensed image A, which has higher S/N ($\sim 20-40$, depending on the wavelength range) and is less affected by absorption in the interstellar medium of the foreground galaxies.

The rest-frame UV spectrum of the lensed image A of HLock01-B, shown in Figure 4.3, is remarkably similar to the high S/N composite spectrum from Rigby et al. (2018b) constructed from 11 strong gravitational lensed galaxies. It shows a damped Ly$\alpha$ absorption line, and a series of strong absorption lines associated either with stellar winds from massive stars (e.g., C IV $\lambda\lambda$1548,1550), and ISM lines of several species. However, there are significant differences between the expected wavelengths and velocities ($\Delta v \simeq 500$ km s$^{-1}$) of the ISM in the $z \simeq 3$ template (in orange in Figure 4.3) and in our spectrum (discussed in Section 4.4.2). The OSIRIS spectrum also shows several narrow absorption lines produced by intervening systems at lower redshifts along the line of sight to HLock01-B. At least two intervening metal systems were identified at $z = 1.4583 \pm 0.0008$, and $z = 2.1889 \pm 0.0007$. Some of these absorption lines may contaminate the profiles of lines of HLock01-B, and hence they are taken into account in our analysis (in Section 4.4.2).

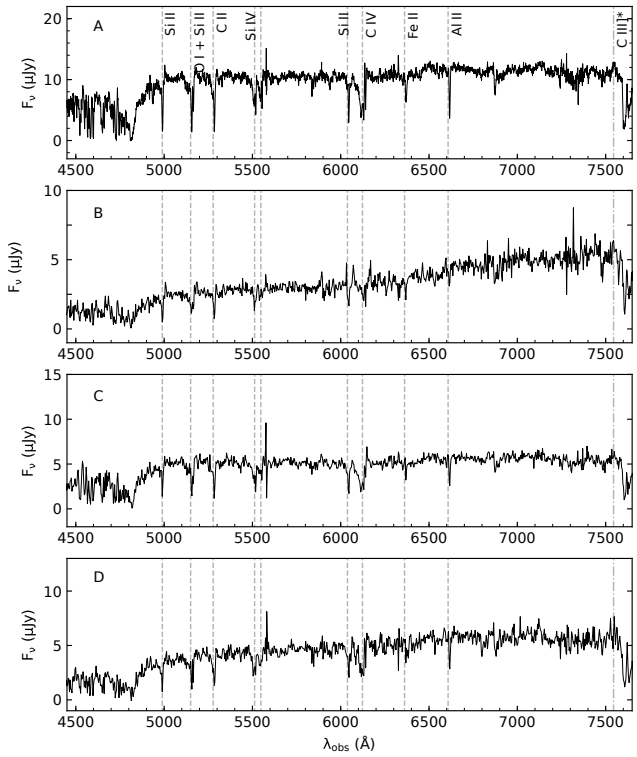


Figure 4.2: GTC/OSIRIS rest-frame UV spectrum of the lensed images A, B, C and D (offset for clarity). Vertical lines identify strong absorption lines. There are no differences in the profiles of the absorption features and no evidence for velocity offsets between the spectra of the lensed images, as expected. Spectra of the lensed images B and D show redder UV slopes ($\beta$), likely due to differential extinction from the proximity of their light path to the foreground galaxies.

### 4.4.1 Systemic redshift of HLock01-B

Stellar photospheric features are formed in the photospheres of hot stars, and although much weaker than the ISM lines, they can provide a measurement of the systemic redshift of the galaxy. Within the wavelength range covered by our data, several photospheric absorption features are identified (marked with dotted lines in Figure 4.3), but some of them are blends from multiple transitions. Using the cleanest among

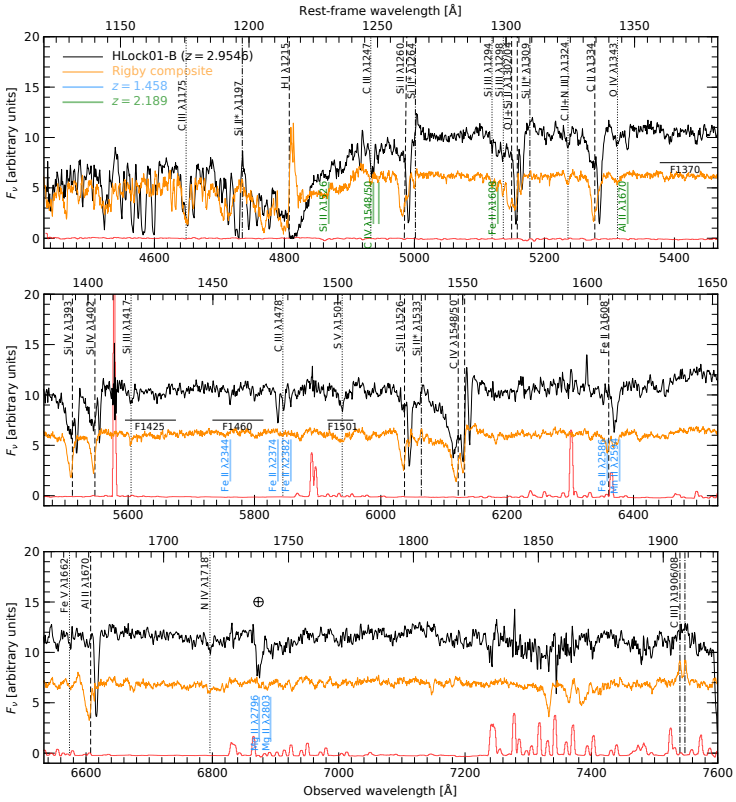


Figure 4.3: Combined GTC/OSIRIS rest-frame UV spectrum of the lensed image A of HLock01-B. Vertical dotted lines identify the best defined photospheric absorption lines used to derive the systemic redshift of HLock01-B ($z_{\rm sys} = 2.9546 \pm 0.0004$). Strong absorption lines associated with interstellar gas and stellar winds are marked with vertical dashed lines. The C III] $\lambda\lambda$1906,1908 nebular emission doublet and fine-structure emission lines of Si II are marked with dash-dotted lines. For comparison, the high S/N composite spectrum from Rigby et al. (2018b) constructed from 11 strong gravitational lensed galaxies is shown at the systemic redshift of HLock01-B (orange, downshifted for clarity). The wavelength windows of four metallicity indices (e.g., F1370, etc.), used to derive the metallicity of young stars in HLock01-B, are also marked. Short vertical blue and green lines mark the positions of absorption lines of intervening systems at $z \simeq 1.458$ and $z \simeq 2.189$, respectively. The sky emission is also plotted in red, showing the locations of strong sky emission lines.

these, listed in Table 4.2 and shown in Figure 4.4, the mean redshift of the stars is $z_{\rm stars} = 2.9546 \pm 0.0004$.

Table 4.2: Stellar photospheric lines in HLock01-B.

| Ion | $\lambda^{\rm a}_{\rm lab}$ (Å) | $\lambda^{\rm b}_{\rm obs}$ (Å) | $z_{\rm stars}$ |
|---|---|---|---|
| Si III | 1294.54 | 5119.71 | $2.9548 \pm 0.0003$ |
| C II | 1323.93 | 5235.54[c] | $2.9543 \pm 0.0006$[c] |
| N III | 1324.35 | 5235.54[c] | $2.9543 \pm 0.0006$[c] |
| O IV | 1343.35 | 5312.72 | $2.9546 \pm 0.0010$ |
| Si III | 1417.24 | 5604.64 | $2.9546 \pm 0.0010$ |
| S V | 1501.76 | 5939.25 | $2.9548 \pm 0.0003$ |
| N IV | 1718.55 | 6796.37 | $2.9548 \pm 0.0004$ |

**Notes.**
[a] Vacuum wavelengths.
[b] Values measured from the centroid for the individual photospheric line.
[c] Value refers to the blended C II and N III photospheric lines.

The nebular C III] $\lambda\lambda$1906,1908 emission is weakly detected ($3\sigma$) at $z_{\rm CIII]} = 2.954 \pm 0.002$, in agreement with $z_{\rm stars}$, but the doublet is not resolved in our spectrum, and the existing data are too noisy for a reliable measurement of this feature. Therefore, throughout this Chapter the redshift of stellar photospheric lines is adopted as the systemic redshift of HLock01-B, $z_{\rm sys} = 2.9546 \pm 0.0004$.

The difference of $\Delta v = 210$ kms$^{-1}$ between the systemic redshift of HLock01-B $z_{\rm sys} = 2.9546$, and the redshift of HLock01-R from the molecular gas lines $z_{\rm CO} = 2.9574$ (Riechers et al. 2011; Scott et al. 2011) cannot be explained by errors in redshift measurements. The velocity offset derived here and the complex dynamical structure of the molecular gas reservoir discussed in Riechers et al. (2011) suggest that HLock01-B is a separate galaxy, different from the *Herschel* SMG (HLock01-R), but both forming a close merger. Nevertheless, similar velocity offsets, interpreted as rotational velocities in some cases, have been found in a few massive galaxies at high-$z$ (e.g., Law et al. 2012; Jiménez-Andrade et al. 2017; Toft et al. 2017). A more detailed discussion is presented in Section 4.8.1.

### 4.4.2 Kinematics of the ISM

Within our spectral range, 11 strong absorption features are identified, including low-ionization lines (Si II $\lambda\lambda$1260, O I $\lambda\lambda$1302, Si II $\lambda\lambda$1304, C II $\lambda\lambda$1334, Si II $\lambda\lambda$1526, Fe II $\lambda\lambda$1608, and Al II $\lambda\lambda$1670) and high-ionization lines associated with a hot gas

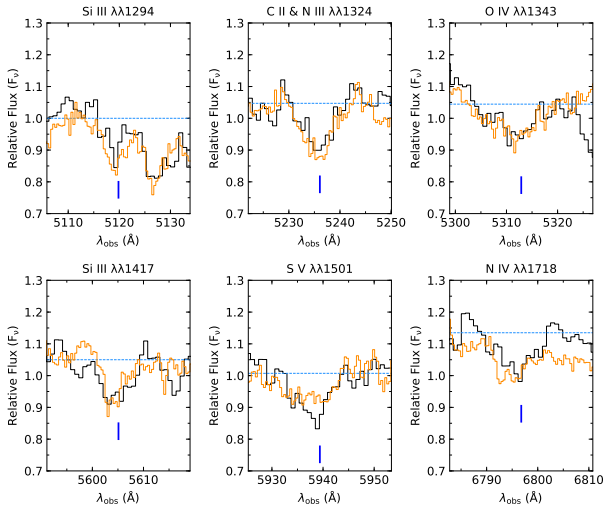


Figure 4.4: Portions of the spectrum of HLock01-B encompassing faint stellar photospheric absorption lines used for the determination of the systemic redshift of the galaxy as $z_{sys} = 2.9546 \pm 0.0004$ (see Table 4.2) Blue ticks mark the position of the centroids of each line. In orange is shown the high S/N composite spectrum from Rigby et al. (2018b) constructed from 11 strong gravitational lensed galaxies at the systemic redshift of HLock01-B.

phase (Si IV $\lambda\lambda$1393,1402, and C IV $\lambda\lambda$1548,1550). In low-ionization lines, the interstellar component usually dominates over the stellar contribution, thus these lines are useful for studying the kinematics of the ISM (Shapley et al. 2003; Steidel et al. 2010). High-ionization lines are associated with strong winds from young stars, and predominantly trace gas at higher temperatures ($T \geq 10^4$ K).

For the kinematic analysis of the ISM, the GTC/OSIRIS spectrum of HLock01-B was firstly normalized using the pseudo-continuum windows that are free of absorption and emission features identified by Rix et al. (2004). Figure 4.5 shows the normalized profiles of the strongest absorption lines seen in our spectrum.

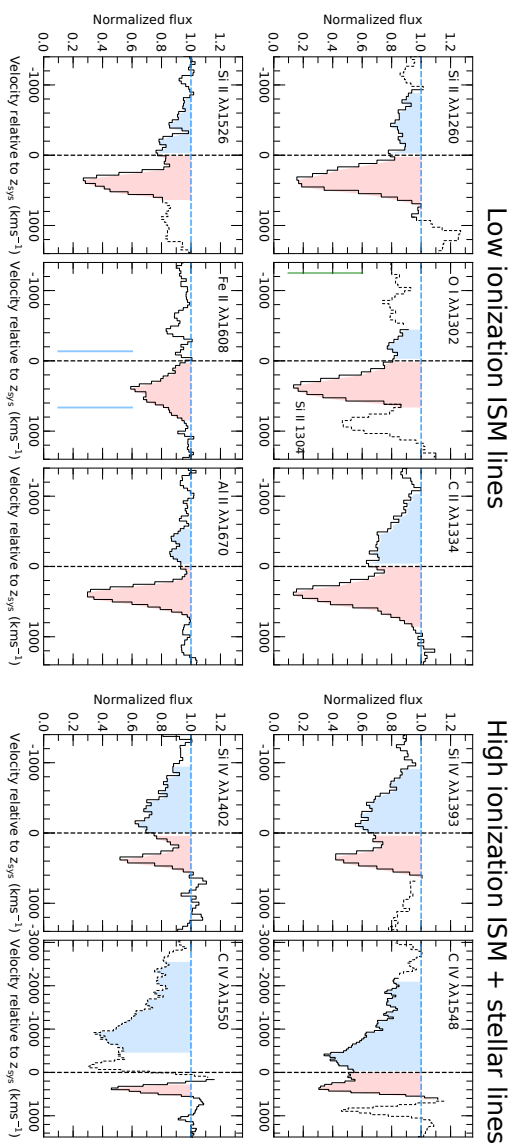


Figure 4.5: Normalized profiles of low- and high-ionization absorption lines associated with the ISM and stellar winds, as indicated. The $x$ axis is the velocity (in km s$^{-1}$) relative to the stars of HLock01-B, $z_{sys} = 2.9546$, and the $y$ axis is the normalized flux. Almost all ISM and wind lines present an unusual velocity profile, with two distinct absorption components on either side of systemic velocity (negative and positive velocities shaded in blue and red, respectively, for visual purpose only). The absorption component with the maximum intensity is located at $v \simeq +370$ km s$^{-1}$ (shaded in red). Another broader component is also detected in high-ionization lines, like C IV λλ1548,1550 and Si IV λλ1393,1402, and in some ISM lines (shaded in blue). Dotted lines indicate spectral features in HLock01 other than those to which the label in each plot refers. Short vertical blue and green solid lines mark the expected positions of absorption lines from intervening metal systems at lower redshift.

All ISM lines present an unusual velocity profile with the maximum optical depth located at a mean $v = (+370 \pm 30)$ km s$^{-1}$ relative to the stars of HLock01-B, or $v = (+170 \pm 30)$ km s$^{-1}$ relative to the *Herschel* SMG at $z_{\rm CO} = 2.9574$. This can be understood as gas apparently moving towards the young stars, since all the interstellar lines are seen against the UV stellar continuum. This absorption is strong in the low-ionization lines (the first three columns in Figure 4.5), likely with saturated profiles,[6] but it is also present, although notably weaker in high-ionization ones, like C IV and Si IV (the last two columns in Figure 4.5). The spectrum of HLock01-B also shows a secondary, but broader absorption component centered at a mean $v = (-220 \pm 60)$ km s$^{-1}$ relatively to its systemic redshift, which is a characteristic of large-scale outflows of material in HLock01-B. This blueshifted component is stronger in high-ionization lines than in low-ionization ones (it is detected in C II $\lambda\lambda$1334, Si II $\lambda\lambda$1260, and Si II $\lambda\lambda$1526, but is not detected in O I $\lambda\lambda$1302, Fe II $\lambda\lambda$1608 or Al II$\lambda\lambda$1670), suggesting that the outflowing gas is mostly ionized, or the neutral gas has a lower covering factor than the ionized gas.

The absorption profiles resulting from these two components extend over a velocity range $\Delta v \simeq 1700$ km s$^{-1}$, from $\sim -1000$ to $\sim +700$ km s$^{-1}$, much larger than in other high-$z$ lensed LBGs (Pettini et al. 2000, 2002; Cabanac et al. 2008; Quider et al. 2009, 2010; Dessauges-Zavadsky et al. 2010). The C IV doublet is even broader than the ISM lines, with $\Delta v \gtrsim 3000$ km s$^{-1}$, indicative of a strong contribution from winds due to radiation pressure of the most massive, and luminous stars of HLock01-B. The velocity profile of the C IV doublet shows a strong P-Cygni profile, with the red-emission wing being attenuated by the two narrow, redshifted ($v \simeq +370$ km s$^{-1}$) interstellar absorption components of C IV.

In order to understand the blueshifted and redshifted ISM absorption components, we simultaneously fit two Gaussians to the low- and high-ionization lines. Figure 4.6 shows an example of our fit to the low-ionization C II $\lambda\lambda$1334, and high-ionization Si IV $\lambda\lambda$1393 lines, and Table A.2 summarizes the results for all strong absorption lines, except for the ones that are affected by the proximity of other lines (O I $\lambda\lambda$1302, Si II $\lambda\lambda$1304, and Fe II $\lambda\lambda$1608). In C IV $\lambda\lambda$1548,1550 we only fit the redshifted component, as the blueshifted is affected by strong winds.

[6] We test if some of these lines are saturated, by considering the linear part of the curve of growth. In this case, the ratios of the rest-frame equivalent widths ($EW_0$) of different transitions of a given ion can be related through their oscillator strengths. For example, for the Si II lines in the unsaturated case we would expect $EW_0(1260)$ / $EW_0(1526) \simeq 5$, $EW_0(1260)$ / $EW_0(1304) \simeq 10$, and $EW_0(1304)$ / $EW_0(1526) \simeq 0.5$. Our spectrum shows ratios of $\simeq 1.0, 2.5$, and 0.4, respectively, suggesting that at least Si II $\lambda\lambda$1260 may be saturated.

Table 4.3: Strong Interstellar Absorption Features in the Spectrum of HLock01-B.

| Ion | $\lambda_{lab}$ | $\Delta v$ | $EW_0^{total}$ | Blue (Outflowing) | | | Red (Inflowing) | | |
|---|---|---|---|---|---|---|---|---|---|
| | | | | $z_b$ | $EW_0$ | FWHM | $z_r$ | $EW_0$ | FWHM |
| | (Å) | (km s$^{-1}$) | (Å) | | (Å) | (km s$^{-1}$) | | (Å) | (km s$^{-1}$) |
| (1) | (2) | (3) | (4) | (5) | (6) | (7) | (8) | (9) | (10) |
| Si II | 1260.42 | $-950 \pm 750$ | $1.94 \pm 0.23$ | 2.9503 | $0.69 \pm 0.20$ | 900 | 2.9596 | $1.32 \pm 0.26$ | 309 |
| O I | 1302.17 | $-950 \pm 750$ | $2.52 \pm 0.21$ | — | — | — | 2.9598 | $1.61 \pm 0.24$ | 373 |
| Si II | 1304.37 | $-950 \pm 750$ | $2.52 \pm 0.21$ | — | — | — | 2.9597 | $0.76 \pm 0.12$ | 244 |
| C II | 1334.53 | $-1000 \pm 900$ | $2.59 \pm 0.26$ | 2.9520 | $1.40 \pm 0.20$ | 898 | 2.9599 | $1.26 \pm 0.12$ | 310 |
| Si II | 1526.71 | $-900 \pm 700$ | $1.82 \pm 0.27$ | 2.9531 | $0.76 \pm 0.15$ | 740 | 2.9596 | $1.09 \pm 0.16$ | 230 |
| Fe II | 1608.45 | $-800 \pm 950$ | $1.27 \pm 0.36$[a] | — | — | — | 2.9607[a] | $1.07 \pm 0.21$[a] | 468[a] |
| Al II | 1670.79 | $-800 \pm 750$ | $1.58 \pm 0.44$ | 2.9510 | $0.43 \pm 0.20$ | 554 | 2.9599 | $1.16 \pm 0.13$ | 198 |
| Si IV | 1393.76 | $-1000 \pm 650$ | $2.25 \pm 0.25$ | 2.9520 | $1.71 \pm 0.19$ | 798 | 2.9592 | $0.50 \pm 0.10$ | 104 |
| Si IV | 1402.77 | $-1000 \pm 650$ | $1.64 \pm 0.27$ | 2.9514 | $1.45 \pm 0.15$ | 859 | 2.9599 | $0.29 \pm 0.08$ | <180 |
| C IV | 1548.20 | $-2600 \pm 1000$ | $5.76 \pm 0.40$ | — | — | — | 2.9593 | $1.07 \pm 0.40$ | <180 |
| C IV | 1550.78 | $-2600 \pm 1000$ | $5.76 \pm 0.40$ | — | — | — | 2.9596 | $0.54 \pm 0.20$ | <180 |

**Notes.** — Columns are as follows: (1) and (2) ion and the corresponding vacuum wavelength; (3) velocity range for the measurements of the total rest-frame equivalent width (blueshifted and redshifted components); (4) total rest-frame equivalent width and $1\sigma$ error; (5), (6) and (7) redshift, rest-frame equivalent width, and full width half maximum (FWHM $= 2\sqrt{2\ln 2}\sigma$) of the blueshifted absorption component from the Gaussian fit; (8), (9), and (10) are the same as (5), (6), and (7), but in this case applied to the redshifted absorption component from the Gaussian fit.

[a] The profile of Fe II $\lambda\lambda$1608 is affected by other absorption lines from an intervening system at $z = 1.4583 \pm 0.0005$.

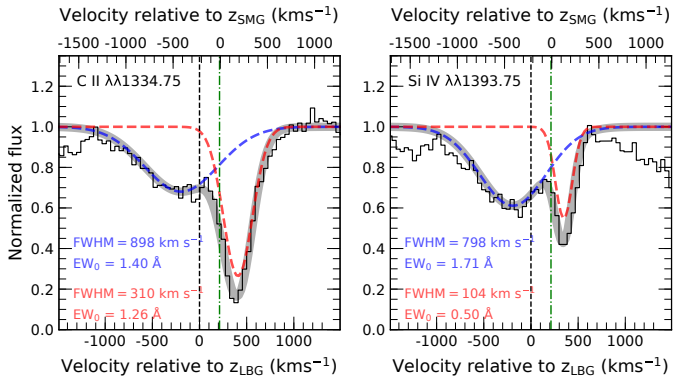


Figure 4.6: Example of the double-Gaussian fit of the low- (C II λλ1334) and high-ionization lines (Si IV λλ1393). Lower and upper $x$ axes are the velocity (in km s$^{-1}$) relative to the stars of the LBG (HLock01-B) and to the molecular gas of the SMG (HLock01-R), respectively. The $y$ axis is the normalized flux. The redshifted (red color) and blueshifted (blue color) components represent outflowing and inflowing gas along the line of sight of HLock01-B, respectively. The sum of the two components is also shown in gray. Black dashed and green dot-dashed vertical lines mark the zero velocity position with respect to $z_{sys} = 2.9546$ (HLock01-B) and $z_{CO} = 2.9574$ (HLock01-R), respectively.

The fitted blueshifted component (blue dashed lines in Figure 4.6) has its peak located at $z_{blue} = 2.9519 \pm 0.0009$ (or $v_{blue} \simeq -220$ km s$^{-1}$ relative to the systemic redshift of HLock01-B), and shows a broad profile (FWHM $\simeq 900$ km s$^{-1}$, after accounting for the instrumental broadening) extended over a velocity range from about $-1000$ to $+600$ km s$^{-1}$. Despite the fact that a potentially large contribution from stellar winds may be present in the high-ionization lines, for the low-ionization lines, this effect is negligible. Thus, the broadness of the blueshifted component in the low-ionization line C II (as well as in others like Si II λλ1260, Si II λλ1526, see Figure 4.5) suggests highly turbulent kinematics of the outflowing gas. As a comparison, the velocity profile of the low-ionization interstellar lines in the $z \sim 3$ LBGs composite spectrum of Shapley et al. (2003) shows an average FWHM $= (560 \pm 150)$ km s$^{-1}$. Despite the broadness of the outflowing low-ionization lines in HLock01-B, they show smaller rest-frame equivalent widths (by a factor of two) than in typical LBGs.

The fitted redshifted component (red dashed line in Figure 4.6) has its peak located at $z_{red} = 2.9596 \pm 0.0003$, and shows a narrow profile (FWHM $= 310$ and $104$ km s$^{-1}$, for C II and Si IV, respectively). If dynamically related to HLock01, its positive velocity relatively to both HLock01-B ($v \simeq +370$ km s$^{-1}$) and HLock01-R ($v \simeq +170$ km s$^{-1}$) is indicative of gas moving towards the system. This narrower component

is seen in all absorption lines, but appears almost unresolved in the high-ionization lines, suggesting that these lines are dominated by the interstellar component. Moreover, the differences in the FWHM between the redshifted component in low- and high-ionization lines (see Table A.2) also suggests that cold and warm gas may have different kinematics and origins. A more clear picture of the origin of this redshifted component of the ISM may come from deeper and higher spectral resolution observations. In particular, fully resolved ISM components of HLock01-B with unsaturated profiles may be used to derive chemical abundances, using the apparent optical depth method, as has been done in other studies of strongly lensed star-forming galaxies (e.g., Pettini et al. 2002; Quider et al. 2009; Dessauges-Zavadsky et al. 2010).

### 4.4.3 Stellar metallicity and age of HLock01-B

Leitherer et al. (2001), Rix et al. (2004), and, later on, Sommariva et al. (2012) showed that several blends of stellar UV photospheric absorption lines can be used to trace the metallicity of young stars, by measuring equivalent widths of these blends in specific wavelength windows. These metallicity indicators have been successfully applied in several works using high S/N spectra due to the faintness of these absorption lines (e.g., Quider et al. 2009, 2010; Patrício et al. 2016). These indicators are defined as the F1370, F1425, F1460, F1501, and F1978 indices, and their wavelength windows are shown in Figure 4.3 (except for the latter one which is not covered by our data).

We measured the equivalent width of features in each of these spectral windows using our normalized spectrum. We then applied the calibrations of Sommariva et al. (2012) to obtain the corresponding metallicity. Table 4.4 summarize our measurements. All indices agree in a sub-solar metallicity, and we use the mean value to derive the metallicity of the UV stars in HLock01-B as $Z_{\rm stars} = (0.4 \pm 0.1) Z_{\odot}$.

Table 4.4: Metallicity estimates following Sommariva et al. (2012).

| Index | Range (Å) | EW (Å) | $Z/Z_{\odot}$ |
|---|---|---|---|
| F1370 | 1360 – 1380 | $1.4 \pm 0.2$ | 0.35 |
| F1425 | 1415 – 1435 | $0.9 \pm 0.1$ | 0.28 |
| F1460 | 1450 – 1470 | $1.0 \pm 0.1$ | 0.39 |
| F1501 | 1496 – 1506 | $0.6 \pm 0.1$ | 0.59 |

The derived metallicity can also be qualitatively observed, when we compare the synthetic stellar spectra of Rix et al. (2004) with our HLock01-B spectrum, after smoothing it to the 2.5 Å resolution of the Rix et al. models. Figure 4.7 shows the comparison for the F1370 and F1425 indexes of our smoothed OSIRIS spectrum and

the Rix et al. (2004) models, for metallicities ranging from 0.001 to 0.4 ($0.05 - 2Z_{\odot}$). A good match is seen for $Z = 0.4Z_{\odot}$, particularly in the F1425 index, in agreement with the metallicity derived above.

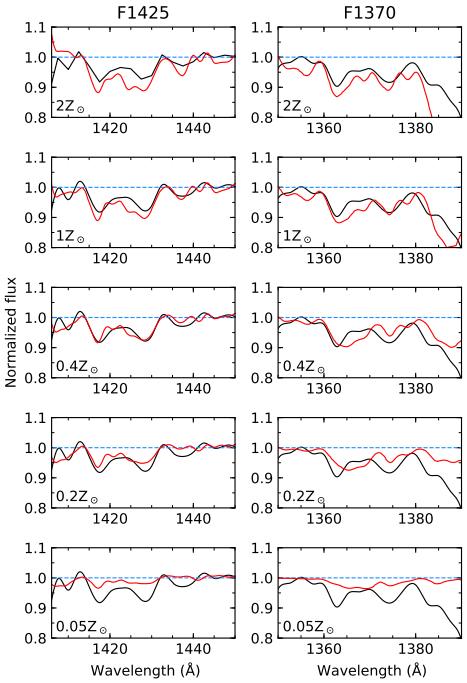


Figure 4.7: Comparison of the smoothed GTC spectrum of HLock01-B (black solid lines) with Rix et al. (2004) model spectra (red solid lines) in the regions including the F1425 (left panels) and F1370 (right panels) indexes, for metallicities ranging from 1/20 to twice of solar, as indicated. A good match is seen for $Z = 0.4Z_{\odot}$, in particular in the F1425 index, in agreement with the metallicity derived using the method of Sommariva et al. (2012).

The strength of any P-Cygni features formed in the expanding winds of the most massive stars is also sensitive to the metallicity, along with the age and the initial mass function (IMF) of the stellar population. In order to study the P-Cygni stellar wind features in HLock01-B we use model spectra computed with the spectral synthesis code STARBURST99 (Leitherer et al. 1999, 2001) and perform $\chi^2$ minimization to our

normalized data. In generating the STARBURST99 spectra, we assumed both continuous and instantaneous star-formation scenarios. We adopt a Salpeter slope for the IMF between 1 and 100 $M_{\odot}$, and ages ranging from 1 to 100 Myr. STARBURST99 models were generated using libraries of empirical UV spectra from Large and Small Magallenic Cloud stars (LMC/SMC, which correspond to a metallicity $Z_{\rm MC} \simeq 0.4Z_{\odot}$) and Galactic stars ($\simeq 1Z_{\odot}$).

Figure 4.8 shows two high-ionization lines associated with stellar winds used in this fit: N V $\lambda\lambda$1238,1242 (left panels); and C IV $\lambda\lambda$1548,1550 (middle panels). STARBURST99 models are plotted for continuous (upper panels) and instantaneous (lower panels) star-formation scenarios. We excluded in the fit the region encompassing the interstellar absorption in C IV, between 1543 and 1553 Å, which is not associated with the stellar P-Cygni profile.

The $\chi^2$ ($N_{\rm dof} = 38$) as a function of the age of the stellar population for all models is shown in the right panel of Figure 4.8. The model using LMC/SMG stars ($0.4Z_{\odot}$) with a $\sim 6$ Myr old burst matches the data better ($\chi^2/N_{\rm dof} = 39/38$), reproducing quite well both the line profiles of N V and C IV, in particular the regions of the blueshifted absorption wind component of the C IV P-Cygni profile and its red-emission wing (regions of 1536 to 1542 and 1554 to 1563 Å, respectively). Bursts over sightly longer periods ($\lesssim 25$ Myr) can also recover the stellar blueshifted absorption of C IV, but fail to reproduce the red emission wing of HLock01-B (see lower panels of Figure 4.8 for an example of a 15 Myr old burst). However, our results should be treated with care, since the P-Cygni profile of N V $\lambda\lambda$1238,1242 could be affected by the red wing of the damped Ly$\alpha$ absorption line (see Section 4.4.4).

All methods used in this work to derive the metallicity of the young stars in HLock01-B point to a $Z_{\rm stars} \simeq 0.4Z_{\odot}$ value. Our metallicity measurements are slightly different from the measurement of gas metallicity in HLock01-R ($0.6 < Z_{\rm gas}/Z_{\odot} < 1.0$) by Rigopoulou et al. (2018), using the [O III]88/[N II]122 line ratio as a metallicity indicator. This provides additional evidence that the bright *Herschel*-SMG (HLock01-R) and the bright LBG-like galaxy (HLock01-B) are likely different galaxies with distinct enrichment histories.

### 4.4.4 The damped Ly$\alpha$ profile

The Ly$\alpha$ line in the spectrum of HLock01-B shows a strong, damped Ly$\alpha$ profile, with the minimum lying in the range from $\simeq 4809$ to 4815 Å (or $v \simeq +100$ to $+500$ km s$^{-1}$ relative to $z_{\rm sys}$, see Figure 4.9). We used the software PYASTRONOMY[7] to generate theoretical Voigt profiles and perform $\chi^2$ minimization to the Ly$\alpha$ profile. However, we noted differences in the absorption profile in the blue and red damping

[7] https://github.com/sczesla/PyAstronomy

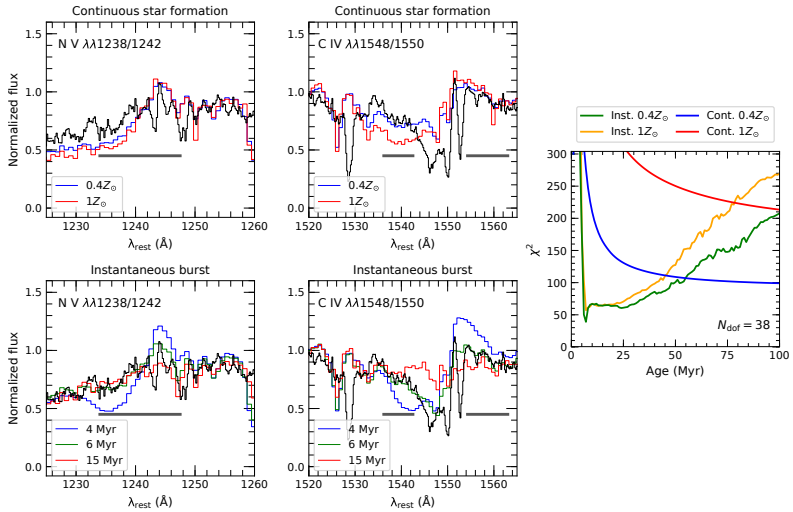


Figure 4.8: Comparison of the normalized spectrum of HLock01-B (black solid lines) with empirical models from STARBURST99 for high-ionization lines associated with stellar winds: N V λλ1238,1242 (left panels); and C IV λλ1548,1550 (middle panels). Upper panels show models for continuous star formation with a stellar population age $t = 100$ Myr, and for metallicities of $0.4Z_\odot$ (LMC/SMG stars, blue solid lines) and $1Z_\odot$ (Galactic stars, red solid lines). Lower panels show the comparison of the spectrum of HLock01-B with models for an instantaneous burst with $Z = 0.4Z_\odot$ and ages of 4 (blue), 6 (green), and 15 (red) Myr. The wavelength windows used to perform the $\chi^2$ minimization are marked in gray. Note that we exclude in this fit the region of strong interstellar absorption in C IV (between 1543 and 1553). The right panel shows the $\chi^2$ ($N_{\rm dof} = 38$) as a function of the age of the stellar population for continuous and instantaneous star formation models, and metallicities of $0.4Z_\odot$ and $1Z_\odot$, as indicated. A good fit is seen for models using LMC/SMG stars ($0.4Z_\odot$) with around 6 Myr old burst.

wings, with the absorption being more pronounced in the latter. The blue wing is more noisy and less constrained than the red one, likely due to additional absorption from the intergalactic medium in the line of sight towards HLock01-B. The red wing is well fitted with a neutral hydrogen column density $N(\text{H I}) = (5.83 \pm 1.24) \times 10^{20}$ cm$^{-2}$ centered at $\simeq 4813$Å or $v \simeq +370$ km s$^{-1}$ with respect to $z_{\rm sys}$. Therefore, we interpret that most of the damped absorption is due to the redshifted component of the ISM seen in the spectrum of HLock01-B, which consists primarily of neutral gas, and presents a large optical depth. Our derived column density of H I is in the range of typical values measured in other lensed galaxies (e.g., Pettini et al. 2000; Cabanac et al. 2008; Dessauges-Zavadsky et al. 2010).

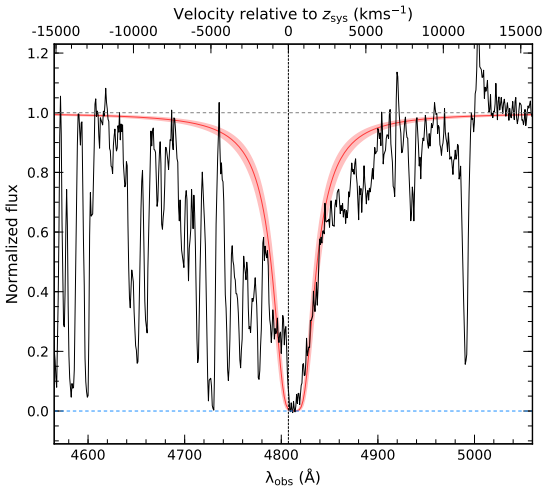


Figure 4.9: Portion of the spectrum of HLock01-B encompassing the region of the Ly$\alpha$ absorption line. The $x$ axis is the observed wavelength and the $y$ axis is the normalized intensity. Overlaid is the best Voigt profile fit (red solid line) for $N$(H I) $= (5.83 \pm 1.24) \times 10^{20}$ cm$^{-2}$ centered at $z_{\mathrm{Ly}\alpha} = 2.9594$, as well as the $1\sigma$ error (red filled area).

### 4.4.5 Weak emission lines

As discussed in Section 4.4.1, the nebular C III] $\lambda\lambda$1906,1908 emission is barely detected in our OSIRIS spectrum, and the doublet is not resolved. Despite the low significance of the detection ($3\sigma$) we fit a Gaussian to the unresolved C III] doublet. We derive $z_{\mathrm{CIII]}} = 2.954 \pm 0.002$ and $\mathrm{EW}_0^{\mathrm{CIII]}} = (1.0 \pm 0.3)$ Å. Other semiforbidden transitions often detected in the spectra of star-forming galaxies are the O III] $\lambda\lambda$1661,1666 lines, but these are not detected in our spectrum, despite the high continuum S/N in this spectral region (around 25). The absence of these nebular lines in HLock01-B may be due to their faintness or to contamination with the overlapping blueshifted component of the Al II $\lambda\lambda$1670 interstellar line.

In addition to C III], we also detect emission features from the excited fine-structure transitions Si II* $\lambda\lambda$1264, 1309, and 1533. Their profiles appear slightly asymmetric (see Figure 4.3), with the centroids redshifted with respect to $z_{\mathrm{sys}}$ by a mean of $\simeq 120 \pm 50$ km s$^{-1}$. This velocity offset may be due to the neighboring red component of resonance absorption features (Si II $\lambda\lambda$1260, O I + Si II $\lambda\lambda$1303, and

Si II $\lambda\lambda$1526), that attenuates the blue edges of the fine-structure emission profiles. We measure rest-frame equivalent widths of $0.32 \pm 0.06$, $0.22 \pm 0.09$, and $0.26 \pm 0.14$ Å for Si II* $\lambda\lambda$1264, 1309, and 1533, respectively. In the left panel of Figure 4.10 are the normalized profiles of S II* fine-structure emission lines.

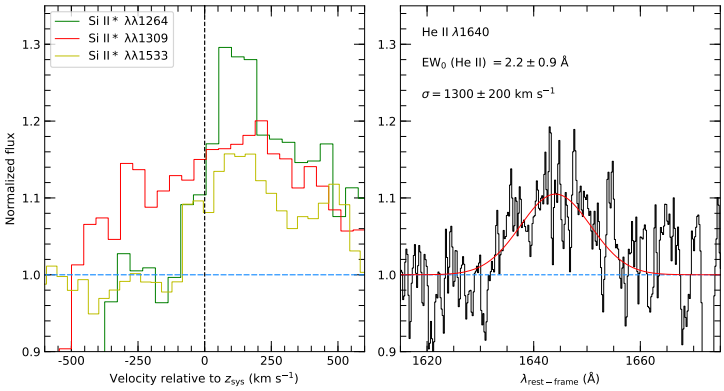


Figure 4.10: Left panel: normalized profiles of S II* $\lambda\lambda$1265, 1309, 1533 fine-structure emission lines seen in the spectrum of HLock01-B. The $x$ axis is the velocity (in km s$^{-1}$) relative to $z_{sys} = 2.9545$, and the $y$ axis is the normalized intensity of each line. The S II* $\lambda\lambda$1533 emission line was normalized considering also the broad wind component of C IV. All profiles appear slightly asymmetric and are redshifted relative to the $z_{sys}$ with a mean of $\simeq +130 \pm 50$ km s$^{-1}$. Right panel: Normalized profile of the stellar He II $\lambda\lambda$1640 emission line. The He II line has stellar origin and indicates a significant presence of WR stars (e.g., Schaerer 2003).

The spectrum of HLock01-B also shows an emission line (barely detected with a significance of $2-3\sigma$) at $\approx 6500$ Å, consistent with He II $\lambda\lambda$1640 line. This line (right panel of Figure 4.10) shows a broad profile (FWHM $\simeq 3000$ km s$^{-1}$, after accounting for the instrumental broadening), it is redshifted by $\simeq 640$ km s$^{-1}$ with respect to the systemic redshift, and has a rest-frame equivalent width of $2.2 \pm 0.9$ Å. Given the width of the emission profile, it is likely that this line has stellar origin, rather than nebular origin. Bringing together the young age ($\approx 6$ Myr) of the stellar population of HLock01-B derived in Section 4.4.3, this stellar feature is indicative of significant presence of Wolf-Rayet (WR) stars (e.g., Schaerer 2003; Brinchmann et al. 2008; Cassata et al. 2013), as WR features disappear within ages $\sim 10$ Myr after the burst. Following Schaerer & Vacca (1998), the ratio of the total number of WR stars to O

stars is related with the equivalent width of He II $\lambda\lambda$1640 in the form:

$$\log\left[\frac{\mathrm{WR}}{\mathrm{WR+O}}\right] = (-1.31 \pm 0.03) + (1.52 \pm 0.05)\log[\mathrm{EW}_0(\mathrm{HeII})]\,, \qquad (4.1)$$

which for $\mathrm{EW}_0(\mathrm{He\,II}) = 2.2 \pm 0.9$ Å implies a ratio $\mathrm{O/WR} \simeq 5$.

### 4.5 Lensing galaxy group and enviroment

We have also carried out long-slit spectroscopic observations to measure the redshifts of the galaxies responsible for the gravitational lensing of HLock01 (G1 to G6 in Figure 4.1). Apart from G2, G4, and G6, which are covered by the slits defined to observe the lensed images of HLock01, we obtained additional long-slit spectra for the images, with OSIRIS using the lower spectral resolution grism R1000R, with a total wavelength coverage of $5100 - 10000$ Å.

For the galaxies G1 and G2 we detect several absorption lines (e.g., K and H of Ca II $\lambda\lambda$3934,3969, $H_\delta$ $\lambda\lambda$4102, and Mgb $\lambda\lambda$5176) as well as prominent Balmer breaks at redshift $z_{\mathrm{G1}} = 0.6464 \pm 0.0007$, and $z_{\mathrm{G2}} = 0.6492 \pm 0.0009$, respectively. The spectra of G3, G4, and G5 are too noisy for a reliable measurement of their redshifts, but we marginally detect a jump at $6500 - 6600$ Å, compatible with a Balmer break at $z \simeq 0.65$. Thus, it appears that these galaxies belong to a group at $z \simeq 0.65$, slightly larger than the previously assumed redshift ($z_{\mathrm{phot}} = 0.6 \pm 0.04$; Oyaizu et al. 2008). For the brightest member of the group, G1, we measure a large velocity dispersion $\sigma = (438 \pm 30)$ km s$^{-1}$, in agreement with the velocity dispersion of the deflector found in the lens model presented in Gavazzi et al. (2011) ($\sigma = 473 \pm 15$ km s$^{-1}$) , indicating that the background sources (both the LBG and the SMG) are lensed by a galaxy group-scale dark matter halo. A more detailed analysis of this group of galaxies, based on recent observations with the Oxford-SWIFT integral-field spectrograph (Thatte et al. 2006), will be presented in Foster et al. (private communication).

Additionally, we serendipitously detected in two of our 1.2″-wide GTC long-slit spectra (PA $= -39°.5$ and 44°) three strong, asymmetric lines that we interpret as Ly$\alpha$ emission at $z = 2.721 \pm 0.001$, $z = 3.145 \pm 0.001$, and $z = 3.327 \pm 0.001$, at 2.37′, 4.35′, and 14″ from the lensing galaxy G1, respectively. Figure 4.11 shows the profiles of the Ly$\alpha$ emission, as well as the coordinates and magnitudes of the associated objects seen in CFHT *R*-band data.

In particular, the broad Ly$\alpha$ emission at $z = 3.327$ (a more detailed analysis of this object is presented in Chapter 4) shows an unusual and unresolved (FWHM $<$ 180 km s$^{-1}$) absorption line at $5281.2 \pm 0.9$ Å (see Figure 4.11, right panel), which is not related to this galaxy. This could be an absorption system at any lower redshift, but surprisingly it is consistent with C II $\lambda\lambda$1334 absorption at $z = 2.9574 \pm 0.0008$,

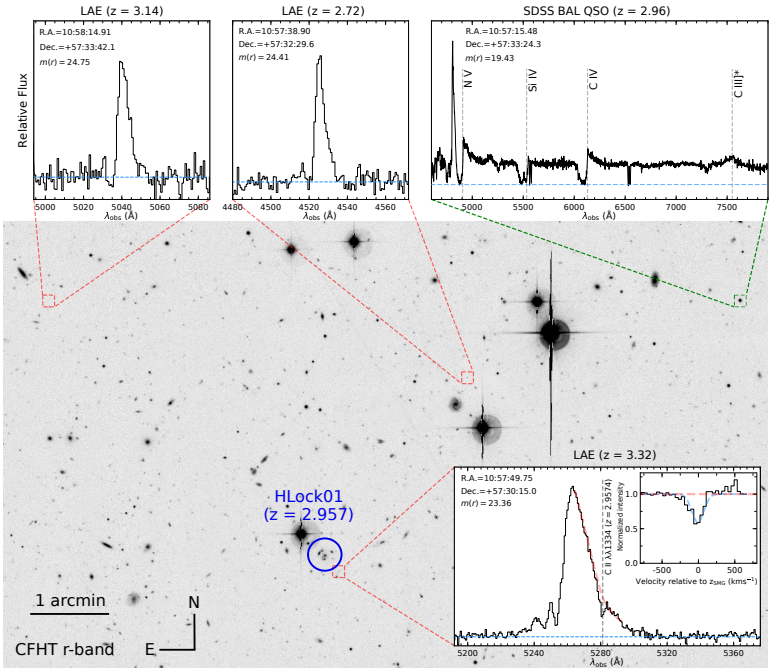


Figure 4.11: CFHT *R*-band showing the spatial distribution of the $z \simeq 2.96$ BAL QSO SDSS J105715.48+573324.3 (top right corner, green dashed square), and three high-redshift galaxies (LAEs) serendipitously detected in two of our GTC long-slit spectra (red dashed squares). The position of HLock01 is marked in blue. The redshift of the Ly$\alpha$ lines, as well as the coordinates and *R*-band magnitudes of the associated objects, are labeled in each panel. In particular, the $z = 3.327$ Ly$\alpha$ emission (bottom right corner) shows an unresolved absorption line at 5281 in its red wing. This absorption is consistent with the low-ionization line C II $\lambda\lambda$1334 at $z = 2.9574 \pm 0.0008$ (inset panel), very close ($\Delta v = -8 \pm 76$ km s$^{-1}$) to the redshift of HLock01-R measured from the molecular gas ($z_{\rm CO} = 2.9574 \pm 0.0001$; Riechers et al. 2011; Scott et al. 2011).

very close ($\Delta v = -8 \pm 76$ km s$^{-1}$) to the redshift of HLock01-R measured from the molecular gas ($z_{\rm CO} = 2.9574 \pm 0.0001$; Riechers et al. 2011; Scott et al. 2011). If this absorption is physically related with HLock01, it may suggest a substantial gas reservoir in its halo, at an impact parameter $b = 110$ kpc.

We also report on a $z = 2.961$ quasar, SDSS J105715.48+573324.3, at 5.5′ NW from HLock01 (see Figure 4.11 at the top right corner). This object was cataloged as a broad absorption line quasar (BAL QSO) by Trump et al. (2006) from the third edition

of the Sloan Digital Sky Survey (SDSS: York et al. 2000) Quasar Catalog (Schneider et al. 2005). The redshift of this BAL QSO is very close to the one of HLock01-R ($\Delta v \simeq 300$ km s$^{-1}$) and is located at a projected distance of 2.5 Mpc.

### 4.6 Lens modeling

In this section we use the high S/N and high spatial resolution *HST*/F110W imaging data to update the lens model already described in Gavazzi et al. (2011). The procedure is identical and uses the dedicated code SL_FIT (for more details see also: Gavazzi et al. 2007, 2008, 2011, 2012). We fit model parameters of simple analytical lensing potentials and model background galaxies as simple elliptical Sérsic profiles. The lensing potential is primarily constrained by the *HST* data, with the highest resolution and S/N. The mass distribution is then held fixed in order to fit for the parameters defining the light distribution in the other channels. We assume the deflector to be made of an isothermal elliptical mass distribution centered on the galaxy G1 and we also include the perturbing galaxies G2, G3 and G4 as point masses centered on the substructure light emission. We allow for the presence of a core radius that softens the inner mass distribution in each case. Unlike in Gavazzi et al. (2011) we do not place masses at G5 and G6, since they have a negligible impact on the mass model and their masses are essentially unconstrained. G1, being by far the most massive galaxy in the vicinity, is assumed to be at the center of the group-scale total mass distribution. The collective effect of a few possible perturbing galaxies 10-20″ South of G1 may induce some external shear, which will contribute to the quadrupole of the mass distribution, but having too few constraints spanning too small a radial range around G1, we assume that the ellipticity of the mass distribution centered on G1 will absorb the total quadrupole. Higher order effects (like $m = 1$ or $m = 3$ multipoles) would also be hard to constrain with the current data.

The lensed features exhibiting a cross-like (or barely fold-like) configuration requires a source relatively close to the optical axis, and thus, relatively far for a widely opened main astroid caustic. We do not expect much magnification nor huge spatial variations of the magnification over the extent of the source. This contrasts with a cusp configuration (see e.g. the cluster MS 0451.6-0305 MacKenzie et al. 2014).

Modeling the *HST* F110W data first, we assume the background source is made of one single elliptical exponential profile for which we adjust source plane position, ellipticity, orientation, effective radius, and flux. Before fitting the lensed light emission, we performed a fit to the foreground light emission (i.e., G1 to G5) in order to subtract it off. The result is shown in the top row panels of Figure 4.12. The formal uncertainty on the recovered Einstein radius (i.e. lens amplitude) is unrealistically small ($\sim 0.2\%$ relative), given the high signal-to-noise ratio of the widely extended lensed images.

However, large-scale structure mass fluctuations along the line of sight, as well as unaccounted for substructures in the lensing mass distribution, should place a lower limit of order 1-2% on the accuracy to which the Einstein radius can be measured. By artificially increasing the pixel rms errors in the F110W imaging data by a factor of 10, we are able to mimic this additional source of noise. As a result, we achieve a one percent accuracy on the recovered Einstein radius as $4\farcs08 \pm 0\farcs05$, consistent with the previous model of Gavazzi et al. (2011). The core radius is found to be $1\farcs1 \pm 0\farcs1$, and the mass distribution is very elongated, with an axis ratio $b/a = 0.38 \pm 0.03$. The total mass of perturbing galaxies is poorly constrained: $M_{\rm G2} = (6.0^{+5.1}_{-4.3}) \times 10^{10} {\rm M}_{\odot}$, $M_{\rm G3} \leq 4.4 \times 10^{10} {\rm M}_{\odot}$, except the case of G4 which induces a splitting of one of the multiple images (B1-B2), yielding $M_{\rm G4} = (9.1^{+6.0}_{-2.6}) \times 10^{10} {\rm M}_{\odot}$. We find a total magnification $\mu = 8.5 \pm 0.5$ in the *HST* F110W band. The formal errors on magnification do not account for the mass-sheet degeneracy (related to a strong assumption about the mass density slope), which is responsible for the differences with the magnification we reported in Gavazzi et al. (2011). Channel-to-channel differential magnifications are, on the other hand, more robust and do not depend on the assumed mass distribution. From the best-fit mass model inferred from *HST* F110W data, we extract for the position, ellipticity, size, and flux of an exponential disk in the GTC, VLA, PdBI CO ($J = 5 \rightarrow 4$), and SMA continuum data. We find magnification factors of $\mu = 8.3 \pm 0.3$ for GTC, $\mu = 8.2^{+0.6}_{-0.8}$ for VLA, $\mu = 9.2 \pm 0.8$ for PdBI CO ($J = 5 \rightarrow 4$), and $\mu = 9.2 \pm 0.5$ for the SMA dust continuum. There is thus little evidence for differential magnification between wavebands.

The output of the modeling in all the channels is shown in Figure 4.12. From top to bottom, each row represents the results of *HST* F110W, GTC $g$ band, 880 $\mu$m SMA, PdBI CO ($J = 5 \rightarrow 4$), and VLA 1.4 GHz observations. The overall aspect does not change much with respect to the model of Gavazzi et al. (2011). The geometry of the source at long wavelengths is poorly determined and the elongated shape of the best-fit sources in the lower panels is not significant. In Figure 4.13 we show the mean positions and ellipses characterizing the galaxy shapes in the source plane for all the channels. Stellar emission in the Optical/NIR is coincident and slightly offset from the mutually coincident VLA, CO, and dust emission. The relative offset between *HST* F110W and VLA in the source plane is $0\farcs42 \pm 0\farcs07$, which corresponds to $3.3 \pm 0.6$ kpc for the adopted cosmology, in line with the results of Gavazzi et al. (2011). The posterior mean shape of long wavelength sources is much less elongated than in the right panels of Figure 4.12

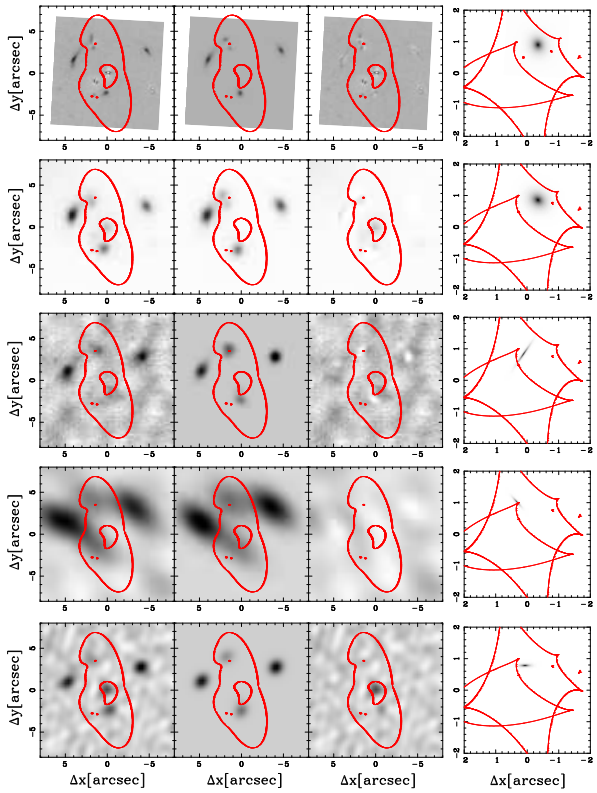


Figure 4.12: Lens inversion results in several bands. Top to bottom: *HST* F110W; GTC $g$ band; 880 $\mu$m SMA; PdBI CO ($J = 5 \rightarrow 4$); and VLA 1.4 GHz observations. From left to right: input image (foreground deflectors are preliminarily subtracted off for *HST*); reconstructed image plane model; residual of input − reconstructed image; and finally the source-plane reconstruction. All the images are centered on the lensing galaxy G1 ($\alpha = +$10:57:50.959, $\delta = +$57:30:25.66, J2000) and oriented such that north is up and east is to the left. At long wavelengths, the limited spatial resolution induces large fluctuations in the shown reconstructed maximum a posteriori sources (right panels), which can get very elongated (see Figure 4.13, for a comparison of more realistic posterior mean sources).

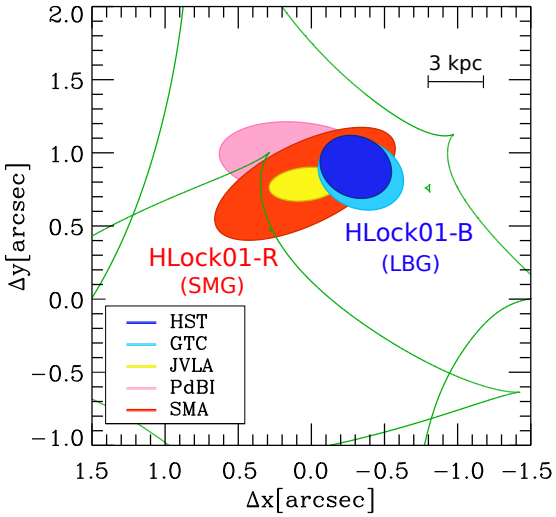


Figure 4.13: Source plane reconstruction of HLock01. The posterior mean effective ellipses of the reconstructed components of HLock01-B (LBG) from *HST* F110W and GTC *g*-band are represented by blue colored ellipses. Pink, yellow and red colored ellipses represent the effective radius of the reconstructed components of CO, VLA and dust emission associated with HLock01-R (SMG), respectively. A relative offset of $0.''42 \pm 0.''07$ is seen between *HST* F110W and VLA, which corresponds to $3.3 \pm 0.6$ kpc. Unlike for the best-fit maximum a posteriori reconstructed source shown in the right panels of Figure 4.12, posterior means are less elongated at long wavelength and their overall orientation is quite consistent between SMA, JVLA and PdBI data.

## 4.7 Physical Properties

### 4.7.1 Broad-band photometry

In addition to the photometry presented in Conley et al. (2011) and Wardlow et al. (2013), we also performed photometry on the new imaging data. These measurements are summarized in Table 4.5.

We use aperture photometry in the *U* band from the corresponding CFHT/MEGACAM catalog, which contains detections of all four lensed images, since the light contamination from the red lensing galaxies is negligible in *U*-band. For GTC *g*-band, we applied aperture photometry on the lensed images A, C, and D. We exclude photometry of the lensed image B, as it is strongly blended with the lens galaxy G4, but we use the lens model to correct for the omitted light from image B (a roughly

15% correction).

Despite the short exposure time of the *HST* F110W data, faint emission is seen close to the radio and submm lensed images A and C (see Figure 4.14). *K*-band imaging from WHT/LIRIS and NIRC2/Keck-II (the latter discussed in Gavazzi et al. 2011; Calanog et al. 2014) also reveal faint emission at these positions. The red color regions in the optical to 2.2 $\mu$m image (seen in Figure 4.14 left panel and Table 4.5) suggest that this faint emission corresponds to the obscured rest-frame UV and optical light of the *Herschel* SMG. Associating this faint emission to HLock01-R, we measure the flux in a small aperture (0.77″ diameter) at the position of the faint near-IR source detected close to the radio and submm lensed image C. For HLock01-B, we use larger apertures ($2'' - 3''$) on the lensed images A, C, and D, and then subtract the contribution of HLock01-R, which in any case is less than 5%. The lens model was used again to add the light from the lensed image B.

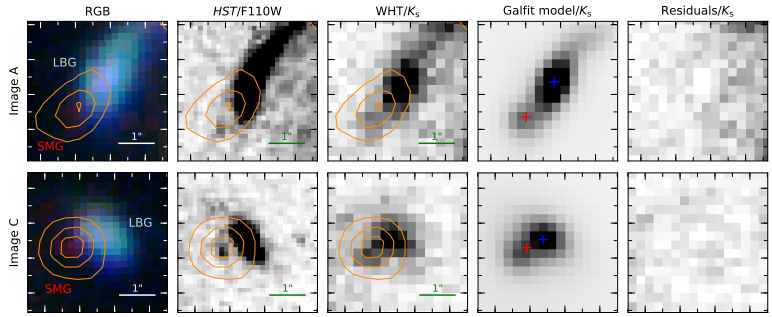


Figure 4.14: $4'' \times 4''$ cutouts of the lensed images A (upper panels) and C (lower panels) of HLock01. From left to right we show: a *g*, *I*, and $K_s$ color image; high-resolution *HST*/WFC3 F110W; near-IR WHT/$K_s$; GALFIT model of the $K_s$ data; and finally the resulting residuals after subtracting the $K_s$ GALFIT model. 1.4GHz VLA contours are in orange and correspond to the positions of two of the lensed images of the *Herschel* SMG. Blue and red crosses mark, respectively, the positions of the LBG and the SMG in our GALFIT model.

Near-IR WHT/$K_s$ photometry of the individual components (SMG and LBG of HLock01) was obtained after modeling the light distribution of each component in the lensed images A and C, using the two dimensional fitting program GALFIT (Peng et al. 2002, 2010). We use Sérsic profiles centered at the centroids of the *HST*/F110W emission, allowing only one pixel freedom ($\simeq 0.254''$). A nearby star was chosen as a point-spread function (PSF) model. Note that we only perform the fit in the lensed images A and C, the only ones that show detections of the faint, obscured counterparts

of the SMG [8]. The lens model of Gavazzi et al. (2011) was used again to add the light from the lensed images B and C. Figure 4.14 shows our GALFIT model, as well as the resulting residuals after subtracting the $K_s$ GALFIT model.

This field has been observed by the SWIRE survey (Lonsdale et al. 2003) in the cryogenic phase of *Spitzer* and to deeper levels in the two first bands of IRAC (3.6 and 4.5$\mu$m) by the SERVS survey (Mauduit et al. 2012) in the post-cryogenic phase. In the *Spitzer* Enhanced Imaging Products (SEIP) catalog[9] of this area (based on the SWIRE data) the individual lensed images A and C are the only ones resolved and detected. However their fluxes appear relatively large and inconsistent ($f_A/f_C \lesssim 1$) with the expected values from the individual magnifications provided by the lens model of Gavazzi et al. (2011) ($f_A/f_C \simeq 1.7$). Given the limited spatial resolution of IRAC ($\simeq 2''$), the cataloged fluxes of the lensed images A and C are likely contaminated by foreground light, mainly due to the G1, G4, and G6 lensing galaxies. To perform better photometry on HLock01, we use GALFIT to model the light distribution of both foreground and background components in the SERVS images (see the results of the modeling in Figure 4.15). We use Sérsic profiles centered at the positions of the detected *HST*/F110W counterparts, and a nearby star was chosen as a PSF model. We then measure the flux density of our best-fit model of the lensed images A and C, and use the lens model to add the expected light from the other lensed images to obtain the total observed flux.

Modeling the light distribution using GALFIT to separate the fluxes from the SMG and the LBG does not help and will introduce significant uncertainties in their measurements, since the spatial separation of the SMG and the LBG in the lensed images A and C is substantially lower ($\simeq 0.9''$) than the intrinsic PSF in IRAC data ($\simeq 2''$ FWHM). Finally, in the 8.0 $\mu$m IRAC band the foreground light contamination appears to be much lower than in the other IRAC bands, thus we use the $3.8''$ aperture photometry for the lensed images A and C provided in the SEIP catalog, with the appropriate aperture corrections. Again we use the lens model to add the expected light of the lensed images B and D.

### 4.7.2 Analysis of the Spectral Energy Distribution

Conley et al. (2011) analyzed the SED of HLock01, considering only a single lensed background source. They simultaneously fitted the emission in the optical/near-IR with longer wavelength data (far-IR and submm), but the fit did not explain the IRAC fluxes and overestimated the $K_p$ and MIPS 70$\mu$m flux densities by a factor of 2 or

[8] This can be explained through the lensed images A and C being less affected by foreground contamination and their lensing magnifications are higher than the ones of images B and D (see Gavazzi et al. 2011).

[9] http://irsa.ipac.caltech.edu/data/SPITZER/Enhanced/SEIP/

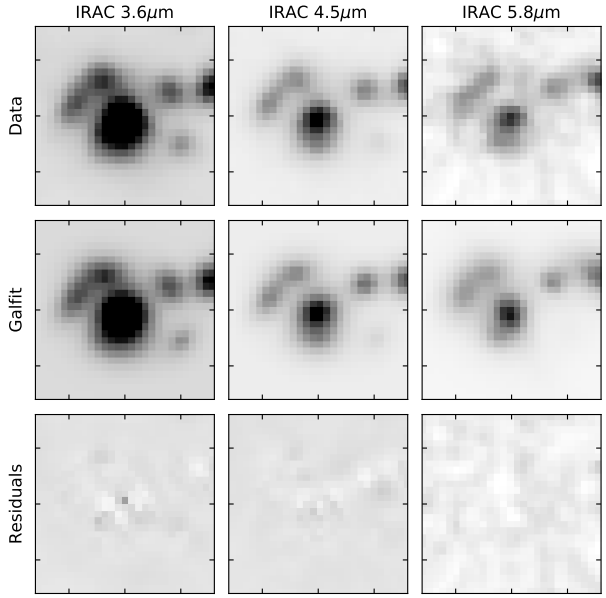


Figure 4.15: $16'' \times 16''$ *Spitzer*/IRAC cutouts of HLock01. From left to right we show the three IRAC channels, I1, I2, and I3, respectively. From top to bottom we show the IRAC data, our best GALFIT model, and the resulting residuals after subtracting the models.

more. We now know that HLock01 is composed of two different, spatially and spectrally offset sources, and thus the energy balance method (between dust-absorbed stellar continuum and the reprocessed dust emission in the far-IR), which was previously invoked, cannot be applied to the integrated photometry by considering a single source. The SEDs of the components are well defined at short (HLock01-B) and long wavelengths (HLock01-R), where these two components dominate, respectively. HLock01-B is very bright in the rest-frame UV and optical, but faint (or undetected) in the current VLA and SMA data. On the other hand, HLock01-R shows a very red and obscured counterpart in the rest-frame UV and optical, but is very bright in the submm. However, to deblend the emission from the two components in the IRAC bands is challenging, given the limitation of the low spatial resolution. The centroids of the bright lensed images A and C seen in the IRAC 3.6 and 4.5 $\mu$m bands are slightly offset ($\simeq 0.7''$) with respect to the bright counterparts in the optical

Table 4.5: Photometry of HLock01.

| Telescope/Detector | $\lambda$ ($\mu$m) | HLock01-B[a] (LBG) | HLock01-R[a] (SMG) | Units |
|---|---|---|---|---|
| CFHT/MEGACAM ($U$) | 0.38 | $8.2 \pm 0.6$ | — | $\mu$Jy |
| GTC/OSIRIS ($g$) | 0.48 | $29.7 \pm 0.8$ | — | $\mu$Jy |
| INT/WFC ($R$) | 0.63 | $46.5 \pm 0.6$ | — | $\mu$Jy |
| Subaru/SuprimeCam ($I$) | 0.76 | $47.9 \pm 0.04$ | — | $\mu$Jy |
| *HST*/F110W | 1.16 | $53.5 \pm 2.5$ | $2.3 \pm 0.6$ | $\mu$Jy |
| WHT/LIRIS ($K_s$) | 2.20 | $60.8 \pm 4.7$[b] | $16.3 \pm 3.8$[b] | $\mu$Jy |
| *Spitzer*/IRAC (I1) | 3.6 | $74 \pm 9$[c] | $82 \pm 9$[d] | $\mu$Jy |
| *Spitzer*/IRAC (I2) | 4.5 | $75 \pm 11$[c] | $113 \pm 11$[d] | $\mu$Jy |
| *Spitzer*/IRAC (I3) | 5.8 | $76 \pm 20$[c] | $219 \pm 20$[d] | $\mu$Jy |
| *Spitzer*/IRAC (I4) | 8.0 | $63 \pm 20$[c] | $341 \pm 20$[d] | $\mu$Jy |
| *Spitzer*/MIPS | 24 | — | $1.24 \pm 0.02$ | mJy |
| *Spitzer*/MIPS | 72 | — | $16.1 \pm 0.3$ | mJy |
| *Spitzer*/MIPS | 160 | — | $244.4 \pm 1.4$ | mJy |
| *Herschel*/SPIRE | 250 | — | $403 \pm 7$ | mJy |
| *Herschel*/SPIRE | 350 | — | $377 \pm 10$ | mJy |
| *Herschel*/SPIRE | 510 | — | $249 \pm 7$ | mJy |
| SMA | 880 | — | $52.8 \pm 0.5$ | mJy |
| CSO/Z-Spec | 1000 – 1100 | — | $27.5 \pm 0.6$ | mJy |
| CSO/Z-Spec | 1100 – 1200 | — | $20.4 \pm 0.5$ | mJy |
| CSO/Z-Spec | 1200 – 1300 | — | $16.2 \pm 0.5$ | mJy |
| CSO/Z-Spec | 1300 – 1400 | — | $12.0 \pm 0.5$ | mJy |
| CSO/Z-Spec | 1400 – 1500 | — | $9.9 \pm 0.6$ | mJy |
| CARMA | 3400 | — | $0.61 \pm 0.19$ | mJy |
| VLA | 214000 | — | $0.97 \pm 0.05$ | mJy |

**Notes.**
[a] Total flux densities of the four lensed components, uncorrected for lensing magnification. [b] Obtained by modeling the light profiles using GALFIT. [c] Expected *Spitzer*/IRAC fluxes of HLock01-B, extrapolated from the best fit SED using flux measurements from 0.38 to 2.20 $\mu$m (see Section 4.7.2). [d] Refers to the difference between the total flux densities measured in Section 4.7.1 (156, 188, 295, and 404 $\mu$Jy for the *Spitzer*/IRAC bands I1, I2, I3, and I4, respectively) and the expected flux densities of HLock01-B from the best-fit SED.

and submm, suggesting a contribution of both to the total flux density in IRAC bands. However, the low Balmer/4000 Å break color (F110W $-$ $K_s = 0.15$ mag) and the small rest-frame UV spectral slope $\beta = -1.9 \pm 0.1$ of HLock01-B, measured from the observed $R$ ($\lambda_{\rm eff} = 6231$ Å) and $I$ ($\lambda_{\rm eff} = 7625$ Å) bands, and assuming a simple power law $F_\lambda = \lambda^\beta$ so that

$$\beta = \frac{\log(f_{\lambda_1}/f_{\lambda_2})}{\log(\lambda_1/\lambda_2)} = \frac{0.4 \times (m_2 - m_1)}{\log(\lambda_1/\lambda_2)} - 2, \tag{4.2}$$

suggest that the contribution of the LBG in the mid-IR is modest compared with the emission from the SMG. Also, typical LBGs are faint in the mid-IR ($S_{24\mu{\rm m}} \simeq 20-30$ $\mu$Jy; Magdis et al. 2010c; Reddy et al. 2012), even those showing a redder UV $\beta$ slope (Reddy et al. 2006; Coppin et al. 2007; Siana et al. 2008, 2009; Reddy et al. 2010; Magdis et al. 2017), which are on average more massive and show larger infrared luminosities.

Additionally, in strong gravitational lensing, the finite extend of one or multiple background sources can lead to significant differential magnification, and their intrinsic properties, derived from photometric or spectroscopic diagnostics, can be incorrect if this effect is not taken into account (e.g., Hezaveh et al. 2012; Serjeant 2012). Of particular importance in treating differential magnification are the cases with multiple background sources with significantly different SEDs and positions in the source plane. Such as an example is the $z \sim 2.9$ gravitational lensed system analyzed in MacKenzie et al. (2014) behind the massive galaxy cluster MS 0451.6-0305. This system consists of several background sources, some of them bright in the UV, and others bright in the far-IR and radio, in a way similar to HLock01. However, in the case of HLock01, the differential magnification appears to be small, since the bulk of the source emission of the LBG and SMG stands relatively far from the caustics without crossing them (see Figure 4.13), and thus changes of magnification as a function of source plane position vary very little. We thus assume, for simplicity, lensing magnifications of $\mu_{\rm HST} = 8.5 \pm 0.5$ and $\mu_{\rm SMA} = 9.2 \pm 0.5$ to be the same in the spectral range in which the LBG and the SMG are well detected, respectively.

We firstly used the SED-fitting code FAST (Fitting and Assessment of Synthetic Templates; Kriek et al. 2009) to derive the stellar population properties of HLock01-B. Optical $U$, $g$, $R$, and $I$, and near-IR F110W and $K_s$ flux measurements were used in this fit. We excluded fluxes from IRAC from this fit, given the uncertainties of the contribution of HLock01-B in these bands. However, the 2.2 $\mu$m $K_s$ band corresponds to rest-frame emission at 5600 Å, above the Balmer/4000 Å break, which is sensitive to the age of the stellar population. We assume stellar population synthesis models of Bruzual & Charlot (2003), the Chabrier (2003) IMF, and an exponentially declining star-formation history ($\propto {\rm e}^{-{\rm t}/\tau}$). We adopt a grid for the age of the stellar population, ranging from 20 Myr to the maximum age of the Universe at

$z \simeq 2.95$, and star-formation histories with $\tau$ between 0.3 and 10 Gyr, both in steps of 0.1 dex. The attenuation curve of Calzetti et al. (2000) was adopted, and the allowed $A_V$ range was $0-3$ mag in steps of 0.05 mag. We also fixed the metallicity to $Z/Z_\odot = 0.4$, the value measured in Section 4.4.3 for the young O and B stars. The best-fit model ($\chi^2/N_{\rm dof} = 1.6/3$) gives an intrinsic (i.e., corrected for the lensing magnification $\mu_{\rm HST} = 8.5 \pm 0.5$ and assumed to be the same in the spectral range in which the LBG is well detected) stellar mass $\log(M_*/{\rm M}_\odot) = 10.1^{+0.3}_{-0.1}$, and an attenuation of the stellar light of $A_V = 0.84^{+0.12}_{-0.25}$, with age $\log({\rm age}_M/{\rm yr}^{-1}) = 7.3^{+0.6}_{-0.0}$. Errors refer to 68% confidence intervals derived using 500 Monte Carlo simulations. After correction for the lensing magnification, the star-formation rate of the best fit model is ${\rm SFR} = 710^{+180}_{-420}\,{\rm M}_\odot{\rm yr}^{-1}$.

We further performed a multi-band SED fit of HLock01-R using the high-$z$ extension of MAGPHYS (Multi-wavelength Analysis of Galaxy Physical Properties; da Cunha et al. 2008, 2015) to explore its SFR, and stellar and dust mass ($M_{\rm d}$). MAGPHYS uses the Bruzual & Charlot (2003) stellar populations with a Chabrier (2003) IMF and assumes the attenuation model of Charlot & Fall (2000). We used the flux measurements from 1.1$\mu$m to radio. In the *Spitzer*/IRAC bands, we used the difference between the total fluxes (measured in Section 4.7.1) and the expected flux of HLock01-B from the best-fit SED, as indicated in Table 4.5. The best-fit model (reduced $\chi^2 = 3.1$) gives a lensing corrected ($\mu_{\rm SMA} = 9.2 \pm 0.5$) stellar mass $\log(M_*/{\rm M}_\odot) = 11.7^{+0.2}_{-0.1}$, a mass weighted age $\log({\rm age_M/yr}) = 8.6 \pm 0.1$, and a large attenuation $A_V = 4.26^{+0.35}_{-0.10}$ mag. We find a dust mass $\log(M_{\rm d}/{\rm M}_\odot) = 8.8 \pm 0.1$, with a dust temperature $T_{\rm d} = (53.6 \pm 0.2)$ K. The uncertainties are derived from the 16th and 84th percentiles. The best-fit SED also yields an intrinsic total infrared luminosity $L_{\rm IR} = (1.5 \pm 0.1) \times 10^{13}{\rm L}_\odot$, which is defined as the luminosity from $8-1000$ $\mu$m in the rest frame. Using the Kennicutt relation (Kennicutt 1998) with a Chabrier IMF (Chabrier 2003), the total infrared luminosity implies a star-formation rate of $1500 \pm 200\,{\rm M}_\odot{\rm yr}^{-1}$. All values were corrected for the lensing magnification derived from the SMA 880$\mu$m data ($\mu_{\rm SMA} = 9.2 \pm 0.5$, see Section 4.6), which for simplicity, we assume to be the same from the observed near-IR to submm bands for HLock01-R.

We followed Delvecchio et al. (2017) and Miettinen et al. (2017) to look for a possible AGN contribution in HLock01-R. We use the three-component fitting code SED3FIT (Berta et al. 2013), which accounts simultaneously for stellar, dust, and AGN emission. However, the stellar and dust components of SED3FIT use the model libraries of da Cunha et al. (2008), rather than the ones used in the new high-$z$ extension of MAGPHYS (da Cunha et al. 2015), which are expected to be better suited for high-$z$ SMGs. We found a poor fit to our data with a $\chi^2 = 15.4$ for the best fit model, which is much higher than the $\chi^2$ of the standard MAGPHYS fit. Nevertheless, the mean AGN contribution to the total $L_{\rm IR}$ was found to be 1%, and less than 20% in the IRAC bands.

Our analysis does not completely exclude the possibility that HLock01-R may harbor an AGN (see also Conley et al. 2011; Riechers et al. 2011; Scott et al. 2011; Magdis et al. 2014, for a discussion of the presence of an AGN in HLock01), but its contribution to the total $L_{\rm IR}$ and $M_*$ is not substantial, as also pointed out by Rigopoulou et al. (2018).

Figure 4.16 shows our best-fit SED models for HLock01-B (FAST) and HLock01-R (MAGPHYS). Our results show that both galaxies are undergoing simultaneous episodes of star-formation activity (unobscured, nearly dust-free in HLock01-B, and dust-enshrouded star formation in HLock01-R), but they are physically very distinct. While HLock01-R is a very massive galaxy with an evolved stellar population, HLock01-B appears to be a young, lower-mass satellite of HLock01-R, as we discuss in the next section.

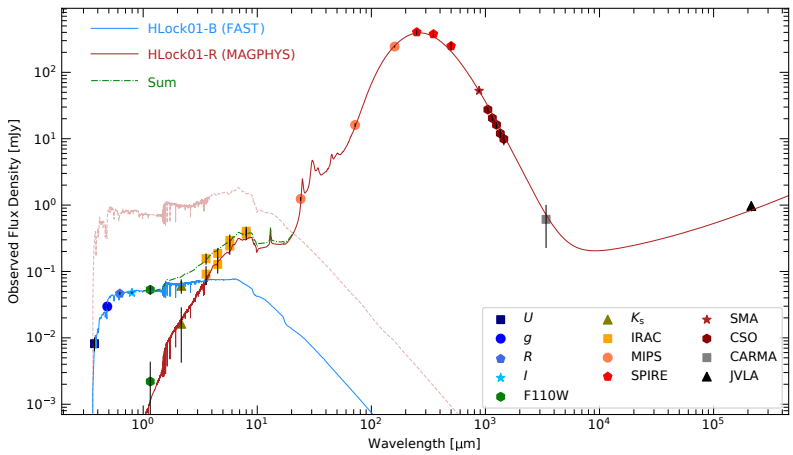


Figure 4.16: Best-fit model of the spectral energy distribution of HLock01-B (LBG, blue solid line) using FAST (Kriek et al. 2009), and HLock01-R (SMG, red solid line) using MAGPHYS (da Cunha et al. 2008, 2015) The LBG fit uses photometry from CFHT $U$ to WHT $K_s$ bands, whereas for the SMG the fit uses photometry from the rest-frame UV (*HST* WFC3 F110W) to radio. We also used the estimated fluxes in the *Spitzer* bands (3.6, 4.5, 5.8, and 8.0 $\mu$m) as explained in the text. The unattenuated SED of the SMG is plotted as a red dashed line.

## 4.8 Discussion

### 4.8.1 Close merger or a large rotational disk?

Our high S/N GTC/OSIRIS spectrum of the optically bright lensed images of HLock01 (HLock01-B) shows several well-defined UV photospheric absorption lines, for which we secured the systemic redshift $z_{\rm sys} = 2.9546 \pm 0.0004$. This value differs by $-210$ km s$^{-1}$ from the redshift of HLock01-R measured from the molecular gas lines $z_{\rm CO} = 2.9574 \pm 0.0001$ (Riechers et al. 2011; Scott et al. 2011). A spatial offset of 3.3 kpc (in projection) has also been found in the source plane between the bulk of the stars that emit at rest-frame UV/optical wavelengths (HLock01-B), and the molecular gas and dust distribution associated with the luminous far-IR emitting source HLock01-R.

Although similar or even larger rotational velocities have been found in massive disk SMGs at high-$z$ (e.g., Carilli et al. 2010; Daddi et al. 2010; Jiménez-Andrade et al. 2017; Jones et al. 2017), a scenario with HLock01-B being a dust-free region, that is part of a large rotational disk of HLock01-R, is unlikely. Such asymmetry in the dust distribution, with the lack of dust attenuation in HLock01-B, would be difficult to explain. Additionally, despite the large errors, the differences in the metallicity measured in the stars of HLock01-B and in the gas of the *Herschel* SMG HLock01-R (Rigopoulou et al. 2018) suggest they are different galaxies with different enrichment histories.

Therefore, bringing together our GTC spectroscopic results and the complex velocity structure seen in the molecular gas reservoir in HLock01-R (Riechers et al. 2011), we argue that HLock01 comprises two close but different sources forming a pair of merging galaxies (HLock01-B and HLock01-R) separated by 3.3 kpc in projection. The merger scenario is also sustained by the broadness of the blueshifted ISM absorption lines seen in the spectrum of HLock01-B, suggesting highly turbulent gas likely produced by the close merger. While HLock01-R appears to be an evolved massive galaxy with a very large obscured star-formation rate, HLock01-B is a young lower-mass satellite galaxy with photometric properties similar to those of LBGs, yet undergoing a young burst ($\gtrsim 6$ Myr) of star formation, likely triggered by the gravitational interaction with the nearby massive SMG.

It is worth mentioning that without the gravitational lensing effect our results could easily be mistaken. Firstly, without the magnification in the apparent flux of HLock01-B, the systemic redshift, measured from faint stellar photospheric lines, would be difficult to obtain. In the absence of strong UV nebular emission lines, as is the case of HLock01-B, a significant continuum S/N is required to detect faint photospheric absorption lines. Secondly, the projected 3.3 kpc spatial offset seen between the two different objects in the source plane would correspond to only $0.4''$ without the lens-

ing distortion, which is challenging to observe due to the limitation on the spatial resolution and sensitivity of current instruments.

It is thus no surprise that most high-$z$ close mergers ($\lesssim$ 10 kpc projected separation) have been discovered through the gravitational lensing effect (e.g., Ivison et al. 2010a; MacKenzie et al. 2014; Messias et al. 2014; Rawle et al. 2014; Wuyts et al. 2014; Spilker et al. 2015; Marrone et al. 2018), with a few exceptions of unlensed, well separated, SMG-SMG, SMG-QSO or SMG-LBG bright interacting pairs resolved with interferometric observations (e.g., Ivison et al. 2002, 2008; Smail et al. 2003; Salomé et al. 2012; Oteo et al. 2016; Lu et al. 2017; Riechers et al. 2017).

### 4.8.2 Outflow/Inflowing gas

Turning to the rest-frame UV spectral features, the internal kinematics of HLock01-B are very complex and different from what is observed in typical LBGs, showing two distinct components of the ISM. The blueshifted component of the ISM is centered at $v_{\rm ISM} \simeq -220$ kms$^{-1}$ relative to the stars, which we associate with galaxy-scale outflows of material via stellar and supernova-driven winds, as seen in many other high-$z$ star-forming galaxies (e.g. Shapley et al. 2003; Steidel et al. 2010). This component is stronger (i.e., larger equivalent widths) in high ionization lines, like Si IV and C IV, similar to what is found in other young, low-metallicity galaxies (e.g., Erb et al. 2010; James et al. 2014). It is also detected in some low-ionization lines, but with a much broader profile (FWHM $\simeq$ 900 kms$^{-1}$) than in typical LBGs ($\simeq$ 560 kms$^{-1}$; Shapley et al. 2003; Steidel et al. 2010), extending over a large velocity range from approximately $-1000$ to $+600$ km s$^{-1}$. We interpret that the width of the blueshifted absorption lines in HLock01-B is the result of a combination of strong winds of massive stars in the LBG and a complex velocity structure due to the close gravitational interaction with the massive SMG.

On the other hand, the redshifted component seen in all strong absorption lines (see Figures 4.5 and 4.6) is highly unusual and not seen in the many high-$z$ galaxies studied (e.g., Shapley et al. 2003; Steidel et al. 2010). This component can be understood as gas apparently moving towards the young stars of HLock01-B, because the absorbing gas must lie in front of the LBG. We relate this component with the large column density of foreground neutral gas ($N$(H I)$= (5.83 \pm 1.24) \times 10^{20}$ cm$^{-2}$) giving rise to the damped Ly$\alpha$ absorption seen in the spectrum of HLock01-B (see Section 4.4.4). The detection of this absorption in both low- and high-ionization ISM lines also suggests that the gas has a broad range of temperatures, from cold, mostly neutral (e.g., O I) to warmer and ionized gas (e.g., Si IV, and C IV).

The origin and nature of the redshifted component seen in all strong absorption lines in the spectrum of HLock01-B is unclear, and with the available data we cannot arrive at a definite conclusion. Interpreting the redshifted component also depends

strongly on the spatial location of the SMG and LBG along our line of sight. The relatively low dust attenuation in HLock01-B ($A_V = 0.8^{+0.1}_{-0.3}$) may suggest that the SMG is located in the background, otherwise the stellar continuum of the LBG would be highly attenuated by the foreground dust content of HLock01-R (see Figure 4.13). Therefore, it is unlikely that the redshifted component is associated with outflows from HLock01-R or rotating gas in its disk seen from the background HLock01-B.

In this sense, the redshifted component could be associated with a dwarf galaxy or a damped Ly$\alpha$ system falling towards HLock01. Gas ejected by a previous episode of star formation or AGN activity in HLock01 would not easily escape its intense gravitational pull. If cooled enough, these reservoirs of gas would provide additional fuel to prolong the star-formation activity (e.g., Davé et al. 2011; Hopkins et al. 2014; Narayanan et al. 2015; Wang et al. 2015; Emonts et al. 2016). Assuming that the gas is dynamically linked and collapsing towards HLock01, it is more likely that the gas is falling into the massive SMG with $v \simeq +170$ km s$^{-1}$, instead of falling to HLock01-B with $v \simeq +370$ km s$^{-1}$, which seems too high for a $10^{10}$ M$_\odot$ galaxy.

Evidence of accretion of cool, metal-enriched gas has been found in only a few spectra of star-forming galaxies at moderately low-$z$ (e.g., Sato et al. 2009; Coil et al. 2011; Rubin et al. 2012; Martin et al. 2012), and is more elusive at high-$z$ (e.g., Bouché et al. 2013; Wiseman et al. 2017) due to the faintness of individual high-$z$ galaxies. Some authors suggest that the low detection rate of infalling gas is due to the geometry and alignment of the streams, which can only be detected in absorption if favorably aligned with our line of sight (Kimm et al. 2011; Martin et al. 2012). Nevertheless, accretion of cold gas, either in the form of cold flows, mergers or recycled gas from stellar feedback, plays an important role in star-formation histories and galaxy growth.

Deriving the metallicity of the inflowing gas could, in principle, rule out some of the possible scenarios. However, higher spectral resolution observations are need to fully resolved the absorption components of the inflowing gas in order to derive chemical abundances (e.g., using the apparent optical depth method).

### 4.8.3 Extended gas reservoir?

We showed in Section 4.5 a detection of an unusual absorption line at $\simeq 5281$ Å in the red-wing of a bright Ly$\alpha$ emission at $z \simeq 3.327$, associated with an object $14''$ SW of HLock01. This absorption is consistent with C II $\lambda\lambda$1334 at $z = 2.9574 \pm 0.0008$, very close by $\Delta v = (-8 \pm 76)$ km s$^{-1}$ to the redshift of HLock01-R measured from the molecular gas ($z_{CO} = 2.9574 \pm 0.0001$). The limited spectral coverage of the Ly$\alpha$ emission line and the faintness of the continuum associated with the $z \simeq 3.327$ galaxy does not let us unambiguously confirm if the absorption line is C II at the redshift of HLock01-R, or a different absorption line system at a lower redshift. If related with HLock01-R, it may suggest a substantial gas reservoir in the halo at an impact

parameter of 110 kpc. It is worth noting that Fu et al. (2016) used QSO absorption line spectroscopy in three high-$z$ SMG-QSO close pairs, with the QSO at a larger redshift than the SMG, to probe the circumgalactic medium (CGM) at similar impact parameters. However, they did not find evidence of optically thick H I gas or strong neutral absorbers in the CGM. Our results suggest that at least massive SMGs, such as HLock01-R, may have prominent cool gas reservoirs in their halos, that could fuel a prolonged star formation phase.

### 4.8.4 Physical Properties

The intrinsic physical properties (corrected for lensing magnification) derived from multiband SED fitting reveal that HLock01-R is a far-IR luminous SMG (as already discussed in earlier papers, e.g., Conley et al. 2011; Wardlow et al. 2013), with an ongoing SFR $\simeq 1500$ $M_{\odot}yr^{-1}$, but yet heavily obscured at short wavelengths. Our new analysis reveals a large, highly obscured stellar mass, similar to the most massive and extreme SMGs during the peak of star formation (e.g., Hainline et al. 2011b; Ma et al. 2015; Schinnerer et al. 2016; Miettinen et al. 2017; Nayyeri et al. 2017). However, as already discussed in Conley et al. (2011) and Wardlow et al. (2013), HLock01-R has a moderately low $q_{\rm IR} = 1.8 \pm 0.4$ (which is the logarithmic ratio of $L_{\rm IR}$ and the rest-frame 1.4GHz flux density), compared with the mean value for HerMES sources ($q_{\rm IR} = 2.40 \pm 0.12$; Ivison et al. 2010b). This may indicate a hidden, radio emitting AGN, but from our SED analysis in Section 4.7.2, we have shown that if HLock01-R harbors an AGN, its contribution to the total $L_{\rm IR}$ and SFR is modest ($\simeq 1\%$), as also noted by Rigopoulou et al. (2018), and even assuming a maximum of 20% of an AGN contribution to the IRAC fluxes, the stellar mass of HLock01-R will be lower only by 0.1 dex, which is within our measurement errors. Moreover, Hayward & Smith (2015) have also shown that the physical properties derived using MAGPHYS are robust even when the AGN contributes 25% of the total UV to IR luminosity. Our deep GTC/OSIRIS rest-frame UV spectroscopy does not show any line or continuum emission at the positions of the lensed images of HLock01-R, as some of them are included in the regions covered by our long-slit spectra (see Figure 4.1, left panel). However, follow-up observations are required to constrain the presence of an AGN in HLock01-R. Nevertheless, even assuming a small AGN contribution, our results show that HLock01-R has already formed the majority of its stellar content, with a gas mass fraction of $f_{\rm gas} \equiv M_{\rm gas}/M_* = 0.07 \pm 0.02$ (for $M_{\rm gas} = 3.3 \times 10^{10}$ $M_{\odot}$, as measured in Riechers et al. 2011), a specific star formation rate $\mathrm{sSFR} \equiv \mathrm{SFR}/M_* = 2.76^{1.22}_{-0.85}$ $\mathrm{Gyr}^{-1}$, and a depletion time scale ($\tau_{\rm d} \equiv M_{\rm gas}/\mathrm{SFR}$) of only 22 Myr (assuming no gas input). Moreover, it is plausible that additional gas input from the ongoing merger and inflows of material from a substantial gas reservoir in the halo will extend the starburst phase of HLock01 for a prolonged time, becoming

an even more massive elliptical galaxy in the local Universe.

On the other hand, HLock01-B appears to be a young, lower-stellar mass galaxy with very different properties than HLock01-R. In the optical, it is one of the brightest gravitationally lensed high-$z$ star-forming galaxies known so far (e.g., Yee et al. 1996; Allam et al. 2007; Belokurov et al. 2007; Smail et al. 2007; Lin et al. 2009; Wuyts et al. 2010; Bayliss et al. 2011; Dahle et al. 2016; Marques-Chaves et al. 2017), with an apparent total magnitude of $R = 19.73 \pm 0.01$. Even after accounting for the magnification produced by the lensing group of galaxies ($\mu_{\rm HST} = 8.5 \pm 0.5$), it is still very luminous in the rest-frame UV with an absolute magnitude $M_{\rm UV} = -23.4$, two and a half magnitudes more luminous than typical LBGs ($L^*_{\rm UV}$) at a similar redshift (Reddy & Steidel 2009). The stellar mass and SFR derived in Section 4.7.2 yield a specific star formation rate of 55 Gyr$^{-1}$, well above the main sequence at that redshift (e.g., Mannucci et al. 2009; Magdis et al. 2010b; Álvarez-Márquez et al. 2016). The nature and properties of this kind of UV ultra-luminous galaxies (i.e., $M_{\rm UV} \lesssim -23$) are still poorly understood, given the lack of examples reported in the literature (e.g., Allam et al. 2007; Bian et al. 2012; Le Fèvre et al. 2013; Ono et al. 2017; Marques-Chaves et al. 2017). This is due in part to the fact that this kind of galaxy is extremely rare, and finding them requires wider-field surveys with deep, multi-band observations. The high UV luminosities also place these sources in the transition between luminous galaxies and faint AGNs, needing either extensive multi-wavelength imaging (e.g., X-ray, mid-IR, and radio) or spectroscopic follow-up. However, we stress that the unusual kinematics of the ISM and its high UV luminosity and SFR are not representative of the $z \sim 3$ LBG population. Our results suggest that the gravitational interaction with the massive SMG may have triggered the larger UV luminosity and SFR. The interaction may also be the origin of the large obscured SFR and far-IR luminosity in the SMG. Despite this, HLock01-B shares many of its properties with the population of $z \sim 3$ LBGs. Its UV colors, $(G-R) \simeq 0.5$, and $(U-G) \simeq 1.4$, are consistent with the standard color selection criteria of $z \sim 3$ LBGs (Steidel et al. 1996, 2003). However, HLock01-B presents $(R-K) = 0.29 \pm 0.07$, bluer than typical $z \sim 3$ LBGs ($(R-K) \simeq 1.0$; Shapley et al. 2001) and Ly$\alpha$ emitting galaxies ($(R-K) \simeq 0.4$; Ono et al. 2010).

Table 4.6 summarizes the main physical properties of both components of HLock01.

## 4.9 Summary and Conclusions

We have presented a detailed study of HLock01, one of the first gravitational lensed sources discovered in the HerMES survey. Unlike other SMGs, HLock01 is apparently very bright in all observed spectral bands, even in the optical. It is magnified

Table 4.6: De-magnified Physical Properties of HLock01.

| Quantity | HLock01-B | HLock01-R | Unit |
|---|---|---|---|
| $z$ | $2.9546 \pm 0.0004$ | $2.9574 \pm 0.0001$ | – |
| $\log(M_*)$ | $10.1^{+0.3}_{-0.1}$ | $11.7^{+0.2}_{-0.1}$ | $\log(M_\odot)$ |
| log(Age) | $7.3^{+0.6}_{-0.0}$ | $8.6 \pm 0.1$ | log(yr) |
| $A_V$ | $0.8^{+0.1}_{-0.3}$ | $4.3^{+0.4}_{-0.1}$ | mag |
| SFR | $710^{+180}_{-420}$ | $1500 \pm 200$ | $M_\odot yr^{-1}$ |
| sSFR | $55^{+14}_{-27}$ | $2.76^{+1.22}_{-0.85}$ | $Gyr^{-1}$ |
| $Z$ | $0.4 \pm 0.1$ | $0.8 \pm 0.2$ | $Z_\odot$ |

by a factor of around 9 by a galaxy group-scale dark matter halo at $z = 0.645$ and comprises four images in the observed plane. We have used OSIRIS on the GTC to secure a high S/N ($\simeq 30$) rest-frame UV spectrum of the optically bright lensed images of HLock01, with an intermediate-resolution ($\simeq 180$ km s$^{-1}$), covering the wavelength interval $1150 - 1950$ Å in the rest-frame. From the analysis of these data together with other existing observations of HLock01, we arrive at the following main results.

1. We measured the systemic redshift of the optically bright lensed images of HLock01 (HLock01-B) $z_{sys} = 2.9546 \pm 0.0004$ using weak stellar photospheric lines. This value is offset by $-210$ km s$^{-1}$ from the redshift measured previously from the molecular gas lines $z_{CO} = 2.9574 \pm 0.0001$ associated with the luminous far-IR source of HLock01 (HLock01-R). Our results show that the dust-obscured, far-IR emitting source HLock01-R, and the optically bright source HLock01-B, are most likely different galaxies undergoing a close merger or an interacting pair separated by only 3.3 kpc in projection.

2. We find a stellar metallicity for the stars in HLock01-B $Z_{stars} \simeq 0.4 Z_\odot$ based on two independent methods: blends of stellar photospheric lines; and P-Cygni profiles from the most luminous O and B stars. This value differs slightly from that measured for the gas in HLock01-R ($0.6 < Z_{gas}/Z_\odot < 1.0$), based on far-IR fine-structure line ratios. A young ($\gtrsim 6$ Myr) starburst model with a Salpeter IMF, stellar masses from 1 to 100 $M_\odot$, and an LMC/SMC metallicity explains well the properties of the high-ionization lines in HLock01-B.

3. The interstellar absorption lines in the spectrum of HLock01-B exhibit two distinct components. One is blueshifted by $-220$ km s$^{-1}$ relative to the stars of

HLock01-B, which we associate with galaxy-scale outflows via stellar and supernovae driven winds. However, it also shows a broader profile (FWHM $\simeq 900$ km s$^{-1}$) than in most star-forming galaxies at $z = 2-3$, indicating highly turbulent kinematics of the outflowing gas likely due to the close merger. This component is stronger in high ionization lines, suggesting that the gas is mostly ionized or the neutral gas has a lower covering factor than the ionized gas.

Another absorption component is seen in the spectrum of HLock01-B, but is redshifted relative to either HLock01-B and HLock01-R by $+370$ and $+170$ km s$^{-1}$, respectively, which can be understood as gas moving towards both galaxies. We relate this component with the strong damped Ly$\alpha$ line seen in HLock01-B, with a column density of $N$(H I)$= (5.83 \pm 1.24) \times 10^{20}$ cm$^{-2}$. Although with the available data we cannot arrive at a definitive conclusion on its nature and origin, we interpret this absorption feature as gas falling towards HLock01-R, which is more massive, with $v \simeq 170$ km s$^{-1}$, but viewed in absorption along a favorable line of sight towards HLock01-B. This component is detected in both low- and high-ionization interstellar lines, but with slightly different absorption line profiles, suggesting that the gas has a broad range of temperatures, and possibly different origin.

4. Three strong and asymmetric Ly$\alpha$ lines at $z = 2.72$, 3.15, and 3.27 were serendipitously detected in two of our GTC long-slit spectra associated with Ly$\alpha$ emitting galaxies at 2.37′ NW, 4.35′ NE, and 14″ SW from the lensing galaxy G1, respectively. In particular, the red wing of the bright Ly$\alpha$ emission at $z \simeq 3.327$ shows an unusual absorption line, that we tentatively associate with C II $\lambda\lambda$1334 at the redshift of HLock01-R. If this absorption is related with HLock01-R and not with an absorbing system at a different redshift, it indicates a substantial gas reservoir in the halo of HLock01 at a projected distance of 110 kpc. Additionally, we report a broad absorption line QSO at a projected distance of 2.5 Mpc from HLock01, with a redshift very close to HLock01-R ($\Delta v \simeq 300$ km s$^{-1}$).

5. Our revised SED fitting with two different galaxies, one very bright in the optical and the other in the far-IR, implies that both are physically very distinct. HLock01-B appears to be a young, lower-mass satellite galaxy of HLock01-R, undergoing an intense episode of star formation activity likely triggered by the interaction. HLock01-R shows an already evolved stellar population, and its high stellar mass in combination with the low gas fraction suggests that the SMG has already assembled most of its stellar mass. However, additional gas input from the satellite galaxy HLock01-B and from the reservoir of gas around HLock01-R may extend the starburst phase of the SMG, eventually forming one of the most massive galaxies in the local Universe.

# 5

# Discovery of a 100 kpc luminous Ly$\alpha$ nebula at $z = 3.33$

This Chapter reports the discovery of a large, extended Ly$\alpha$ nebula at $z = 3.33$ likely associated with a type 2 active galaxy. I present results from follow-up observations using Gran Telescopio Canarias (GTC) OSIRIS medium-band imaging and spectroscopy and derive the main physical properties of this nebula and compare with other Ly$\alpha$ nebulae from the literature.

## 5.1 Introduction

Extended regions of Ly$\alpha$ emission, also called as Ly$\alpha$ blobs (LABs), were initially discovered around high redshift powerful radio sources (Chambers et al. 1990; Heckman et al. 1991a,b). Later on, dedicated narrow-band imaging surveys have discovered similar Ly$\alpha$ nebulae in regions of high galaxy density with no clear association to radio galaxies (e.g., Francis et al. 1996; Fynbo et al. 1999; Keel et al. 1999; Steidel et al. 2000).

These spectacular objects are characterized by high Ly$\alpha$ luminosities ($\sim 10^{+44}$ erg s$^{-1}$) with sizes of up to a few hundred kpc (e.g., Matsuda et al. 2004). Ly$\alpha$ nebulae have been found associated with a diverse population of galaxies, from powerful high-$z$ radio galaxies (HzRGs; e.g., Chambers et al. 1990; Kurk et al. 2002; Reuland et al. 2003; Villar-Martín et al. 2003; Venemans et al. 2007; Villar-Martín et al. 2007a), quasi stellar objects (QSOs; e.g., Heckman et al. 1991a,b; Bunker et al. 2003; Weidinger et al. 2004; Christensen et al. 2006; Cantalupo et al. 2014; Borisova et al.

2016; Arrigoni Battaia et al. 2018), Lyman-break galaxies (LBGs; e.g., Matsuda et al. 2004), and sub-millimetre galaxies (SMGs; e.g., Chapman et al. 2001; Geach et al. 2005; Matsuda et al. 2007; Geach et al. 2014). Many others have been found without any clear galaxy counterpart (e.g, Nilsson et al. 2006), although deep data have revealed that the majority of them are associated with highly obscured active galactic nuclei (type 2 AGNs; e.g, Dey et al. 2005; Geach et al. 2009; Overzier et al. 2013; Hennawi et al. 2015; Ao et al. 2017). For all these reasons, there is a consensus that these extended regions of Ly$\alpha$ emission are expected to occupy the dense dark matter regions of the Universe, tracing large-scale mass overdensities (e.g., Steidel et al. 2000; Matsuda et al. 2004; Prescott et al. 2008; Saito et al. 2015; Cai et al. 2017; Oteo et al. 2018).

There are possible explanations for the origin of circumgalactic Ly$\alpha$ emission. These include (1) photoinization radiation powered by strong UV ionizing sources (e.g., Cantalupo et al. 2005; Geach et al. 2009; Kollmeier et al. 2010), (2) radiation from shock-heated gas, powered by relativistic winds or jets resulting from gas accretion onto supermassive black holes and/or supernovae events (e.g. Taniguchi & Shioya 2000; Villar-Martín et al. 2007a), (3) resonant scattering of Ly$\alpha$ (e.g., Hayes et al. 2011; Cantalupo et al. 2014), and (4) cooling radiation when the gas falls towards galaxies (e.g., Fardal et al. 2001; Dijkstra & Loeb 2009).

In this chapter, I present the discovery of a large ($\sim 110$ kpc) and luminous ($L_{\mathrm{Ly}\alpha} \simeq 6 \times 10^{44}$ erg s$^{-1}$) Ly$\alpha$ nebula at $z = 3.33$, nicknamed "HLock01-LAB" hereafter, close in projection, but physically unrelated to HLock01 discussed in chapter 4. Throughout this chapter, a cosmology with $\Omega_{\mathrm{m}} = 0.274$, $\Omega_{\Lambda} = 0.726$, and $H_0 = 70$ km s$^{-1}$ Mpc$^{-1}$ is adopted. All quoted magnitudes are in the AB system.

## 5.2 Discovery of an Extended Ly$\alpha$ Emission

In section 4.5 of chapter 4 we have reported a serendipitous detection of a bright Ly$\alpha$ emitting region at 5264 Å (i.e. at $z = 3.33$) close to the strong gravitational lensed system HLock01 ($z \simeq 2.95$). The Ly$\alpha$ emission is detected in different spatial positions with two long-slit spectroscopic observations with OSIRIS at GTC (slits #1 and #2 in Figure 5.1) $\simeq 14 - 15''$ SW from HLock01. The approximate locations of the peaks of the Ly$\alpha$ emission at $z = 3.327$ found in slit #1 and #2 are spatially separated by $\sim 2''$ and are marked with circles in Figure 5.1. The total Ly$\alpha$ flux within the two slits is $\simeq 1.8 \times 10^{-15}$ erg cm$^{-2}$ s$^{-1}$, which corresponds to a Ly$\alpha$ luminosity of $\simeq 1.9 \times 10^{+44}$ erg s$^{-1}$ at $z = 3.33$. This Ly$\alpha$ luminosity is much higher ($40 \times L^{*}_{\mathrm{Ly}\alpha}$) than those found in typical Ly$\alpha$ emitting galaxies at similar redshifts ($L^{*}_{\mathrm{Ly}\alpha} \sim 5 \times 10^{+42}$ erg s$^{-1}$, e.g., Ouchi et al. 2008; Sobral et al. 2018a, see also chapters 2 and 3). The Ly$\alpha$ emission seen in two different spatial locations and its large luminosity suggests that this

emission comes from a more extended region, similar to what is found in high-$z$ LABs.

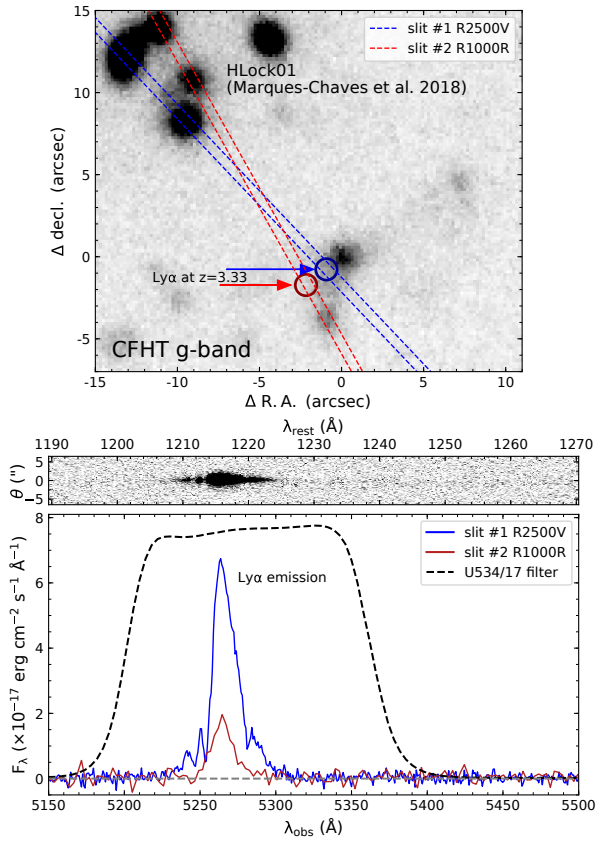


Figure 5.1: Top panel: CFHT $g$-band showing the locations on the sky of the OSIRIS long slits (dashed lines) used in the analysis of HLock01 (chapter 4), and the positions where bright Ly$\alpha$ emission was serendipitously detected (circles). The bright gravitational lensed galaxy HLock01 discussed in chapter 4 is located in the top left corner. Bottom panel: 2D (up, for the slit #1) and 1D (down) spectra encompassing the region of the Ly$\alpha$ emission detected in both long-slit spectra. The dashed line shows the transmission of the SHARDS U534/17 medium-band filter used to measure the extension of the Lya nebula.

## 5.3 Follow-up Observations

### 5.3.1 Ly$\alpha$ imaging with medium-band SHARDS filters

In order to better understand the origin of the Ly$\alpha$ emission seen in two different spatial locations, we obtained OSIRIS deep imaging of the Ly$\alpha$ line using the SHARDS (Pérez-González et al. 2013)[1] medium-band filter U534/17 ($\lambda_{\rm cent} \simeq 5340$ Å; FWHM $\simeq 177$ Å). Additional observations with the consecutive filter, U551/17 ($\lambda_{\rm cent} \simeq 5510$ Å; FWHM $\simeq 138$ Å), were obtained to perform the continuum subtraction of sources not related with the Ly$\alpha$ emission. These observations were obtained in service mode in 2017 April 24 in dark conditions as part of the GTC program GTC61-17A (PI: R. Marques-Chaves). The total exposure time was 3000 and 3750 s for U534/17 and U551/17, respectively, split into 10 individual exposures adopting a $5''$ dither pattern. The registration and combination of the individual images was done using SCAMP (Bertin 2006) and SWARP (Bertin 2010) (see section 3.2.1 of chapter 3 for details). The seeing of the final images was $0.9''$ FWHM.

### 5.3.2 Long-slit spectroscopic observations

We also obtained additional GTC spectroscopic observations of HLock01-LAB. These were carried out in service mode in 2017 May 19 (Program: GTC61-17A). We used the $1.5''$-wide long slit centered on a bright reference star $\simeq 40''$ SE of HLock01-LAB and oriented so as to encompass the brightest region of the Ly$\alpha$ emission, at a sky position angle PA $= -69.9°$. The GTC grism R1000R was used, providing a spectral coverage of $5100 - 10000$ Å. The total exposure time was 4650 s, split into 6 individual exposures of 760 s each. In addition, we obtained a spectrum of the Ly$\alpha$ emission with a wider long-slit ($5.0''$-wide), in an attempt to measure and calibrate the total flux of the Ly$\alpha$ emission. The data were processed with standard IRAF and PYTHON tasks (see again section 3.2.1 for details). Table 5.1 summarizes the new GTC spectroscopic observations.

### 5.3.3 Ancillary data

Since this object lies very close to the HLock01 system (see chapter 4), we use the ancillary data available in this field that was already discussed in the previous chapter. These consist of optical imaging from OSIRIS/GTC ($g$-band), MEGACAM ($r$-band) on the Canada-France-Hawaii Telescope (CFHT), Subaru Telescope ($I$-band), and

[1] https://guaix.fis.ucm.es/~pgperez/SHARDS/

Table 5.1: OSIRIS spectroscopic observations of HLock01-LAB

| Date | Grim | Slit width ($''$) | Time | PA ($^\circ$) | Seeing ($''$) |
|---|---|---|---|---|---|
| 2017 May 19 | R1000R | 1.2 | $6 \times 760$ | $-69.9$ | 0.6 |
| 2017 Feb 03 | R2500V | 5.0 | $3 \times 600$ | $-69.9$ | 0.9 |

near-IR imaging from *Hubble Space Telescope* (*HST*) Wide Field Camera 3 F110W (1.1 $\mu$m), and LIRIS on the William Herschel Telescope (WHT) ($K_s$ 2.2 $\mu$m). We also use mid-IR *Spitzer*/IRAC images and catalogs from the Spitzer Extragalactic Representative Volume Survey (SERVS; Mauduit et al. 2012) and the Spitzer Wide-Area InfraRed Extragalactic survey (SWIRE; Lonsdale et al. 2003). In addition, sub-mm imaging from the Submillimeter Array (SMA) at 880 $\mu$m and radio data from the Very Large Array (VLA) at 1.4 GHz were also used. The details of these data can be found in section 4.3 of chapter 4 and in the references therein.

## 5.4 Analysis

### 5.4.1 Morphology and total flux of the nebula

In Figure 5.2 we show the images of HLock01-LAB in the SHARDS medium-band filters, U534/17 and U551/17, that have similar depths, probing respectively the Ly$\alpha$ + continuum emission and only continuum emission redward of Ly$\alpha$. The U534/17 image shows a clear flux excess due to the strong Ly$\alpha$ emission. We also overplot the GTC/OSIRIS spectral slits.

In the same Figure, the continuum subtracted Ly$\alpha$ image is also shown. We smooth the image using a Gaussian kernel with $\sigma = 1''$, as done in others studies (e.g., Cantalupo et al. 2014; Hennawi et al. 2015; Cai et al. 2017). The Ly$\alpha$ nebula shows an elongated morphology (PA $= -68^\circ$) and extends over $\simeq 11''$ within the $2\sigma$ detection limit.

In Figure 5.3 we show 2D GTC spectra (with the $1.5''$-wide slit) encompassing the regions of the Ly$\alpha$ $\lambda$1215, C IV $\lambda$1548,1550, and He II $\lambda$1640. The integrated Ly$\alpha$ flux above a $3\sigma$ level ($8 \times 10^{-18}$ erg s$^{-1}$ cm$^{-2}$) in the 2D spectrum is detected over a significantly larger region, about $15''$, that at $z = 3.33$ corresponds to $\simeq 110$ kpc. C IV emission appears to have the same extension, although much fainter, whereas He II emission is only detected in the NW component.

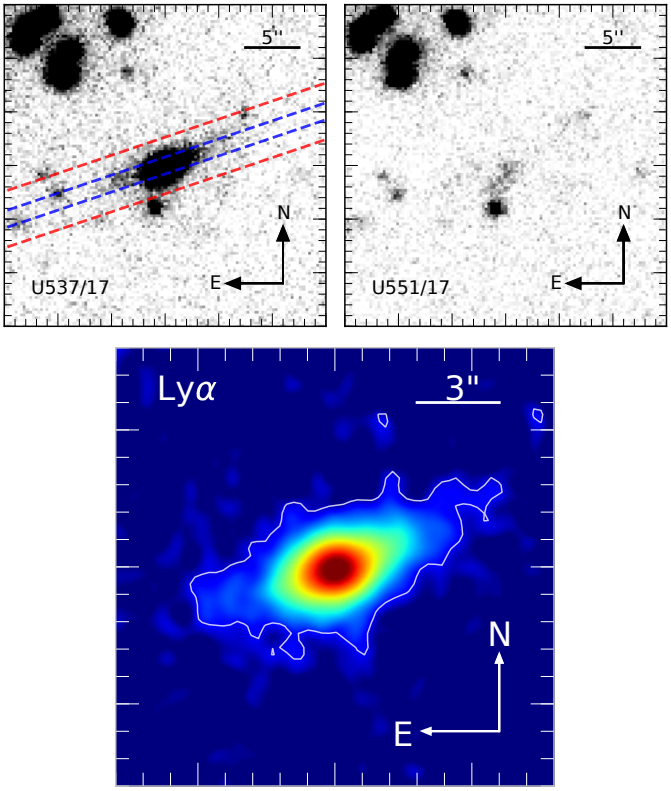


Figure 5.2: Top panel: SHARDS medium-band imaging of the Ly$\alpha$ (U537/17 filter, left) and nearby continuum emission (U551/17 filter, right) of HLock01-LAB. The size of the images is $30'' \times 30''$ centered on the Ly$\alpha$ nebula. The orientation of the long slits are also plotted with dashed lines. Bottom panel: Continuum-subtracted, smoothed (with a Gaussian kernel with $\sigma = 1''$) image of HLock01-LAB ($16'' \times 16''$). The white contour indicates the area above the $2\sigma$ detection limit for the Ly$\alpha$ emission, and it extends over $\simeq 11'' \times 5''$. In all panels, North is up and East is to the left.

Since the SHARDS medium-band filter only probes the high level of the observed surface brightness of the Ly$\alpha$ emission, we use the wide ($5''$, displayed with red dashed lines in Figure 5.2) GTC long-slit spectrum to measure the total Ly$\alpha$ flux. Using a large aperture of $15''$ we measure a total Ly$\alpha$ flux $F_{\mathrm{Ly}\alpha} = (6.04 \pm 0.08) \times 10^{-15}$ erg s$^{-1}$ cm$^{-2}$. At $z = 3.33$ this corresponds to a Ly$\alpha$ luminosity $L_{\mathrm{Ly}\alpha} = (6.00 \pm 0.08) \times 10^{+44}$

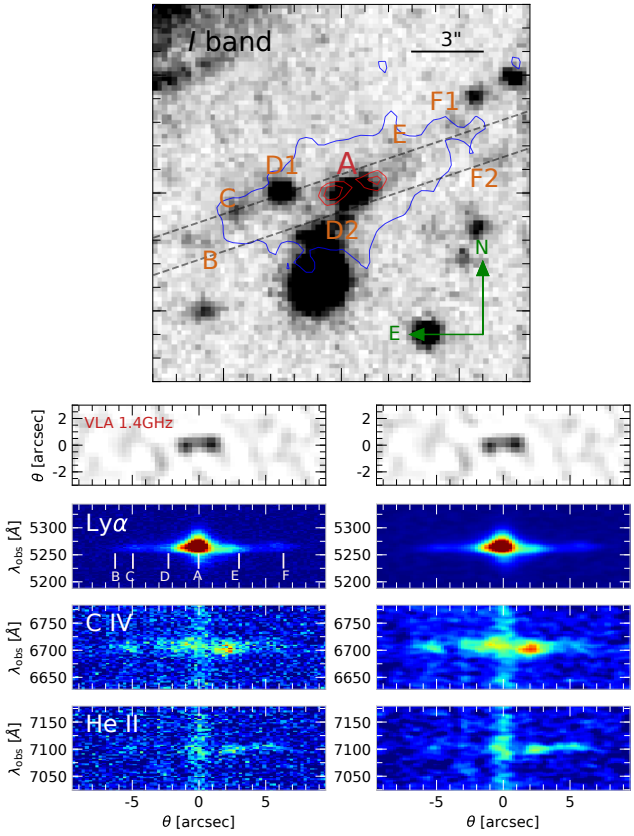


Figure 5.3: Upper panel: Subaru *I* band image ($16'' \times 16''$) with labeled multiply sources (orange) within the $2\sigma$ detection of the Ly$\alpha$ emission (blue contour). VLA 1.4 GHz contours are also plotted in red (3 and $4\sigma$ levels). The orientation of the GTC $1.5''$-wide long slit is also plotted with grey dashed lines. Bottom panels: 2D spectra of Ly$\alpha$ $\lambda$1215 (up), C IV $\lambda$1548,1550 (middle), and He II $\lambda$1640 (down) from the R1000R grism (the right panels show smoothed spectra). Ly$\alpha$ is detected over $\simeq 15''$, which at $z = 3.33$ it corresponds to $\simeq 110$ kpc. C IV emission appears to have the same extension, whereas He II emission is mainly detected in the NW component.

erg $s^{-1}$.

### 5.4.2 The central galaxy: source "A"

**UV spectral properties**

Figure 5.3 shows the Subaru *I* band image in the region of HLock01-LAB. It shows several sources within the Ly$\alpha$ nebula. In particular, the peak of the Ly$\alpha$ emission lies very close ($\simeq 0.6''$), but not coincident, to the source labeled as "A" in Figure 5.3. Source "A" is compact, but is slightly resolved in the ground-based Subaru *I* band and in the high spatial resolution *HST* F110W image. A radial profile fitting with a Gaussian function of source "A" in the *HST* WFC3 F110W image gives a FWHM $\simeq 0.3''$ or $\simeq 2.3$ kpc at $z = 3.33$, after correcting it for the intrinsic F110W point spread function (PSF) FWHM ($\simeq 0.23''$) measured using several stars in the field. Moreover, VLA 1.4 GHz data shows faint emission on both sides of source "A" with similar intensities, with flux densities of $0.136 \pm 0.03$ and $0.139 \pm 0.03$ mJy for the West and East component, respectively, suggestive of faint radio jets or lobes (red contours in Figure 5.3). However, we do not detect any emission in SMA 880 $\mu$m at a significance level $3\sigma = 2.5$ mJy. Following Magnelli et al. (2015), we use the empirical far-IR/radio correlation to study the radio excess in HLock01-LAB. The $q_{\rm IR}$ parameter is defined as:

$$q_{\rm IR} = \log\left(\frac{L_{\rm IR}[{\rm W}]}{3.75 \times 10^{12}}\right) - \log(L_{1.4{\rm GHz}}[{\rm WHz}^{-1}]), \tag{5.1}$$

where $L_{\rm IR}$ is the integrated luminosity from the rest-frame 8 to 1000 $\mu$m, and $L_{1.4{\rm GHz}}$ is the 1.4 GHz radio luminosity. By re-scaling the far-IR spectral energy distribution of ALESS galaxies (da Cunha et al. 2015) to the SMA 880 $\mu$m lower limit, we find a IR luminosity $L_{\rm IR} < 2.1 \times 10^{+12}\ L_{\odot}$ ($3\sigma$) yielding to a $q_{\rm IR} < 1.5$. This suggest a radio excess, indicative of the presence of an AGN (e.g., Ao et al. 2017).

We extract the OSIRIS 1D spectrum of source "A" using the $1.5''$-wide, R1000R long-slit spectrum and a small aperture of 6 pixels in the spatial direction, which corresponds to $\simeq 1.5''$. Figure 5.4 shows the 1D spectrum of source "A". It shows a strong Ly$\alpha$ emission with an observed flux $F^{\rm obs}_{{\rm Ly}\alpha} = (1.69 \pm 0.06) \times 10^{-15}$ erg s$^{-1}$ cm$^{-2}$.

We detect other emission lines, including C IV $\lambda$1548,1550, He II $\lambda$1640, and C III] $\lambda$1906,1908. These lines are much weaker than the Ly$\alpha$ line, with observed fluxes of $F^{\rm obs}_{\rm CIV} = (3.2 \pm 0.4) \times 10^{-17}$, $F^{\rm obs}_{\rm HeII} = (2.8 \pm 0.8) \times 10^{-17}$, and $F^{\rm obs}_{\rm CIII]} = (1.1 \pm 0.4) \times 10^{-17}$ erg s$^{-1}$ cm$^{-2}$, for C IV, He II, and C III], respectively.

The systemic redshift of source "A" is determined from the central wavelength of a Gaussian fit to the He II emission line (we do not use the C IV line, because of its scattering behaviour), yielding a $z_{\rm A} = 3.326 \pm 0.002$. The spectrum does not show emission in N V $\lambda$1240, although we note that the continuum emission of source "A" in this region is barely detected due to the low efficiency of OSIRIS and its R1000R

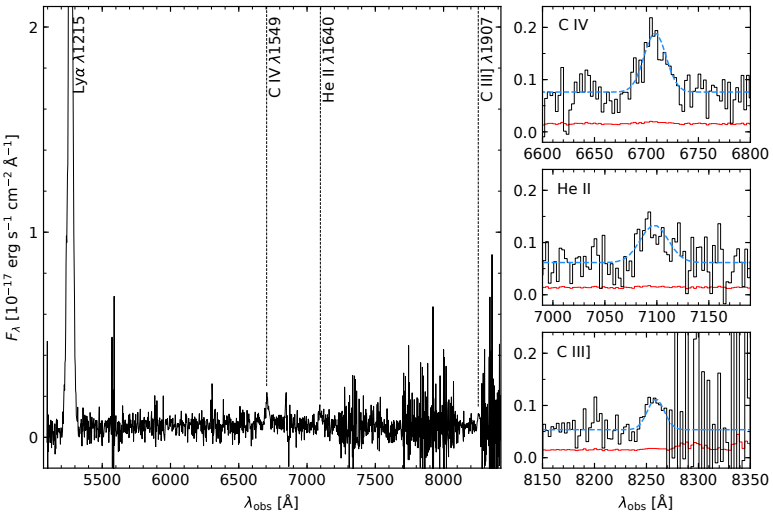


Figure 5.4: Left: OSIRIS/GTC 1D spectrum of source "A". The spectrum shows a strong Ly$\alpha$ line ($F^{obs}_{Ly\alpha} = (1.93 \pm 0.05) \times 10^{-15}$ erg s$^{-1}$ cm$^{-2}$) and faint emission in C IV, He II, and C III] (marked with vertical dashed lines). Right: Gaussian fit (blue dashed lines) to the spectral profiles of C IV, He II, and C III].

grism at short wavelengths.

To gain insight into the physical conditions of the ionized gas traced by C IV, He II, and C III], we use rest-frame UV emission-line diagnostics to identify the source of photoionization (ionization by stars or by AGN). Following Nakajima et al. (2018b), the line ratios of C IV/C III] (C4C3) and (C III]+C IV)/He II (C34) can be used to distinguish star-forming galaxies from AGNs. From our GTC spectrum, we find line ratios of C4C3$= 3.0 \pm 0.7$ and C34$= 1.6 \pm 0.3$. These ratios show that the ionized gas in source "A" is powered by an AGN (see Figure 5.5). Moreover, these lines appear *relatively* narrow with FWHM $\simeq 1000$ km s$^{-1}$, after accounting for the instrumental broadening. Given this, and the weak continuum emission ($m_I = 23.25 \pm 0.08$), source "A" can be classified as a type-II AGN (e.g., Zakamska et al. 2003; Alexandroff et al. 2013).

We also extracted 1D spectra of the NW and SE components of HLock01-LAB. In this case, two large apertures of $\simeq 6.6''$ and $\simeq 6.4''$, separated by $\simeq 0.8''$ of source "A", were extracted along the slit for the NW and SE components, respectively. The line ratios C4C3 and C34, listed in Table 5.2, also show that the extended emission of C IV,

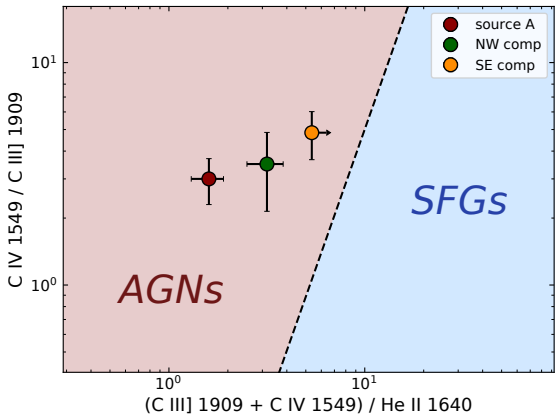


Figure 5.5: Positions of source "A", and NW and SE components of HLock01-LAB in the diagram of C4C3 vs. C34. The line ratios of C IV/C III] (C4C3) and (C III]+C IV)/He II (C34) clearly show that the gas is powered by an AGN.

Table 5.2: Emission-line ratios of HLock01-LAB.

| Components | Aperture ($''$) | Ly$\alpha$/C IV | Ly$\alpha$/He II | (C III]+C IV)/He II (C34) | C IV/C III] (C4C3) |
|---|---|---|---|---|---|
| Source "A" | 1.5 | $53 \pm 3$ | $60 \pm 3$ | $1.6 \pm 0.3$ | $3.0 \pm 0.7$ |
| NW comp. | 6.6 | $10 \pm 1$ | $52 \pm 3$ | $3.2 \pm 0.7$ | $3.5 \pm 1.4$ |
| SE comp. | 6.4 | $7.6 \pm 0.9$ | $> 45$ | $> 5.4$ | $4.8 \pm 1.2$ |

He II, and C III] in the NW and SE components of HLock01-LAB are likely powered by an AGN (Figure 5.5), although the non detection of He II in the SE component cannot rule out photoionization by star formation.

**Multi-wavelength properties**

In Figure 5.6, we show broad-band continuum images in the region of HLock01-LAB, including Subaru *I*, *HST* WFC3 F110W, WHT/LIRIS $K_s$, *Spitzer* IRAC 3.6, 4.5, 5.8, and 8.0 $\mu$m, and MIPS 24 $\mu$m.

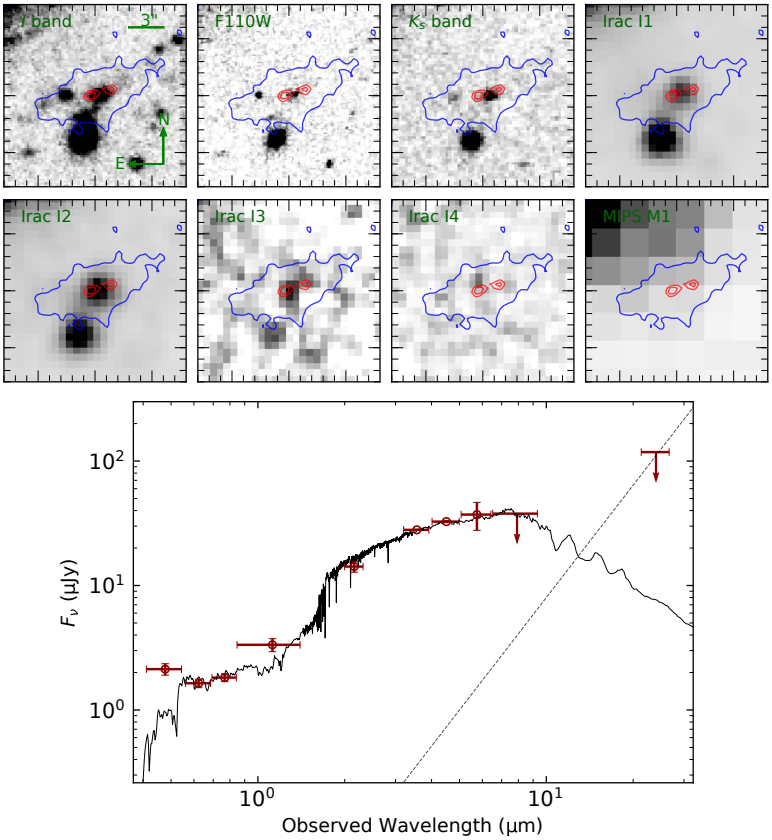


Figure 5.6: Top panel: cutout images ($16'' \times 16''$ centered on the source "A") of HLock01-LAB in the Subaru *I* band, *HST* WFC3 F110W, WHT $K_s$-band, *Spitzer* IRAC 3.6, 4.5, 5.8, and 8.0 $\mu$m, and MIPS 24 $\mu$m. The Ly$\alpha$ emission from the continuum-subtracted SHARDS medium-band image is plotted in blue contour. VLA 1.4 GHz contours are also plotted in red (3 and 4$\sigma$ levels). All images are oriented such as North is up and East is to the left. Bottom panel: best-fit model of the spectral energy distribution of source "A" using FAST (Kriek et al. 2009). The fit uses photometry from CFHT *R* to IRAC 5.8 $\mu$m (see Table 5.2). The non detection in the *Spitzer* IRAC 8.0 $\mu$m and MIPS 24 $\mu$m bands excludes a strong emission from an AGN dusty torus (a power law $F_\nu \propto \nu^\alpha$ with $\alpha = -3$, marked with a dashed line, represents an upper limit of the thermal dust emission; see also: Villar-Martín et al. 2006).

Table 5.3: Photometry of source "A"

| Band | $\lambda_{obs}$ ($\mu$m) | Flux ($\mu$Jy) |
|---|---|---|
| $g$ | 0.48 | $2.1 \pm 0.2$ |
| $R$ | 0.62 | $1.6 \pm 0.1$ |
| $I$ | 0.77 | $1.8 \pm 0.1$ |
| F110W | 1.12 | $3.3 \pm 0.4$ |
| $K_s$ | 2.16 | $14.2 \pm 0.9$ |
| IRAC I1 | 3.6 | $28.0 \pm 0.3$ |
| IRAC I2 | 4.5 | $32.6 \pm 0.6$ |
| IRAC I3 | 5.8 | $37 \pm 9$ |
| IRAC I4 | 8.0 | $\leq 38$ ($5\sigma$) |
| MIPS M1 | 24.0 | $\leq 118$ ($5\sigma$) |
| SMA | 880.0 | $\leq 4100$ ($5\sigma$) |
| VLA | 214000 | $0.28 \pm 0.04$ |

We performed photometry of source "A" using the broad-band imaging data. These measurements are summarized in Table 5.3. We use aperture photometry in the GTC $g$, Subaru $I$, *HST* WFC3 F110W, and WHT $K_s$ bands. To do so, we measure the flux in a small aperture with a diameter of 2.5 the PSF FWHM of each image. For $R$ band, we use the photometry from the corresponding CFHT/MEGACAM catalog downloaded from the Canadian Astronomy Data Centre (CADC[2]). In the *Sptizer* IRAC bands, we use the $3.8''$ aperture photometry provided by the *Spitzer* Enhanced Imaging Products (SEIP) catalog[3], which includes catalogs from deeper imaging in the two first IRAC bands (3.6 and 4.5 $\mu$m), and shallower IRAC (5.8 and 8.0 $\mu$m) and MIPS (24 $\mu$m) imaging from the Spitzer Wide-Area InfraRed Extragalactic survey (SWIRE: Lonsdale et al. 2003). However, source "A" is not detected in the IRAC 8.0 $\mu$m and MIPS 24 $\mu$m bands at $5\sigma$ confidence level, which correspond to upper limits of 38 and 118 $\mu$Jy, respectively.

It is interesting to note that the spectral energy distribution (SED) of source "A" shows a clear rise between optical and IRAC 5.8 $\mu$m, but then falls at longer wavelengths, supported by the 8.0 and 24 $\mu$m upper limits. We thus argue that the emission from the optical to, at least, IRAC 5.8 $\mu$m is dominated by stellar emission of the

[2] 0http://www.cadc-ccda.hia-iha.nrc-cnrc.gc.ca/en/cfht/
[3] 5http://irsa.ipac.caltech.edu/data/SPITZER/Enhanced/SEIP/

galaxy associated with the LAB, rather than a thermal dust contribution of the AGN, otherwise source "A" should be detected in the 8.0 $\mu$m IRAC and 24 $\mu$m MIPS bands.

We then use the SED Fitting and Assessment of Synthetic Templates code (FAST: Kriek et al. 2009) to derive the stellar population properties of source "A". We use in this fit optical *R* and *I*, near-IR F110W and $K_s$, and mid-IR *Spitzer* 3.6, 4.5, and 5.8 $\mu$m flux measurements. We exclude the photometry in the GTC *g* band in this fit, given the large contribution of the Ly$\alpha$ emission to the flux measured in this band.

Similar to the model performed in chapter 4 we assume stellar population synthesis models of Bruzual & Charlot (2003), the Chabrier (2003) initial mass function, and an exponentially declining star formation history (i.e., $\propto e^{-t/\tau}$). We use a grid for the age of the stellar population ranging from 20 Myr to the maximum age of the universe at $z = 3.33$, and star formation histories with $\tau$ between 0.3 and 100 Gyr, both in steps of 0.1 dex. We also use the attenuation curve of Calzetti et al. (2000), and the allowed $A_V$ range was $0-4$ mag in steps of 0.1 mag. We assume that the redshift is the same as the one measured from the LAB emission lines, i.e. $z = 3.326$.

The best-fit model ($\chi^2 = 1.1$, shown in Figure 5.6) gives a stellar mass $\log(M_*/M_\odot) = 11.53^{+0.11}_{-0.01}$, and an attenuation of the stellar emission of $A_V = 0.10^{+0.08}_{-0.0}$, with age $\log(\mathrm{age_M/yr^{-1}}) = 9.1^{+0.1}_{-0.4}$. The star formation rate (SFR) of the best-fit model is found to be $\mathrm{SFR} = 33^{+250}_{-2}\ M_\odot\ \mathrm{yr}^{-1}$. Errors refer to 68% confidence intervals derived using 500 Monte Carlo simulations.

### 5.4.3 Kinematics of the ionized gas

Despite the low spectral resolution of the R1000R grism ($\approx 600$ km s$^{-1}$), the visual inspection of the 2D spectra reveals variations of the kinematics of the gas along, and well beyond the radio structures.

Figure 5.7 shows how the kinematics of the Ly$\alpha$, C IV, and He II emission varies spatially along the slit (we do not show the kinematics of C III] because of the low S/N). The emission lines were fitted with Gaussian profiles using one dimensional spectra extracted from different apertures with widths along the slit of 3 pixels (for Ly$\alpha$ emission) and 6 pixels (for C IV, and He II), which correspond to $\sim 0.76''$ and $1.5''$, respectively. FWHM and velocities are plotted at each location along the slit only where emission lines are detected with significance of $\geq 5\sigma$. Values of FWHM have already been corrected for the instrumental broadening in the form of:

$$\mathrm{FWHM_{intrinsic}} = \sqrt{\mathrm{FWHM^2_{obs}} - \mathrm{FWHM^2_{instrumental}}}, \tag{5.2}$$

where $\mathrm{FWHM_{instrumental}} \simeq 600$ km s$^{-1}$. The velocities refer to the velocities relative to the systemic redshift of source "A" using the He II emission line.

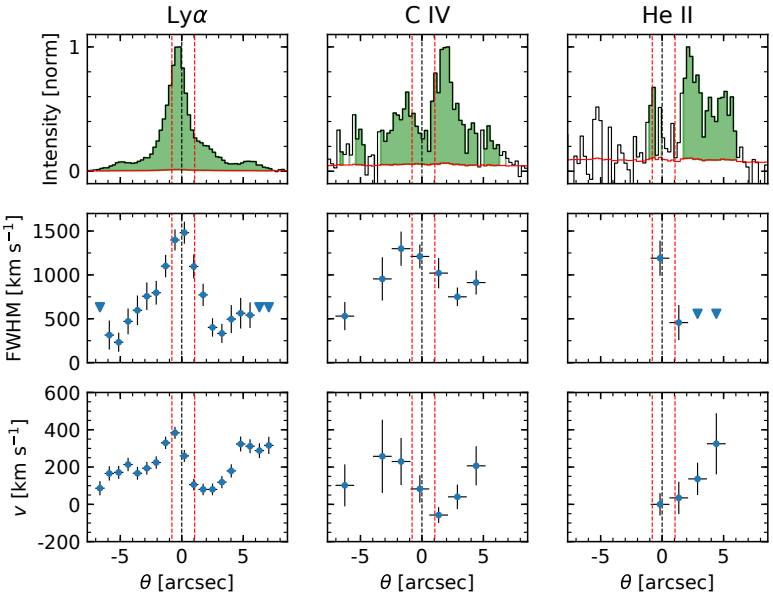


Figure 5.7: Spatial variation of the Ly$\alpha$, C IV, and He II emission lines (left to right, respectively) along the slit (PA $= -69.9$, with $\theta$ being negative/positive for SE/NW, respectively). From top to bottom we show the spatial distribution of the normalized flux, FWHM (already corrected for the instrumental broadening), and the velocity relative to the systemic redshift of source "A". The spatial zero marks the location of source "A", whereas spatial locations of the VLA radio emission components are marked with red dashed lines.

Perturbed kinematics, i.e. FWHM $\gtrapprox 1000$ km s$^{-1}$, are detected almost exclusively in the regions around source "A" (black dashed line) and the VLA radio emission (red dashed lines). At locations far from this region, the emission lines are narrower profiles with FWHM of about 500 km s$^{-1}$.

Turning to the velocities, Figure 5.7 shows a clear change in the relative velocity of Ly$\alpha$ around the central region of HLock01-LAB, roughly around source "A" and the radio emission. The variation in velocity of the Ly$\alpha$ line between the two radio components is $\Delta v \simeq 300$ km s$^{-1}$, from $\simeq 400$ km s$^{-1}$ for the SE component, to 100 km s$^{-1}$ for the NW component. Such kinematic behavior, along with the large FWHM, may suggest that the gas traced by the Ly$\alpha$ emission is expanding in an outflow, with the SE component moving away and the NW component moving towards the observer. C IV appears to share the same kinematic pattern as the Ly$\alpha$ emission in the central

Table 5.4: Properties of HLock01-LAB.

| | Value | Unit |
|---|---|---|
| R.A.$^{a)}$ | 10:57:49.74 | J2000 |
| Dec.$^{a)}$ | +57:30:15.0 | J2000 |
| $z$ | $3.326 \pm 0.002$ | |
| Extension | $\sim 110$ | kpc |
| $L_{\mathrm{Ly}\alpha}$ | $6 \times 10^{+44}$ | erg s$^{-1}$ |
| $L_{\mathrm{IR}}^{a)}$ | $< 2.1 \times 10^{+12}$ | $L_{\odot}$ |
| $M_{*}^{a)}$ | $3.4 \times 10^{+11}$ | $M_{\odot}$ |

**Notes:** $^{a)}$ refers to source "A".

region of the nebula (despite the offset in velocity), although the low signal-to-noise ratio in this line does not allow us to confirm it unambiguously.

## 5.5 Discussion and Conclusions

We have presented the serendipitous discovery of HLock01-LAB, a bright Ly$\alpha$ nebula at $z = 3.326$. Table 5.4 summarizes the main properties of this Ly$\alpha$ nebulae.

HLock01-LAB shows Ly$\alpha$ emission extended over $\simeq 15'' \times 5''$, or $\simeq 110 \times 40$ kpc at $z = 3.3$. The observed Ly$\alpha$ extension should, however, be regarded as a lower limit, since the efficiency of the OSIRIS and the R1000R grism at 5250 Å is roughly 7%, and the exposure times were relatively short. We detect Ly$\alpha$ emission at a significance level of $3\sigma \simeq 2 \times 10^{-17}$ erg s$^{-1}$ cm$^{-2}$, that corresponds roughly to a surface brightness flux of $\mathrm{SB}_{\mathrm{Ly}\alpha} \simeq 1.5 \times 10^{-17}$ erg s$-1$ cm$^{-2}$ arcsec$^{-2}$. However, by comparison with other studies, we expect to find a larger extension if the source is observed with lower limit of surface brightness similar to those achieved in Arrigoni Battaia et al. (2018), Cai et al. (2018), or Ginolfi et al. (2018) with VLT/MUSE and Keck/KCWI deep observations ($\mathrm{SB}_{\mathrm{Ly}\alpha} \sim 2 - 6 \times 10^{-18}$ erg s$^{-1}$ cm$^{-2}$ arcsec$^{-2}$). A more detailed characterization of the real extension, luminosity, and excitation conditions of the gas of HLock01-LAB should be possible with deeper observations with MEGARA[4], the new GTC integral field unit and multi-object spectrograph.

From the GTC wide slit spectroscopic observations, we measured a total Ly$\alpha$ luminosity $L_{\mathrm{Ly}\alpha} = (6.00 \pm 0.08) \times 10^{+44}$ erg s$^{-1}$. In Figure 5.8 we compare the maxi-

[4] http://www.gtc.iac.es/instruments/megara/megara.php

mum projected size of Ly$\alpha$ emission and the total luminosity of HLock01-LAB with a compilation of other giant Ly$\alpha$ nebulae presented in Overzier et al. (2013).[5] This compilation includes LABs (blue diamonds; the majority associated with type-II AGNs; e.g., Overzier et al. 2013), radio-quiet and radio-loud QSOs (green circles and yellow squares, respectively), high-$z$ powerful radio galaxies (black crosses), and Ly$\alpha$ emitters (red pentagons; CR7 and Himiko galaxies Ouchi et al. 2009; Sobral et al. 2015, respectively). The Ly$\alpha$ luminosity places HLock01-LAB as one of the most luminous Ly$\alpha$ nebulae known without strong radio emission.

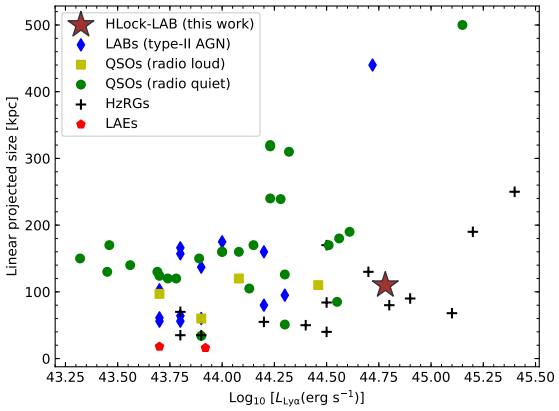


Figure 5.8: Ly$\alpha$ luminosity and maximum projected extension of HLock01-LAB compared to other Ly$\alpha$ nebula (see Overzier et al. 2013, and references therein).

At the center of the nebula, close to the peak of the Ly$\alpha$ emission, there is a massive ($M_* = 3.4 \times 10^{11}\ M_\odot$) galaxy (source "A"), whose emission line spectrum is consistent with excitation by a hidden AGN rather than by star formation. Our deep VLA 1.4 GHz radio data also reveal two faint ($\simeq 0.14$ mJy) sources on both sides of source "A" (at $\simeq 1''$), compatible with radio jets or lobes originated in a central, obscured AGN associated with the massive galaxy "A". However, our multi-wavelength analysis reveals that the AGN within this galaxy presents very weak thermal dust con-

[5] We updated the collection reported in Overzier et al. (2013) with additional giant Ly$\alpha$ nebulae associated with radio-quiet QSOs (Bergeron et al. 1999; Barrio et al. 2008; Cantalupo et al. 2014; Hennawi et al. 2015; Borisova et al. 2016), type-II AGNs (Cai et al. 2017), and Ly$\alpha$ emitters (Ouchi et al. 2009; Sobral et al. 2015).

tribution supported by its non detection in the mid-IR *Spitzer* 8.0 and 24 $\mu$m bands.

It is interesting to note that the Ly$\alpha$ morphology probed by the medium-band SHARDS image is apparently aligned with the radio faint axis. Giant and luminous Ly$\alpha$ nebulae have been found surrounding high-$z$ radio galaxies and, in general, they are often aligned with the radio source axis (e.g., McCarthy et al. 1987, 1995; Villar-Martín et al. 2003, 2007b; Morais et al. 2017). It is well accepted that the interaction between powerful radio structures and the ambient gas may distort the morphological and kinematic properties of the surrounding gas (e.g., Bicknell et al. 2000). Our kinematic analysis of the HLock01-LAB (Figure 5.7) shows that the gas within the radio structures has higher surface brightness and broad FWHM ($> 1000$ km s$^{-1}$), likely as a consequence of jet-gas interactions. Moreover, apart from the perturbed kinematics of the gas, there is a clear change in the velocity of the Ly$\alpha$ emission between the two radio structures, suggesting an outflowing gas (although there are other possible interpretations of the velocity field, such as a rotating gas disk). On the other hand, the gas beyond the radio emission shows low surface brightness with quiescent kinematics with FHWM $\lesssim 500$ km s$^{-1}$ and velocity shifts ($\Delta v \sim 100$ km s$^{-1}$) that could be consistent with gravitational motion around the massive galaxy (e.g., Villar-Martín et al. 2002, 2003).

Despite the general similarities between HLock01-LAB and other giant and luminous Ly$\alpha$ nebulae around powerful HzRGs, such as the alignment of the nebula and the radio structures, its large Ly$\alpha$ luminosity, and the detection of extended emission in metal lines, there are striking differences that should be discussed. First of all, the radio emission seen in HLock01-LAB is much weaker (total flux density $S_{1.4\mathrm{GHz}} = 0.27 \pm 0.04$ mJy) than those found in HzRGs, showing typically very strong radio emission with flux densities up to hundreds of mJy (e.g., Roettgering et al. 1994; De Breuck et al. 2000, 2004). Secondly, Ly$\alpha$ emission has been found beyond the radio structures in some HzRGs (e.g., Maxfield et al. 2002; Villar-Martín et al. 2002, 2003; Humphrey et al. 2008), although the relative extension of the ionized gas and the extremities of the radio structures rarely exceeds a factor of two. In the case of HLock01-LAB, the Ly$\alpha$ emission extends over $\sim 110$ kpc, whereas the radio components are contained within the central $\sim 8$ kpc (although we note this can be due to the low flux limit of our VLA radio data). Moreover, since extended emission in metal lines is also detected, such as in C IV, He II, and C III] the material within the nebula is not primordial. The pressure in the radio jets may have polluted the intergalactic medium with metals. Since these metal lines are detected well beyond the radio structures (over $\simeq 90$, 50, and 35 kpc for C IV, He II, and C III], respectively), our data may indicate that the AGN activity (as well as the radio jets) has been more intense in the past than what we observe today.

# 6

# Conclusions

In this Thesis I have presented a detailed study of the properties of different galaxy populations at $2.3 < z < 3.3$. These include young Ly$\alpha$ emitting galaxies, a very active dust-enshrouded SMG detected with the *Herschel Space Observatory*, and a giant and luminous Ly$\alpha$ nebula. Given the typical faintness of these high-$z$ galaxies, I have employed the strong gravitational lensing effect in high signal-to-noise (S/N) studies, with particular emphasis on their rest-frame UV properties. The Thesis presented here highlights the power of gravitational lensing in probing deeply into the physics of high-$z$ star-forming galaxies in the epoch of the Universe when the star formation rate density reaches its peak.

## 6.1 Summary of the main results

**BELLS GALLERY Ly$\alpha$ emitting galaxies**

We tackled our work to search for strong gravitationally lensed Ly$\alpha$ emitting galaxies from the BELLS GALLERY survey. This survey consists in the search for secondary and asymmetric emission lines, i.e. redshifted Ly$\alpha$ emission, in a sample of $\sim 1.5 \times 10^6$ optical spectra of massive early type galaxies at $z \sim 0.5$ obtained with the 2.5m Sloan telescope.

In addition, in chapters 2 and 3 I report the discovery of two very bright ($R \simeq 20-21$, AB) lensed LAEs with large image separations ($> 4.5''$), BG1429+1202 and BG1501+3042. The lensing nature of these systems were confirmed with imaging and spectroscopic observations with the GTC and WHT, and the main properties of both the background lensed LAEs and the lensing galaxies were derived. Our principal

conclusions are as follows.

- BG1429+1202 is a quadruply lensed LAE at $z = 2.824$, magnified by an early type galaxy at $z = 0.552$. This LAE is one of the brightest galaxy-scale lensed LAE known so far at any redshift, and even accounting for the lensing magnification ($\mu \simeq 9$) it is intrinsically very luminous in the rest-frame UV and Ly$\alpha$ by about 19 and 5 times the typical $L^*_{\rm UV}$ and $L^*_{\rm Ly\alpha}$ of LAEs at similar redshifts.
- BG1501+3042 is a $z = 2.643$ LAE lensed by a $z = 0.638$ early type galaxy producing a magnification of $\simeq 6$. This LAE presents an uncommon lensing configuration showing three lensed images in the image plane. Our results show that a possible sub-halo of dark matter with $M \sim 3 \times 10^9 M_\odot\ h^{-1}$ in the outer part of the early type galaxy ($\simeq 3.8''$ SE, or $\simeq 25$ kpc at $z = 0.638$) is likely responsible for this odd lensing configuration, splitting the brightest lensed image in two pieces (A and B, see Figure 3.3).

Then, in chapter 3, I presented the results of the first detailed study of this new type of strong galaxy-scale lenses. To do so, we have carried out imaging and spectroscopic observations with the GTC and WHT of six BELLS GALLERY LAEs. We arrive at the following main results.

- These LAEs span a wide range of UV and Ly$\alpha$ luminosities, $M_{\rm UV} \simeq -20$ to $-23$ (AB) and $L_{\rm Ly\alpha} \simeq (0.1 - 2.8) \times 10^{+43}$ erg s$^{-1}$. Our spectral and morphological analysis show that these LAEs are purely star-forming galaxies without any evidence for an AGN.
- Some of them show prominent star formation rates, up to 110 $M_\odot$ yr$^{-1}$, despite their low dust content. We show that purely star forming LAEs have luminosities brighter than $M_{\rm UV} < -21.5$ (AB) and $L_{\rm Ly\alpha} > 2 \times 10^{+43}$ erg s$^{-1}$ without appeal to an AGN component, as opposed to the recent claim by Sobral et al. (2018b) that all UV- and/or Ly$\alpha$-bright galaxies are AGNs.
- We determined the systemic redshifts of these LAEs by measuring nebular emission from H II regions, stellar absorption from the photospheres of massive stars, or fine-structure emission lines. We showed that fine-structure emission lines can also be used to recover the systemic redshift of a galaxy with uncertainties lower than 100 km s$^{-1}$ when observed with significant spectral resolution.
- Our kinematic analysis shows that the profiles of the ISM absorption lines in luminous LAEs are more blueshifted (up to 200 km s$^{-1}$) than in low luminosity LAEs. These results evidence that LAEs with large star formation rates present stronger outflows due to the radiation pressure of the most luminous and massive stars.

- These LAEs show Ly$\alpha$ escape fractions of $7-30\%$. However, we found that for some of these LAEs, the spatial Ly$\alpha$ spatial distribution presents different structure than the rest-frame UV continuum.

**The Herschel-selected Submillimeter Galaxy HLock01**

In chapter 4 I presented a detailed study of one of the first and brightest gravitational lensed sources discovered in the HerMES survey, the SMG HLock01 at $z = 2.957$. Our results, based on the highest S/N spectroscopic studies of this type of galaxies performed so far, show that:

- HLock01 is a merger system composed of the *Herschel*-selected SMG and an optically bright LBG, separated by only 3.3 kpc in projection. While the SMG appears very massive ($M_* = 5 \times 10^{11} M_\odot$), with a highly extinguished stellar component ($A_V = 4.3$), the LBG is a young, lower-mass ($M_* = 1 \times 10^{10} M_\odot$), but still luminous ($10 \times L^*_{\rm UV}$) satellite galaxy.
- The spectrum of the LBG shows complex kinematics of the gas, exhibiting both blueshifted and redshifted absorption components. While the blueshifted component is associated with strong galactic outflows from the massive stars in the LBG, as is common in most star-forming galaxies, the redshifted component may be associated with gas inflow seen along a favorable sightline to the LBG. These results are one of the first observational confirmations[1] that gas accretion, along with on-going mergers, are the main mechanisms responsible for such extremely large SFRs seen in many SMGs such as HLock01 (SFR $= 1500 \pm 200$ $M_\odot {\rm yr}^{-1}$), as suggested by simulations (e.g., Narayanan et al. 2015).
- We also find evidence of an extended gas reservoir around HLock01 at an impact parameter of 110 kpc, through the detection of C II $\lambda$1334 absorption in the red wing of a bright Ly$\alpha$ emission line from a Ly$\alpha$ nebula at $z = 3.325$.

**Ly$\alpha$ nebula HLock01-LAB**

Finally, in chapter 5 I have presented the serendipitous discovery and first analysis of a large, extended Ly$\alpha$ nebula at $z = 3.325$. Our principal results are as follows.

- The nebula shows Ly$\alpha$ emission extended over 110 kpc with a total luminosity $L_{{\rm Ly}\alpha} = (6.00 \pm 0.08) \times 10^{+44}$ erg s$^{-1}$. It also shows extended emission of

[1] At the time of writing this Thesis Falgarone et al. (2017) also found evidence of inflowing gas in two gravitational lensed SMGs, through the detection of redshifted methylidyne cation ($CH^+$) absorption lines in the far-IR.

C IV $\lambda$1548,50, He II $\lambda$1640, and C III] $\lambda$1906,08 over $\sim$ 90, 50, and 35 kpc, respectively.

- The origin of the nebula is likely associated with a massive ($M_* = 3.4 \times 10^{11} M_\odot$) type 2 active galaxy that shows two faint radio lobes or jets contained within the central $\sim$ 8 kpc. The jet-gas interaction in the central region of the nebula may explain the very perturbed kinematics of the gas, with FWHM $> 1000$ km s$^{-1}$.

- The pressure of the radio jets may have polluted the intergalactic medium with metals. However, C IV, He II, and C III] are also detected well beyond the radio structures, suggesting that we are only probing the brightest part of the radio emission, or that the AGN activity has been more intense in the past than the currently observed fluxes, supported by the non detection of strong emission from an AGN dusty torus.

## 6.2 Future Perspectives

The BELLS GALLERY is the first, and still unique, dedicated survey aimed to search for strong gravitational lensed systems with LAEs as background sources. Considering the high success rate (80%) of finding strong gravitational lenses in the 21 BELLS GALLERY LAEs observed with the *HST*, we expect more than 100 galaxy-LAE lens systems among the remaining 166 candidates from the parent sample. Such examples are the two lensed LAEs discovered and analyzed in this Thesis, BG1429+1202 and BG1501+3042, that are among the brightest LAEs known so far. Therefore, observational efforts should be made in the follow-up of these systems, preferentially in the entire sample, to confirm their lensing nature and to perform high S/N studies of their properties by using, e.g., multi-band optical imaging in good seeing conditions, with adaptive optics instruments, or additional *HST* observations.

In the near future, many aspects of LAEs properties can be studied with additional follow-up observations. Given the faintness of typical high-$z$ LAEs, the strong magnification in the BELLS GALLERY LAEs ($< \mu > \sim 13$ on average) offers a rare opportunity to study individually each LAE in a broad spectral range, from the rest-frame UV to the far-IR and sub-mm. For instance, the spatial distribution of the Ly$\alpha$ emission can be studied with narrow-band imaging or IFU spectroscopic observations (see an example in Figure 3.12). Complementary optical/near-IR imaging and spectroscopy can also be used to study the kinematics of the ISM, the properties of the ionized gas, and to infer other global properties of these galaxies, such as stellar masses, star formation rates, and star formation histories through spectral energy distribution fitting. Moreover, far-IR and sub-mm follow-up observations with ALMA, NOEMA,

or SMA may probe the dust and molecular gas content in this young star-forming galaxies, and derive quantities such as dust masses and IR luminosities, important to determine total SFRs and Ly$\alpha$ escape fractions.

# List of Figures

# List of Tables

# Bibliography

Ahn, C. P., Alexandroff, R., Allende Prieto, C., et al. 2012, ApJS, 203, 21

Ajiki, M., Taniguchi, Y., Fujita, S. S., et al. 2003, AJ, 126, 2091

Alaghband-Zadeh, S., Chapman, S. C., Swinbank, A. M., et al. 2012, MNRAS, 424, 2232

Alexandroff, R., Strauss, M. A., Greene, J. E., et al. 2013, MNRAS, 435, 3306

Allam, S. S., Tucker, D. L., Lin, H., et al. 2007, ApJ, 662, L51

Álvarez-Márquez, J., Burgarella, D., Heinis, S., et al. 2016, A&A, 587, A122

Amorín, R., Fontana, A., Pérez-Montero, E., et al. 2017, Nature Astronomy, 1, 0052

Antonucci, R. 1993, ARA&A, 31, 473

Antonucci, R. R. J., & Miller, J. S. 1985, ApJ, 297, 621

Ao, Y., Matsuda, Y., Henkel, C., et al. 2017, ApJ, 850, 178

Arrigoni Battaia, F., Prochaska, J. X., Hennawi, J. F., et al. 2018, MNRAS, 473, 3907

Asboth, V., Conley, A., Sayers, J., et al. 2016, MNRAS, 462, 1989

Baker, J. G., & Menzel, D. H. 1938, ApJ, 88, 52

Barger, A. J., Cowie, L. L., Sanders, D. B., et al. 1998, Nature, 394, 248

Barrio, F. E., Jarvis, M. J., Rawlings, S., et al. 2008, MNRAS, 389, 792

Basu-Zych, A. R., Hornschemeier, A. E., Hoversten, E. A., Lehmer, B., & Gronwall, C. 2011, ApJ, 739, 98

Bayliss, M. B., Hennawi, J. F., Gladders, M. D., et al. 2011, ApJS, 193, 8

Bayliss, M. B., Rigby, J. R., Sharon, K., et al. 2014, ApJ, 790, 144

Belokurov, V., Evans, N. W., Moiseev, A., et al. 2007, ApJ, 671, L9

Benn, C., Dee, K., & Agócs, T. 2008, in Proc. SPIE, Vol. 7014, Ground-based and Airborne Instrumentation for Astronomy II, 70146X

Bergeron, J., Petitjean, P., Cristiani, S., et al. 1999, A&A, 343, L40

Berta, S., Lutz, D., Santini, P., et al. 2013, A&A, 551, A100

Bertin, E. 2006, in Astronomical Society of the Pacific Conference Series, Vol. 351, Astronomical Data Analysis Software and Systems XV, ed. C. Gabriel, C. Arviset, D. Ponz, & S. Enrique, 112

Bertin, E. 2010, SWarp: Resampling and Co-adding FITS Images Together, Astrophysics Source Code Library, ascl:1010.068

Bertin, E., & Arnouts, S. 1996, A&AS, 117, 393

Bian, F., Fan, X., Jiang, L., et al. 2012, ApJ, 757, 139

Bicknell, G. V., Sutherland, R. S., van Breugel, W. J. M., et al. 2000, ApJ, 540, 678

Blain, A. W., Smail, I., Ivison, R. J., Kneib, J.-P., & Frayer, D. T. 2002, Phys. Rep., 369, 111

Bolton, A. S., Burles, S., Koopmans, L. V. E., et al. 2008a, ApJ, 682, 964

Bolton, A. S., Burles, S., Koopmans, L. V. E., Treu, T., & Moustakas, L. A. 2006, ApJ, 638, 703

Bolton, A. S., Burles, S., Schlegel, D. J., Eisenstein, D. J., & Brinkmann, J. 2004, AJ, 127, 1860

Bolton, A. S., Treu, T., Koopmans, L. V. E., et al. 2008b, ApJ, 684, 248

Bom, C. R., Makler, M., Albuquerque, M. P., & Brandt, C. H. 2017, A&A, 597, A135

Bond, N. A., Gawiser, E., Gronwall, C., et al. 2009, ApJ, 705, 639

Bond, N. A., Gawiser, E., Guaita, L., et al. 2012, ApJ, 753, 95

Borisova, E., Cantalupo, S., Lilly, S. J., et al. 2016, ApJ, 831, 39

Bouché, N., Murphy, M. T., Kacprzak, G. G., et al. 2013, Science, 341, 50

Bournaud, F., Perret, V., Renaud, F., et al. 2014, ApJ, 780, 57

Bouwens, R. J., Illingworth, G. D., Franx, M., & Ford, H. 2007, ApJ, 670, 928

Bouwens, R. J., Illingworth, G. D., Oesch, P. A., et al. 2011, ApJ, 737, 90

Bouwens, R. J., Oesch, P. A., Illingworth, G. D., et al. 2013, ApJ, 765, L16

Bouwens, R. J., Bradley, L., Zitrin, A., et al. 2014, ApJ, 795, 126

Bouwens, R. J., Illingworth, G. D., Oesch, P. A., et al. 2015, ApJ, 803, 34

Bridge, C. R., Appleton, P. N., Conselice, C. J., et al. 2007, ApJ, 659, 931

Brinchmann, J., Pettini, M., & Charlot, S. 2008, MNRAS, 385, 769

Brownstein, J. R., Bolton, A. S., Schlegel, D. J., et al. 2012, ApJ, 744, 41

Bruzual, G., & Charlot, S. 2003, MNRAS, 344, 1000

Bunker, A., Smith, J., Spinrad, H., Stern, D., & Warren, S. 2003, Ap&SS, 284, 357

Burgarella, D., Pérez-González, P. G., Tyler, K. D., et al. 2006, A&A, 450, 69

Bussmann, R. S., Pérez-Fournon, I., Amber, S., et al. 2013, ApJ, 779, 25

Cabanac, R. A., Valls-Gabaud, D., Jaunsen, A. O., Lidman, C., & Jerjen, H. 2005, A&A, 436, L21

Cabanac, R. A., Valls-Gabaud, D., & Lidman, C. 2008, MNRAS, 386, 2065

Cabanac, R. A., Alard, C., Dantel-Fort, M., et al. 2007, A&A, 461, 813

Cai, Z., Fan, X., Yang, Y., et al. 2017, ApJ, 837, 71

Cai, Z., Hamden, E., Matuszewski, M., et al. 2018, ArXiv e-prints, arXiv:1803.10781

Calanog, J. A., Fu, H., Cooray, A., et al. 2014, ApJ, 797, 138

Calzetti, D., Armus, L., Bohlin, R. C., et al. 2000, ApJ, 533, 682

Cantalupo, S., Arrigoni-Battaia, F., Prochaska, J. X., Hennawi, J. F., & Madau, P. 2014, Nature, 506, 63

Cantalupo, S., Porciani, C., & Lilly, S. J. 2008, ApJ, 672, 48

Cantalupo, S., Porciani, C., Lilly, S. J., & Miniati, F. 2005, ApJ, 628, 61

Capak, P., Carilli, C. L., Lee, N., et al. 2008, ApJ, 681, L53

Carilli, C. L., Daddi, E., Riechers, D., et al. 2010, ApJ, 714, 1407

Casey, C. M., Narayanan, D., & Cooray, A. 2014, Phys. Rep., 541, 45

Casey, C. M., Cooray, A., Killi, M., et al. 2017, ApJ, 840, 101

Cassata, P., Le Fèvre, O., Charlot, S., et al. 2013, A&A, 556, A68

Chabrier, G. 2003, ApJ, 586, L133

Chambers, K. C., Miley, G. K., & van Breugel, W. J. M. 1990, ApJ, 363, 21

Chapman, S. C., Blain, A. W., Smail, I., & Ivison, R. J. 2005, ApJ, 622, 772

Chapman, S. C., Lewis, G. F., Scott, D., et al. 2001, ApJ, 548, L17

Chapman, S. C., Smail, I., Blain, A. W., & Ivison, R. J. 2004, ApJ, 614, 671

Charlot, S., & Fall, S. M. 2000, ApJ, 539, 718

Chisholm, J., Tremonti, C. A., Leitherer, C., & Chen, Y. 2017, MNRAS, 469, 4831

Christensen, L., Jahnke, K., Wisotzki, L., & Sánchez, S. F. 2006, A&A, 459, 717

Chu, Z., Li, G. L., Lin, W. P., & Pan, H. X. 2016, MNRAS, 461, 4466

Coil, A. L., Weiner, B. J., Holz, D. E., et al. 2011, ApJ, 743, 46

Conley, A., Cooray, A., Vieira, J. D., et al. 2011, ApJ, 732, L35

Conti, P. S., Leitherer, C., & Vacca, W. D. 1996, ApJ, 461, L87

Coppin, K. E. K., Swinbank, A. M., Neri, R., et al. 2007, ApJ, 665, 936

Cornachione, M. A., Bolton, A. S., Shu, Y., et al. 2018, ApJ, 853, 148

Cowie, L. L., & Hu, E. M. 1998, AJ, 115, 1319

Curtis-Lake, E., McLure, R. J., Dunlop, J. S., et al. 2016, MNRAS, 457, 440

da Cunha, E., Charlot, S., & Elbaz, D. 2008, MNRAS, 388, 1595

da Cunha, E., Walter, F., Smail, I. R., et al. 2015, ApJ, 806, 110

Daddi, E., Dickinson, M., Morrison, G., et al. 2007, ApJ, 670, 156

Daddi, E., Bournaud, F., Walter, F., et al. 2010, ApJ, 713, 686

Dahle, H., Gladders, M. D., Sharon, K., et al. 2013, ApJ, 773, 146

Dahle, H., Aghanim, N., Guennou, L., et al. 2016, A&A, 590, L4

Danielson, A. L. R., Swinbank, A. M., Smail, I., et al. 2017, ApJ, 840, 78

Davé, R., Oppenheimer, B. D., & Finlator, K. 2011, MNRAS, 415, 11

Dawson, K. S., Schlegel, D. J., Ahn, C. P., et al. 2013, AJ, 145, 10

De Breuck, C., Hunstead, R. W., Sadler, E. M., Rocca-Volmerange, B., & Klamer, I. 2004, MNRAS, 347, 837

De Breuck, C., van Breugel, W., Röttgering, H. J. A., & Miley, G. 2000, A&AS, 143, 303

Dekel, A., Birnboim, Y., Engel, G., et al. 2009, Nature, 457, 451

Delvecchio, I., Smolčić, V., Zamorani, G., et al. 2017, A&A, 602, A3

Dessauges-Zavadsky, M., D'Odorico, S., Schaerer, D., et al. 2010, A&A, 510, A26

Dey, A., Bian, C., Soifer, B. T., et al. 2005, ApJ, 629, 654

Dickinson, M., Papovich, C., Ferguson, H. C., & Budavári, T. 2003, ApJ, 587, 25

Dijkstra, M. 2017, ArXiv e-prints, arXiv:1704.03416

Dijkstra, M., Lidz, A., & Wyithe, J. S. B. 2007, MNRAS, 377, 1175

Dijkstra, M., & Loeb, A. 2009, MNRAS, 400, 1109

Dowell, C. D., Conley, A., Glenn, J., et al. 2014, ApJ, 780, 75

Draine, B. T. 2006, ApJ, 636, 1114

Du, X., Shapley, A. E., Reddy, N. A., et al. 2018, ArXiv e-prints, arXiv:1803.05912

Eisenstein, D. J., Weinberg, D. H., Agol, E., et al. 2011, AJ, 142, 72

Eldridge, J. J., & Stanway, E. R. 2009, MNRAS, 400, 1019

—. 2016, MNRAS, 462, 3302

Eldridge, J. J., Stanway, E. R., Xiao, L., et al. 2017, PASA, 34, e058

Ellingson, E., Yee, H. K. C., Bechtold, J., & Elston, R. 1996, ApJ, 466, L71

Ellis, R. S., McLure, R. J., Dunlop, J. S., et al. 2013, ApJ, 763, L7

Elmegreen, B. G., & Elmegreen, D. M. 2005, ApJ, 627, 632

Emonts, B. H. C., Lehnert, M. D., Villar-Martín, M., et al. 2016, Science, 354, 1128

Emonts, B. H. C., Lehnert, M. D., Dannerbauer, H., et al. 2018, MNRAS, 477, L60

Erb, D. K. 2015, Nature, 523, 169

Erb, D. K., Pettini, M., Shapley, A. E., et al. 2010, ApJ, 719, 1168

Erb, D. K., Steidel, C. C., Shapley, A. E., et al. 2006, ApJ, 646, 107

Falgarone, E., Zwaan, M. A., Godard, B., et al. 2017, Nature, 548, 430

Fardal, M. A., Katz, N., Gardner, J. P., et al. 2001, ApJ, 562, 605

Farrah, D., Verma, A., Oliver, S., Rowan-Robinson, M., & McMahon, R. 2002, MNRAS, 329, 605

Farrah, D., Rowan-Robinson, M., Oliver, S., et al. 2001, MNRAS, 326, 1333

Feltre, A., Charlot, S., & Gutkin, J. 2016, MNRAS, 456, 3354

Finkelstein, S. L., Rhoads, J. E., Malhotra, S., & Grogin, N. 2009, ApJ, 691, 465

Finkelstein, S. L., Cohen, S. H., Windhorst, R. A., et al. 2011a, ApJ, 735, 5

Finkelstein, S. L., Hill, G. J., Gebhardt, K., et al. 2011b, ApJ, 729, 140

Finley, H., Bouché, N., Contini, T., et al. 2017, A&A, 605, A118

France, K., Nell, N., Green, J. C., & Leitherer, C. 2010, ApJ, 722, L80

Francis, P. J., Woodgate, B. E., Warren, S. J., et al. 1996, ApJ, 457, 490

Fu, H., Cooray, A., Feruglio, C., et al. 2013, Nature, 498, 338

Fu, H., Hennawi, J. F., Prochaska, J. X., et al. 2016, ApJ, 832, 52

Fynbo, J. U., Møller, P., & Warren, S. J. 1999, MNRAS, 305, 849

Gaia Collaboration, Brown, A. G. A., Vallenari, A., et al. 2016, A&A, 595, A2

Gallagher, J. S., & Hunter, D. A. 1983, ApJ, 274, 141

Gavazzi, R., Treu, T., Koopmans, L. V. E., et al. 2008, ApJ, 677, 1046

Gavazzi, R., Treu, T., Marshall, P. J., Brault, F., & Ruff, A. 2012, ApJ, 761, 170

Gavazzi, R., Treu, T., Rhodes, J. D., et al. 2007, ApJ, 667, 176

Gavazzi, R., Cooray, A., Conley, A., et al. 2011, ApJ, 738, 125

Gawiser, E., Francke, H., Lai, K., et al. 2007, ApJ, 671, 278

Geach, J. E., Matsuda, Y., Smail, I., et al. 2005, MNRAS, 363, 1398

Geach, J. E., Alexander, D. M., Lehmer, B. D., et al. 2009, ApJ, 700, 1

Geach, J. E., Bower, R. G., Alexander, D. M., et al. 2014, ApJ, 793, 22

Geller, M. J., & Huchra, J. P. 1989, Science, 246, 897

Giavalisco, M., Steidel, C. C., & Szalay, A. S. 1994, ApJ, 425, L5

Ginolfi, M., Maiolino, R., Carniani, S., et al. 2018, MNRAS, 476, 2421

González, J. E., Lacey, C. G., Baugh, C. M., & Frenk, C. S. 2011, MNRAS, 413, 749

González Delgado, R. M., Leitherer, C., Heckman, T., et al. 1998, ApJ, 495, 698

Greenstein, J. L., & Matthews, T. A. 1963, AJ, 68, 279

Greve, T. R., Bertoldi, F., Smail, I., et al. 2005, MNRAS, 359, 1165

Griffin, M. J., Abergel, A., Abreu, A., et al. 2010, A&A, 518, L3

Guo, Y., Ferguson, H. C., Bell, E. F., et al. 2015, ApJ, 800, 39

Gwyn, S. D. J. 2008, PASP, 120, 212

Haan, S., Surace, J. A., Armus, L., et al. 2011, AJ, 141, 100

Hagen, A., Ciardullo, R., Gronwall, C., et al. 2014, ApJ, 786, 59

Haiman, Z., Spaans, M., & Quataert, E. 2000, ApJ, 537, L5

Hainline, K. N., Shapley, A. E., Greene, J. E., & Steidel, C. C. 2011a, ApJ, 733, 31

Hainline, K. N., Shapley, A. E., Kornei, K. A., et al. 2009, ApJ, 701, 52

Hainline, L. J., Blain, A. W., Smail, I., et al. 2011b, ApJ, 740, 96

Halliday, C., Daddi, E., Cimatti, A., et al. 2008, A&A, 479, 417

Hamann, W.-R., Barniske, A., Liermann, A., et al. 2011, Bulletin de la Societe Royale des Sciences de Liege, 80, 98

Hashimoto, T., Verhamme, A., Ouchi, M., et al. 2015, ApJ, 812, 157

Hashimoto, T., Laporte, N., Mawatari, K., et al. 2018, ArXiv e-prints, arXiv:1805.05966

Hayes, M. 2015, PASA, 32, e027

Hayes, M., Scarlata, C., & Siana, B. 2011, Nature, 476, 304

Hayward, C. C., Narayanan, D., Kereš, D., et al. 2013, MNRAS, 428, 2529

Hayward, C. C., & Smith, D. J. B. 2015, MNRAS, 446, 1512

Heckman, T. M., Lehnert, M. D., Miley, G. K., & van Breugel, W. 1991a, ApJ, 381, 373

Heckman, T. M., Lehnert, M. D., van Breugel, W., & Miley, G. K. 1991b, ApJ, 370, 78

Heckman, T. M., Robert, C., Leitherer, C., Garnett, D. R., & van der Rydt, F. 1998, ApJ, 503, 646

Hennawi, J. F., Prochaska, J. X., Cantalupo, S., & Arrigoni-Battaia, F. 2015, Science, 348, 779

Hezaveh, Y. D., Marrone, D. P., & Holder, G. P. 2012, ApJ, 761, 20

Hodge, J. A., Swinbank, A. M., Simpson, J. M., et al. 2016, ApJ, 833, 103

Hopkins, P. F., Kereš, D., Oñorbe, J., et al. 2014, MNRAS, 445, 581

Hu, E. M., Cowie, L. L., & McMahon, R. G. 1998, ApJ, 502, L99

Hu, E. M., Cowie, L. L., Songaila, A., et al. 2016, ApJ, 825, L7

Hughes, D. H., Serjeant, S., Dunlop, J., et al. 1998, Nature, 394, 241

Humphrey, A., Villar-Martín, M., Vernet, J., et al. 2008, MNRAS, 383, 11

Ivison, R. J., Smail, I., Le Borgne, J.-F., et al. 1998, MNRAS, 298, 583

Ivison, R. J., Smail, I., Papadopoulos, P. P., et al. 2010a, MNRAS, 404, 198

Ivison, R. J., Greve, T. R., Smail, I., et al. 2002, MNRAS, 337, 1

Ivison, R. J., Morrison, G. E., Biggs, A. D., et al. 2008, MNRAS, 390, 1117

Ivison, R. J., Magnelli, B., Ibar, E., et al. 2010b, A&A, 518, L31

Ivison, R. J., Swinbank, A. M., Smail, I., et al. 2013, ApJ, 772, 137

Ivison, R. J., Lewis, A. J. R., Weiss, A., et al. 2016, ApJ, 832, 78

Iye, M., Ota, K., Kashikawa, N., et al. 2006, Nature, 443, 186

Jõeveer, M., Einasto, J., & Tago, E. 1978, MNRAS, 185, 357

Jacobs, C., Glazebrook, K., Collett, T., More, A., & McCarthy, C. 2017, MNRAS, 471, 167

James, B. L., Auger, M., Pettini, M., et al. 2018, ArXiv e-prints, arXiv:1802.00455

James, B. L., Pettini, M., Christensen, L., et al. 2014, MNRAS, 440, 1794

Jiménez-Andrade, E. F., Magnelli, B., Karim, A., et al. 2017, ArXiv e-prints, arXiv:1710.10181

Jones, G. C., Carilli, C. L., Shao, Y., et al. 2017, ApJ, 850, 180

Jones, T., Stark, D. P., & Ellis, R. S. 2012, ApJ, 751, 51

Kashikawa, N., Shimasaku, K., Yasuda, N., et al. 2004, PASJ, 56, 1011

Kashikawa, N., Shimasaku, K., Matsuda, Y., et al. 2011, ApJ, 734, 119

Keel, W. C., Cohen, S. H., Windhorst, R. A., & Waddington, I. 1999, AJ, 118, 2547

Kelly, P. L., Rodney, S. A., Treu, T., et al. 2015, Science, 347, 1123

Kelly, P. L., Diego, J. M., Rodney, S., et al. 2018, Nature Astronomy, 2, 334

Kennicutt, Jr., R. C. 1998, ARA&A, 36, 189

Kennicutt, Jr., R. C., Armus, L., Bendo, G., et al. 2003, PASP, 115, 928

Kereš, D., Katz, N., Weinberg, D. H., & Davé, R. 2005, MNRAS, 363, 2

Kimm, T., Slyz, A., Devriendt, J., & Pichon, C. 2011, MNRAS, 413, L51

Kojima, T., Ouchi, M., Nakajima, K., et al. 2017, PASJ, 69, 44

Kollmeier, J. A., Zheng, Z., Davé, R., et al. 2010, ApJ, 708, 1048

Kriek, M., van Dokkum, P. G., Labbé, I., et al. 2009, ApJ, 700, 221

Kudritzki, R.-P., & Puls, J. 2000, ARA&A, 38, 613

Kurk, J. D., Pentericci, L., Röttgering, H. J. A., & Miley, G. K. 2002, in Revista Mexicana de Astronomia y Astrofisica Conference Series, Vol. 13, Revista Mexicana de Astronomia y Astrofisica Conference Series, ed. W. J. Henney, W. Steffen, L. Binette, & A. Raga, 191–195

Lagache, G., Puget, J.-L., & Dole, H. 2005, ARA&A, 43, 727

Laporte, N., Streblyanska, A., Clement, B., et al. 2014, A&A, 562, L8

Laporte, N., Streblyanska, A., Kim, S., et al. 2015, A&A, 575, A92

Laporte, N., Infante, L., Troncoso Iribarren, P., et al. 2016, ApJ, 820, 98

Laporte, N., Ellis, R. S., Boone, F., et al. 2017, ApJ, 837, L21

Law, D. R., Shapley, A. E., Steidel, C. C., et al. 2012, Nature, 487, 338

Lawrence, A., & Elvis, M. 1982, ApJ, 256, 410

Lawrence, A., Warren, S. J., Almaini, O., et al. 2007, MNRAS, 379, 1599

Le Fèvre, O., Cassata, P., Cucciati, O., et al. 2013, A&A, 559, A14

Leclercq, F., Bacon, R., Wisotzki, L., et al. 2017, A&A, 608, A8

Leitherer, C., Ekström, S., Meynet, G., et al. 2014, ApJS, 212, 14

Leitherer, C., Leão, J. R. S., Heckman, T. M., et al. 2001, ApJ, 550, 724

Leitherer, C., Ortiz Otálvaro, P. A., Bresolin, F., et al. 2010, ApJS, 189, 309

Leitherer, C., Tremonti, C. A., Heckman, T. M., & Calzetti, D. 2011, AJ, 141, 37

Leitherer, C., Schaerer, D., Goldader, J. D., et al. 1999, ApJS, 123, 3

Lilly, S. J., Le Fevre, O., Hammer, F., & Crampton, D. 1996, ApJ, 460, L1

Lin, H., Buckley-Geer, E., Allam, S. S., et al. 2009, ApJ, 699, 1242

Lonsdale, C. J., Smith, H. E., Rowan-Robinson, M., et al. 2003, PASP, 115, 897

Lu, N., Zhao, Y., Díaz-Santos, T., et al. 2017, ApJ, 842, L16

Ly, C., Malkan, M. A., Treu, T., et al. 2009, ApJ, 697, 1410

Ma, B., Cooray, A., Calanog, J. A., et al. 2015, ApJ, 814, 17

MacKenzie, T. P., Scott, D., Smail, I., et al. 2014, MNRAS, 445, 201

Madau, P., & Dickinson, M. 2014, ARA&A, 52, 415

Madau, P., Ferguson, H. C., Dickinson, M. E., et al. 1996, MNRAS, 283, 1388

Madau, P., & Haardt, F. 2015, ApJ, 813, L8

Magdis, G. E., Elbaz, D., Daddi, E., et al. 2010a, ApJ, 714, 1740

Magdis, G. E., Rigopoulou, D., Huang, J.-S., & Fazio, G. G. 2010b, MNRAS, 401, 1521

Magdis, G. E., Elbaz, D., Hwang, H. S., et al. 2010c, ApJ, 720, L185

Magdis, G. E., Rigopoulou, D., Hopwood, R., et al. 2014, ApJ, 796, 63

Magdis, G. E., Rigopoulou, D., Daddi, E., et al. 2017, A&A, 603, A93

Magnelli, B., Lutz, D., Santini, P., et al. 2012, A&A, 539, A155

Magnelli, B., Ivison, R. J., Lutz, D., et al. 2015, A&A, 573, A45

Malhotra, S., & Rhoads, J. E. 2004, ApJ, 617, L5

Mannucci, F., Cresci, G., Maiolino, R., et al. 2009, MNRAS, 398, 1915

Marques-Chaves, R., Pérez-Fournon, I., Shu, Y., et al. 2017, ApJ, 834, L18

Marques-Chaves, R., Pérez-Fournon, I., Gavazzi, R., et al. 2018, ApJ, 854, 151

Marrone, D. P., Spilker, J. S., Hayward, C. C., et al. 2018, Nature, 553, 51

Martin, C. L. 2005, ApJ, 621, 227

Martin, C. L., Shapley, A. E., Coil, A. L., et al. 2012, ApJ, 760, 127

Maseda, M. V., Brinchmann, J., Franx, M., et al. 2017, A&A, 608, A4

Matsuda, Y., Iono, D., Ohta, K., et al. 2007, ApJ, 667, 667

Matsuda, Y., Yamada, T., Hayashino, T., et al. 2004, AJ, 128, 569

—. 2011, MNRAS, 410, L13

—. 2012, MNRAS, 425, 878

Matthee, J., Sobral, D., Darvish, B., et al. 2017, MNRAS, 472, 772

Matthee, J., Sobral, D., Santos, S., et al. 2015, MNRAS, 451, 400

Matthews, T. A., & Sandage, A. R. 1963, ApJ, 138, 30

Mauduit, J.-C., Lacy, M., Farrah, D., et al. 2012, PASP, 124, 714

Maxfield, L., Spinrad, H., Stern, D., Dey, A., & Dickinson, M. 2002, AJ, 123, 2321

McCarthy, P. J., Spinrad, H., Djorgovski, S., et al. 1987, ApJ, 319, L39

McCarthy, P. J., Spinrad, H., & van Breugel, W. 1995, ApJS, 99, 27

Messias, H., Dye, S., Nagar, N., et al. 2014, A&A, 568, A92

Meurer, G. R., Heckman, T. M., & Calzetti, D. 1999, ApJ, 521, 64

Michałowski, M. J., Dunlop, J. S., Cirasuolo, M., et al. 2012, A&A, 541, A85

Michałowski, M. J., Dunlop, J. S., Koprowski, M. P., et al. 2017, MNRAS, 469, 492

Miettinen, O., Delvecchio, I., Smolčić, V., et al. 2017, A&A, 606, A17

Momose, R., Ouchi, M., Nakajima, K., et al. 2014, MNRAS, 442, 110

—. 2016, MNRAS, 457, 2318

Morais, S. G., Humphrey, A., Villar-Martín, M., et al. 2017, MNRAS, 465, 2698

More, A., Cabanac, R., More, S., et al. 2012, ApJ, 749, 38

More, A., Verma, A., Marshall, P. J., et al. 2016, MNRAS, 455, 1191

Murayama, T., Taniguchi, Y., Scoville, N. Z., et al. 2007, ApJS, 172, 523

Nakajima, K., Ellis, R. S., Iwata, I., et al. 2016, ApJ, 831, L9

Nakajima, K., Fletcher, T., Ellis, R. S., Robertson, B. E., & Iwata, I. 2018a, MNRAS, arXiv:1801.03085

Nakajima, K., & Ouchi, M. 2014, MNRAS, 442, 900

Nakajima, K., Ouchi, M., Shimasaku, K., et al. 2012, ApJ, 745, 12

Nakajima, K., Schaerer, D., Le Fèvre, O., et al. 2018b, A&A, 612, A94

Narayanan, D., Turk, M., Feldmann, R., et al. 2015, Nature, 525, 496

Nayyeri, H., Keele, M., Cooray, A., et al. 2016, ApJ, 823, 17

Nayyeri, H., Cooray, A., Jullo, E., et al. 2017, ApJ, 844, 82

Negrello, M., Hopwood, R., De Zotti, G., et al. 2010, Science, 330, 800

Negrello, M., Amber, S., Amvrosiadis, A., et al. 2017, MNRAS, 465, 3558

Nesvadba, N. P. H., Lehnert, M. D., Eisenhauer, F., et al. 2006, ApJ, 650, 693

Newville, M., Stensitzki, T., Allen, D. B., & Ingargiola, A. 2014, LMFIT: Non-Linear Least-Square Minimization and Curve-Fitting for Python, doi:10.5281/zenodo.11813

Nilsson, K. K., Fynbo, J. P. U., Møller, P., Sommer-Larsen, J., & Ledoux, C. 2006, A&A, 452, L23

North, P. L., Courbin, F., Eigenbrod, A., & Chelouche, D. 2012, A&A, 542, A91

Oesch, P. A., Bouwens, R. J., Illingworth, G. D., et al. 2013, ApJ, 773, 75

Oesch, P. A., van Dokkum, P. G., Illingworth, G. D., et al. 2015, ApJ, 804, L30

Oguri, M., Inada, N., Pindor, B., et al. 2006, AJ, 132, 999

Oguri, M., Ofek, E. O., Inada, N., et al. 2008, ApJ, 676, L1

Oke, J. B., & Gunn, J. E. 1983, ApJ, 266, 713

Olivares, V., Treister, E., Privon, G. C., et al. 2016, ApJ, 827, 57

Oliver, S. J., Bock, J., Altieri, B., et al. 2012, MNRAS, 424, 1614

Ono, Y., Ouchi, M., Shimasaku, K., et al. 2010, MNRAS, 402, 1580

Ono, Y., Ouchi, M., Harikane, Y., et al. 2017, PASJ, arXiv:1704.06004

Osterbrock, D. E. 1962, ApJ, 135, 195

Ota, K., Iye, M., Kashikawa, N., et al. 2017, ApJ, 844, 85

Oteo, I., Bongiovanni, Á., Cepa, J., et al. 2013, MNRAS, 433, 2706

Oteo, I., Ivison, R. J., Dunne, L., et al. 2016, ApJ, 827, 34

—. 2018, ApJ, 856, 72

Ouchi, M., Shimasaku, K., Furusawa, H., et al. 2003, ApJ, 582, 60

Ouchi, M., Shimasaku, K., Akiyama, M., et al. 2005, ApJ, 620, L1

—. 2008, ApJS, 176, 301

Ouchi, M., Ono, Y., Egami, E., et al. 2009, ApJ, 696, 1164

Ouchi, M., Shimasaku, K., Furusawa, H., et al. 2010, ApJ, 723, 869

Ouchi, M., Harikane, Y., Shibuya, T., et al. 2018, PASJ, 70, S13

Overzier, R. A., Nesvadba, N. P. H., Dijkstra, M., et al. 2013, ApJ, 771, 89

Oyaizu, H., Lima, M., Cunha, C. E., et al. 2008, ApJ, 674, 768

Paraficz, D., Courbin, F., Tramacere, A., et al. 2016, A&A, 592, A75

Partridge, R. B., & Peebles, P. J. E. 1967, ApJ, 147, 868

Patrício, V., Richard, J., Verhamme, A., et al. 2016, MNRAS, 456, 4191

Paulino-Afonso, A., Sobral, D., Ribeiro, B., et al. 2018, MNRAS, 476, 5479

Peng, C. Y., Ho, L. C., Impey, C. D., & Rix, H.-W. 2002, AJ, 124, 266

—. 2010, AJ, 139, 2097

Penzias, A. A., & Wilson, R. W. 1965, ApJ, 142, 419

Pérez-González, P. G., Cava, A., Barro, G., et al. 2013, ApJ, 762, 46

Pérez-Montero, E., & Amorín, R. 2017, MNRAS, 467, 1287

Perlmutter, S., Aldering, G., Goldhaber, G., et al. 1999, ApJ, 517, 565

Pettini, M., Rix, S. A., Steidel, C. C., et al. 2002, ApJ, 569, 742

Pettini, M., Steidel, C. C., Adelberger, K. L., Dickinson, M., & Giavalisco, M. 2000, ApJ, 528, 96

Pilbratt, G. L., Riedinger, J. R., Passvogel, T., et al. 2010, A&A, 518, L1

Planck Collaboration, Ade, P. A. R., Aghanim, N., et al. 2016, A&A, 594, A13

Prescott, M. K. M., Kashikawa, N., Dey, A., & Matsuda, Y. 2008, ApJ, 678, L77

Prinja, R. K. 1990, MNRAS, 246, 392

Quider, A. M., Pettini, M., Shapley, A. E., & Steidel, C. C. 2009, MNRAS, 398, 1263

Quider, A. M., Shapley, A. E., Pettini, M., Steidel, C. C., & Stark, D. P. 2010, MNRAS, 402, 1467

Rauch, M., Haehnelt, M., Bunker, A., et al. 2008, ApJ, 681, 856

Rawle, T. D., Egami, E., Bussmann, R. S., et al. 2014, ApJ, 783, 59

Reddy, N., Dickinson, M., Elbaz, D., et al. 2012, ApJ, 744, 154

Reddy, N. A., Erb, D. K., Pettini, M., Steidel, C. C., & Shapley, A. E. 2010, ApJ, 712, 1070

Reddy, N. A., & Steidel, C. C. 2009, ApJ, 692, 778

Reddy, N. A., Steidel, C. C., Fadda, D., et al. 2006, ApJ, 644, 792

Reddy, N. A., Steidel, C. C., Pettini, M., et al. 2008, ApJS, 175, 48

Rees, M. J. 1984, ARA&A, 22, 471

Refregier, A. 2003, ARA&A, 41, 645

Reuland, M., van Breugel, W., Röttgering, H., et al. 2003, ApJ, 592, 755

Rhoads, J. E., Malhotra, S., Dey, A., et al. 2000, ApJ, 545, L85

Ribeiro, B., Le Fèvre, O., Tasca, L. A. M., et al. 2016, A&A, 593, A22

Richard, J., Jones, T., Ellis, R., et al. 2011, MNRAS, 413, 643

Riechers, D. A., Cooray, A., Omont, A., et al. 2011, ApJ, 733, L12

Riechers, D. A., Bradford, C. M., Clements, D. L., et al. 2013, Nature, 496, 329

Riechers, D. A., Carilli, C. L., Capak, P. L., et al. 2014, ApJ, 796, 84

Riechers, D. A., Leung, T. K. D., Ivison, R. J., et al. 2017, ApJ, 850, 1

Riess, A. G., Filippenko, A. V., Challis, P., et al. 1998, AJ, 116, 1009

Rigby, J. R., Bayliss, M. B., Gladders, M. D., et al. 2015, ApJ, 814, L6

Rigby, J. R., Bayliss, M. B., Sharon, K., et al. 2018a, AJ, 155, 104

Rigby, J. R., Bayliss, M. B., Chisholm, J., et al. 2018b, ApJ, 853, 87

Rigopoulou, D., Pereira-Santaella, M., Magdis, G. E., et al. 2018, MNRAS, 473, 20

Rix, S. A., Pettini, M., Leitherer, C., et al. 2004, ApJ, 615, 98

Roberts-Borsani, G. W., Bouwens, R. J., Oesch, P. A., et al. 2016, ApJ, 823, 143

Roettgering, H. J. A., Lacy, M., Miley, G. K., Chambers, K. C., & Saunders, R. 1994, A&AS, 108, 79

Rowan-Robinson, M. 1977, ApJ, 213, 635

Rubin, K. H. R., Prochaska, J. X., Koo, D. C., & Phillips, A. C. 2012, ApJ, 747, L26

Rupke, D. S., Veilleux, S., & Sanders, D. B. 2005a, ApJS, 160, 87

—. 2005b, ApJS, 160, 115

Saito, T., Matsuda, Y., Lacey, C. G., et al. 2015, MNRAS, 447, 3069

Salomé, P., Guélin, M., Downes, D., et al. 2012, A&A, 545, A57

Salpeter, E. E. 1955, ApJ, 121, 161

Santos, S., Sobral, D., & Matthee, J. 2016, MNRAS, 463, 1678

Sato, T., Martin, C. L., Noeske, K. G., Koo, D. C., & Lotz, J. M. 2009, ApJ, 696, 214

Savage, B. D., & Sembach, K. R. 1991, ApJ, 379, 245

Schaerer, D. 2003, A&A, 397, 527

Schaerer, D., & Pelló, R. 2002, Ap&SS, 281, 475

Schaerer, D., & Vacca, W. D. 1998, ApJ, 497, 618

Schaerer, D., & Verhamme, A. 2008, A&A, 480, 369

Schinnerer, E., Groves, B., Sargent, M. T., et al. 2016, ApJ, 833, 112

Schlafly, E. F., & Finkbeiner, D. P. 2011, ApJ, 737, 103

Schneider, D. P., Hall, P. B., Richards, G. T., et al. 2005, AJ, 130, 367

Scott, K. S., Lupu, R. E., Aguirre, J. E., et al. 2011, ApJ, 733, 29

Seitz, S., Saglia, R. P., Bender, R., et al. 1998, MNRAS, 298, 945

Serjeant, S. 2012, MNRAS, 424, 2429

Seyfert, C. K. 1943, ApJ, 97, 28

Shapley, A. E., Steidel, C. C., Adelberger, K. L., et al. 2001, ApJ, 562, 95

Shapley, A. E., Steidel, C. C., Pettini, M., & Adelberger, K. L. 2003, ApJ, 588, 65

Shibuya, T., Ouchi, M., Harikane, Y., et al. 2018, PASJ, 70, S15

Shu, Y., Bolton, A. S., Moustakas, L. A., et al. 2016a, ApJ, 820, 43

Shu, Y., Bolton, A. S., Brownstein, J. R., et al. 2015, ApJ, 803, 71

Shu, Y., Bolton, A. S., Kochanek, C. S., et al. 2016b, ApJ, 824, 86

Shu, Y., Bolton, A. S., Mao, S., et al. 2016c, ApJ, 833, 264

Shu, Y., Brownstein, J. R., Bolton, A. S., et al. 2017, ApJ, 851, 48

Siana, B., Teplitz, H. I., Chary, R.-R., Colbert, J., & Frayer, D. T. 2008, ApJ, 689, 59

Siana, B., Smail, I., Swinbank, A. M., et al. 2009, ApJ, 698, 1273

Silk, J. 1977, ApJ, 211, 638

Smail, I., Chapman, S. C., Ivison, R. J., et al. 2003, MNRAS, 342, 1185

Smail, I., Ivison, R. J., & Blain, A. W. 1997, ApJ, 490, L5

Smail, I., Swinbank, A. M., Richard, J., et al. 2007, ApJ, 654, L33

Smit, R., Swinbank, A. M., Massey, R., et al. 2017, MNRAS, 467, 3306

Sobral, D., Matthee, J., Darvish, B., et al. 2015, ApJ, 808, 139

Sobral, D., Santos, S., Matthee, J., et al. 2018a, MNRAS, arXiv:1712.04451

Sobral, D., Matthee, J., Best, P., et al. 2017, MNRAS, 466, 1242

Sobral, D., Matthee, J., Darvish, B., et al. 2018b, ArXiv e-prints, arXiv:1802.10102

Sommariva, V., Mannucci, F., Cresci, G., et al. 2012, A&A, 539, A136

Songaila, A., Hu, E. M., Barger, A. J., et al. 2018, ArXiv e-prints, arXiv:1805.00490

Sonnenfeld, A., Chan, J. H. H., Shu, Y., et al. 2018, PASJ, 70, S29

Spilker, J. S., Aravena, M., Marrone, D. P., et al. 2015, ApJ, 811, 124

Spitzer, L. 1978, Physical processes in the interstellar medium, doi:10.1002/9783527617722

Stanway, E. R., Eldridge, J. J., & Becker, G. D. 2016, MNRAS, 456, 485

Steidel, C. C., Adelberger, K. L., Giavalisco, M., Dickinson, M., & Pettini, M. 1999, ApJ, 519, 1

Steidel, C. C., Adelberger, K. L., Shapley, A. E., et al. 2000, ApJ, 532, 170

—. 2003, ApJ, 592, 728

Steidel, C. C., Bogosavljević, M., Shapley, A. E., et al. 2011, ApJ, 736, 160

Steidel, C. C., Erb, D. K., Shapley, A. E., et al. 2010, ApJ, 717, 289

Steidel, C. C., Giavalisco, M., Pettini, M., Dickinson, M., & Adelberger, K. L. 1996, ApJ, 462, L17

Steidel, C. C., & Hamilton, D. 1993, AJ, 105, 2017

Steidel, C. C., Pettini, M., & Hamilton, D. 1995, AJ, 110, 2519

Steidel, C. C., Shapley, A. E., Pettini, M., et al. 2004, ApJ, 604, 534

Steidel, C. C., Strom, A. L., Pettini, M., et al. 2016, ApJ, 826, 159

Strandet, M. L., Weiss, A., De Breuck, C., et al. 2017, ApJ, 842, L15

Swinbank, A. M., Chapman, S. C., Smail, I., et al. 2006, MNRAS, 371, 465

Swinbank, A. M., Smail, I., Chapman, S. C., et al. 2004, ApJ, 617, 64

Swinbank, A. M., Smail, I., Bower, R. G., et al. 2005, MNRAS, 359, 401

Swinbank, A. M., Lacey, C. G., Smail, I., et al. 2008, MNRAS, 391, 420

Tacconi, L. J., Genzel, R., Smail, I., et al. 2008, ApJ, 680, 246

Tacconi, L. J., Genzel, R., Neri, R., et al. 2010, Nature, 463, 781

Talia, M., Mignoli, M., Cimatti, A., et al. 2012, A&A, 539, A61

Taniguchi, Y., & Shioya, Y. 2000, ApJ, 532, L13

Taniguchi, Y., Ajiki, M., Nagao, T., et al. 2005, PASJ, 57, 165

Taniguchi, Y., Murayama, T., Scoville, N. Z., et al. 2009, ApJ, 701, 915

Thatte, N., Tecza, M., Clarke, F., et al. 2006, in Proc. SPIE, Vol. 6269, Society of Photo-Optical Instrumentation Engineers (SPIE) Conference Series, 62693L

Toft, S., Zabl, J., Richard, J., et al. 2017, Nature, 546, 510

Treu, T. 2010, ARA&A, 48, 87

Trump, J. R., Hall, P. B., Reichard, T. A., et al. 2006, ApJS, 165, 1

Urry, C. M., & Padovani, P. 1995, PASP, 107, 803

van der Wel, A., Franx, M., van Dokkum, P. G., et al. 2014, ApJ, 788, 28

Venemans, B. P., Röttgering, H. J. A., Miley, G. K., et al. 2007, A&A, 461, 823

Verhamme, A., Schaerer, D., Atek, H., & Tapken, C. 2008, A&A, 491, 89

Vieira, J. D., Marrone, D. P., Chapman, S. C., et al. 2013, Nature, 495, 344

Villar-Martín, M., Humphrey, A., De Breuck, C., et al. 2007a, MNRAS, 375, 1299

Villar-Martín, M., Sánchez, S. F., Humphrey, A., et al. 2007b, MNRAS, 378, 416

Villar-Martín, M., Vernet, J., di Serego Alighieri, S., et al. 2003, MNRAS, 346, 273

—. 2002, MNRAS, 336, 436

Villar-Martín, M., Sánchez, S. F., De Breuck, C., et al. 2006, MNRAS, 366, L1

Walsh, D., Carswell, R. F., & Weymann, R. J. 1979, Nature, 279, 381

Wang, L., Dutton, A. A., Stinson, G. S., et al. 2015, MNRAS, 454, 83

Wardlow, J. L., Cooray, A., De Bernardis, F., et al. 2013, ApJ, 762, 59

Wardlow, J. L., Malhotra, S., Zheng, Z., et al. 2014, ApJ, 787, 9

Weidinger, M., Møller, P., & Fynbo, J. P. U. 2004, Nature, 430, 999

Weidner, C., Kroupa, P., & Pflamm-Altenburg, J. 2011, MNRAS, 412, 979

Wilkins, S. M., Gonzalez-Perez, V., Lacey, C. G., & Baugh, C. M. 2012, MNRAS, 424, 1522

Wiseman, P., Perley, D. A., Schady, P., et al. 2017, A&A, 607, A107

Wisotzki, L., Bacon, R., Blaizot, J., et al. 2016, A&A, 587, A98

Wuyts, E., Rigby, J. R., Gladders, M. D., & Sharon, K. 2014, ApJ, 781, 61

Wuyts, E., Barrientos, L. F., Gladders, M. D., et al. 2010, ApJ, 724, 1182

Yang, H., Malhotra, S., Rhoads, J. E., et al. 2017, ApJ, 838, 4

Yee, H. K. C., Ellingson, E., Bechtold, J., Carlberg, R. G., & Cuillandre, J.-C. 1996, AJ, 111, 1783

York, D. G., Adelman, J., Anderson, Jr., J. E., et al. 2000, AJ, 120, 1579

Zakamska, N. L., Strauss, M. A., Krolik, J. H., et al. 2003, AJ, 126, 2125

Zavala, J. A., Montaña, A., Hughes, D. H., et al. 2018, Nature Astronomy, 2, 56

Zheng, Z.-Y., Malhotra, S., Rhoads, J. E., et al. 2016, ApJS, 226, 23

Zheng, Z.-Y., Wang, J., Rhoads, J., et al. 2017, ApJ, 842, L22

Zitrin, A., Labbé, I., Belli, S., et al. 2015, ApJ, 810, L12

Zwicky, F. 1937a, Physical Review, 51, 290

—. 1937b, Physical Review, 51, 679

# A

# Spectroscopic Features in the BELLS GALLERY LAEs

This appendix shows the GTC OSIRIS spectra of the six BELLS GALLERY lensed LAEs analyzed in chapter 3 (Figure A.1 to A.6). It presents also the measurements of the spectroscopic features associated to the low- and high-ionization ISM. These are presented in Tables A.1 and A.2, respectively.

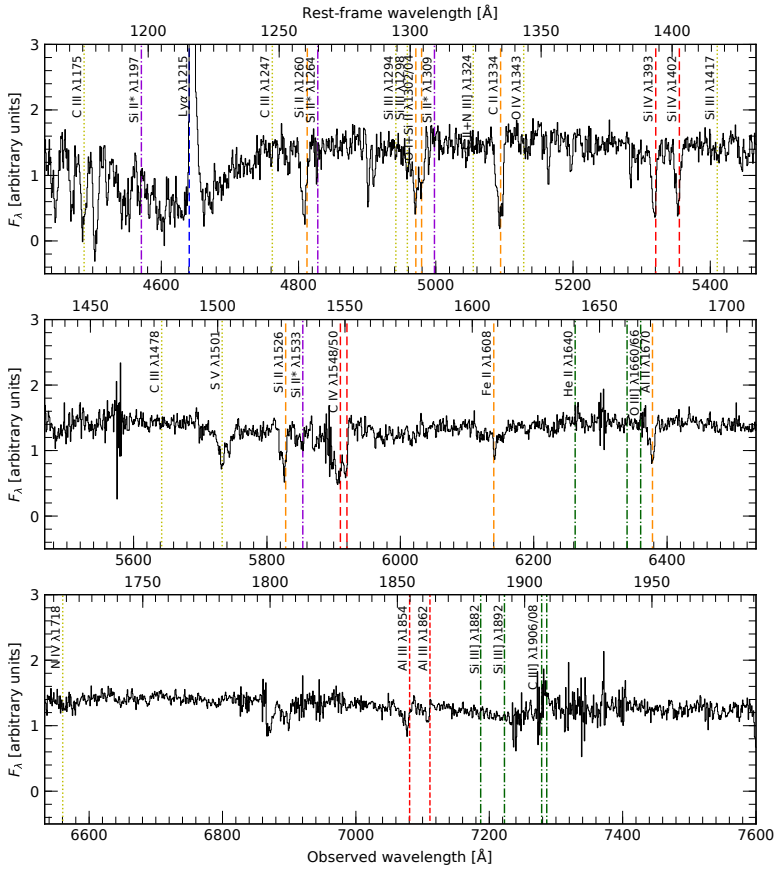


Figure A.1: Combined GTC/OSIRIS rest-frame UV spectrum of the lensed LAE BG0201+3228. Vertical lines identify absorption and emission features associated with: stellar photospheric absorption (yellow), low- and high-ionization ISM absorption (orange and red, respectively), nebular emission from H II regions (green), Ly$\alpha$ emission (blue), and fine-structure emission (violet).

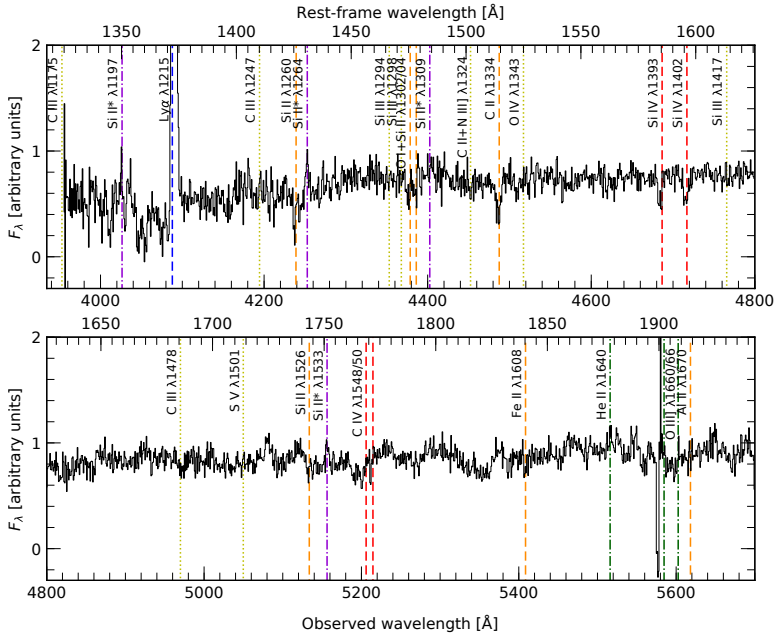


Figure A.2: Same as Figure A.1, but for BG0742+3341.

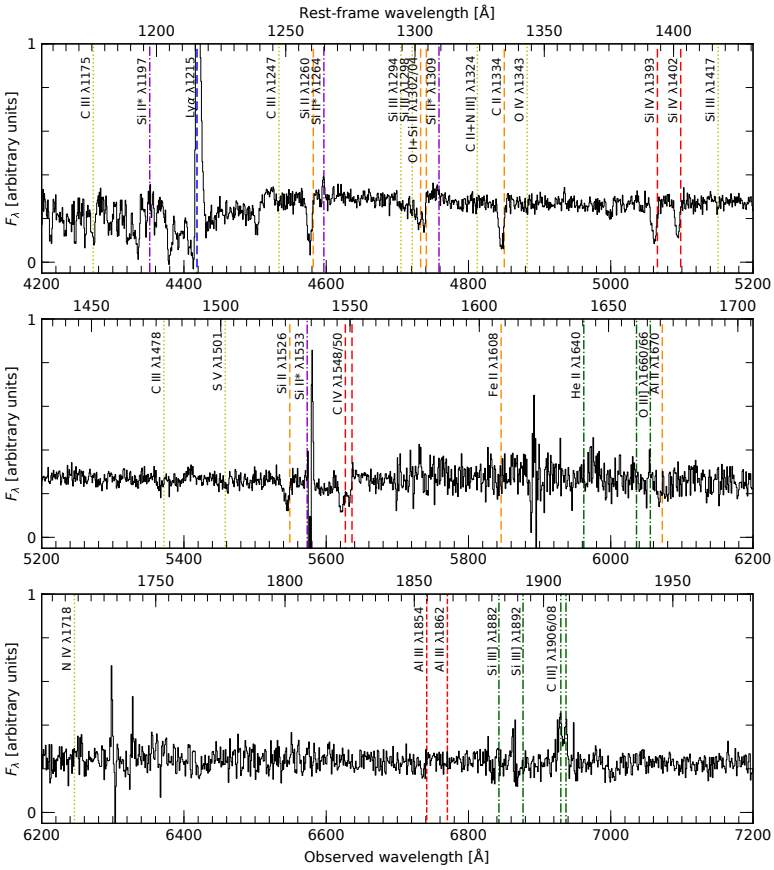


Figure A.3: Same as Figure A.1, but for BG0755+3445.

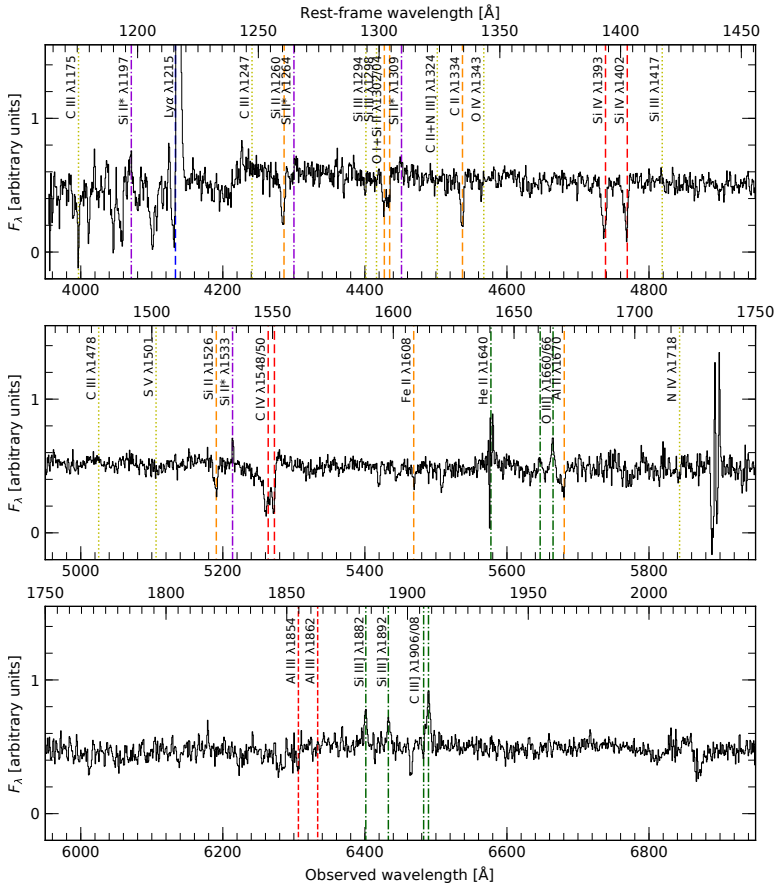


Figure A.4: Same as Figure A.1, but for BG0918+5104.

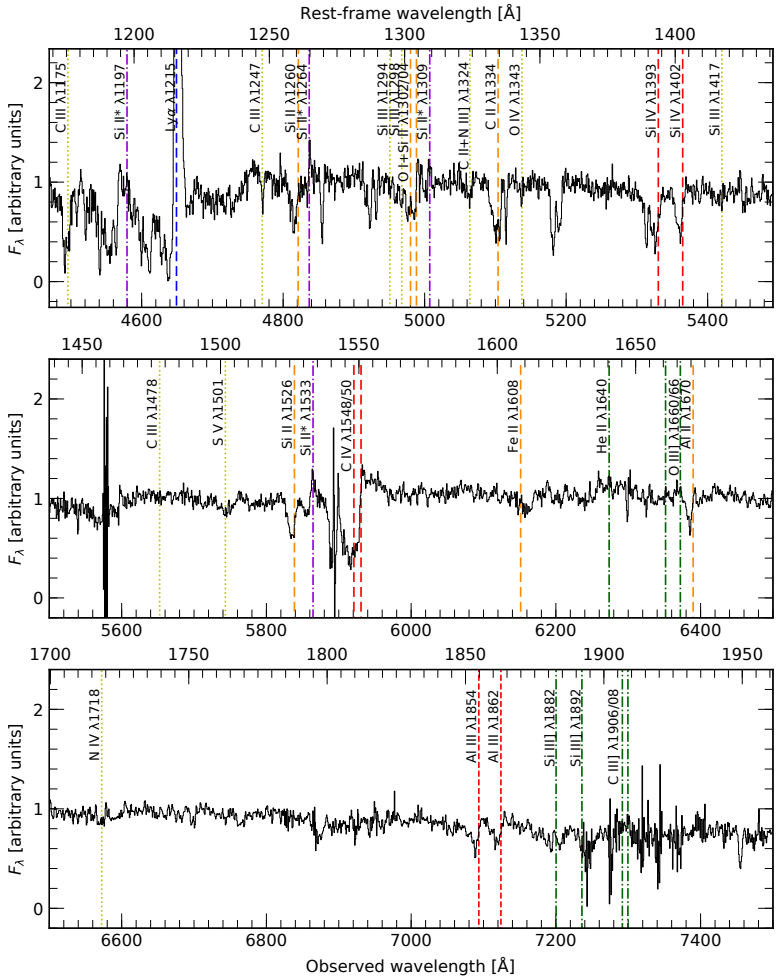


Figure A.5: Same as Figure A.1, but for BG1429+1202.

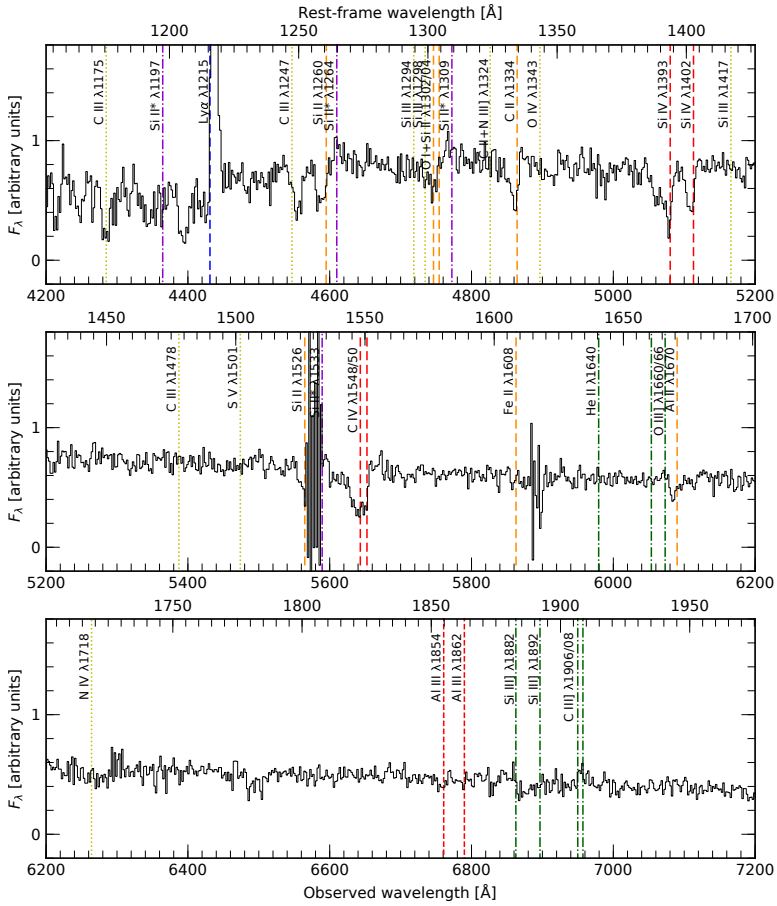


Figure A.6: Same as Figure A.1, but for BG1501+3042.

Table A.1: Low-ionization Interstellar Absorption Features.

| LAE | Si II | | O I | | Si II | | C II | | Si II | | Fe II | | Al II | |
|---|---|---|---|---|---|---|---|---|---|---|---|---|---|---|
| | $\lambda_0 = 1260.42$ | | $\lambda_0 = 1302.17$ | | $\lambda_0 = 1304.37$ | | $\lambda_0 = 1334.53$ | | $\lambda_0 = 1526.71$ | | $\lambda_0 = 1608.45$ | | $\lambda_0 = 1670.79$ | |
| | $EW_o$ (Å) | FWHM (km s$^{-1}$) | $EW_o$ (Å) | FWHM (km s$^{-1}$) | $EW_o$ (Å) | FWHM (km s$^{-1}$) | $EW_o$ (Å) | FWHM (km s$^{-1}$) | $EW_o$ (Å) | FWHM (km s$^{-1}$) | $EW_o$ (Å) | FWHM (km s$^{-1}$) | $EW_o$ (Å) | FWHM (km s$^{-1}$) |
| BG0201+3228 | 2.34 | 478.18 | 2.30 | 510.54 | 1.57 | 436.71 | 3.01 | 536.38 | 1.62 | 414.88 | 0.48 | $< 220$ | 1.13 | 284.92 |
| BG0742+3341 | 0.98 | 272.19 | 0.57 | 300.64 | 0.57 | 316.69 | 1.04 | 377.19 | 0.29 | 204.79 | - | - | - | - |
| BG0755+3445 | 1.62 | 416.65 | 0.91 | 365.28 | 0.65 | $< 220$ | 1.81 | 431.57 | 1.25 | 479.70 | - | - | - | - |
| BG0918+5104 | 1.32 | 344.76 | 0.82 | 402.20 | 0.63 | $< 220$ | 1.20 | 245.52 | 0.83 | 292.30 | 0.36 | $< 220$ | 0.43 | $< 220$ |
| BG1429+1202 | 1.09 | 476.02 | 0.80 | 396.24 | 0.70 | 325.11 | 1.92 | 776.08 | 1.14 | 508.17 | - | - | 0.62 | 471.99 |
| BG1501+3042 | 1.82[a] | 816.90[a] | 1.31 | 761.95 | 1.31 | 761.95 | 1.61 | 681.44 | - | - | - | - | 0.80 | $< 450$ |

**Notes.** — [a] The profiles are affected by other absorption lines from intervening systems at lower redshifts.

Table A.2: High-ionization Absorption Features.

| LAE | Si IV | | Si IV | | C IV | | C IV | | Al II | | Al II | |
|---|---|---|---|---|---|---|---|---|---|---|---|---|
| | $\lambda_0 = 1393.76$ | | $\lambda_0 = 1402.77$ | | $\lambda_0 = 1548.20$ | | $\lambda_0 = 1550.77$ | | $\lambda_0 = 1854.72$ | | $\lambda_0 = 1862.80$ | |
| | $EW_o$ (Å) | FWHM ($km\,s^{-1}$) | $EW_o$ (Å) | FWHM ($km\,s^{-1}$) | $EW_o$ (Å) | FWHM ($km\,s^{-1}$) | $EW_o$ (Å) | FWHM ($km\,s^{-1}$) | $EW_o$ (Å) | FWHM ($km\,s^{-1}$) | $EW_o$ (Å) | FWHM ($km\,s^{-1}$) |
| BG0201+3228 | 1.60 | 348.74 | 1.52 | 374.07 | 2.16 | 564.06 | 1.18 | 275.63 | 0.60 | 283.9 | 0.27 | $< 220$ |
| BG0742+3341 | 0.52 | 201.37 | 0.65 | 346.80 | 0.57 | 316.59 | 0.18 | $< 220$ | - | - | - | - |
| BG0755+3445 | 1.56 | 481.05 | 1.16 | 360.45 | 1.45 | 465.09 | 0.62 | 279.00 | - | - | - | - |
| BG0918+5104 | 1.59 | 326.58 | 1.43 | 311.34 | 2.63 | 635.88 | 0.79 | $< 220$ | - | - | - | - |
| BG1429+1202 | 2.06[a] | 741.32[a] | 1.31 | 521.40 | 4.58[b] | 1113.08[b] | 4.58[b] | 1113.08[b] | 0.80 | 362.8 | 0.70 | 420.96 |
| BG1501+3042 | 2.44[a] | 693.46[a] | 1.60 | 420.83 | 4.57[b] | 1191.09[b] | 4.57[b] | 1191.09[b] | - | - | - | - |

**Notes.** — [a] The profiles are affected by other absorption lines from intervening systems at lower redshifts; [b] Refers to the C IV $\lambda$1548,1550 doublet.